

Multiphysical dynamic fracture analysis of biomimetic composites based on non-Fourier heat conduction

by

Weilin Yang

A thesis submitted in partial fulfillment of the requirements for the degree of

Doctor of Philosophy

Department of Mechanical Engineering
University of Alberta

© Weilin Yang, 2023

Abstract

In the world of engineering, strength and toughness are two highly desirable properties to materials design. Biological materials have already mastered both of these properties within the threads they protect themselves in harsh nature. The key to both the biomaterial's ability to resist external injury and the highly energy dissipative behavior is a type of hierarchical structure called brick-and-mortar structure, which is comprised of soft collagen matrix and hard hydroxyapatite crystals. Recently, researchers have incorporated metal phases into various sizes of polymeric matrix to improve their mechanical properties. However, there is not as much fundamental understanding of how the heterogeneity of these combinations dictates fracture behavior, either in a single- or in multi-physical fields.

In this thesis, we use the non-Fourier heat conduction law to explore biomimetic gradation design under different surrounding environments. The thesis includes three parts of work. First, a multiphysical model was developed to investigate the fracture behavior of biomimetic materials under thermoelectromechanical loading. In particular, a piezoelectric material model is used to mimic the multiphysical behavior of biological materials, such as wood and nacre. A simplified, homogeneous piezoelectric material is used to mathematically model the dynamic multiphysical fracture behavior of biomimetic materials. With the aid of fractional heat conduction equation and Maxwell's equations, we analyze the effects of temperature and electrical disturbances on the stress-electric displacement intensity factors. In the second part, a brick-and-mortar graded (BM-GRAD) model was proposed to investigate how material heterogeneity interacts with its crack resistance. It was found that the BM-GRAD always shows a smaller zone of extreme stress localization as well as lower values of the normal stress, which significantly improves the crack

resistance. It is also highlighted that BM-GRAD microstructure is easier to form deflecting crack once a fracture happens and the crack propagation is more likely to be terminated. Finally, we combined the gradient design and multiphysical behavior and carried out a comprehensive analysis of various multiphysical, gradient designs in the third part. The results showed that multiphysical conditions have a significant influence on the fracture resistance of heterogeneous material, while temperature is a vital factor that cannot be ignored. To describe thermal transport more accurately in biomaterials, the non-Fourier theory incorporated with thermal relaxation effect describes thermal transport more accurately than classical heat conduction equations which indicates the speed of thermal propagation is infinite. The results of a cracked functionally graded piezoelectric strip mimicking biomaterials under thermoelectromechanical loading shows that a sudden temperature fall will cause an opening-mode failure risk, while a positive electric shock will slightly reduce the likelihood of fracture occurrence compared to a negative electric loading.

From our fracture resistance results, a strong dependence of peak stress on the electromechanical gradation coefficient Ω and thermal gradation coefficient Ψ was observed. Except the case of a singular thermal environment, the configuration without gradients demonstrates exceptional crack resistance performance. Incorporating graded design principles into biomimetic piezoelectric structures can effectively enhance their ability to resist crack propagation under single stress, single electric, and thermo-electromechanical environments. Specifically, the symmetric gradient configuration, characterized by a higher order of the electromechanical gradation coefficient Ω and thermal gradation coefficient Ψ , shows remarkable fracture resistance under single stress or single electric environment. For coupled heating-mechanical-electrical and cooling-mechanical-electrical fields, the symmetric functional gradient

configuration with $(\Omega, \Psi) = (1, -0.5)$ and $(1, -1)$, respectively, displays lower stress intensity in the vicinity of crack tips.

In addition to the theoretical studies, we also first replicated the effect of the multiphysics based on non-Fourier theory within finite element simulations. To do so, we first defined time-dependent thermal partial differential equations in COMSOL Multiphysics platform and further coupled static solid mechanics and electrostatics physics. The temperature and stresses simulation results are in good agreement with our theoretical results for gradation design.

Collectively, these findings provide us with new insights into the correlations between fracture mechanics and heterogenous functional gradations of biomimetic composites for different environments, and guidelines to tune the gradation coefficients of bio-inspired materials under complex environments.

Preface

This thesis is an original work by Weilin Yang (W. Yang) under the supervision of Prof. Zengtao Chen (Z. Chen), and is organized in a paper-based format.

Chapter 1 provides a brief introduction of biomaterials.

Chapter 2 outlines the research objectives and conducts the literature survey of related biomimetic composite materials.

Chapter 3 has been published as:

Yang W, Chen Z. Multiphysical model to predict thermomechanical fracture of functional hierarchical biomimetic composites. *Composite Structures* 2023; 303: 116261.

Chapter 4 has been published as:

Yang W, Nourazar M, Chen Z, Hu K, Zhang X. Dynamic response of a cracked thermopiezoelectric strip under thermoelectric loading using fractional heat conduction. *Applied Mathematical Modelling* 2022; 103: 580-603.

Chapter 5 has been submitted as:

Yang W, Nikrad SF, Nourazar M, Chen Z. Functionally graded Design of Bio-composite Material for Fracture Resistance under Multiphysical Application.

Chapter 6 implements Multiphysics Finite element simulations of a cracked Functionally graded Piezoelectric strip based on non-Fourier heat conduction.

Chapter 7 is the summary of the thesis and prospection of the future works.

Acknowledgements

First and foremost, I would like to be sincerely grateful to my supervisor, Dr. Zengtao Chen, for his careful guidance, unwavering support, and exemplary supervision during my PhD program at the University of Alberta. His extensive knowledge, enthusiasm, and gracious demeanor will benefit me throughout my lifetime.

I would like to thank to the members of my committee, Dr. Xiaodong Wang and Dr. Chongqing Ru. Thanks for their insightful feedback, constructive critiques, and comprehensive evaluations. Their expertise has greatly enriched the quality and depth of my research.

My heartfelt thanks go to my colleagues, Mahsa Nourazar, Sara Keypoursangsari, and Seyed Farzad Nikrad, for their camaraderie, discussions, and collaborative efforts, which enriched my academic experience. Even though we are from different countries, we have forged a close friendship that defies cultures and fosters genuine care for each other.

Last but not least, my deepest gratitude goes to my parents and friends for their understanding, and patience throughout this challenging journey. Their love and support have been my constant motivation.

Table of Contents

Abstract.....	ii
Preface.....	v
Acknowledgements.....	vi
Table of Contents.....	vii
List of Tables.....	xi
List of Figures.....	xii
Chapter 1 Introduction.....	1
1.1 Background.....	1
1.1.1 Hierarchical structure.....	1
1.1.2 Multiphysical functionality.....	3
1.2 Significance.....	5
Chapter 2 Motivation and Objectives.....	8
2.1 Motivation.....	8
2.1.1 Structural design.....	8
(1) Reuss Material Model.....	10
(2) Local Representative Volume Element Mode.....	11
(3) Mori-Tanaka Material Model.....	11
(4) Power Law Material Model.....	12
(5) Exponential Material Model.....	12
2.1.2 Multiphysical behavior.....	12
2.1.3 Fracture criteria.....	16
(1) Interface damage model.....	17
(2) Stress intensity factor.....	17
(3) Energy release rate.....	19
(4) Critical intensity factor.....	20
2.2 Challenges.....	20
(1) Hyperbolic heat conduction.....	21
(2) Dual-phase-lag heat conduction.....	21

(3) Fractional heat conduction	22
2.3 Objectives and Methods	23
2.4 Structure of the thesis	24
Chapter 3 Dynamic response of a cracked thermopiezoelectric strip under thermoelectric loading using fractional heat conduction	26
3.1 Introduction	27
3.2 Problem statement and basic equations.....	29
3.3 Fractional heat conduction equation	30
3.4 Piezothermoelastic governing equation	32
3.5 General solutions.....	34
3.5.1 Temperature field.....	34
3.5.2 Electromechanical field	38
3.6 Numerical results and discussions.....	48
3.6.1 Verifications.....	48
3.6.2 The temperature and elastic-electric results.....	49
3.6.3 The dynamic stress and electric displacement intensity factors	54
3.7 Conclusions	59
Chapter 4 Multiphysical model to predict thermomechanical fracture of functional hierarchical biomimetic composites	60
4.1 Introduction	61
4.2 Materials and Constitutive Model	63
4.2.1 Microstructure design and material properties	63
4.2.2 Thermomechanical constitutive model.....	64
4.3 General solutions and stress intensity factors	68
4.3.1 Temperature distribution.....	68
4.3.2 General solutions and multiphysical model.....	71
4.3.3 Stress intensity factors	75
4.4 Results and Verifications	76
4.4.1 Model verifications	77
4.4.2 Thermal loading.....	79
4.4.3 Thermal-mechanical loading	80

4.4.4	Initial crack propagation predictions	82
4.5	Conclusions	85
Chapter 5 Functionally graded Design of Bio-composite Material for Fracture Resistance under Multiphysical Application		87
5.1	Introduction	88
5.2	Statement of the problem	90
5.2.1	Microstructure of FGPM and its properties	90
5.2.2	Thermo-electromechanical orthotropic constitutive model and boundary conditions 91	
5.3	General solutions and stress intensity factors	95
5.4	Numerical results and Discussions.....	105
5.4.1	Model reliability.....	106
5.4.2	Functional gradient piezoelectric material (FGPM) design.....	109
5.4.3	FGPM design under a single physical field	110
(1)	Single dynamic mechanical loading	110
(2)	Single dynamic electrical loading.....	111
(3)	Single dynamic Thermal loading	112
5.4.4	Fracture evaluation of FGPM under Single field.....	114
5.4.5	Thermo-electro-mechanical FGPM design.....	119
(1)	Thermomechanical and Thermoelectrical Fields.....	120
(2)	Thermo-electromechanical Field	121
5.4.6	Gradation profile selection.....	122
5.5	Conclusions	128
Chapter 6 Multiphysics Finite element simulations of a cracked Functionally graded Piezoelectric strip based on non-Fourier heat conduction.....		130
6.1	Introduction	131
6.2	Finite Element Modelling.....	132
6.2.1	Design conditions.....	132
6.2.2	Non-Fourier thermal Modeling.....	134
(1)	User-defined partial differential equations (PDEs).....	134
(2)	Thermal boundary conditions	135
(3)	Element quality check.....	136

6.2.3	Functionally graded Piezoelectric Modeling	137
(1)	Piezoelectricity, Solid	137
(2)	Boundary conditions	138
6.2.4	Coupled Thermo-Piezo-Electro-Mechanical Model.....	139
(1)	Thermal expansion.....	139
(2)	Piezoelectric Material	139
6.3	Results and Discussions	139
6.3.1	Temperature distributions	140
6.3.2	Stress distributions.....	142
6.4	Conclusions	144
Chapter 7	Conclusions and Future Perspectives.....	145
7.1	Conclusions	145
7.2	Future perspectives.....	147
References	148
Appendix A	Supporting information for Chapter 3	173
Appendix B	Supporting information for Chapter 4	180
Appendix C	Supporting information for Chapter 5	185

List of Tables

Table 3. 1 Static temperature, stress and electric displacement intensity factors a parallel crack in a strip.....	49
Table 3. 2 Material constants for cadmium selenide ¹⁶³	49
Table 4. 1 The experimental coefficients of Young’s modulus ¹⁷⁷	76
Table 4. 2 The values of the coefficients of the volume fraction of the hard phase ¹⁷⁷	76
Table 4. 3 The ratio of the energy release rate for different environments.	85
Table 5. 1 Material properties of homogeneous piezoelectric ceramics.....	107
Table 5. 2 Sketches choice under single thermal load.....	119
Table 5. 3 Profile suggestions for thermo-electromechanical loading.	126
Table 5. 4 Different sketches compare at the crack tip.....	128
Table 6. 1 Material properties of homogeneous PZT-5H ceramics.....	133
Table 6. 2 Thermal properties of homogeneous PZT-5H ceramics.....	139

List of Figures

Figure 1. 1 Schematic of the molluscan shell anatomy ¹²	2
Figure 1. 2 The toughening mechanisms: (a) mineral bridge; (b) nano-asperities; (c) organic glue ¹⁰	2
Figure 1. 3 Scheme showing the hierarchical organization of bone from the macro- to the nanoscale ^{11,13,14}	3
Figure 1. 4 Positive piezoelectric effect of collagen ²³	4
Figure 1. 5 Multiphysical stimulus in bone healing engineering ²⁷	4
Figure 1. 6 Biomimetic composites applications of lightweight and strong properties: (a) Bone-inspired steel ³¹ ; (b) Nacre-inspired helmet ³²	6
Figure 1. 7 Bio-inspired materials smart applications of piezoelectric performance: (a) Water vapor response sensor ³⁸ ; (b) Self-healing engineering ⁴²	7
Figure 2. 1 Biomimetic microstructure with different unit element ²²	9
Figure 2. 2 Hierarchical size of brick-and-mortar microstructure.....	9
Figure 2. 3 Several laws of functionally graded model: (a) Electroelastic properties ⁴⁷ ; (b) Elastic properties ⁴⁸	10
Figure 2. 4 Effect of temperature changes on residual stress near the crack tip ⁷⁰	15
Figure 2. 5 Effect of temperature changes on residual stress near the crack tip.....	18
Figure 2. 6 Coordinate near the crack tip.....	19
Figure 2. 7 Structure of the thesis.....	25
Figure 3. 1 A piezoelectric strip with an insulated crack under thermal-electric loading.....	30

Figure 3. 2 Verification of the solutions. $\left(\frac{h_2}{h} = 0.25, \frac{c}{h} = 0.5\right)$	49
Figure 3. 3 Distribution of the temperature on the crack surfaces and extended line at various times. $\left(\frac{h_2}{h} = 0.25, \frac{c}{h} = 0.5, \tau_q = 0.2, \alpha = 0.5\right)$	50
Figure 3. 4 The effects of the relaxation time and the fractional order on the temperature at the crack center (a) $z \rightarrow 0^-$ ($\alpha = 0.5$); (b) $z \rightarrow 0^+$ ($\alpha = 0.5$); (c) $z \rightarrow 0^-$ ($\tau_q = 0.2$); (d) $z \rightarrow 0^+$ ($\tau_q = 0.2$). $\left(\frac{h_2}{h} = 0.25, \frac{c}{h} = 0.5\right)$	51
Figure 3. 5 The effect of the geometry parameters on the temperature at the crack center: (a) the effect of crack size $\left(\frac{h_2}{h} = 0.25\right)$; (b) the effect of the distance $\left(\frac{c}{h} = 0.5\right)$	52
Figure 3. 6 Strip's stress and electric displacement distributions at normalized time $F = 0.1$ at different surfaces: (a) σ_{zz} ; (c) σ_{zx} ; (e) D_z ; and around crack tip(b) σ_{zz} ; (d) σ_{zx} ; (f) D_z . $\left(\frac{h_2}{h} = 0.25, \frac{c}{h} = 0.5, \tau_q = 0.2, \alpha = 0.5, D = 0\right)$	53
Figure 3. 7 Distributions of stress and electric displacement in z-direction of the bisection plane of the crack at various times: (a) normal stress σ_{zz} ; (b) electric displacement D_z . $\left(\frac{h_2}{h} = 0.25, \frac{c}{h} = 0.5, \tau_q = 0.2, \alpha = 0.5, D = 0\right)$	54
Figure 3. 8 Normalized dynamic stress and electric displacement intensity factors vs. normalized time as a function of the relaxation time and fractional order: (a) K_I ($\alpha = 0.5$); (b) K_I ($\tau_q = 0.2$); (c) K_{II} ($\alpha = 0.5$); (d) K_{II} ($\tau_q = 0.2$); (e) K_D ($\alpha = 0.5$); and (f) K_D ($\tau_q = 0.2$). $\left(\frac{h_2}{h} = 0.25, \frac{c}{h} = 0.5, D = 0\right)$	56
Figure 3. 9 The effect of the crack size on the stress and electric displacement intensity factors: (a) K_I ; (b) K_{II} ; (c) K_D . $\left(\frac{h_2}{h} = 0.25, \tau_q = 0.2, \alpha = 0.5, D = 0\right)$	57
Figure 3. 10 The effect of the distance between crack face and thermal loading on the stress and electric displacement intensity factors K_I, K_{II}, K_D . $\left(\frac{c}{h} = 0.5, \tau_q = 0.2, \alpha = 0.5, D = 0\right)$	58

Figure 3. 11 The effect of the electric load on the stress and electric displacement intensity factors: (a) K_I ; (b) K_{II} ; (c) K_D . $\left(\frac{c}{h} = 0.5, \frac{h_2}{h} = 0.25, \tau_q = 0.2, \alpha = 0.5\right)$	58
Figure 4. 1 Brick-and-mortar multiphysical functional biomimetic hierarchical model: (a) SEM micrographs of the nacre ²⁰⁰ ; (b) Multiphysical model.....	64
Figure 4. 2 A center cracked multiphysical functional brick-and-mortar plane model: (a) multiphysical plane model; (b) unite cell.....	65
Figure 4. 3 Crack propagation likelihood of functional brick and unbrick microstructures: (a) stress intensity factors under pure tensile stress; (b) experimental and theoretical stress-strain curves ¹⁷⁷	77
Figure 4. 4 The strain patterns around the crack tip obtained from the present model, DIC experiments ¹⁷⁷ , and Abaqus simulations ¹⁷⁷	78
Figure 4. 5 Temperature results with different heat conduction models.	79
Figure 4. 6 Stress intensity factors under single thermal loading. $(t = 1, \rho = 0.1)$	80
Figure 4. 7 The plots of the SIFs with different microstructures. $(t = 1, \rho = 0.1)$	81
Figure 4. 8 The stress distribution around the crack surface and crack tips. $(t = 1, \rho = 0.1)$	82
Figure 4. 9 Initial crack propagation directions under a single stress field.	84
Figure 4. 10 Initial crack propagation direction predictions: (a) Penetrate; (b) Deflect.....	85
Figure 5. 1 Microstructure of an FGPM that is graded from material A to material B: (a) SEM micrograph of a bamboo ²⁶³ ; (b) the gradation profile of FGPM material.	90
Figure 5. 2 FGPM strip model and boundary conditions.....	92
Figure 5. 3 Boundary conditions under thermo-electro-mechanical loading stresses and Dz variations (a) insulated crack; (b) permeable crack along thickness $(x = 0)$. $(t = 1)$	106
Figure 5. 4 Boundary conditions under thermo-electro-mechanical loading: stresses and Dz variations at the crack surface and extended line $z = 0$. $(t = 1)$	107

Figure 5. 5 Normalized DSIFs variation of permeable and impermeable crack conditions.....	108
Figure 5. 6 Sketch of functionally graded piezoelectric material (FGPM).....	109
Figure 5. 7 DSIFs versus time under a single mechanical field.....	111
Figure 5. 8 DSIFs versus time under a single electrical field.	112
Figure 5. 9 Thermal distribution and DSIFs: (a) stable temperature distribution at t=50s; (b) DSIFs versus time under a single thermal field.	113
Figure 5. 10 Fracture criteria comparison.....	115
Figure 5. 11 Critical intensity factor K_C comparison (a) under single mechanical load (single P); (b) under single electrical load (single D).....	117
Figure 5. 12 K_C variation and sketch choice of single thermal load.....	119
Figure 5. 13 Critical intensity factor comparison under different loading ratios (a) RS of thermomechanical field; (b) RD of thermoelectrical field.....	120
Figure 5. 14 The impact of hermos-electromechanical loading.	122
Figure 5. 15 Graded piezoelectric material based on the FGM concept with several laws of gradation.	123
Figure 5. 16 Gradation coefficient Ψ of the thermal property profile.	123
Figure 5. 17 Gradation coefficient Ω of the electromechanical property profile.....	124
Figure 5. 18 The value of K_C with different gradation profile for thermo-electromechanical loading.....	126
Figure 5. 19 Suggested gradation profile of FGPM and comparison.	127
Figure 6. 1 Geometry: (a) gradation law; (b) mesh element around crack tip; (c) whole strip. .	133
Figure 6. 2 Thermal boundary conditions.....	136
Figure 6. 3 Measure of mesh quality in the thermal model around crack tip.	137

Figure 6. 4 Mechanical-electrical boundary conditions.....	138
Figure 6. 5 Measure of mesh quality in the thermal model around crack tip: (a) non-Fourier; (b) Fourier.....	140
Figure 6. 6 Temperature distributions of: (a) Sym-FGPM; (b) Non-FGPM.	141
Figure 6. 7 Von Mises stress distribution around crack tip of Sym-FGPM: (a) Mechanical; (b) Thermal-mechanical.	142
Figure 6. 8 Thermal-mechanical-electrical von Mises stress distribution around crack tip: (a) Sym-FGPM (1, -0.5); (b) Non-FGPM; (c) Expo-FGPM (-0.5, -0.5); (d) Expo-FGPM (1, -0.5).	143

Chapter 1

Introduction

1.1 Background

It is a classic problem in materials design that the two key material properties — strength and toughness — tend to be mutually exclusive. Extremely stiff materials like ceramics tend to be brittle, and tough materials like rubber are easily deformable. Clues from nature, biological materials have evolved for millions of years, enabling them to perform perfectly in both strength and toughness properties and far surpass those of its individual components ¹⁻³.

1.1.1 Hierarchical structure

In nature, most of biological materials are usually in the form of combination of a soft protein and stiff but brittle minerals ⁴⁻⁶. For instance, mollusks protect their soft body against external predators and foreign bodies with a three-layered shell ⁷⁻⁹: the outermost layer “periostracum”, the middle layer “prismatic”, and the inner layer “nacre” (Figure 1.1). Nacre is a typical brick-and-mortar structure which is composed of the hard aragonite phase and soft organic materials. The hard mineral aragonite offers remarkable strength which can provide resistance to penetration from external impact, while it would be brittle if local high stresses cannot be relieved. The soft organic phase addresses this issue, acting like a lubricant by allowing some movement between the platelets, and provides toughness ¹⁰. The principal toughening mechanisms in nacre are crack bridging and the resulting ‘pull-out’ of mineral bricks and aided by viscoelastic energy dissipation

in the organic layer (Figure 1.2)¹¹. With the aid of the mechanism, nacre exhibits three orders of magnitude higher toughness than aragonite.

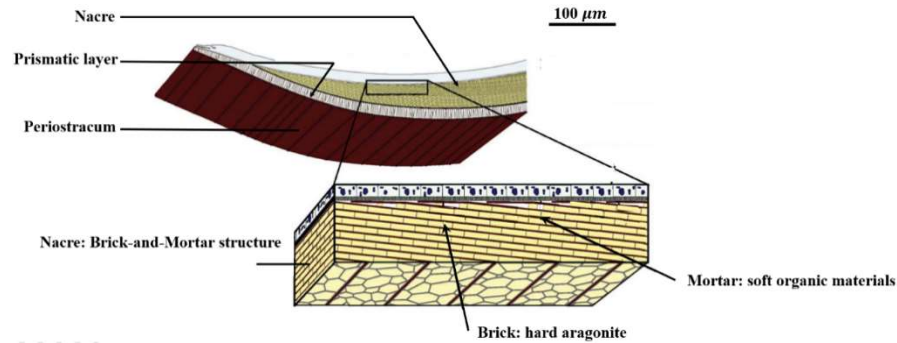


Figure 1. 1 Schematic of the molluscan shell anatomy¹².

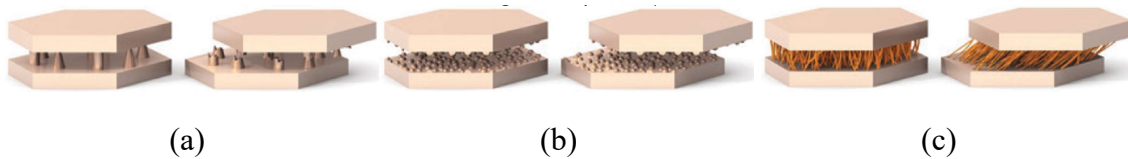


Figure 1. 2 The toughening mechanisms: (a) mineral bridge; (b) nano-asperities; (c) organic glue¹⁰.

Bone is another fine example of damage-tolerant material design in nature. The lamellar structure at the microscopic scale of bone is somewhat similar to nacre and consists of a soft collagen matrix and hard hydroxyapatite crystals. The macroscale arrangement of bone involves both compact bone at the surface and spongy bone in the interior. Compact bone is composed of osteons and Haversian canals, which surround blood vessels. Osteons have a lamellar structure, with individual lamellae consisting of fibrils arranged in geometrical patterns. The fibrils comprise organic (mainly type I collagen) phases and inorganic (mostly carbonated hydroxyapatite) (Figure 1.3)^{11,13,14}. Carbonated hydroxyapatite crystals periodically deposit within the gap zones of collagen. Fracture resistance of bone can be divided into two categories: intrinsic mechanisms that enhance ductility and extrinsic mechanisms that serve to protect against the growth of cracks¹⁵. The intrinsic toughening mechanism operates ahead of the crack tip and involves various features

ranging from atomic to nanoscale, such as molecular uncoiling, fibrillar sliding, and microcracking. On the other hand, the extrinsic toughening mechanisms are situated behind the crack tip and include fibril bridging, crack deflection, and twisting. As a result, the fracture toughness of bone is nearly ten times greater than that of its individual hydroxyapatite phase ¹⁶.

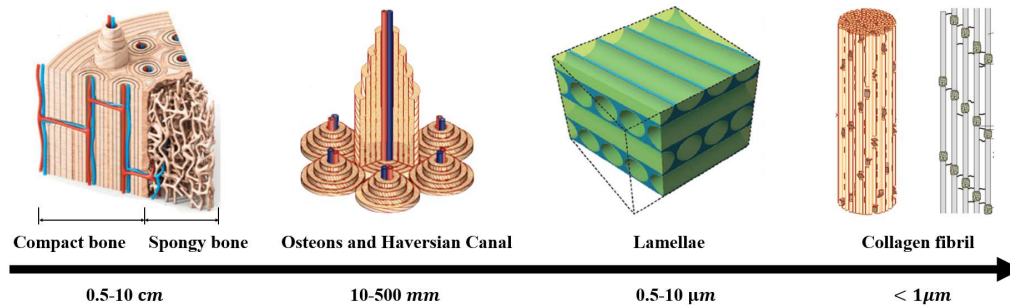


Figure 1.3 Scheme showing the hierarchical organization of bone from the macro- to the nanoscale

11,13,14

The main mechanical function of these hierarchical arrangements is to produce interfaces that will open up in the presence of potentially dangerous cracks, deflecting the cracks and making their travel energetically expensive ¹⁷. This makes biomaterials facilitates efficient high-energy dissipation and fracture resistance ¹⁸⁻²⁰. With their excellent mechanical performance, biomaterials have opened a way to inspire new designs for hierarchical composite materials.

1.1.2 Multiphysical functionality

Biomaterials are sophisticated and highly dynamic systems. Their multifunctional microenvironments instruct cellular behavior via a complex interplay of multiple biochemical and physical cues from the specific extracellular matrix ²¹. Despite the diverse extracellular matrix of biological materials, there is a common feature that almost all the biomaterials exhibit piezoelectric properties ¹⁷. For example, by weight, bone is nearly composed of 70% hydroxyapatite and 30% collagen fibrils ²². These two inorganic and organic materials are the main reason responsible for

the piezoelectricity of bone. Once collagen undergoes fracture, bone exhibits piezoelectric properties. As shown in Figure 1.4, a mechanical strain generates electric fields in the collagen. Generally, the compression area of bone forms electronegative potential, whereas electropositive potential is developed where tensile force is experienced.

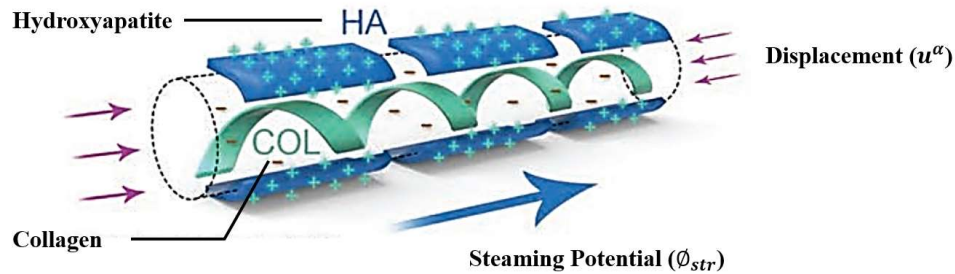


Figure 1. 4 Positive piezoelectric effect of collagen ²³.

Due to the piezoelectric property of collagen, it play an important role in the process of bone healing. Through electrostatic forces, collagen induces conformational changes, stimulating migration, proliferation and differentiation of bone forming (osteoblasts, osteoclasts, and osteocytes) and progenitor cells (Figure 1.5) ²⁴⁻²⁶. Except the piezoelectricity, heat can also accelerate osteogenesis directly by increasing the metabolic rate of osteoblasts, and indirectly, by producing vasodilation and thus increasing the local circulating blood volume (Figure 1.5) ²⁷.

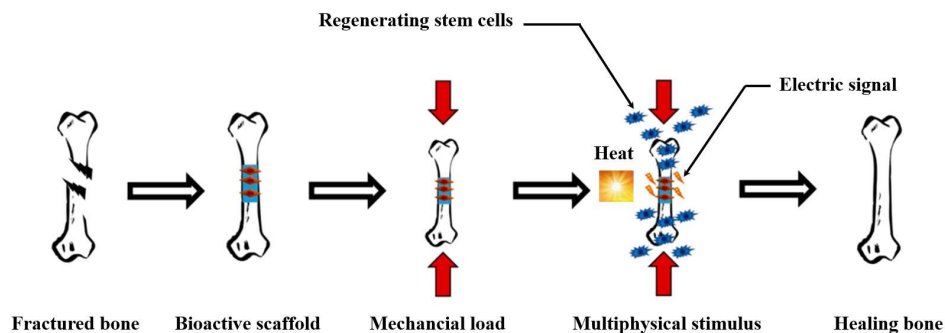


Figure 1. 5 Multiphysical stimulus in bone healing engineering ²⁷.

Overall, biomaterials have the fascinating self-healing property due to their multiphysical

functional performance, and achieve an ideal combination of light weight, high strength, and high toughness owing to their hierarchical structure²⁸. All these merits inspire biomimetic materials to become the newest design concept of functional composites.

1.2 Significance

Benefited from advances in 3D printing, the fabrication of microstructures with arbitrary geometry has become possible and the study of biomimetic composite has been promoted significantly in recent years. With the rapid development of high-speed trains, planes and spacecraft, the security of the components has become the critical challenge to engineers. Because cyclic loads often cause structure failure, higher strength and fatigue resistance are the main goals for failure prevention in component design. The secret of excellent protective performance of nature lies in its sophisticated hierarchical “brick and mortar” architecture, which leads to superior crack resistance by simultaneous activation of multiple mechanisms ranging from nanoscopic/microscopic to macroscopic scales that resist crack propagation^{29,30}. To this end, in pursuit of exceptional improvements in fatigue resistance, engineers were inspired to mimic such hierarchical brick-and-mortar structure in order to replace traditional engineering materials, such as alloys, plastics, and ceramics to achieve higher mechanical performance. Inspired from bone (Figure 1.6 (a)), engineers explored the hierarchical multiphase steels, which were composed of the hard martensite phase and the soft metastable austenite phase. The steels show the superior crack resistance by simultaneous activation of multiple micromechanisms³¹. The outstanding lightweight and strong properties of hierarchical structure also serve as the basis for the design of armor. Recently, a nacre-inspired hierarchical structure of helmet was presented (Figure 1.6 (b)), whose reinforcements of graphene nanoplatelets (GNs) act as bricks with the polymer matrix in between as mortar. The helmet shows lightweight property while exhibiting comparable specific

fracture toughness and strength to the natural nacre³². These biomimetic composites also exhibit potential applications in other fields including electric cables, fire-retardant materials, gas barriers, nanogenerators, and supercapacitors³³⁻³⁷.

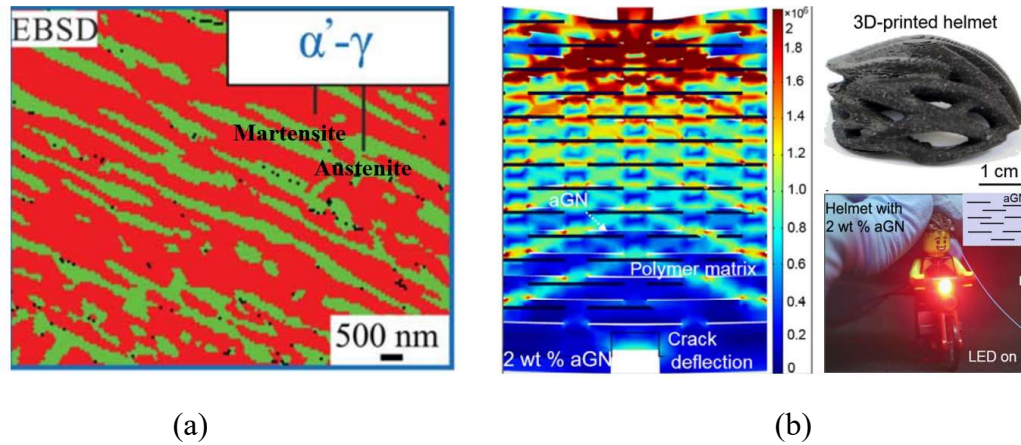


Figure 1. 6 Biomimetic composites applications of lightweight and strong properties: (a) Bone-inspired steel³¹; (b) Nacre-inspired helmet³².

Facing more complex service conditions, the demand for better mechanical property of component become intense, and materials are even developed to achieve self-adaptable and self-recoverable performance under external stimuli. The multiphysical functional property of biomaterials inspires alternative approaches to solving challenging design problems. A water vapor response sensor was fabricated according to multilayer photonic crystal structures on the body surface of damselfish (Figure 7 (a)). The hybrid one-dimensional photonic crystal sensor was prepared by alternating thin films of titania and polymer (2-hydroxyethyl methacrylate-co-glycidyl methacrylate)³⁸. Due to the response of soft polymer to water vapor, the sensor possesses fast water-vapor responsiveness and reversible full-color switching. The deformation of hard materials on or inside the soft matrix can also be used to control the surface morphology^{39,40}. Tissue engineering uses the piezoelectric properties of biomaterials to repair or replace damaged,

malfunctional organs and tissues through regeneration. Electrotherapy is commonly used in bone healing, whose aim is forming the electric potential, and then induce migration, attachment and activity of bone-forming cells in the damaged parts. Figure 1.7 (b) shows the piezoelectric nanofilms on strontium titanate implants which generate a constant built-in electropositive field and strongly interact with the electronegative potential of bone. This stimulation strategy was employed in triggering bone healing in rat femoral defects ^{41,42}.

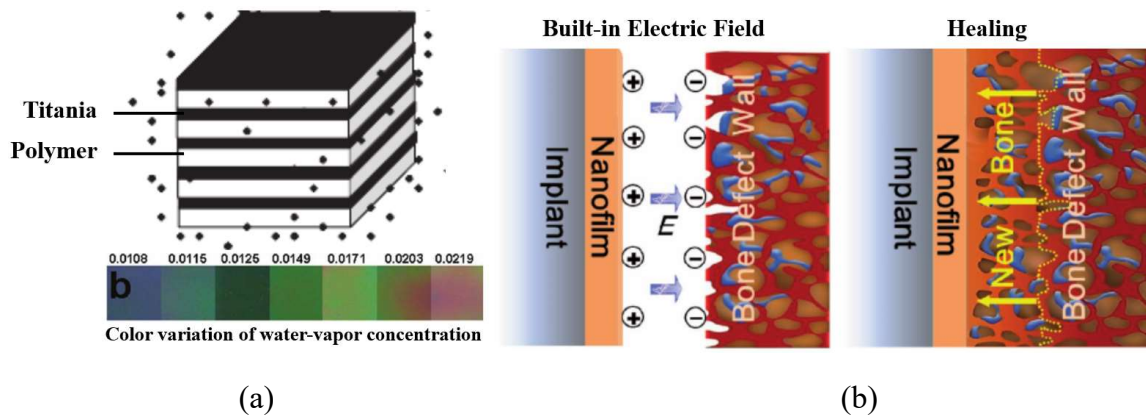


Figure 1. 7 Bio-inspired materials smart applications of piezoelectric performance: (a) Water vapor response sensor ³⁸; (b) Self-healing engineering ⁴².

The mechanical and piezoelectric performances of the biomaterials will inevitably be degraded once cracking happens. Especially, the brick-and-soft hierarchical structure of biomaterials will amplify the responses to the external stimuli ⁴³⁻⁴⁵, which will trigger the formation of crack and promote crack propagation. Even in the lifetime of biomaterials, different environments will inevitably occur simultaneously. Therefore, the fracture performance of different hierarchical structures under multi-physical stimuli demands prompt solutions in the design process.

Chapter 2

Motivation and Objectives

2.1 Motivation

When designing biomimetic materials, two factors are critical: hierarchical structure and multiphysical functional properties, which are the main motivation of the present work.

2.1.1 Structural design

Inspired from the hierarchical structure observed in biological materials, biomimetic materials are composed of two distinct components: soft material and hard material. Benefit from the developments of 3D printing technology and computer simulation software, it is easy to build various hierarchical specimens and the mechanical properties can be obtained by various test methods, such as tensile test, bending test, ductility test and so on. For example, to reveal the underlying toughness-microstructure relationship, four bioinspired material microstructures are investigated under tensile test, including the brick-and-mortar, cross-lamellar, concentric hexagonal, and rotating plywood microstructures (Figure 2.1). Results show that the brick-and-mortar structure displays the maximum load of failure. Its work of fracture per mass is 14 times greater than the single hard phase, making it both tough and strong. Moreover, the rotating plywood structure exhibits the 17 times the work of fracture per mass, but less maximum load of failure compared to the hard phase. Similarly, the concentric hexagonal structure shows the toughness improved by 15 times but weak in strength. Compared to the above structures, the cross

lamellar structure shows relatively small toughness improvements, because the cracks are constrained to the interface, leading to a relatively small fracture processing zone.

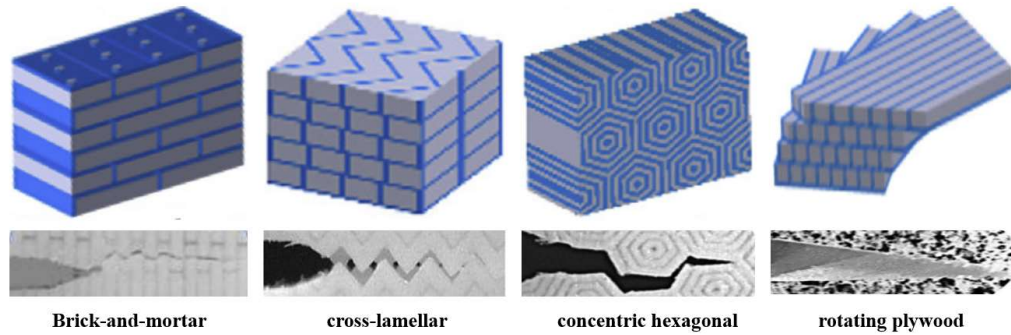


Figure 2. 1 Biomimetic microstructure with different unit element ²⁴.

To expose the effect of soft and hard phases of brick-and-mortar microstructure on the mechanical properties of biomimetic materials, based on the 2D elasticity theory, the effect of the hierarchical size on the stress and strain response has been analyzed (Figure 2.2). Results showed that the stress concentration decreases very fast with increasing protein (soft phase) thickness ^{46,47} and the smaller the aspect ratio of the mineral (hard phase), the more uniform the distribution of shear stress is at the mineral–protein interface ⁴⁸. All these results on bi-material composites have implications on the design of gradient materials that could guide the deflection of the crack when the whole structure is threatened by potential fracture.

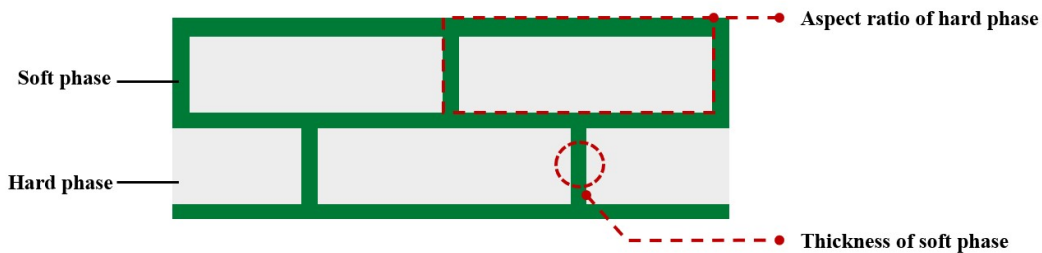


Figure 2. 2 Hierarchical size of brick-and-mortar microstructure.

On the other hand, the feature sizes of these microstructures are controlled to be functionally graded, providing better pictures of how crack resistance interacts with heterogeneity. In functionally graded models, some or all properties of material change along one direction with several gradation laws (Figure 2.3). The most common FGMs are formulated along z-coordinate

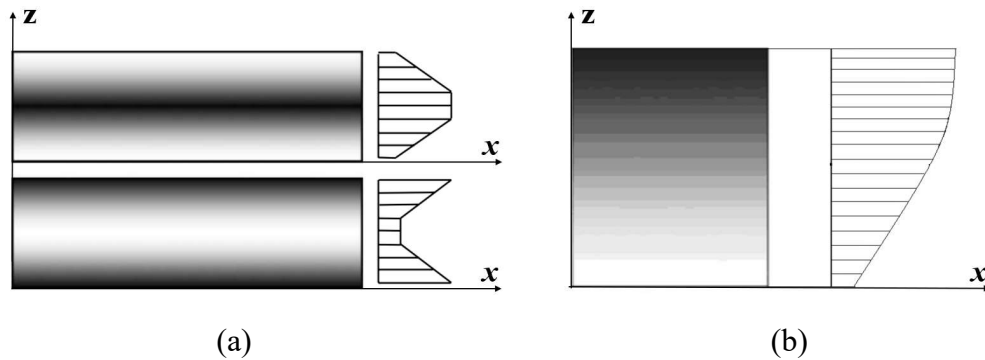


Figure 2. 3 Several laws of functionally graded model: (a) Electroelastic properties ⁴⁹; (b) Elastic properties ⁵⁰.

and refer to the thickness of the material. The following models are widely used in Young's modulus. The indices "t" and "b", used in the following gradient models, represent the top and the bottom face, respectively.

(1) Reuss Material Model

Reuss ⁵¹ assumed Young's modulus E , is a function $E(z)$ of coordinate z , which is represented as ⁵².

$$E(z) = \frac{E_t E_b}{E_t(1 - V_t) + E_b V_t} \quad (2.1)$$

where V_t is the volume fraction of the top material and it is calculated by the relation (2.2).

$$V_t = (0.5 + z/h)^k \quad (2.2)$$

in equations (2.1) and (2.2), the coordinate "z" represents the position of a point along the thickness of the material, "h" denotes the material thickness, and "k" stands for the exponential coefficient, which can take various values.

(2) Local Representative Volume Element Mode

The Local Representative Volume Element Mode (LRVE) ⁵² is applicable to length scales that are significantly larger than the characteristic length scale of individual component particles but still smaller than the characteristic length scale of a macroscopic specimen.

$$E(z) = E_b \left(1 + \frac{V_t}{FE - \sqrt[3]{V_t}} \right) \quad (2.3)$$

$$FE = \frac{E_t E_b}{1 - E_t/E_b} \quad (2.4)$$

The LRVE model relies on the assumption that the microstructure of the heterogeneous material is well-known. The primary input parameter consists of the average volume or the overall average of the microstructure descriptors.

(3) Mori-Tanaka Material Model

In this model ⁵³, the heterogeneous material of functionally graded material is conceptualized as a composite composed of two materials, wherein one is consolidated by randomly distributed spherical particles of the other material.

$$E(z) = E_b + (E_t - E_b) \frac{V_t}{1 + (1 - V_t)(E_t/E_b - 1)(1 + \nu)/[3(1 - \nu)]} \quad (2.5)$$

Typically, the Poisson's ratio (ν) exhibits a small variation ⁵⁴, leading to a minor impact on FGM behavior ⁵⁵. Therefore, in this model, the Poisson's ratio is assumed to remain constant.

(4) Power Law Material Model

Power law material model ^{56,57} is used for the description and obtaining of the properties and in the development of the calculations regarding the deformations and stresses, which is expressed as

$$E(z) = E_b(E_t - E_b)(0.5 + z/h)^k \quad (2.6)$$

(5) Exponential Material Model

The exponential material model is the most used and simplest one in the construction of functionally graded materials.

$$E(z) = E_t e^{\beta z} \quad (2.7)$$

Relying on the exponential, functionally gradient model, mechanical parameters, like stress intensity factors ⁵⁸, fracture toughness ⁵⁹, deflection ⁶⁰ and crack growth resistance behavior ⁶¹ and the effects of gradient direction ⁶² and degree ⁶³, crack position ⁶⁴ and numbers ⁶⁵ on all of the above parameters were extensively investigated.

2.1.2 Multiphysical behavior

The replications in the multiphysical functionality of biomaterial can be filled by the incorporation of smart materials in biomimetic materials. Smart materials are distinguished by their ability to reverse, change, or generate a response from external stimuli in their environment ^{66,67}. Among the available smart materials, piezoelectric materials are widely utilized to mimic

biomaterials because of their ability to exhibit electromechanical responsivity to an external stimulus in either a direct or converse piezoelectric configuration ²³, which is similar to the natural extracellular matrix. The piezoelectric constitutive equations in the stress-charge form are:

$$\begin{aligned}\sigma_{ij} &= C_{ijkl}\epsilon_{kl} - e_{kij}E_k \\ D_i &= e_{ikl}\epsilon_{kl} + \epsilon_{ik}E_k\end{aligned}\quad (2.8)$$

where $i, j, k, l = 1, 2, 3$. Terms σ_{ij} , D_i , ϵ_{kl} and E_k are, respectively, components of the mechanical stress tensor, components of the electric displacement, components of the mechanical strain tensor, and components of the electric field vector. The terms C_{ijkl} , e_{kij} and ϵ_{ij} represent the elastic, piezoelectric and dielectric coefficients, respectively.

The components of the strain tensor ϵ_{kl} are defined by

$$\epsilon_{kl} = \frac{1}{2}(\mathbf{u}_{k,l} + \mathbf{u}_{l,k}) \quad (2.9)$$

where \mathbf{u}_l and \mathbf{u}_k are the components of the displacement vector, and $\mathbf{u}_{k,l} = \partial \mathbf{u}_k / \partial x_l$.

The electric field inside the medium is described by Maxwell's equations, which relate the fields to the microscopic average properties of the material. When the quasistatic approximation is introduced ⁶⁸, the electric field is derivable from a scalar electric potential:

$$\mathbf{E}_k = -\phi_{,k} \quad (2.10)$$

where $\phi_{,k}$ is the electric potential. The following Maxwell's equation is defined by

$$D_{i,i} = 0 \quad (2.11)$$

Without body forces, the equation of motion for a piezoelectric material is

$$\boldsymbol{\sigma}_{ij} = \rho \ddot{\mathbf{u}}_i \quad (2.12)$$

where ρ represents the density of piezoelectric material, $\ddot{\mathbf{u}}_i = \partial^2 \mathbf{u}_k / \partial t^2$, and t is the time.

It is worth noting that the piezoelectric effect of bone under ultrasound irradiation was numerically simulated using the piezoelectric constitutive equations Eq. (2.8)⁶⁹, and the results were proven with the experiments.

To mimic the thermal response of biological material, the temperature change term T is introduced in the piezoelectric constitutive equation⁷⁰.

$$\begin{aligned} \boldsymbol{\sigma}_{ij} &= \mathbf{C}_{ijkl} \boldsymbol{\varepsilon}_{kl} - \mathbf{e}_{kij} \mathbf{E}_k - \boldsymbol{\beta}_{ij} T \\ \mathbf{D}_i &= \mathbf{e}_{ijk} \boldsymbol{\varepsilon}_{jk} + \boldsymbol{\epsilon}_{ij} \mathbf{E}_j + \boldsymbol{\gamma}_i T \end{aligned} \quad (2.13)$$

where $\boldsymbol{\beta}_{ij}$ and $\boldsymbol{\gamma}_i$ are thermal stress and pyroelectric coefficients. For solving temperature difference T , in most classical engineering problems with the macro spatial and temporal scales, the Fourier Law is taken

$$\mathbf{q}(x, t) = -k \nabla T(x, t) \quad (2.14)$$

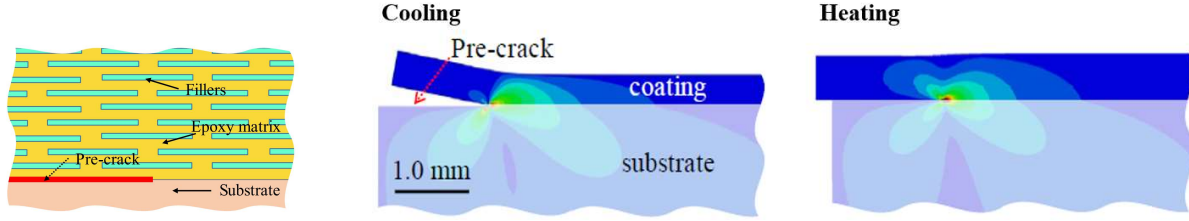
where \mathbf{q} is the heat flux vector, x is the position vector, and k is the thermal conductivity. When the inner heat source is negligible, the conservation of local energy is expressed by:

$$-\nabla \cdot \mathbf{q} = \rho c_\rho \frac{\partial T}{\partial t} \quad (2.15)$$

where c_ρ is the specific heat.

With aid of thermal piezoelectric constitutive equations Eq. (2.15), the thermal stresses at the tip of an interface crack between a brick-and-mortar coating and a substrate were discussed⁷¹.

Clearly from Figure 2.4, for cooling condition, the crack was opened; by contrast, when temperature went higher, the coating was stretched along the substrate.



(a) Cracked brick-and-mortar structure

(b) residual stress near the crack tip

Figure 2. 4 Effect of temperature changes on residual stress near the crack tip ⁷¹.

Based on Fourier heat conduction, more environmental parameters are introduced into the piezoelectric constitutive equations to help researchers study the effect of multiphysical functional properties of biomaterials. For example, the constitutive equations for hygro-thermo-magneto-electro-elastic piezoelectric materials are defined as follows ^{72,73}

$$\begin{aligned}
 \sigma_{ij} &= C_{ijkl}\epsilon_{kl} - e_{kij}E_k - \beta_{ij}T - d_{kij}H_k - \xi_{ij}m \\
 D_i &= e_{ijk}\epsilon_{jk} + \epsilon_{ij}E_j + \gamma_i T + g_{ij}H_j + \chi_i m \\
 B_i &= d_{ijk}\epsilon_{jk} + g_{ij}E_j + \tau_i T + \mu_{ij}H_j + \nu_i m
 \end{aligned} \tag{2.16}$$

in which B_i , H_k and m are the magnetic induction, magnetic field and moisture concentration change, respectively; d_{kij} , ξ_{ij} , g_{ij} , χ_i , μ_{ij} , τ_i and ν_i are, respectively, the piezomagnetic, hygroscopic stress, electromagnetic, hygroelectric, magnetic permeability, pyromagnetic and hygromagnetic coefficients.

Same with electric field, the magnetic field inside of the medium also described by Maxwell's equations where the magnetic field is derivable from a scalar magnetic potential:

$$H_k = -\Psi_{,k}$$

where $\Psi_{,k}$ is the magnetic potential. The following Maxwell's equation is defined

$$\mathbf{B}_{i,i} = 0 \quad (2.17)$$

For solving the moisture concentration change m , based on the Fick's law is defined as

$$\mathbf{q}^{(M)}(x, t) = -D\nabla m(x, t) \quad (2.18)$$

where $\mathbf{q}^{(M)}$ is the moisture flux vector, D is the moisture diffusion coefficient. When the inner moisture source is negligible, the conservation law for the mass of moisture, equivalent to energy conservation for temperature, is given by

$$-\nabla \cdot \mathbf{q}^{(M)} = \frac{\partial m}{\partial t} \quad (2.19)$$

Extracting corresponding fields from Eq. (2.16), Jin and Feng⁷⁴ used the integral equation techniques to obtain the thermal stress-intensity factors at the crack-tips, finding that the graded coating has higher thermal fracture toughness than the homogeneous coating. Ueda et al.^{75,76} gave a thermal shock at the top surface of the hierarchical, functionally graded piezoelectric material (FGPM) and obtained the thermal stress intensity factors. Meanwhile, electro-thermal⁷⁷, magneto-thermal⁷⁸, hygro-thermal⁷⁹, magneto-electro-thermal⁸⁰, hygro-electro-thermal⁸¹, hygro-magneto-electro-thermal⁸² fracture models for functional materials were built.

2.1.3 Fracture criteria

In order to evaluate the fracture properties of biomimetic materials, a variety of theoretical fracture criteria was proposed.

(1) Interface damage model

Based on fracture mechanics theory, Qin and Zhang⁸³ and He and Hutchinson⁸⁴ proposed the interface damage models between dissimilar materials, relying on the ratio of the energy release rate for penetrating the interface and for deflecting into the interface, G_p/G_d , and the ratio of the mode I toughness of the material of branch to the interface toughness, Γ_c/Γ_{ic} . Concretely if

$$\frac{G_p}{G_d} > \frac{\Gamma_c}{\Gamma_{ic}} \quad (2.20)$$

the impinging crack is likely to penetrate the interface, Conversely, the crack will tend to be deflected into the interface when the inequality is reversed. During crack propagation, usually, deflecting crack can dissipates much more energy and be terminated easier than a straight crack, so as to efficiently avoid the overall failure. Through the competition between deflection and penetration using the maximum energy release rate criterion, if a crack propagates from a soft material toward a hard material, the driving force at the crack tip will be reduced significantly, which plays an essential role in toughening the heterogeneous materials⁸⁵⁻⁸⁷.

(2) Stress intensity factor

In fracture mechanics, the stress intensity factor K is used to predict the stress state near the tip of crack. A crack subjected to any arbitrary loading could be resolved into three types of linearly independent cracking modes as shown in Figure 2.5⁸⁸:

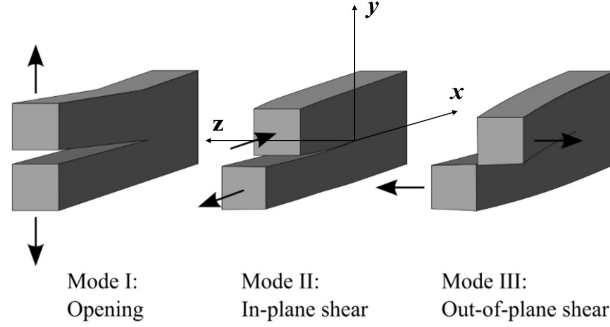


Figure 2. 5 Effect of temperature changes on residual stress near the crack tip.

Mode I refers to an opening (tensile) mode where the crack surfaces move directly away from each other. Mode II is a sliding (in-plane shear) mode where the crack surfaces slide over each other in a direction perpendicular to the leading edge of the crack. Mode III is a tearing (antiplane shear) mode where the crack surfaces move relative to each other and parallel to the leading edge of the crack. The stress intensity factor for each mode is denoted by different subscripts. K_I represents the stress intensity factor for mode I, which applies to the crack opening mode. K_{II} denotes the mode II stress intensity factor, relevant to the crack sliding mode. Lastly, K_{III} represents the mode III stress intensity factor, applicable to the tearing mode. These factors are precisely defined as follows ⁸⁹

$$\begin{aligned}
 K_I &= \lim_{r \rightarrow 0} \sqrt{2\pi r} \sigma_{yy}(r, 0) \\
 K_{II} &= \lim_{r \rightarrow 0} \sqrt{2\pi r} \sigma_{yx}(r, 0) \\
 K_{III} &= \lim_{r \rightarrow 0} \sqrt{2\pi r} \sigma_{yz}(r, 0)
 \end{aligned} \tag{2.21}$$

For piezoelectric material, like stress intensity factors, electric displacement intensity factor is defined as ⁹⁰

$$K_D = \lim_{r \rightarrow 0} \sqrt{2\pi r} D(r, 0) \tag{2.22}$$

The sign of intensity factors in fracture mechanics provides information about the nature and direction of the stresses and deformations near the crack tip. For K_I , positive values indicate conditions that promote crack propagation, while negative values indicate conditions that hinder crack growth or maintain crack stability. The sign of stress intensity factors, K_{II} , K_{III} , and K_D , indicates the direction of the stresses and deformations near the crack tip, while larger magnitudes are more likely to promote crack propagation.

(3) Energy release rate

A generalized fracture criterion for piezoelectric material requires the establishment of a unified theory encompassing mixed mode behavior. Assuming that under applied loadings the crack tip advances along the crack plane from $x = a$ to $x = a + \delta$ ($\delta \ll a$), then the energy release rate at the crack tip $x = a$ per unit length during this process is ^{91,92}

$$G = \lim_{\delta \rightarrow 0^+} \frac{1}{2} \int_0^\delta \{ \sigma_{yy}(r, 0)u(\delta - r) + \sigma_{yx}(r, 0)w(\delta - r) + \sigma_{yz}(r, 0)w(\delta - r) + D(r, 0)\varphi(\delta - r) \} dr$$

$$G = \frac{1}{4} \{K\}^T \mathbf{L}^{-1} \{K\} \quad (2.23)$$

where u, v, w and φ represent the displacements along the respective stress and electric displacement directions. $\{K\} = \{K_I \ K_{II} \ K_{III} \ K_D\}^T$. The greater the energy release rate, the higher the risk of crack propagation.

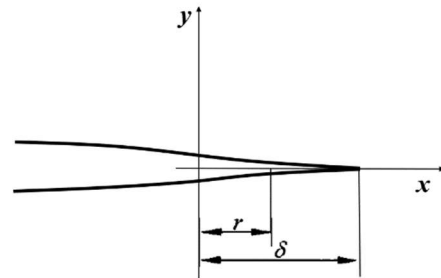


Figure 2. 6 Coordinate near the crack tip.

(4) Critical intensity factor

However, the energy release rate suffers from a theoretical limitation as it neglects the electrical term, as pointed out by Gao et al ⁹³. They argue that the mechanical term is not fundamentally distinct from the electrical term since both are influenced by electromagnetic forces. To solve this problem, the critical intensity factor was proposed which defined by

$$K_C = K_I + \frac{(\mathbf{L}^{-1})_{[2,4]}}{(\mathbf{L}^{-1})_{[2,2]}} K_D \quad (2.24)$$

For piezoelectric material, the coefficient of K_D in Eq. (2.24), i.e. $\frac{(\mathbf{L}^{-1})_{[2,4]}}{(\mathbf{L}^{-1})_{[2,2]}}$, is positive. This implies that a positive electric field will generate tensile stress, leading to increased crack growth, which aligns with the experimental findings of Pak and Sun ⁹⁴.

2.2 Challenges

The current state of research in structure design primarily focuses on single mechanical tests. However, for biomimetic materials to be reliably developed, a comprehensive consideration of their functional properties is imperative as well. Especially for complex configurations, the phase arrangement choice will highly depend on the physical environments.

In the context of functional properties, all the bioheat conduction equations used in assessing multiphysical environment-induced damage in biological materials are based on the classical Fourier heat conduction law, assuming an infinite speed of thermal disturbance propagation. Nevertheless, Kaminski ⁹⁵, Rastegar ⁹⁶, and Mitra et al. ⁹⁷ proved that for biomaterials with heterogeneous microstructures, the heat flux equilibrates to the imposed temperature gradient via a relaxation phenomenon characterized by a thermal characteristic (relaxation) time. To describe

thermal transport more accurately in biomaterials, the thermal relaxation effect ⁹⁸ has been incorporated into the classical heat conduction equations ⁹⁵⁻⁹⁷ and bioheat conduction equations ⁹⁹⁻¹⁰³. Lately, Banerjee and his colleagues ¹⁰⁴ have demonstrated experimentally and theoretically that the hyperbolic heat conduction equation is more accurate than the parabolic heat conduction equation for both short-pulse and continuous-wave laser irradiations when modeling temperature response in biomaterials.

(1) Hyperbolic heat conduction

The thermal wave equation of hyperbolic type was proposed by Cattaneo and Vernotte, taking into account “inertia” of the heat transfer process ^{105,106}

$$\mathbf{q}(x, t) + \tau_q \frac{\partial \mathbf{q}(x, t)}{\partial t} = -k \nabla T(x, t) \quad (2.25)$$

where τ_q is a relaxation time depending on material properties, and the finite thermal wave speed can be calculated as $s_q = \sqrt{\frac{k}{\rho c_p \tau_q}}$, where k is the thermal conductivity, ρ is the mass density, and c_p is the specific heat capacity. When τ_q equals zero, the thermal wave speed will be infinite, and Eq. (2.25) is transformed to the classical Fourier’s Law Eq. (2.14).

(2) Dual-phase-lag heat conduction

In addition, heat conduction in two-phase-systems of biomaterials shows deviation from classical Fourier’s law. Researchers ^{107,108} applied energy conservation and Fourier’s law to the two-phase-biosystems suffering non-thermal equilibrium and found that the heat conduction in two-phase-biosystems was equivalent to dual-phase-lag heat conduction, which is defined as ¹⁰⁹

$$\mathbf{q}(x, t + \tau_q) = -k\nabla T(x, t + \tau_s) \quad (2.26)$$

where \mathbf{q} is heat flux, k is thermal conductivity, T is temperature, and τ_q and τ_s are the time lags of heat flux and temperature gradient respectively. When $\tau_q > \tau_s$, the first order approximation of Eq. (2.26) is hyperbolic type and thermal waves will be generated, while when $\tau_q < \tau_s$, it will become parabolic type without thermal waves.

(3) Fractional heat conduction

Lately, the fractional thermal wave bioheat transfer equation has been widely used in biological tissue ¹¹⁰⁻¹¹⁴. Different from the integer order, the time fractional differential is characterized by its nonlocal property and memory effect, which implies the next state of a system depends on both the current input as well as the historical states, as illustrated by

$$\mathbf{q}(x, t) + \frac{\tau_q^\alpha}{\alpha!} \frac{\partial^\alpha \mathbf{q}(x, t)}{\partial t^\alpha} = -k\nabla T(x, t) \quad (2.27)$$

where

$$\frac{\partial^\alpha f(x, t)}{\partial t^\alpha} = \begin{cases} \frac{1}{\Gamma(1-\alpha)} \int_0^t (t-\tau)^{-\alpha} \frac{\partial f(x, \tau)}{\partial \tau} d\tau & 0 < \alpha < 1 \\ \frac{\partial f(x, t)}{\partial t} & \alpha = 1 \end{cases}$$

Using the fractional time derivative, many biological processes have been successfully modeled. Ezzat and colleagues ^{115,116} introduced a novel fractional bio-heat model using the fractional heat conduction equation. Ghanmi and Abbas ¹¹⁷ examined fractional transient heating occurring within skin tissue due to the movement of a heat source. Mondal et al. ¹¹⁸ explored transient heating within skin tissue resulting from time-dependent thermal therapy, within the

framework of a heat transport law characterized by memory-dependent behavior. Caponetto and his associates ¹¹⁹ further experimentally demonstrated the reliability of enhanced fractional heat conduction theory, and find the fractional order is a powerful characteristic parameter for heterogeneous materials.

For multiphysical behavior of biomaterials, non-Fourier thermal damage analysis becomes a challenging topic, especially when temperature, electric field, moisture and mechanical loading are coupled simultaneously. Until now, there are still gaps in the non-Fourier thermal damage study of biomimetic materials in multiphysical environment, and how to select the appropriate material configuration for different multiphysical fields is another challenge.

2.3 Objectives and Methods

The objective of the thesis is to build the non-Fourier multiphysical model and guide the hierarchical structural design under different physics. To achieve the goal, three tasks need to be tackled:

- (1) Establishment of multiphysical piezoelectric fracture model based on non-Fourier heat conduction.
- (2) Implementation of heterogeneous microstructure in fracture prediction of biomimetic materials.
- (3) Construction of non-Fourier multiphysical piezoelectric model for fracture analysis of hierarchical microstructures.

The main theoretical methods of integral transform and singular integral equations are employed to deal with the governing equations of both the transient thermal fields and dynamic stress and electric fields. In order to solve the non-Fourier thermo-electromechanical problems in

cracked media, Fourier transform is utilized to convert the partial differential equations to ordinary differential equations, while Laplace transform is used to eliminate time dependence and analyze the mathematical problem in the Laplace domain. By incorporating corresponding boundary conditions, the problems are eventually reduced to singular integral equations and then solved numerically to reveal the singularity of thermoelectromechanical response around the cracks.

2.4 Structure of the thesis

The thesis is structured around the three major tasks, particularly on fracture analysis of biomimetic composite materials and structures under multiphysical loading. Nonlinear coupling field and crack properties are explored in the framework of non-Fourier model.

In chapter 3, the non-Fourier, fractional heat conduction equation is introduced in the thermal analysis of a homogenous cracked piezoelectric strip to reflect the influence of thermal waves on the thermoelectric, fracture behavior of biomimetic materials under thermal and electrical shock loadings. In chapter 4, the simulation of hierarchical microstructure in biomimetic materials is effectively realized through the implementation of the functional gradation method and verified by experimental and numerical results under single tensile load. The thermal stress and fracture prediction of different gradations are compared with each other under transient thermal and stress loadings. In chapter 5, the comprehensive thermo-electromechanical analysis is conducted for functionally graded microstructures. The optimal gradation configuration and design guidelines for graded microstructures under various fields are provided. In chapter 6, the results of non-Fourier multiphysical models are verified by finite element simulations using COMSOL Multiphysics software. The non-Fourier heat conduction model is achieved in the numerical work.

Finally, chapter 7 provides conclusions and some perspectives for future work. A detailed flow chart is presented below to elucidate the structure in a clearer manner:

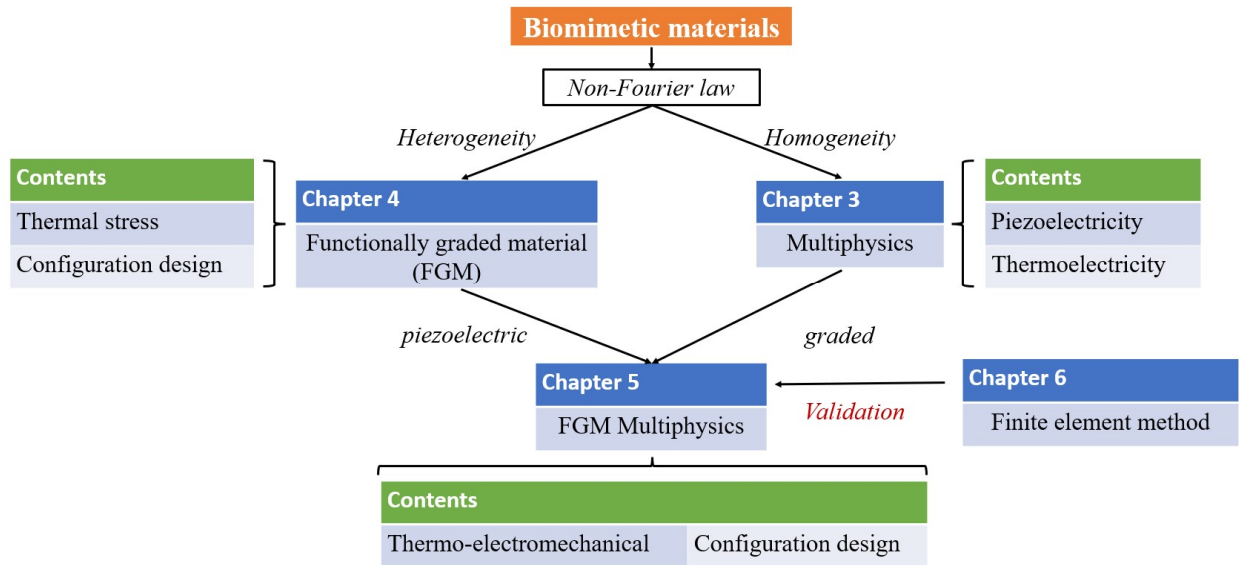


Figure 2. 7 Structure of the thesis.

Chapter 3

Dynamic response of a cracked thermopiezoelectric strip under thermoelectric loading using fractional heat conduction

Piezoelectric materials are a class of smart materials widely used in biomimetic engineering because of their ability to consistently exhibit reproducible and stable electromechanical responses when subjected to electrical or mechanical stimuli, which is similar to the biological materials. This chapter simplifies the materials into homogeneity and employs the constitutive equations of piezoelectric materials to mathematically model the dynamic multiphysical behavior of biomimetic materials. With the aid of fractional heat conduction equation and Maxwell's equations, we analyze the effects of temperature and electrical disturbances on the stress-electric displacement intensity factors. The results reveal that, with the longer relaxation time and higher fractional order, the overshooting phenomenon would be more evident, while the wave behavior becomes weaker and stronger, respectively. There are apparent inflection points on the dynamic stress intensity factors (DSIFs) and the dynamic electric displacement intensity factor (DEDF) curves for different configurations of the strip and the coefficients of the heat conduction model. In addition, the stress intensity factors are insensitive to the electric load which has a dominant influence on the electric displacement intensity factor.

3.1 Introduction

Smart materials can achieve self-adaptable and self-recoverable performance by responding to external stimuli, such as stress, moisture, temperature, electricity, and much more ¹²⁰⁻¹²², and have already found applications in the aerospace, automotive, and many other industries. As a typical smart material, piezoelectric material exhibits high sensitivity and excellent electrical insulating properties and has been widely used in bioengineering applications ^{120,121,123}.

Piezoelectric materials can convert the electric signals into physical deformation, and an applied deformation can also generate an electric current in the piezoelectric material. Most piezoelectric materials are brittle and susceptible to cracking, particularly when they are exposed to extremely high or low temperatures. Therefore, many researchers devoted to the thermal fracture analysis of piezoelectric materials. Ueda et al. ^{76,124} gave a transient heat conduction analysis of the piezoelectric strip with a parallel or perpendicular crack. Wang et al. ^{19,94} derived a general solution for a penny-shaped crack in piezoelectric materials subjected to a uniform or transient heat flow. Arani et al. ¹²⁵ studied thermo-electro-mechanical behaviors of the piezoelectric rotating shaft. Until now, the fracture behavior of piezoelectric materials under different thermal loading conditions has been investigated by many researchers ¹²⁶⁻¹³¹.

It is worth noting that all the above studies were based on the classical Fourier heat conduction law, which allows thermal disturbance to spread at an infinite speed. However, the process of establishment of thermal equilibrium needs a certain period of time. To fix this defect, researchers introduced the non-Fourier heat conduction model, which considers the relaxation time of thermal disturbance ¹³²⁻¹³⁶. Hu and Chen ¹³⁷ employed the hyperbolic heat conduction theory to check the thermoelastic performance of a cracked strip, whose results showed the hyperbolic heat conduction

model gives more conservative results than the Fourier model. Zhou et al.¹³⁸ analyzed a functionally graded piezoelectric strip by hyperbolic heat conduction and compared the results with the Fourier heat conduction model. It showed that the contact stress and surface heat flow reach their peak values later based on the non-Fourier theory than the Fourier theory. Mondal et al.¹³⁹ dealt with the transient behavior of a magnetic-piezoelastic half-space through the dual-phase-lag heat conduction model. They found the new model presents a much better prediction than the Fourier heat conduction. Wang and Li¹⁴⁰ adopted the hyperbolic, non-Fourier heat conduction to study the mechanics of a finite piezoelectric layer with a Griffith cracked under thermal loading. They pointed out that the non-Fourier effect became significant on a small length scale.

In the most previous work, the historical states have not been taken into account. As a part of the non-Fourier theory, the fractional heat conduction model could describe the state of the system containing information about its past state¹⁴¹⁻¹⁴⁶. In the last few years, fractional calculus had been applied successfully in various material modeling to rebuild the physical processes¹⁴⁷⁻¹⁵⁴. Ezzat and El Karamany^{155,156} found the theory of electro-thermoelasticity with fractional derivative order can describe the behavior more realistically than the theory of integer order. Ma and He¹⁵⁷ investigated the dynamic response of a one-dimensional, thermo-piezoelectric rod in the context of fractional order heat conduction theory. Results showed the effects of fractional order on the displacement, temperature and stress results. The researchers¹⁵⁸ further found the response of piezoelectric material becomes more expressive in transient conditions.

From the above overview, there are not sufficient research about the effect of different fractional models and crack locations on the dynamic behaviors of piezoelectric material under multi-physical loading. Concerning the practical problem, the multi-physical field conditions need

to be investigated owing to the importance of engineering applications. In this paper, we investigate the dynamic response of an insulated crack in a piezoelectric strip under the in-plane normal thermal and electrical impacts. The problem is reduced to a system of singular integral equations that can be solved numerically. The numerical results indicate that the thermal-electrical loading combination and the configuration of the crack, as well as the thermal relaxation time and fractional order coefficients of the heat conduction model significantly affect such fracture parameters as the dynamic stress intensity factors and the dynamic electric displacement intensity factor. Especially, the electric displacement intensity factor shows the apparent dynamic response instead of the stress intensity factors for the electric load. And the dynamic intensity factors have obvious inflection points for the configuration of the crack and the coefficients of the heat conduction model considered. In conclusion, the result shows that we can adjust the variables of the heat conduction model to obtain the most reliable numerical results in commercial software according to the inflection points.

3.2 Problem statement and basic equations

Consider an infinite, transversely isotropic, piezoelectric strip of length $h = h_1 + h_2$ with a parallel insulated crack of width $2c$, as shown in Figure 3.1. For convenience, a set of Cartesian coordinate system (x, y, z) is attached to the center of the crack.

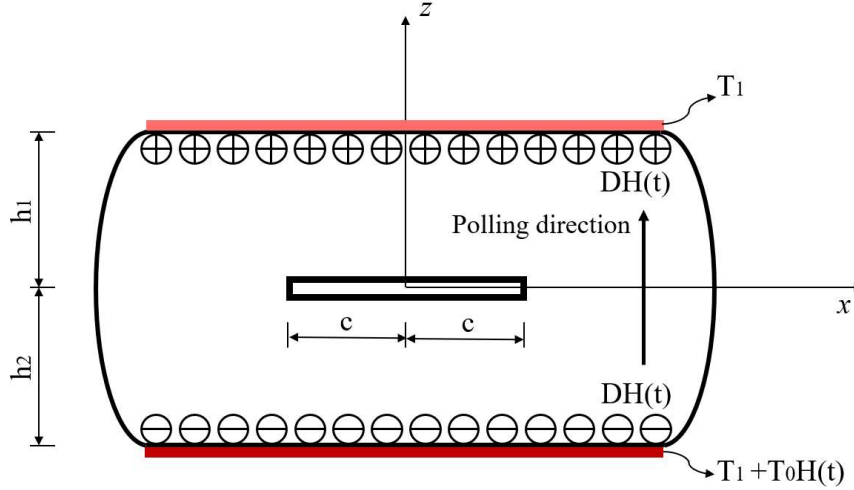


Figure 3. 1 A piezoelectric strip with an insulated crack under thermal-electric loading.

As shown in Figure 3.1, a suddenly uniform thermal shock $T_0H(t)$ is applied on the lower edge, where $H(t)$ is the Heaviside step function, and t denotes time. The initial temperature of the whole plane is T_1 . A transient electric displacement $DH(t)$ is applied in the positive z -direction. And the boundary condition at infinity in x -direction is taken to be zero.

3.3 Fractional heat conduction equation

For the temperature field, considering the relaxation time for the thermal shock, the fractional, non-Fourier heat conduction equation is:

$$\begin{aligned} \left(1 + \frac{\tau_q^\alpha}{\alpha!} \frac{\partial^\alpha}{\partial t^\alpha}\right) q_x &= -k_x \frac{\partial T_i}{\partial x} \\ \left(1 + \frac{\tau_q^\alpha}{\alpha!} \frac{\partial^\alpha}{\partial t^\alpha}\right) q_z &= -k_z \frac{\partial T_i}{\partial z} \end{aligned} \quad 0 < \alpha < 1 \quad (3.1)$$

where q_x, q_z are the heat fluxes in the x - and z - directions, T_i is the change of temperature; $i = 1, 2$ denote the field quantities in the upper ($0 \leq z \leq h_1$) and lower ($-h_2 \leq z \leq 0$) part of the

strip, respectively; τ_q^α is the thermal relaxation time, and k_x and k_z are the thermal conductivities in the x- and z-directions. The Caputo fractional derivative of order α is defined as:

$$\frac{\partial^\alpha f}{\partial t^\alpha} = \begin{cases} \frac{1}{\Gamma(1-\alpha)} \int_0^t (t-\tau)^{-\alpha} \frac{\partial f}{\partial \tau} d\tau & 0 < \alpha < 1 \\ \frac{\partial f}{\partial t} & \alpha = 1 \end{cases} \quad (3.2)$$

and $\Gamma(*)$ is the Gamma function. Combining with energy equation without heat resource:

$$\rho c_\rho \frac{\partial T_i}{\partial t} = -\nabla \cdot \mathbf{q} \quad (3.3)$$

where ρ and c_ρ are the mass density and the specific heat, finally, the non-Fourier fractional heat conduction equation becomes:

$$\frac{1}{\beta} \left(\frac{\partial T_i}{\partial t} + \frac{\tau_q^\alpha}{\alpha!} \frac{\partial^{\alpha+1} T_i}{\partial t^{\alpha+1}} \right) = \kappa \frac{\partial^2 T_i}{\partial x^2} + \frac{\partial^2 T_i}{\partial z^2} \quad 0 < \alpha < 1 \quad (3.4)$$

where $k = \frac{k_x}{k_z}$, and $\beta = \frac{k_z}{\rho c_\rho}$ which is the thermal diffusivity.

According to the problem considered, the thermal initial and boundary conditions in the time domain are:

Initial condition:

$$T_i(x, z, 0) = T_1 \quad (3.5)$$

Assuming an insulating crack, then:

$$\frac{\partial T_1(x, 0, t)}{\partial z} = \frac{\partial T_2(x, 0, t)}{\partial z} = 0 \quad |x| < c \quad (3.6 - 1)$$

And the heat flux and temperature along the extended line of crack is continuous.

$$\frac{\partial T_1(x, 0, t)}{\partial z} = \frac{\partial T_2(x, 0, t)}{\partial z} \quad |x| \geq c \quad (3.6 - 2)$$

$$T_1(x, 0, t) = T_2(x, 0, t) \quad |x| \geq c \quad (3.6 - 3)$$

Boundary conditions at the edges:

$$T_1(x, h_1, t) = T_1 \quad |x| \geq 0 \quad (3.6 - 4)$$

$$T_2(x, -h_2, t) = T_1 + T_0 H(t) \quad |x| \geq 0 \quad (3.6 - 5)$$

3.4 Piezothermoelastic governing equation

The corresponding constitutive relations of linear, transversely isotropic, piezoelectric strip for the elastic and electric field are:

$$\begin{aligned} \sigma_{xxi} &= c_{11} \frac{\partial u_{xi}}{\partial x} + c_{13} \frac{\partial u_{zi}}{\partial z} + e_{31} \frac{\partial \phi_i}{\partial z} - \lambda_{11} T_i \\ \sigma_{zzi} &= c_{13} \frac{\partial u_{xi}}{\partial x} + c_{33} \frac{\partial u_{zi}}{\partial z} + e_{33} \frac{\partial \phi_i}{\partial z} - \lambda_{33} T_i \\ \sigma_{zxi} &= c_{44} \left(\frac{\partial u_{xi}}{\partial z} + \frac{\partial u_{zi}}{\partial x} \right) + e_{15} \frac{\partial \phi_i}{\partial x} \\ D_{xi} &= e_{15} \left(\frac{\partial u_{xi}}{\partial z} + \frac{\partial u_{zi}}{\partial x} \right) - \varepsilon_{11} \frac{\partial \phi_i}{\partial x} \\ D_{zi} &= e_{31} \frac{\partial u_{xi}}{\partial x} + e_{33} \frac{\partial u_{zi}}{\partial z} - \varepsilon_{33} \frac{\partial \phi_i}{\partial z} + p_z T_i \end{aligned} \quad (3.7)$$

in which σ_{xxi} , σ_{zzi} , σ_{zxi} and D_{xi} , D_{zi} are stress tensor and electric displacement components; u_{xi} , u_{zi} , ϕ_i and T_i are displacement in the x-direction, displacement in the z-direction, electric

potential and temperature change; c_{jk} , e_{jk} , ε_{jk} , λ_{jk} and p_z are, respectively, elastic, piezoelectric, dielectric, thermal moduli and pyroelectric constants.

As the strip is under a thermal shock loading, according to the dynamic equilibrium equation, the governing equations for the piezoelectric strip are:

$$\begin{aligned}
(c_{11} \frac{\partial^2}{\partial x^2} + c_{44} \frac{\partial^2}{\partial z^2} - \rho \frac{\partial^2}{\partial t^2}) u_{xi} + (c_{13} + c_{44}) \frac{\partial^2 u_{zi}}{\partial x \partial z} + (e_{31} + e_{15}) \frac{\partial^2 \phi_i}{\partial x \partial z} &= \lambda_{11} \frac{\partial T_i}{\partial x} \\
(c_{13} + c_{44}) \frac{\partial^2 u_{xi}}{\partial x \partial z} + (c_{44} \frac{\partial^2}{\partial x^2} + c_{33} \frac{\partial^2}{\partial z^2} - \rho \frac{\partial^2}{\partial t^2}) u_{zi} + e_{15} \frac{\partial^2 \phi_i}{\partial x^2} + e_{33} \frac{\partial^2 \phi_i}{\partial z^2} &= \lambda_{33} \frac{\partial T_i}{\partial z} \quad (3.8) \\
(e_{15} + e_{31}) \frac{\partial^2 u_{xi}}{\partial x \partial z} + (e_{15} \frac{\partial^2}{\partial x^2} + e_{33} \frac{\partial^2}{\partial z^2}) u_{zi} - \varepsilon_{11} \frac{\partial^2 \phi_i}{\partial x^2} - \varepsilon_{33} \frac{\partial^2 \phi_i}{\partial z^2} &= -p_z \frac{\partial T_i}{\partial z}
\end{aligned}$$

Then, the boundary conditions for the electromechanical field are:

$$\sigma_{zzi}(x, 0, t) = 0 \quad |x| < c \quad (3.9 - 1)$$

$$\sigma_{zxi}(x, 0, t) = 0 \quad |x| < c \quad (3.9 - 2)$$

$$D_{zi}(x, 0, t) = 0 \quad |x| < c \quad (3.9 - 3)$$

$$\sigma_{zz1}(x, 0, t) = \sigma_{zz2}(x, 0, t) \quad |x| \geq c \quad (3.9 - 4)$$

$$\sigma_{zx1}(x, 0, t) = \sigma_{zx2}(x, 0, t) \quad |x| \geq c \quad (3.9 - 5)$$

$$D_{z1}(x, 0, t) = D_{z2}(x, 0, t) \quad |x| \geq c \quad (3.9 - 6)$$

$$u_{z1}(x, 0, t) = u_{z2}(x, 0, t) \quad |x| \geq c \quad (3.9 - 7)$$

$$u_{x1}(x, 0, t) = u_{x2}(x, 0, t) \quad |x| \geq c \quad (3.9 - 8)$$

$$\phi_1(x, 0, t) = \phi_2(x, 0, t) \quad |x| \geq c \quad (3.9 - 9)$$

at the crack surface and extended line, and

$$\sigma_{zz1}(x, h_1, t) = 0 \quad |x| \geq 0 \quad (3.9 - 10)$$

$$\sigma_{zx1}(x, h_1, t) = 0 \quad |x| \geq 0 \quad (3.9 - 11)$$

$$D_{z1}(x, h_1, t) = DH(t) \quad |x| \geq 0 \quad (3.9 - 12)$$

$$\sigma_{zz}(x, -h_2, t) = 0 \quad |x| \geq 0 \quad (3.9 - 13)$$

$$\sigma_{zx2}(x, -h_2, t) = 0 \quad |x| \geq 0 \quad (3.9 - 14)$$

$$D_{z2}(x, -h_2, t) = DH(t) \quad |x| \geq 0 \quad (3.9 - 15)$$

at the boundary surfaces.

3.5 General solutions

3.5.1 Temperature field

According to superposition, the temperature field can be rewritten as the sum of the uniform temperature field without crack, $T^{(1)}$, and the temperature field disturbed by the existence of crack, $T_i^{(2)}$, and the initial temperature T_1 :

$$T_i(x, z, t) = T_1 + T^{(1)}(z, t) + T_i^{(2)}(x, z, t) \quad (3.10)$$

To continue the analysis, the following property of the Laplace transform for fractional derivative

$$\mathcal{L}\left\{\frac{\partial^\alpha f(t)}{\partial t^\alpha}\right\} = p^\alpha f^*(p) - \sum_{k=0}^{m-1} f^{(k)}(0^+) p^{\alpha-1-k} \quad (3.11)$$

will be adopted, where p is the Laplace transform variable, m is the largest integer less than α and the asterisk denotes the Laplace transform of a function. Applying a Laplace transform pair as:

$$f^*(x, z, p) = \int_0^{\infty} f(x, z, t) \exp(-pt) dt$$

$$f(x, z, t) = \frac{1}{2\pi i} \int_{Br} f^*(x, z, p) \exp(pt) dp \quad (3.12)$$

in which Br stands for the Bromwich path of integration ¹⁵⁹, then $T^{(1)}(z, t)$ and $T_i^{(2)}(x, z, t)$ change into $T^{*(1)}(z, p)$ and $T_i^{*(2)}(x, z, p)$, where $T^{*(1)}(z, p)$ satisfies the following definition and boundary conditions:

$$\frac{1}{\beta} p \left(1 + \frac{\tau_q^\alpha}{\alpha!} p^\alpha \right) T^{*(1)} = \frac{d^2 T^{*(1)}}{dz^2} \quad 0 < \alpha < 1 \quad (3.13)$$

$$T^{*(1)}(-h_2, p) = \frac{T_0}{p} H(p) \quad (3.14 - 1)$$

$$T^{*(1)}(h_1, p) = 0 \quad (3.14 - 2)$$

Then, the expression and the corresponding boundary conditions of $T_i^{*(2)}(x, z, p)$ are:

$$\frac{1}{\beta} p \left(1 + \frac{\tau_q^\alpha}{\alpha!} p^\alpha \right) T_i^{*(2)} = \kappa \frac{\partial^2 T_i^{*(2)}}{\partial x^2} + \frac{\partial^2 T_i^{*(2)}}{\partial z^2} \quad 0 < \alpha < 1 \quad (3.15)$$

and

$$\frac{\partial T_1^{*(2)}(x, 0, p)}{\partial z} = \frac{\partial T_2^{*(2)}(x, 0, p)}{\partial z} = -\frac{dT^{*(1)}}{dz} \quad |x| < c \quad (3.16 - 1)$$

$$\frac{\partial T_1^{*(2)}(x, 0, p)}{\partial z} = \frac{\partial T_2^{*(2)}(x, 0, p)}{\partial z} \quad |x| \geq c \quad (3.16 - 2)$$

$$T_1^{*(2)}(x, 0, p) = T_2^{*(2)}(x, 0, p) \quad |x| \geq c \quad (3.16 - 3)$$

at the crack surface and extended line, and

$$T_1^{*(2)}(x, h_1, p) = 0 \quad |x| \geq 0 \quad (3.16 - 4)$$

$$T_2^{*(2)}(x, -h_2, p) = 0 \quad |x| \geq 0 \quad (3.16 - 5)$$

at the edges.

It is easy to solve Eq. (3.13) combined with Eq. (3.14) ¹⁶⁰,

$$T^{*(1)}(z, p) = \frac{T_0\{\exp[-(h_2 + z)\sqrt{\lambda}] - \exp[-(2h_1 + h_2 - z)\sqrt{\lambda}]\}}{p[1 - \exp(-2h\sqrt{\lambda})]} \quad (3.17)$$

where $\lambda = \frac{1}{\beta}p \left(1 + \frac{\tau_q^\alpha}{\alpha!}p^\alpha\right)$.

Applying the Fourier integral transform to Eq. (3.15), and its general solution is obtained:

$$T_1^{*(2)}(x, z, p) = \frac{1}{2\pi} \int_{-\infty}^{\infty} [D_{11} \exp(|s|\tau z) + D_{12} \exp(-|s|\tau z)] \exp(-isx) ds \quad z > 0 \quad (3.18 - 1)$$

$$T_2^{*(2)}(x, z, p) = \frac{1}{2\pi} \int_{-\infty}^{\infty} [D_{21} \exp(|s|\tau z) + D_{22} \exp(-|s|\tau z)] \exp(-isx) ds \quad z < 0 \quad (3.18 - 2)$$

in which, $\tau = \sqrt{\kappa + \frac{\lambda}{s^2}}$, and $D_{ij}(s, p)$ are unknown functions which can be determined by

introducing the density function $G_0(x, p)$:

$$G_0(x, p) = \begin{cases} \frac{\partial}{\partial x} \{T_1^{*(2)}(x, 0, p) - T_2^{*(2)}(x, 0, p)\} & |x| < c \\ 0 & |x| \geq c \end{cases} \quad (3.19)$$

Substituting the general results of Eq. (18) into Eq. (19), based on Eq. (3.16-2), (3.16-4) and (3.16-5), all the functions of $D_{ij}(s, p)$ can be expressed in terms of $D_0(s, p)$:

$$D_{11}(s, p) = -\exp(-2h_1\tau|s|) \frac{\rho_2(s, p)}{\rho_0(s, p)} D_0(s, p) \quad (3.20 - 1)$$

$$D_{12}(s, p) = \frac{\rho_2(s, p)}{\rho_0(s, p)} D_0(s, p) \quad (3.20 - 2)$$

$$D_{21}(s, p) = \frac{\rho_1(s, p)}{\rho_0(s, p)} D_0(s, p) \quad (3.20 - 3)$$

$$D_{22}(s, p) = -\exp(-2h_2\tau|s|) \frac{\rho_1(s, p)}{\rho_0(s, p)} D_0(s, p) \quad (3.20 - 4)$$

and:

$$\left. \begin{aligned} \rho_0(s, p) &= [1 - \exp(-2h_1\tau|s|)]\rho_2 - [1 - \exp(-2h_2\tau|s|)]\rho_1 \\ \rho_1(s, p) &= -[1 + \exp(-2h_1\tau|s|)] \\ \rho_2(s, p) &= 1 + \exp(-2h_2\tau|s|) \end{aligned} \right\} \quad (3.21)$$

where function D_0 can be expressed in terms of $G_0(x, p)$ by using inverse Fourier transform:

$$D_0 = -\frac{1}{is} \int_{-c}^c G_0(\xi, p) \exp(is\xi) d\xi \quad (3.22)$$

Letting $\bar{\xi} = \xi/c$, $\bar{x} = x/c$, then, the singular integral equation of $G_0(\xi, p)$ is finally obtained via Eq. (3.16-1):

$$\frac{1}{2\pi} \int_{-1}^1 \bar{G}_0(\bar{\xi}, p) \left\{ \frac{1}{\bar{\xi} - \bar{x}} + c\bar{M}_0(\bar{x}, \bar{\xi}, p) \right\} d\bar{\xi} = -\frac{dT^{*(1)}}{dz} \quad (3.23)$$

where the kernel function reads:

$$\bar{M}_0(\bar{x}, \bar{\xi}, p) = \int_0^\infty \left(-\frac{2\sqrt{\lambda + s^2}\rho_2\rho_1}{s\rho_0} - 1 \right) \sin[sc(\bar{\xi} - \bar{x})] ds \quad (3.24)$$

From the continuity condition, it is clear that

$$\int_{-1}^1 \overline{G}_0(\bar{\xi}, p) d\bar{\xi} = 0 \quad \text{and,} \quad \overline{G}_0(\bar{\xi}, p) = 0 \quad |\bar{\xi}| \geq 1 \quad (3.25)$$

Employing Erdogan's numerical method ¹⁶¹, the singular integral equation, Eq. (3.23), can be reduced to the following algebraic equation:

$$\frac{1}{2} \sum_{k=1}^n \frac{1}{n} F(\bar{\xi}_k, p) \left\{ \frac{1}{\bar{\xi}_k - \bar{x}_r} + c \overline{M}_0(\bar{x}_r, \bar{\xi}_k, p) \right\} = - \frac{dT^{*(1)}}{dz} \quad |\bar{x}| \leq 1 \quad (3.26)$$

$$\sum_{k=1}^n \frac{\pi}{n} F(\bar{\xi}_k, p) = 0 \quad (3.27)$$

where $\bar{\xi}_k = \cos \frac{(2k-1)\pi}{2n}$, $k = 1, 2, 3, \dots, n$; $\bar{x}_r = \cos \frac{r\pi}{n}$, $r = 1, 2, 3, \dots, n-1$ and

$$F(\bar{\xi}, p) = \overline{G}_0(\bar{\xi}, p) \sqrt{1 - \bar{\xi}^2} \quad |\bar{x}| \leq 1 \quad (3.28)$$

3.5.2 Electromechanical field

Once the temperature field is obtained, the displacement and electric potential in the Laplace domain can be found.

$$\begin{aligned} u_{xi}^*(x, z, p) &= u_{xi}^{*(2)}(x, z, p) \\ u_{zi}^*(x, z, p) &= u_z^{*(1)}(z, p) + u_{zi}^{*(2)}(x, z, p) \quad (i = 1, 2) \quad (3.29) \\ \phi_i^*(x, z, p) &= \phi^{*(1)}(z, p) + \phi_i^{*(2)}(x, z, p) \end{aligned}$$

Under uncracked situation which has no effect on x parameter, the governing equations, Eq. (3.8) change into:

$$\begin{aligned} \left(c_{33} \frac{d^2}{dz^2} - \rho p^2 \right) u_z^{*(1)} + e_{33} \frac{d^2 \phi^{*(1)}}{dz^2} &= \lambda_{33} \frac{dT^{*(1)}}{dz} \\ e_{33} \frac{d^2 u_z^{*(1)}}{dz^2} - \varepsilon_{33} \frac{d^2 \phi^{*(1)}}{dz^2} &= -p_z \frac{dT^{*(1)}}{dz} \end{aligned} \quad (3.30)$$

And the boundary conditions are:

$$\left. \begin{aligned} \sigma_{zz}^{*(1)}(h_1, p) &= 0, \quad \sigma_{zz}^{*(1)}(-h_2, p) = 0 \\ D_z^{*(1)}(h_1) &= \frac{D}{p} H(p), \quad D_z^{*(1)}(-h_2) = \frac{D}{p} H(p) \end{aligned} \right\} \quad (3.31)$$

Solving Eq. (3.30) with Eq. (3.31), the solutions are:

$$\begin{aligned} u_z^{*(1)}(z, p) &= -e_{33} \beta_u [C_1 \exp(\sqrt{\beta_u} z) + C_2 \exp(-\sqrt{\beta_u} z)] \\ &+ C_{uz} \frac{-T_0 \sqrt{\lambda} \{ \exp[-(h_2 + z)\sqrt{\lambda}] + \exp[-(2h_1 + h_2 - z)\sqrt{\lambda}] \}}{p [1 - \exp(-2h\sqrt{\lambda})]} \end{aligned} \quad (3.32)$$

$$\begin{aligned} \phi^{*(1)}(z, p) &= (c_{33} \beta_u - \rho p^2) [C_1 \exp(\sqrt{\beta_u} z) + C_2 \exp(-\sqrt{\beta_u} z)] - \rho p^2 [C_3 z + C_4] \\ &+ C_{pz} \frac{-T_0 \sqrt{\lambda} \{ \exp[-(h_2 + z)\sqrt{\lambda}] + \exp[-(2h_1 + h_2 - z)\sqrt{\lambda}] \}}{p [1 - \exp(-2h\sqrt{\lambda})]} \end{aligned} \quad (3.33)$$

where $\beta_u = \frac{\varepsilon_{33} \rho p^2}{\varepsilon_{33} c_{33} + e_{33}^2}$, and:

$$\left. \begin{aligned}
C_1 &= \frac{(C_{sz1}\varepsilon_{33}T_0 - De_{33}) \exp(-(2h_1 + h_2)\sqrt{\beta_u}) + De_{33} \exp(-\sqrt{\beta_u}h_1)}{C_{sz2}\varepsilon_{33}p[1 + \exp(-2\sqrt{\beta_u}h)]} \\
C_2 &= \frac{De_{33} \exp(-(2h_2 + h_1)\sqrt{\beta_u}) + (C_{sz} \varepsilon_{33}T_0 - De_{33}) \exp(-\sqrt{\beta_u}h_2)}{C_{sz2}\varepsilon_{33}p[1 + \exp(-2\sqrt{\beta_u}h)]} \\
C_{uz} &= \frac{\lambda_{33}\varepsilon_{33} - p_z e_{33}}{(\varepsilon_{33}c_{33} + e_{33}^2)\lambda - \varepsilon_{33}\rho p^2}, \quad C_{pz} = \frac{(e_{33}\lambda_{33} + c_{33}p_z)\lambda - p_z \rho p^2}{(\varepsilon_{33}c_{33} + e_{33}^2)\lambda^2 - \varepsilon_{33}\rho p^2 \lambda} \\
C_{sz1} &= \frac{(\lambda_{33}\varepsilon_{33} - e_{33}p_z)\rho p^2}{(\varepsilon_{33}c_{33} + e_{33}^2)\lambda - \varepsilon_{33}\rho p^2}, \quad C_{sz2} = -\rho p^2 e_{33} \sqrt{\beta_u}
\end{aligned} \right\} \quad (3.34)$$

The normal stress and electric displacement under uncracked conditions can be obtained as follows:

$$\begin{aligned}
\sigma_{zz}^{*(1)}(z, p) &= C_{sz1} \frac{T_0 \{ \exp[-(h_2 + z)\sqrt{\lambda}] - \exp[-(2h_1 + h_2 - z)\sqrt{\lambda}] \}}{p[1 - \exp(-2h\sqrt{\lambda})]} - \frac{e_{33}D}{\varepsilon_{33}p} \\
&\quad + C_{sz2} [C_1 \exp(\sqrt{\beta_u}z) - C_2 \exp(-\sqrt{\beta_u}z)] \quad (3.35)
\end{aligned}$$

$$D_z^{*(1)}(z, p) = \frac{D}{p} \quad (3.36)$$

Then, the dynamic equilibrium equations for plane strain piezoelectricity in the Laplace domain caused by the temperature field $T_i^{*(2)}(x, z, p)$ can be given as:

$$\begin{aligned}
(c_{11} \frac{\partial^2}{\partial x^2} + c_{44} \frac{\partial^2}{\partial z^2} - \rho p^2) u_{xi}^{*(2)} + (c_{13} + c_{44}) \frac{\partial^2 u_{zi}^{*(2)}}{\partial x \partial z} + (e_{31} + e_{15}) \frac{\partial^2 \phi_i^{*(2)}}{\partial x \partial z} &= \lambda_{11} \frac{\partial T_i^{*(2)}}{\partial x} \\
(c_{13} + c_{44}) \frac{\partial^2 u_{xi}^{*(2)}}{\partial x \partial z} + (c_{44} \frac{\partial^2}{\partial x^2} + c_{33} \frac{\partial^2}{\partial z^2} - \rho p^2) u_{zi}^{*(2)} + e_{15} \frac{\partial^2 \phi_i^{*(2)}}{\partial x^2} + e_{33} \frac{\partial^2 \phi_i^{*(2)}}{\partial z^2} &= \lambda_{33} \frac{\partial T_i^{*(2)}}{\partial z} \quad (3.37) \\
(e_{15} + e_{31}) \frac{\partial^2 u_{xi}^{*(2)}}{\partial x \partial z} + (e_{15} \frac{\partial^2}{\partial x^2} + e_{33} \frac{\partial^2}{\partial z^2}) u_{zi}^{*(2)} - \varepsilon_{11} \frac{\partial^2 \phi_i^{*(2)}}{\partial x^2} - \varepsilon_{33} \frac{\partial^2 \phi_i^{*(2)}}{\partial z^2} &= -p_z \frac{\partial T_i^{*(2)}}{\partial z}
\end{aligned}$$

at the crack surface and extended line:

$$\sigma_{zzi}^{*(2)}(x, 0, p) = -\sigma_{zz}^{*(1)}(0, p) \quad |x| < c \quad (3.38 - 1)$$

$$\sigma_{zxi}^{*(2)}(x, 0, p) = -\sigma_{zx}^{*(1)}(0, p) \quad |x| < c \quad (3.38 - 2)$$

$$D_{zi}^{*(2)}(x, 0, p) = -D_z^{*(1)}(0, p) \quad |x| < c \quad (3.38 - 3)$$

$$\sigma_{zz1}^{*(2)}(x, 0, p) = \sigma_{zz}^{*(2)}(x, 0, p) \quad |x| \geq c \quad (3.38 - 4)$$

$$\sigma_{zx}^{*(2)}(x, 0, p) = \sigma_{zx2}^{*(2)}(x, 0, p) \quad |x| \geq c \quad (3.38 - 5)$$

$$D_{z1}^{*(2)}(x, 0, p) = D_{z2}^{*(2)}(x, 0, p) \quad |x| \geq c \quad (3.38 - 6)$$

$$u_{z1}^{*(2)}(x, 0, p) = u_{z2}^{*(2)}(x, 0, p) \quad |x| \geq c \quad (3.38 - 7)$$

$$u_{x1}^{*(2)}(x, 0, p) = u_{x2}^{*(2)}(x, 0, p) \quad |x| \geq c \quad (3.38 - 8)$$

$$\phi_1^{*(2)}(x, 0, p) = \phi_2^{*(2)}(x, 0, p) \quad |x| \geq c \quad (3.38 - 9)$$

at boundary surfaces:

$$\sigma_{zz1}^{*(2)}(x, h_1, p) = 0 \quad \sigma_{zz2}^{*(2)}(x, -h_2, p) = 0 \quad |x| \geq 0 \quad (3.38 - 10)$$

$$\sigma_{zx1}^{*(2)}(x, h_1, p) = 0 \quad \sigma_{zx2}^{*(2)}(x, -h_2, p) = 0 \quad |x| \geq 0 \quad (3.38 - 11)$$

$$D_{z1}^{*(2)}(x, h_1, p) = 0 \quad D_{z2}^{*(2)}(x, -h_2, p) = 0 \quad |x| \geq 0 \quad (3.38 - 12)$$

The solution of Eq. (3.37) is expressed by the general solution of the homogeneous equations, $u_{xi}^{*(21)}$, $u_{zi}^{*(21)}$ and $\phi_i^{*(21)}$ plus the particular solution of the nonhomogeneous equations, $u_{xi}^{*(22)}$, $u_{zi}^{*(22)}$ and $\phi_i^{*(22)}$. According to Ding et al. ¹⁶²,

$$u_{xi}^{*(21)} = H_{21}F_0^*, \quad u_{zi}^{*(21)} = H_{22}F_0^*, \quad \phi_i^{*(21)} = H_{23}F_0^* \quad (3.39)$$

$$u_{xi}^{*(22)} = \sum_{j=1}^3 H_{j1}F_j^*, \quad u_{zi}^{*(22)} = \sum_{j=1}^3 H_{j2}F_j^*, \quad \phi_i^{*(22)} = \sum_{j=1}^3 H_{j3}F_j^* \quad (3.39)$$

where H_{ij} ($i = 1,2; j = 1,2,3$) are co-factors of the differential operator matrix determinant $|D|$, and F_0^* and F_j^* satisfy the following relations:

$$|D|F_0^* = 0, \quad |D|F_1^* = \lambda_{11} \frac{\partial T_i^{*(2)}}{\partial x}, \quad |D|F_2^* = \lambda_{33} \frac{\partial T_i^{*(2)}}{\partial z}, \quad |D|F_3^* = -p_z \frac{\partial T_i^{*(2)}}{\partial z} \quad (3.40)$$

the coefficient matrix D is:

$$D = \begin{bmatrix} c_{11} \frac{\partial^2}{\partial x^2} + c_{44} \frac{\partial^2}{\partial z^2} - \rho p^2 & (c_{13} + c_{44}) \frac{\partial^2}{\partial x \partial z} & (e_{31} + e_{15}) \frac{\partial^2}{\partial x \partial z} \\ (c_{13} + c_{44}) \frac{\partial^2}{\partial x \partial z} & c_{44} \frac{\partial^2}{\partial x^2} + c_{33} \frac{\partial^2}{\partial z^2} - \rho p^2 & e_{15} \frac{\partial^2}{\partial x^2} + e_{33} \frac{\partial^2}{\partial z^2} \\ (e_{15} + e_{31}) \frac{\partial^2}{\partial x \partial z} & e_{15} \frac{\partial^2}{\partial x^2} + e_{33} \frac{\partial^2}{\partial z^2} & -\varepsilon_{11} \frac{\partial^2}{\partial x^2} - \varepsilon_{33} \frac{\partial^2}{\partial z^2} \end{bmatrix}$$

Using Fourier integral transform, the general solutions $u_{xi}^{*(21)}$, $u_{zi}^{*(21)}$ and $\phi_i^{*(21)}$ can be obtained:

$$\begin{aligned} u_{xi}^{*(21)}(x, z, p) &= \frac{i}{2\pi} \sum_{j=1}^3 \int_{-\infty}^{+\infty} \{Z_{j1} \operatorname{sgn}(s) [A_{ij} \exp(|s|\lambda_j z) - B_{ij} \exp(-|s|\lambda_j z)]\} \exp(-isx) ds \\ u_{zi}^{*(21)}(x, z, p) &= \frac{1}{2\pi} \sum_{j=1}^3 \int_{-\infty}^{+\infty} \{Z_{j2} [A_{ij} \exp(|s|\lambda_j z) + B_{ij} \exp(-|s|\lambda_j z)]\} \exp(-isx) ds \\ \phi_i^{*(21)}(x, z, p) &= \frac{1}{2\pi} \sum_{j=1}^3 \int_{-\infty}^{+\infty} \{Z_{j3} [A_{ij} \exp(|s|\lambda_j z) + B_{ij} \exp(-|s|\lambda_j z)]\} \exp(-isx) ds \end{aligned} \quad (3.41)$$

where

$$\begin{aligned} Z_{j1} &= (e_{15}e_{33} + e_{31}e_{33} + c_{13}\varepsilon_{33} + c_{44}\varepsilon_{33})s^4\lambda_j^3 - (e_{15}^2 + e_{15}e_{31} + c_{13}\varepsilon_{11} + c_{44}\varepsilon_{11})s^4\lambda_j \\ Z_{j2} &= -c_{44}\varepsilon_{33}s^4\lambda_j^4 + \{[(e_{15} + e_{31})^2 + c_{44}\varepsilon_{11} + c_{11}\varepsilon_{33}]s^2 + \varepsilon_{33}\rho p^2\}s^2\lambda_j^2 - (c_{11}\varepsilon_{11}s^4 + \varepsilon_{11}\rho p^2s^2) \\ Z_{j3} &= -c_{44}e_{33}s^4\lambda_j^4 - [(c_{44}e_{31} + c_{13}e_{15} + c_{13}e_{31} - c_{11}e_{33})s^2 - e_{33}\rho p^2]s^2\lambda_j^2 - (c_{11}e_{15}s^4 + e_{15}\rho p^2s^2) \end{aligned}$$

the roots λ_j ($j = 1,2,3$) are determined from solving the characteristic equation $|D| = 0$, and given in Appendix A; $A_{ij}(s, p), B_{ij}(s, p)$ are unknowns to be determined.

Based on Eq. (3.39) and Eq. (3.40), the particular solutions are as following:

$$\begin{aligned}
 u_{xi}^{*(22)}(x, z, p) &= \frac{i}{2\pi} \int_{-\infty}^{+\infty} (R_x^1 s^5 + R_x^2 s^3) [D_{i1} \exp(|s|\tau z) + D_{i2} \exp(-|s|\tau z)] \exp(-isx) ds \\
 u_{zi}^{*(22)}(x, z, p) &= \frac{1}{2\pi} \int_{-\infty}^{+\infty} (R_z^1 s^5 + R_z^2 s^3) \text{sgn}(s) [D_{i1} \exp(|s|\tau z) - D_{i2} \exp(-|s|\tau z)] \exp(-isx) ds \\
 \phi_i^{*(22)}(x, z, p) &= \frac{1}{2\pi} \int_{-\infty}^{+\infty} (R_\phi^1 s^5 + R_\phi^2 s^3 + R_\phi^3 s) \text{sgn}(s) [D_{i1} \exp(|s|\tau z) - D_{i2} \exp(-|s|\tau z)] \exp(-isx) ds
 \end{aligned} \tag{3.42}$$

the constants $R_x^1, R_x^2, R_z^1, R_z^2, R_\phi^1, R_\phi^2$ and R_ϕ^3 are shown in Appendix A.

The stress and electric displacement components can be expressed according to Eq. (3.7) as:

$$\begin{aligned}
 \sigma_{zz}^{*(2)}(x, z, p) &= \frac{1}{2\pi} \int_{-\infty}^{+\infty} \sum_{j=1}^3 \{P_{j1} [A_{1j} \exp(|s|\lambda_j z) - B_{1j} \exp(-|s|\lambda_j z)] \exp(-isx) ds \\
 &\quad + \frac{1}{2\pi} \int_{-\infty}^{+\infty} C_1 [D_{11} \exp(|s|\tau z) + D_{12} \exp(-|s|\tau z)] \exp(-isx) ds \\
 \sigma_{zx}^{*(2)}(x, z, p) &= \frac{1}{2\pi} \int_{-\infty}^{+\infty} \sum_{j=1}^3 \{P_{j2} i \text{sgn}(s) [A_{1j} \exp(|s|\lambda_j z) + B_{1j} \exp(-|s|\lambda_j z)] \exp(-isx) ds \\
 &\quad + \frac{1}{2\pi} \int_{-\infty}^{+\infty} C_2 i \text{sgn}(s) [D_{11} \exp(|s|\tau z) - D_{12} \exp(-|s|\tau z)] \exp(-isx) ds \\
 D_{z1}^{*(2)}(x, z, p) &= \frac{1}{2\pi} \int_{-\infty}^{+\infty} \sum_{j=1}^3 \{P_{j3} [A_{1j} \exp(|s|\lambda_j z) - B_{1j} \exp(-|s|\lambda_j z)] \exp(-isx) ds
 \end{aligned} \tag{3.43}$$

$$+ \frac{1}{2\pi} \int_{-\infty}^{+\infty} C_3 [D_{11} \exp(|s|\tau z) + D_{12} \exp(-|s|\tau z)] \exp(-isx) ds$$

where

$$P_{j1}(s, p) = c_{13} Z_{j1} |s| + c_{33} Z_{j2} |s| \lambda_j + e_{33} Z_{j3} |s| \lambda_j$$

$$P_{j2}(s, p) = c_{44} Z_{j1} |s| \lambda_j - c_{44} Z_{j2} |s| - e_{15} Z_{j3} |s|$$

$$P_{j3}(s, p) = e_{31} Z_{j1} |s| + e_{33} Z_{j2} |s| \lambda_j - \varepsilon_{33} Z_{j3} |s| \lambda_j$$

and:

$$C_1(s, p) = c_{13}(R_x^1 s^6 + R_x^2 s^4) + c_{33}(R_z^1 s^6 + R_z^2 s^4) \tau + e_{33}(R_\phi^1 s^6 + R_\phi^2 s^4 + R_\phi^3 s^2) \tau - \lambda_{33}$$

$$C_2(s, p) = c_{44}(R_x^1 s^6 + R_x^2 s^4) \tau - c_{44}(R_z^1 s^6 + R_z^2 s^4) - e_{15}(R_\phi^1 s^6 + R_\phi^2 s^4 + R_\phi^3 s^2)$$

$$C_3(s, p) = e_{31}(R_x^1 s^6 + R_x^2 s^4) + e_{33}(R_z^1 s^6 + R_z^2 s^4) \tau - \varepsilon_{33}(R_\phi^1 s^6 + R_\phi^2 s^4 + R_\phi^3 s^2) \tau + p_z$$

Combining with the boundary conditions Eq. (3.38-4) to Eq. (3.38-6) and Eq. (3.38-10) to Eq. (3.38-12), the unknown functions $A_{ij}(s, p)$, $B_{ij}(s, p)$ ($i = 1, 2; j = 1, 2, 3$) can be expressed in terms of unknowns $B_{1j}(s, p)$ ($j = 1, 2, 3$) as:

$$\begin{aligned} A_{1j}(s, p) &= \sum_{n=1}^3 V_n^{*(j)}(s, h_1, p) B_{1n} + C_{j+4}(s, p) D_0 \\ A_{2j}(s, p) &= \sum_{n=1}^3 I_n^{*(j)}(s, h_1, h_2, p) B_{1n} + C_{j+15}(s, p) D_0 \\ B_{2j}(s, p) &= \sum_{n=1}^3 U_n^{*(j)}(s, h_1, h_2, p) B_{1n} + C_{j+18}(s, p) D_0 \end{aligned} \quad (3.44)$$

where $V_j^{*(n)}(s, h_1, p)$, $U_j^{*(n)}(s, h_1, h_2, p)$, $I_j^{*(n)}(s, h_1, h_2, p)$, $C_{j+4}(s, p)$, $C_{j+15}(s, p)$ and $C_{j+18}(s, p)$ ($j, n = 1, 2, 3$) are known functions defined in Appendix A.

Similar to the temperature analysis, let's define the new unknown functions $G_l(x, p)$ ($l = 1, 2, 3$) to reduce the problem into a system of singular integral equations,

$$\begin{cases} G_1(x, p) \\ G_2(x, p) \\ G_3(x, p) \end{cases} = \frac{\partial}{\partial x} \begin{cases} u_{x1}^*(x, 0^+, p) - u_{x2}^*(x, 0^-, p) \\ u_{z1}^*(x, 0^+, p) - u_{z2}^*(x, 0^-, p) \\ \phi_2^*(x, 0^-, p) - \phi_1^*(x, 0^+, p) \end{cases} \quad |x| < c \quad (3.45)$$

Substituting the solutions Eq. (3.42) and Eq. (3.43) into (3.45), and using the Fourier inverse transform, the following relations can be obtained:

$$\left. \begin{aligned} D_1(s, p) &= \frac{1}{|s|} \int_{-c}^c G_1(\xi, p) \exp(is\xi) d\xi - \frac{(R_x^1 s^6 + R_x^2 s^4) D_0(s, p)}{|s|} \\ D_2(s, p) &= \frac{1}{-is} \int_{-c}^c G_2(\xi, p) \exp(is\xi) d\xi \\ D_3(s, p) &= \frac{1}{-is} \int_{-c}^c G_3(\xi, p) \exp(is\xi) d\xi \end{aligned} \right\} \quad (3.46)$$

Considering the relations in Eq. (3.44), the following relationship can be obtained:

$$B_{1j} = C_{p1}^{(j)}(s, p) D_1 + C_{p2}^{(j)}(s, p) D_2 + C_{p3}^{(j)}(s, p) D_3 + C_{j+24}(s, p) D_0 \quad (3.47)$$

where functions $C_{pm}^{(j)}(s, p)$ and $C_{j+24}(s, p)$ ($m, j = 1, 2, 3$) are defined in Appendix A.

Letting $\bar{\xi} = \xi/c$, $\bar{x} = x/c$, then, the singular integral equations of $G_l(\xi, p)$ ($l = 1, 2, 3$) are finally obtained by Eq. (3.38-1), Eq. (3.38-2) and Eq. (3.38-3):

$$\begin{aligned} & \frac{1}{\pi} \int_{-1}^1 \left\{ cL_{11} \overline{G_1}(\bar{\xi}, p) + \left(\frac{M_{12}^0}{\bar{\xi} - \bar{x}} + cL_{12} \right) \overline{G_2}(\bar{\xi}, p) + \left(\frac{M_{13}^0}{\bar{\xi} - \bar{x}} + cL_{13} \right) \overline{G_3}(\bar{\xi}, p) \right\} d\bar{\xi} \\ & = \sigma_{zz}^{*(1)}(0, p) + f_1(\bar{x}, p) \end{aligned} \quad (3.48)$$

$$\begin{aligned} & \frac{1}{\pi} \int_{-1}^1 \left\{ \left(\frac{M_{21}^0}{\bar{\xi} - \bar{x}} + c\overline{L_{21}} \right) \overline{G_1}(\bar{\xi}, p) + c\overline{L_{22}} \overline{G_2}(\bar{\xi}, p) + c\overline{L_{23}} \overline{G_3}(\bar{\xi}, p) \right\} d\bar{\xi} \\ & = \sigma_{zx}^{*(1)}(0, p) + f_2(\bar{x}, p) \end{aligned} \quad (3.49)$$

$$\begin{aligned} & \frac{1}{\pi} \int_{-1}^1 \left\{ c\overline{L_{31}} \overline{G_1}(\bar{\xi}, p) + \left(\frac{M_{32}^0}{\bar{\xi} - \bar{x}} + c\overline{L_{32}} \right) \overline{G_2}(\bar{\xi}, p) + \left(\frac{M_{33}^0}{\bar{\xi} - \bar{x}} + c\overline{L_{33}} \right) \overline{G_3}(\bar{\xi}, p) \right\} d\bar{\xi} \\ & = D_z^{*(1)}(0, p) + f_3(\bar{x}, p) \end{aligned} \quad (3.50)$$

where $f_1(\bar{x}, p)$, $f_2(\bar{x}, p)$ and $f_3(\bar{x}, p)$ are:

$$f_1(\bar{x}, p) = \frac{1}{2\pi} \int_{-\infty}^{+\infty} \left\{ \varphi_{01}^{(1)} D_0 + C_1 [D_{11} + D_{12}] - \varphi_{11}^{(1)} \frac{(R_x^1 s^6 + R_x^2 s^4) D_0}{|s|} \right\} \exp(-is\bar{x}) ds$$

$$f_2(\bar{x}, p) = \frac{1}{2\pi} \int_{-\infty}^{+\infty} i \operatorname{sgn}(s) \left\{ C_2 [D_{11} - D_{12}] + \varphi_{02}^{(1)} D_0 - \varphi_{12}^{(1)} \frac{(R_x^1 s^6 + R_x^2 s^4) D_0}{|s|} \right\} \exp(-is\bar{x}) ds$$

$$f_3(\bar{x}, p) = \frac{1}{2\pi} \int_{-\infty}^{+\infty} \left\{ \varphi_{03}^{(1)} D_0 + C_3 [D_{11} + D_{12}] - \varphi_{13}^{(1)} \frac{(R_x^1 s^6 + R_x^2 s^4) D_0}{|s|} \right\} \exp(-is\bar{x}) ds$$

and $M_{lm}^0 = \lim_{s \rightarrow \infty} \frac{\varphi_{ml}^{(1)}}{s}$, then the kernel functions are as follow:

$$\overline{L_{lm}}(\bar{x}, \bar{\xi}, p) = \int_0^\infty \left(\frac{\varphi_{ml}^{(1)}}{s} - M_{lm}^0 \right) \sin[sc(\bar{\xi} - \bar{x})] ds \quad (l = 1, 3; m = 2, 3)$$

$$\overline{L_{21}}(\bar{x}, \bar{\xi}, p) = \int_0^\infty \left(\frac{\varphi_{12}^{(1)}}{s} - M_{21}^0 \right) \sin[sc(\bar{\xi} - \bar{x})] ds$$

$$\overline{L_{l1}}(\bar{x}, \bar{\xi}, p) = \int_0^\infty \left(\frac{\varphi_{1l}^{(1)}}{-s} \right) \cos[sc(\bar{\xi} - \bar{x})] ds \quad (l = 1, 3)$$

$$\overline{L_{2m}}(\bar{x}, \bar{\xi}, p) = \int_0^\infty \left(\frac{\varphi_{m2}^{(1)}}{s} \right) \cos[sc(\bar{\xi} - \bar{x})] ds \quad (m = 2, 3)$$

where $\varphi_{ml}^{(1)}$ ($m = 0,1,2,3; l = 1,2,3$) are defined in Appendix A.

The Lobatto-Chebyshev method ¹⁶³ is employed to transform the singular integral equations Eq. (3.48) - (3.50) into the following algebraic equations:

$$\begin{aligned} \frac{1}{\pi} \sum_{k=1}^n A_k \left\{ cF_1(\bar{\xi}_k, p) \bar{L}_{11}(\bar{x}_r, \bar{\xi}_k, p) + F_2(\bar{\xi}_k, p) \left(\frac{M_{12}^0}{\bar{\xi}_k - \bar{x}_r} + c\bar{L}_{12}(\bar{x}_r, \bar{\xi}_k, p) \right) \right. \\ \left. + F_3(\bar{\xi}_k, p) \left(\frac{M_{13}^0}{\bar{\xi}_k - \bar{x}_r} + c\bar{L}_{13}(\bar{x}_r, \bar{\xi}_k, p) \right) \right\} = \sigma_{zz}^{*(1)}(0, p) + f_1(\bar{x}, p) \quad |\bar{x}| \leq 1 \quad (3.51) \end{aligned}$$

$$\begin{aligned} \frac{1}{\pi} \sum_{k=1}^n A_k \left\{ F_1(\bar{\xi}_k, p) \left(\frac{M_{21}^0}{\bar{\xi}_k - \bar{x}_r} + c\bar{L}_{21}(\bar{x}_r, \bar{\xi}_k, p) \right) + cF_2(\bar{\xi}_k, p) \bar{L}_{22}(\bar{x}_r, \bar{\xi}_k, p) \right. \\ \left. + cF_3(\bar{\xi}_k, p) \bar{L}_{23}(\bar{x}_r, \bar{\xi}_k, p) \right\} = \sigma_{zx}^{*(1)}(0, p) + f_2(\bar{x}, p) \quad |\bar{x}| \leq 1 \quad (3.52) \end{aligned}$$

$$\begin{aligned} \frac{1}{\pi} \sum_{k=1}^n A_k \left\{ cF_1(\bar{\xi}_k, p) \bar{L}_{31}(\bar{x}_r, \bar{\xi}_k, p) + F_2(\bar{\xi}_k, p) \left(\frac{M_{32}^0}{\bar{\xi}_k - \bar{x}_r} + c\bar{L}_{32}(\bar{x}_r, \bar{\xi}_k, p) \right) \right. \\ \left. + F_3(\bar{\xi}_k, p) \left(\frac{M_{33}^0}{\bar{\xi}_k - \bar{x}_r} + c\bar{L}_{33}(\bar{x}_r, \bar{\xi}_k, p) \right) \right\} = D_z^{*(1)}(0, p) + f_3(\bar{x}, p) \quad |\bar{x}| \leq 1 \quad (3.53) \end{aligned}$$

$$\sum_{k=1}^n A_k F_l(\bar{\xi}_k, p) = 0 \quad (l = 1,2,3) \quad (3.54)$$

where $\bar{\xi}_k = \cos \frac{(k-1)\pi}{n-1}$, $k = 1,2,3, \dots, n$; $\bar{x}_r = \cos \frac{(2r-1)\pi}{2(n-1)}$, $r = 1,2,3, \dots, n-1$; $A_k = \frac{\pi}{2(n-1)}$, $k =$

$1, n$; $A_k = \frac{\pi}{n-1}$, $k = 2, 3, \dots, n-1$; and:

$$F_l(\bar{\xi}, p) = \bar{G}_l(\bar{\xi}, p) \sqrt{1 - \bar{\xi}^2} \quad |\bar{x}| \leq 1 \quad (l = 1,2,3) \quad (3.55)$$

Therefore, the stress intensity factors $K_I^*(p)$, $K_{II}^*(p)$ and the electric displacement intensity factor $K_D^*(p)$ in the Laplace domain are:

$$\left. \begin{aligned} K_I^*(p) &= -\lim_{x \rightarrow c^+} \sqrt{2\pi(x-c)} \sigma_{zz}^{*(2)}(x, 0, p) = -\sqrt{\pi c} [M_{12}^0 F_2(1, p) + M_{13}^0 F_3(1, p)] \\ K_{II}^*(p) &= -\lim_{x \rightarrow c^+} \sqrt{2\pi(x-c)} \sigma_{zx1}^{*(2)}(x, 0, p) = -\sqrt{\pi c} M_{21}^0 F_1(1, p) \\ K_D^*(p) &= -\lim_{x \rightarrow c^+} \sqrt{2\pi(x-c)} D_{z1}^{*(2)}(x, 0, p) = -\sqrt{\pi c} [M_{32}^0 F_2(1, p) + M_{33}^0 F_3(1, p)] \end{aligned} \right\} \quad (3.56)$$

The stress intensity factors and the electric displacement intensity factor in the time domain are then obtained from Laplace inverse transform:

$$\left. \begin{aligned} K_I(t) &= -\sqrt{\pi c} \frac{1}{2\pi i} \int_{Br} [M_{12}^0 F_2(1, p) + M_{13}^0 F_3(1, p)] \exp(pt) dp \\ K_{II}(t) &= -\sqrt{\pi c} \frac{1}{2\pi i} \int_{Br} [M_{21}^0 F_1(1, p)] \exp(pt) dp \\ K_D(t) &= -\sqrt{\pi c} \frac{1}{2\pi i} \int_{Br} [M_{32}^0 F_2(1, p) + M_{33}^0 F_3(1, p)] \exp(pt) dp \end{aligned} \right\} \quad (3.57)$$

3.6 Numerical results and discussions

3.6.1 Verifications

To first verify the solutions, letting the phase-lag of heat flux $\tau_q = 0$ and time t goes to infinite, we restrict our attention to the static case of the Fourier model. Solutions of the temperature on the upper and lower crack surfaces and extended line have been compared with the previous work¹²⁴ as shown in Figure 3.2, with perfect agreement. The stress and electric displacement intensity factors also shows excellent agreement with Ueda¹²⁴ when the current results reduced to the static case, as shown in Table 3.1.

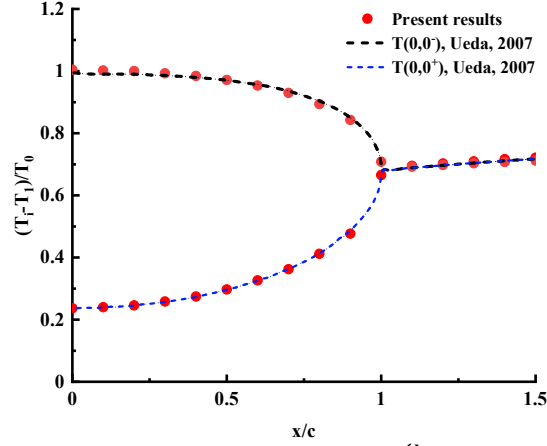
Figure 3. 2 Verification of the solutions. $\left(\frac{h_2}{h} = 0.25, \frac{c}{h} = 0.5\right)$

Table 3. 1 Static temperature, stress and electric displacement intensity factors a parallel crack in a strip.

Variables		h_2/h ($c/h=0.5$)			c/h ($h_2/h=0.25$)		D ($h_2/h=0.25, c/h=0.5$)			
		0.25	0.50	0.75	0.50	0.75	1.00	-0.50	0.00	0.50
Normalized K_I	Ueda ¹²⁴	0.011	0.00	-0.013	0.011	0.019	0.020	0.013	0.017	0.018
	Present	0.008	0.00	-0.009	0.008	0.010	0.011	0.008	0.008	0.008
Normalized K_{II}	Ueda ¹²⁴	0.038	0.040	0.038	0.038	0.041	0.040	0.041	0.039	0.038
	Present	0.035	0.01	0.036	0.035	0.038	0.036	0.036	0.035	0.034
Normalized K_D	Ueda ¹²⁴	-0.018	0.00	0.021	-0.018	-0.021	-0.020	-0.650	-0.010	0.601
	Present	-0.014	0.00	0.015	-0.014	-0.019	-0.019	-0.608	-0.014	0.580

3.6.2 The temperature and elastic-electric results

To study the effect of electro-thermo-elastic interaction on the temperature and stress field, the material constants of piezoelectric ceramic are taken in the calculation as listed in Table 3.2

Table 3. 2 Material constants for cadmium selenide ¹⁶⁴.

Properties	Constants	Properties	Constants
$c_{11}(N/m^2)$	7.41×10^{10}	$\lambda_{11}(N/m^2K)$	0.621×10^6
$c_{44}(N/m^2)$	1.32×10^{10}	$\lambda_{33}(N/m^2K)$	0.551×10^6
$c_{13}(N/m^2)$	3.93×10^{10}	$\varepsilon_{11}(C/Vm)$	0.825×10^{-10}
$c_{33}(N/m^2)$	8.36×10^{10}	$\varepsilon_{33}(C/Vm)$	0.903×10^{-10}
$e_{31}(C/m^2)$	-0.160	$p_z(C/Km^2)$	-2.940×10^{-6}
$e_{15}(C/m^2)$	-0.138	$\rho(kg/m^3)$	5.684×10^3
$e_{33}(C/m^2)$	0.347	κ	1.500

The temperature results in the time domain can be obtained by using the numerical inverse Laplace transform¹⁶⁵. Since the crack is assumed to be thermally insulated, the temperature on the crack surface will absolutely be disturbed. When the distance between crack surface and heat source $\frac{h_2}{h} = 0.25$, crack size $\frac{c}{h} = 0.5$, relaxation time $\tau_q = 0.2$ and fractional order $\alpha = 0.5$, the normalized temperature distributions on the crack faces and extended line ($|x| > 0, z = 0$) at different values of normalized time $F = \frac{t\beta}{c^2}$ are shown in Figure 3.3. It can be found that, due to a thermal shock loaded on the lower surface ($i = 2$), the temperature on the lower crack face is much higher than on the upper surface ($i = 1$). With the time increasing, the difference tends to be more pronounced at first, until reaching a peak value and then reduced, and finally it will remain at a stable stage consistent with the steady state results.

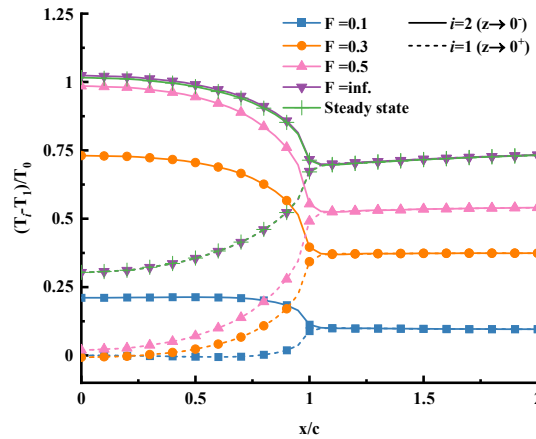


Figure 3. 3 Distribution of the temperature on the crack surfaces and extended line at various times.

$$\left(\frac{h_2}{h} = 0.25, \frac{c}{h} = 0.5, \tau_q = 0.2, \alpha = 0.5 \right)$$

Figure 3.4 shows the effect of the heat conduction model on the normalized temperature. When $\tau_q = 0$, $\alpha = 1$, the heat conduction is reduced to the Fourier model. All the figures show the Fourier model leads to the immediate response to the thermal shock, but the thermal response is delayed with τ_q increasing or advanced with increase α for the fractional heat conduction

model. Because of the thermal shock, overshooting occurs for all the models. With the increase of τ_q and α , overshooting becomes more severe. On the other hand, the wave behavior is aggravated by decreasing τ_q or increasing α .

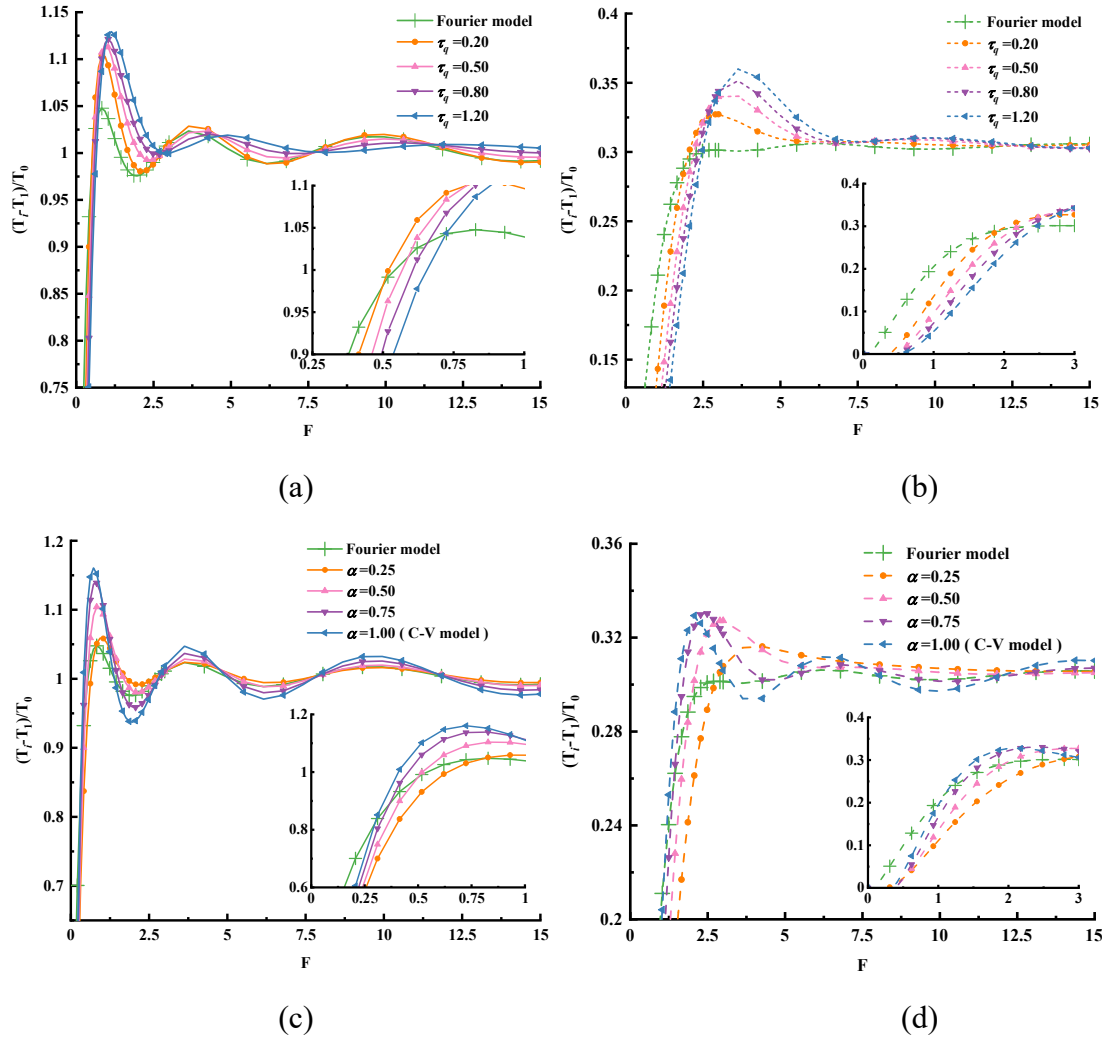


Figure 3. 4 The effects of the relaxation time and the fractional order on the temperature at the crack

center (a) $z \rightarrow 0^-$ ($\alpha = 0.5$); (b) $z \rightarrow 0^+$ ($\alpha = 0.5$); (c) $z \rightarrow 0^-$ ($\tau_q = 0.2$); (d) $z \rightarrow 0^+$ ($\tau_q =$

$$0.2). \left(\frac{h_2}{h} = 0.25, \frac{c}{h} = 0.5 \right)$$

In order to study the influence of the geometric size on the temperature filed, Figure 3.5 shows the normalized temperature changes with F for the crack center when $\tau_q = 0.2$ and $\alpha = 0.5$. With

the increase of crack size, $\frac{c}{h}$, the temperature difference between the upper and the lower surface of the crack becomes more prominent. However, the difference does not change with $\frac{h_2}{h}$.

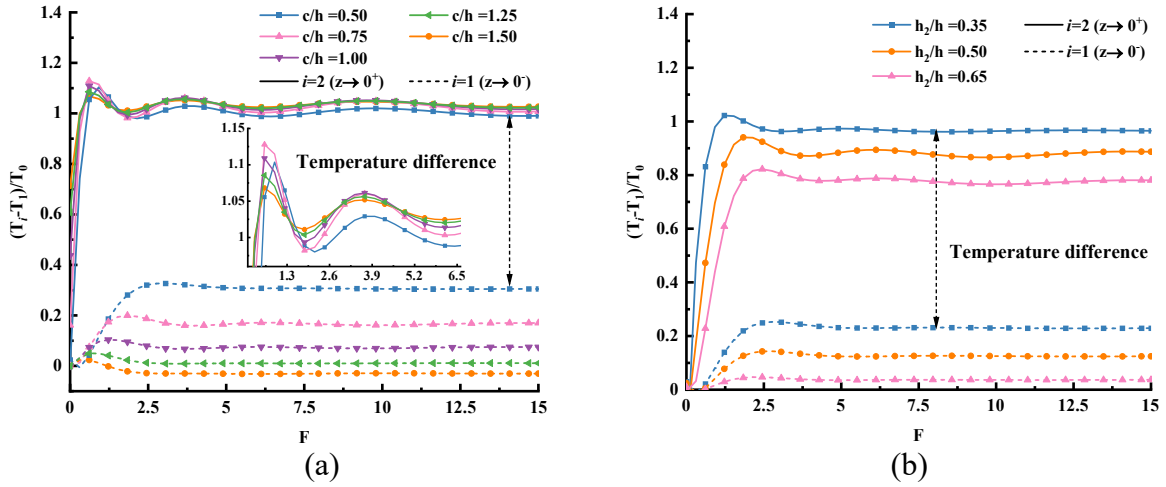


Figure 3. 5 The effect of the geometry parameters on the temperature at the crack center: (a) the effect of crack size ($\frac{h_2}{h} = 0.25$); (b) the effect of the distance ($\frac{c}{h} = 0.5$).

The stress and electric displacement results are shown in Figure 3.6 and Figure 3.7. Here, the geometric size $\frac{h_2}{h} = 0.25, \frac{c}{h} = 0.5$, the fractional model coefficients $\tau_q = 0.2, \alpha = 0.5$ and the electric load $D = 0$.

Figure 3.6 shows the results at normalized time $F = 0.1$. It is evident that the normalized stresses σ_{zz}, σ_{zx} and displacement D_z increase drastically around the crack tips. At the crack face ($z = 0, |x| < c$), the stresses and electric displacement are almost zero, which satisfies the boundary conditions Eq. (3.9-1) to (3.9-3). From figures Fig 3.5 (a) and (b), under the same distance from the crack face, the absolute values of normalized σ_{zz} and D_z of the upper area are bigger than the lower area. However, the normalized shear stress σ_{zx} in the upper and lower regions are almost the same near the crack face. As the distance from the crack face increases, the shear stress of the upper region is significantly higher than that of the lower region.

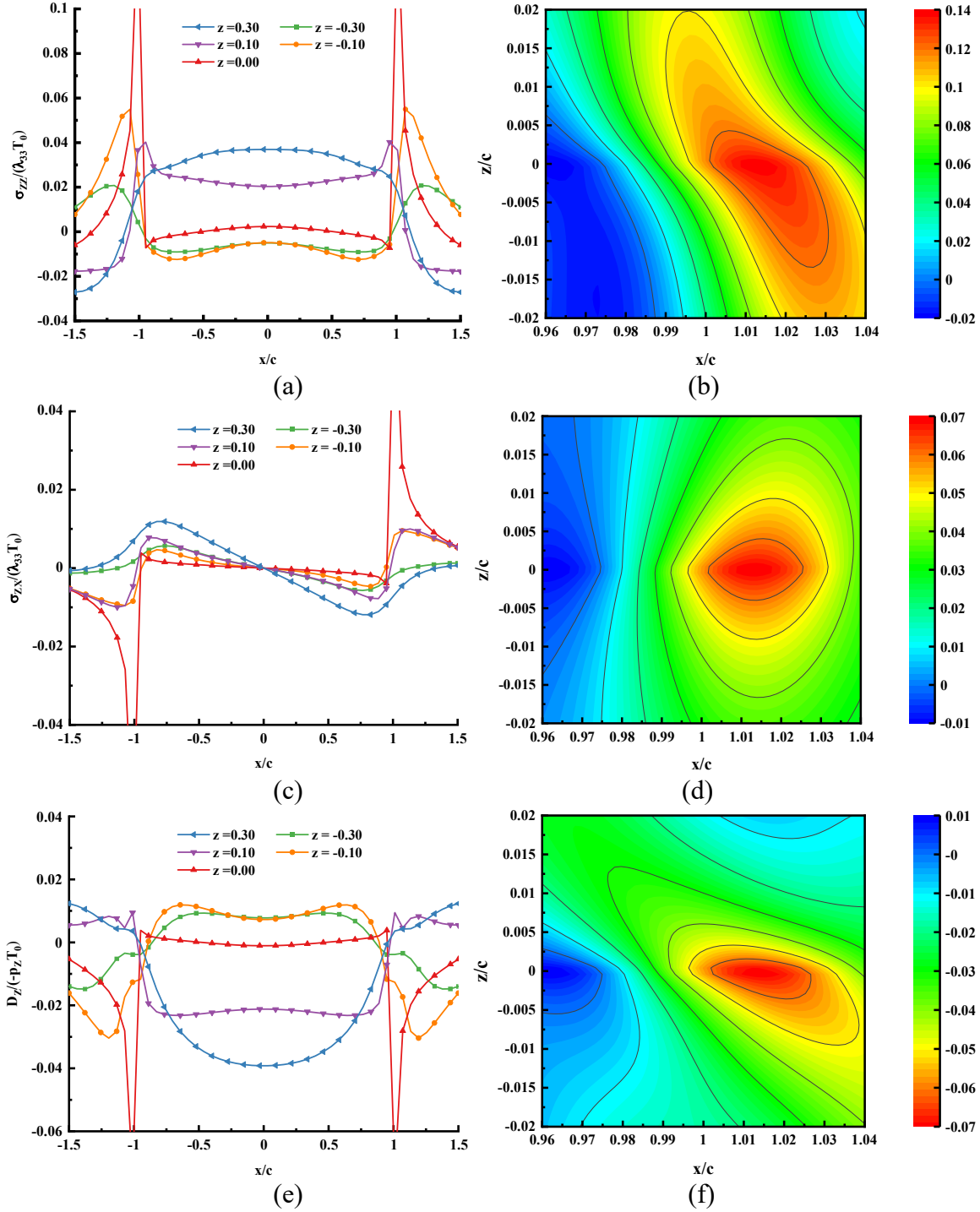


Figure 3. 6 Strip's stress and electric displacement distributions at normalized time $F = 0.1$ at different surfaces: (a) σ_{zz} ; (c) σ_{zx} ; (e) D_z ; and around crack tip (b) σ_{zz} ; (d) σ_{zx} ; (f) D_z . $\left(\frac{h_2}{h} = 0.25, \frac{c}{h} = 0.5, \tau_q = 0.2, \alpha = 0.5, D = 0\right)$

According to Figure 3.6 (c), there is no shear stress in the plane of $x = 0$, which bisects the crack. The distributions of normal stress and electric displacement in z -direction of the bisection plane of the crack are given in Figure 3.7. At the free surface, all the results are zero, which contends with the boundary conditions for the upper and the lower edges of the strip. From the crack face to the upper edge, the absolute values of the results are climbing first and then descending to zero. With time increasing to infinity, the curve rises to its highest level, and eventually meets the results of steady state. Therefore, the dynamic response will become increasingly apparent with the distance between crack face and free edge increasing.

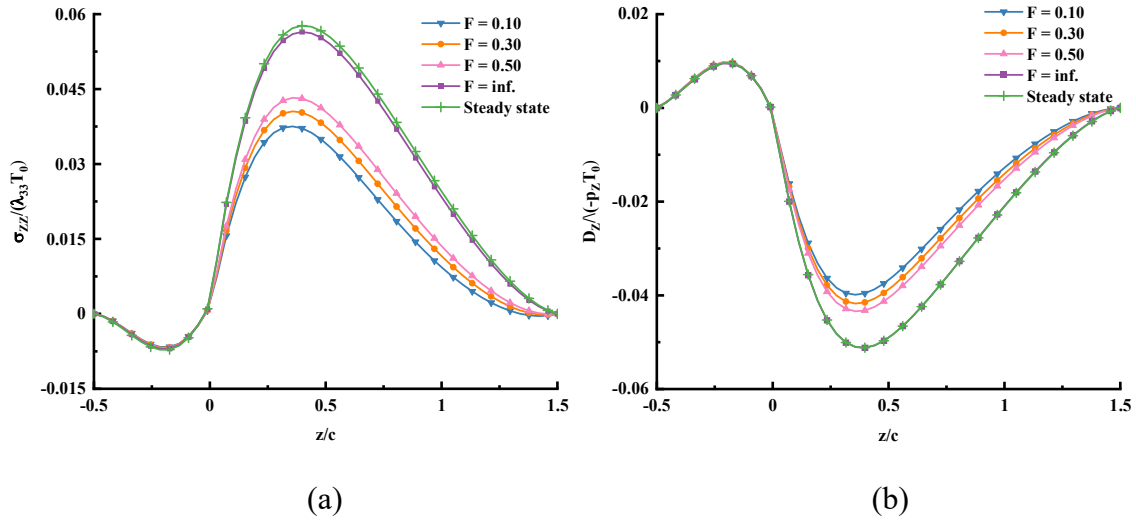


Figure 3. 7 Distributions of stress and electric displacement in z -direction of the bisection plane of the crack at various times: (a) normal stress σ_{zz} ; (b) electric displacement D_z . $\left(\frac{h_2}{h} = 0.25, \frac{c}{h} = 0.5, \tau_q = 0.2, \alpha = 0.5, D = 0\right)$

3.6.3 The dynamic stress and electric displacement intensity factors

Next, let's consider the effect of the heat conduction model, the geometric size and electric loading on the fracture response. To do so, we study the results of dynamic stress intensity factors (DSIFs) and dynamic electric displacement intensity factor (DEDIF). In the calculations to follow,

the normal stress and shear stress intensity factors (K_I, K_{II}) are normalized by $\lambda_{33}T_0\sqrt{\pi c}$, while the electric displacement intensity factor (K_D) is normalized by $-p_zT_0\sqrt{\pi c}$.

Taking the ratio $\frac{h_2}{h}$ and $\frac{c}{h}$ as 0.25 and 0.5, respectively, without electric shock, the DSIFs are plotted in Figure 3.8, which shows the influence of heat conduction model. For different values of relaxation time, τ_q , the histories of K_I and K_{II} both always show three distinct stages. At the first stage, the stress intensity factors are decreasing with increasing τ_q . After F exceeds around 1.60 for K_I and 1.10 for K_{II} , the stress intensity factors start to increase with increasing τ_q . When F arrives at around 8.45 for K_I and 7.50 for K_{II} , the trend goes inversely. So, with the increase of τ_q , the crack will be retarded first, promoted next, and finally retarded again. However, the effect of fractional order α shows an opposite effect at each stage compared to the effect of τ_q . It is worth noting that K_D only possesses the latest two stages of K_I and K_{II} , with the least influence of the heat conduction model.

As a conclusion, the variation of coefficients of the heat conduction model will retard or promote the likelihood of crack propagation at different stages of the loading process. K_I is the most sensitive to the heat conduction model, K_D is the least one. Between the coefficients τ_q and α , all the DSIFs and DEDIF are more responsive to τ_q .

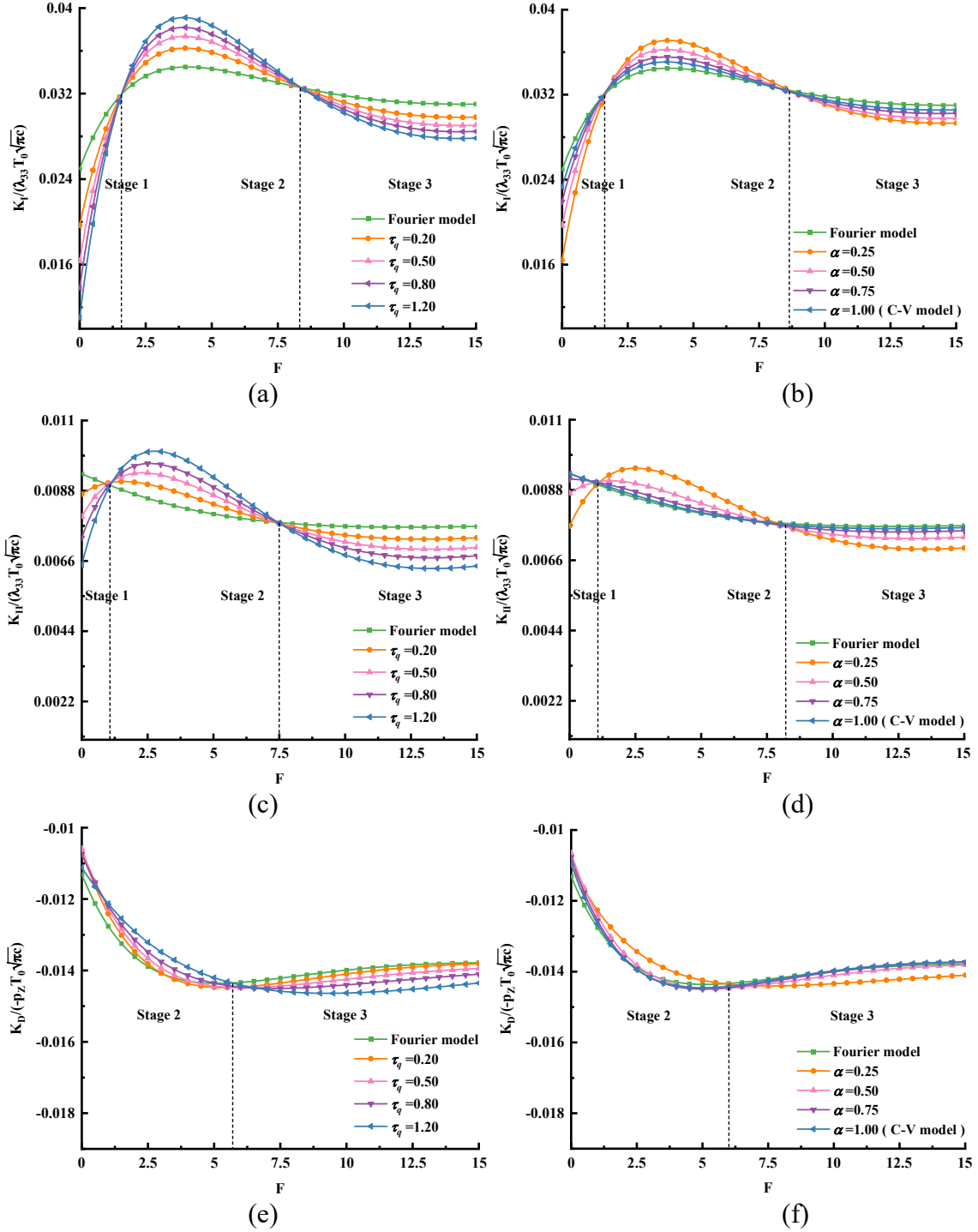


Figure 3. 8 Normalized dynamic stress and electric displacement intensity factors vs. normalized time as a function of the relaxation time and fractional order: (a) K_I ($\alpha = 0.5$); (b) K_I ($\tau_q = 0.2$); (c) K_{II} ($\alpha = 0.5$);

(d) K_{II} ($\tau_q = 0.2$); (e) K_D ($\alpha = 0.5$); and (f) K_D ($\tau_q = 0.2$). $\left(\frac{h_2}{h} = 0.25, \frac{c}{h} = 0.5, D = 0\right)$

To illustrate the effect of crack size $\frac{c}{h}$ on the propagation of a crack in a piezoelectric material, Figure 3.9 plots the normalized DSIFs and DEDIF versus normalized time as a function of $\frac{c}{h}$. With the increase of crack size, K_{II} keeps increasing. When $\frac{c}{h}$ increases to a value, say larger than 1.25, the impact on K_{II} will become insignificant. For K_I and K_D , the higher the size of crack $\frac{c}{h}$, the higher the absolute values of them. After the crack size increases beyond 1.0, increasing the size of crack leads to a decrease in the absolute values of K_I and K_D .

The results imply that the inflection point for the history of K_I and K_D is $\frac{c}{h} = 1$, before which K_I will be enhanced with increasing crack size, whilst, K_D will be impeded. Once $\frac{c}{h}$ exceeding unity, all the results are inverted. Unlike K_I and K_D , K_{II} is always promoted with increasing $\frac{c}{h}$.

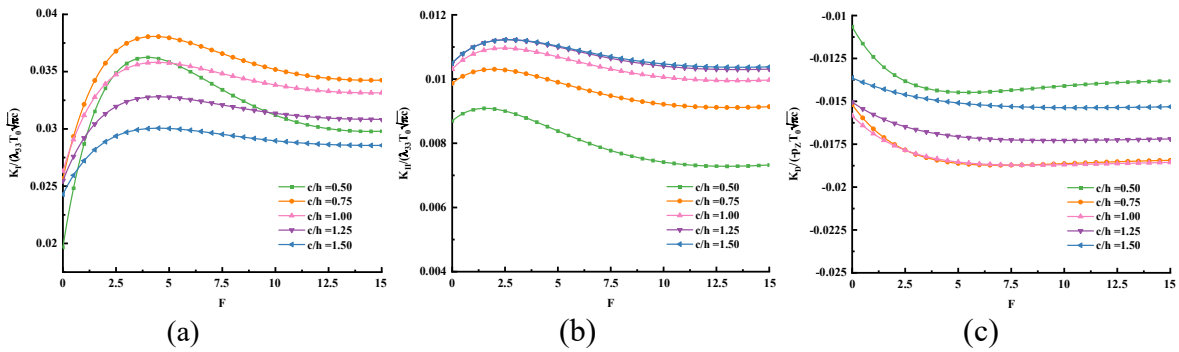


Figure 3.9 The effect of the crack size on the stress and electric displacement intensity factors: (a) K_I ; (b)

$$K_{II}; \text{ (c) } K_D. \left(\frac{h_2}{h} = 0.25, \tau_q = 0.2, \alpha = 0.5, D = 0 \right)$$

Figure 3.10 shows the variation of the normalized DSIFs and DEDIF as a function of the distance between crack face and the edge where thermal shock is applied. With the value of $\frac{h_2}{h}$ increasing, DSIFs keep decreasing, but DEDIF increases. K_I and K_D show strong dependence on $\frac{h_2}{h}$, and both vanish once the ratio reaches 0.5. On the other hand, $\frac{h_2}{h}$ shows a much mild

influence on K_{II} .

It is worth pointing out that the distance between the crack face and thermal shock will govern the fracture behavior of the cracked strip. Increasing the distance will retard the model I and II fracture but promote DEDIF and the likelihood of electric fracture. Moreover, when the crack locates at the center of the strip, only sliding fracture is likely to happen as both K_I and K_D vanish.

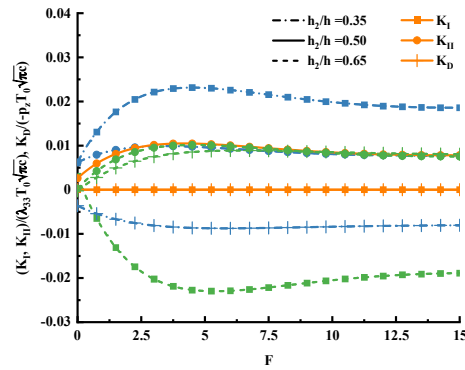


Figure 3. 10 The effect of the distance between crack face and thermal loading on the stress and electric displacement intensity factors K_I, K_{II}, K_D . ($\frac{c}{h} = 0.5, \tau_q = 0.2, \alpha = 0.5, D = 0$)

Finally, the impact of the electric load on the fracture response is shown in Figure 3.11. The results show that the DEDIF remains constant and the value increases remarkably with the electric load, whilst the DSIFs slightly decreasing with increasing of D .

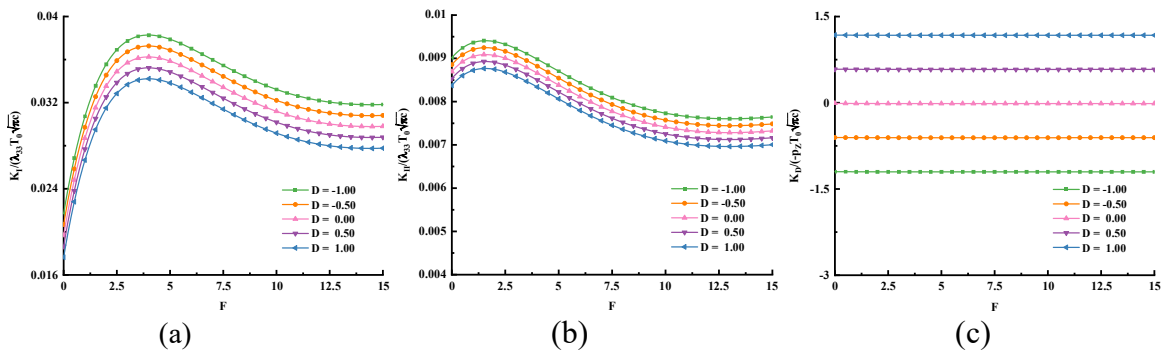


Figure 3. 11 The effect of the electric load on the stress and electric displacement intensity factors: (a)

$$K_I; (b) K_{II}; (c) K_D. \left(\frac{c}{h} = 0.5, \frac{h_2}{h} = 0.25, \tau_q = 0.2, \alpha = 0.5\right)$$

3.7 Conclusions

In the chapter, the dynamic response of a cracked piezoelectric strip subjected to thermoelectric impact has been investigated. The field equations are reduced to the solutions of Cauchy-type singular integral equations by using the dislocation density functions. The results reveal that the fractional heat conduction model is superior in comparison to the Fourier and C-V models, as the relaxation time and fractional order coefficients modify the overshooting and wave behavior of dynamic thermal response. Some interesting observations are listed as follows:

- (1) With the increasing of relaxation time, the overshooting phenomenon would be more obvious, while wave behavior is weaker. For higher fractional order, the thermal wave and overshooting behaviors both become apparent.
- (2) Stress and electric displacement intensity factors are greatly affected by the relaxation time and fractional order coefficients and exhibit an apparent inflection point between different stages of the historical spectrums.
- (3) The larger the crack, the higher values of the DSIFs, and the lower value of the DEDIF. Once the crack is bigger than the length of the strip, the mode I fracture and electric fracture modes will be impeded with increasing of crack size, as the normalized mode I DSIF and DEDIF decrease.
- (4) As the distance between the crack and the thermal shock increases, the crack is dominated by a mode I fracture combined with electric fracture.
- (5) The electric load will reduce DSIFs slightly but enhance DEDIF significantly.

Chapter 4

Multiphysical model to predict thermomechanical fracture of functional hierarchical biomimetic composites

In this chapter, following the study of thermoelectric performance, the emphasis is placed on the mathematical modeling of the microstructural characteristics of biomimetic materials. Functionally graded models enable the control of feature sizes within the layered structure of biological materials. Thus, inspired by nacre, we propose a brick-and-mortar graded (BM-GRAD) model and employ it to investigate how material heterogeneity interacts with its crack resistance. The interface damage model is further used to estimate the crack propagation direction between dissimilar materials under thermal and stress fields. Results show that the BM-GRAD microstructure can remarkably increase the strength of the biomimetic composite under the pure stress field; however, the temperature has a high impact on structures, and a sudden cooling will highly likely cause an opening-mode failure. Moreover, although multiphysical leads structure to become more risky, compared with functional unbrick single gradient (GRAD) design, the BM-GRAD arrangement has a great advantage, the deflecting cracks form more easily in the BM-GRAD microstructure which progress of crack propagation is much easier to be terminated.

4.1 Introduction

Stiffness and toughness are two desirable properties hard to be combined. Biomaterial exhibits a remarkable combination of stiffness, strength, and lightweight due to its hierarchical soft-hard structure, in which hard aragonite tablets are glued together with soft organic materials to form tiles⁴⁻⁶. As an excellent mechanical performance, biomaterial has opened a way to inspire new designs for hierarchical composite materials^{3,166-169}.

With the advent of 3D printing techniques, arbitrary hierarchical geometry can be designed. For example, staggered microstructures inspired by nacles¹⁷⁰ were printed with lamellar and brick-and-mortar (BM) architectures. Compared to lamellar microstructure, a BM structure realized over 2 times increase in fracture toughness under quasistatic bending loading. Similar tests were conducted between the BM and the cross lamellar¹⁷¹, branch lamellar¹⁷², concentrated hexagon¹¹, and rotating plywood¹⁷³ microstructures, and the BM always showed a higher load of failure, and its work of fracture per unit mass even over 14 times greater than single hard or soft phase²⁴, uncovering the design benefits of brick-and-mortar arrangement. Besides shapes of microstructure, fibers were controlled to arrange in different dislocation patterns¹⁷⁴, thickness¹⁶⁸, and direction¹⁷⁵, imparting high strength and preventing early fracture simultaneously. Furthermore, with the change of material ingredient, BM hierarchical structures with functional gradients were printed¹⁷⁶⁻¹⁷⁸, and the continuous gradient offered a 2-fold increase in stiffness and ultimate strength¹⁷⁷.

These works on printing hierarchical biomimetic composites improve our understanding of how microstructure can be controlled to produce tougher materials. But there are still many open questions. First, most researches focus on one single tensile or compressive mechanical environment while complex working circumstances are inevitable during the lifetime of the

hierarchical composites¹⁷⁹⁻¹⁸³. Varying temperature is the most common issue, especially for the structures with a brick-and-mortar architecture, where the material would display a lower strength and easier to emerge crack¹⁸⁴ at high temperature, yet the crack-growth resistance can be improved due to enhanced ductility in the metallic mortar². Besides, in need of high technology service, composites are required to keep stable in extreme temperature conditions^{71,185-187}, thus the effects of coupled, extreme thermal and mechanical environments on the BM structure are vital issues to be considered to evaluate the fracture performance in these nacre-like hierarchical composites. Second, when testing fracture behaviors of biomaterial specimens, the applied method is based on ASTM standard empirical formula. In such a scenario, only the force-induced tensile stress intensity factor can be presented^{24,168,174,175}. The more complex mechanism-the interaction between temperature and mechanics, is hard to be revealed. In contrast, studying the whole stress and displacement fields brings a more detailed picture of the multiphysical loading-induced fracture behaviors. Even though theoretical models that consider crack propagation in extreme temperature and thermomechanical environments¹⁸⁸⁻¹⁹² have been proposed in many studies, most of these studies applied the traditional Fourier heat conduction model which will render unreasonable temperature predictions when the temperature is extremely low, the temperature gradient is extremely high, or the material has a heterogeneous microstructure¹⁹³⁻¹⁹⁵. To fix this problem, the non-Fourier heat conduction model should be employed with a so-called relaxation time which measures the time lag between temperature and heat flux. Besides, while many studies have extended these theoretical models with FEM simulations¹⁹⁶⁻²⁰⁰, application of the non-Fourier models to 3D printed hierarchical composites to guide the design of biomimetic microstructures under multi-field is rather rare in the literature.

In this work, we have built a coupled thermal-mechanical model for functional, hierarchical, biomimetic materials based on the non-Fourier heat conduction model. The material properties are controlled to be a function of the volume fraction of the hard phase. General solutions to stress and displacement fields are eventually obtained. Subsequently, the fracture strength is evaluated using the linear elastic stress-intensity values. Fracture theories are further used to predict crack propagation. We also consider the effects of cooling-heating conditions, multiple physical fields, and hierarchical degree on the failure mechanism and failure stress. Finally, the results are compared with the experiments and numerical results, which verifies the accuracy of the present model.

4.2 Materials and Constitutive Model

4.2.1 Microstructure design and material properties

Inspired by the scanning electron microscope (SEM) micrographs of nacre (Figure 4.1a), the biomimetic composite is structured to be composed of a hard brick phase and a soft mortar phase (Figure 4.1 (b)). All bricks have the same size and are arranged hierarchically. From SEM micrographs, the degree of grey color is not the same for the whole part, thus a functional gradient is introduced in the z -direction. Then, to analyze the multiphysical fracture performance of the biomimetic composite, tensile stress and temperature fields are both applied at upper and lower surfaces. A multiphysical, functional, hierarchical, biomimetic composite model is finally built as shown in Figure 4.1 (b).

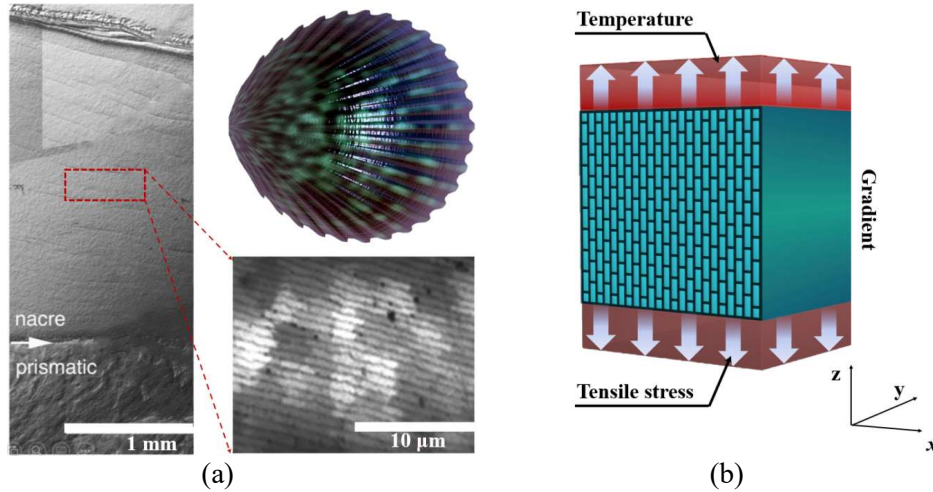


Figure 4. 1 Brick-and-mortar multiphysical functional biomimetic hierarchical model: (a) SEM micrographs of the nacre ²⁰¹; (b) Multiphysical model.

The material properties can be obtained by the volume fraction of the hard brick phase, γ ¹⁷⁸

$$E = e_1\gamma^2 + e_2\gamma - e_3 \quad (4.1)$$

where E and ρ are position-dependent Young's modulus and mass density, e_1, e_2, e_3 are material constants related to modulus. The volume fraction of the hard phase, γ is also the function of z , and $\gamma(z)$ varies along the z -direction.

4.2.2 Thermomechanical constitutive model

Along with the thickness of the composite, there are no changes in material properties and the applied physical fields. Thus the 3D model can be changed into a plane problem to build the constitutive model as shown in Figure 4.2 (a). To test fracture performance, an insulated crack of width $2c$ is set in the center of the composite. According to the symmetry of the nanostructure, a brick-and-mortar united cell of the composite is shown in Figure 4.2 (b), where the black and white parts are denoted as soft and hard phases, respectively, d_m is the length of hard material, d_{hard} is

the thickness of hard material, and d_{soft} is the thickness of soft material. For the crack tip stress field, a polar coordinate system (r, ϑ) is set at the crack tip.

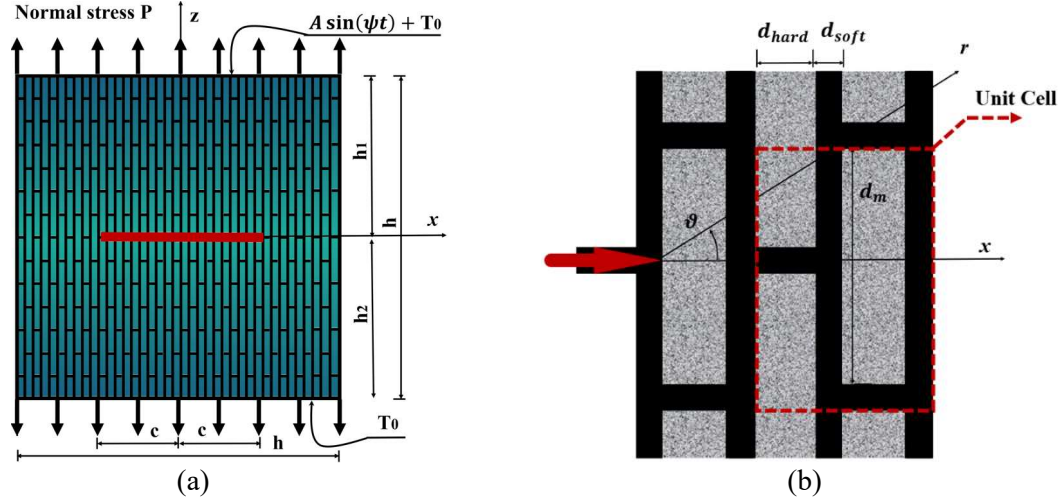


Figure 4. 2 A center cracked multiphysical functional brick-and-mortar plane model: (a) multiphysical plane model; (b) unite cell.

A Cartesian coordinate system (x, y, z) is attached to the midpoint of the crack. Suppose the initial temperature is T_0 . Then a tensile stress P is applied on both the upper and lower faces of the composite, along with a thermal pulse $A \sin(\psi t)$ on the upper face, at time t .

As the material is under a thermal shock loading, according to the classical theory of elasticity, the dynamic equilibrium equations for a 2D problem in the absence of body forces are given as

$$\frac{\partial \sigma_{xx}}{\partial x} + \frac{\partial \sigma_{xz}}{\partial z} = \rho \frac{\partial^2 u_x}{\partial t^2}, \quad \frac{\partial \sigma_{zz}}{\partial z} + \frac{\partial \sigma_{xz}}{\partial x} = \rho \frac{\partial^2 u_z}{\partial t^2} \quad (4.2)$$

where ρ is the mass density; u_x and u_z are the displacement in x and z directions, respectively.

the strain is related to the displacement by

$$\varepsilon_{xx} = \frac{\partial u_x}{\partial x}, \quad \varepsilon_{zz} = \frac{\partial u_z}{\partial z}, \quad \varepsilon_{xz} = \frac{1}{2} \left(\frac{\partial u_x}{\partial z} + \frac{\partial u_z}{\partial x} \right) \quad (4.3)$$

Then, the constitutive equations for the thermomechanical multiphysical model can be expressed as follow

$$\begin{bmatrix} \sigma_{xxi} \\ \sigma_{zzi} \\ \sigma_{zxi} \end{bmatrix}_{(\gamma)} = \begin{bmatrix} \frac{E(\gamma)}{1-\nu^2} & \frac{\nu E(\gamma)}{1-\nu^2} & 0 \\ \frac{\nu E(\gamma)}{1-\nu^2} & \frac{E(\gamma)}{1-\nu^2} & 0 \\ 0 & 0 & \frac{E(\gamma)}{2(1+\nu)} \end{bmatrix} \begin{bmatrix} \varepsilon_{xxi} \\ \varepsilon_{zzi} \\ \gamma_{zxi} \end{bmatrix}_{(\gamma)} - \begin{bmatrix} \frac{E(\gamma)}{1-\nu^2} (\lambda_{xx} + \nu \lambda_{zz}) \\ \frac{E(\gamma)}{1-\nu^2} (\nu \lambda_{xx} + \lambda_{zz}) \\ 0 \end{bmatrix} T_i \quad (4.4)$$

in which σ_{xxi} , σ_{zzi} , σ_{zxi} are the stress tensor components; ε_{xxi} , ε_{zzi} , γ_{zxi} are the strain components; λ_{xx} and λ_{zz} are thermal expansion coefficients in x and z directions, respectively; ν is the Poisson's ratio. T_i is temperature change. $i = 1, 2$ denote the field quantities in the upper ($0 \leq z \leq h_1$) and lower ($-h_2 \leq z \leq 0$) part of the composite.

Considering heterogeneous properties and high temperature gradients in the z-direction, the heat conduction equation based on the non-Fourier law is written as ²⁰²

$$\frac{1}{\beta} \left(\frac{\partial T_i}{\partial t} + \tau_q \frac{\partial^2 T_i}{\partial t^2} \right) = \kappa \frac{\partial^2 T_i}{\partial x^2} + \frac{\partial^2 T_i}{\partial z^2} \quad (4.5)$$

where τ_q is the thermal relaxation time; $\kappa = \frac{k_x}{k_z}$, that k_x and k_z are the thermal conductivities in the x- and z-directions, respectively; and $\beta = \frac{k_z}{\rho c_p}$, is the thermal diffusivity, c_p is the specific heat parameter.

In Eq. (4.4), set $c_{11} = \frac{E(\gamma)}{1-\nu^2}$, $c_{12} = \frac{\nu E(\gamma)}{1-\nu^2}$, $c_{66} = \frac{E(\gamma)}{2(1+\nu)}$, $\lambda_{11} = c_{11} \lambda_{xx} + c_{12} \lambda_{zz}$, $\lambda_{22} = c_{12} \lambda_{xx} + c_{11} \lambda_{zz}$. By introducing the following dimensionless quantities

$$\bar{T}_i = \frac{T_i}{T_0}, (\bar{t}, \bar{\tau}_q) = \frac{(t, \tau_q)}{c^2/\beta}, (\bar{x}, \bar{z}) = \frac{(x, z)}{c}, (\bar{u}_{xi}, \bar{u}_{zi}) = \frac{(u_{xi}, u_{zi})}{c}, \bar{\rho} = \frac{\rho}{Ec^2/\beta^2}$$

$$\bar{\sigma}_{ij} = \frac{\sigma_{ij}}{E} \quad (i, j = x, z), \bar{c}_{ij} = \frac{c_{ij}}{E} \quad (i, j = 1, 2), \bar{\lambda}_{ij} = \frac{\lambda_{ij}T_0}{E} \quad (i = j = x, z)$$

the dimensionless governing equations for the plane model of the multiphysical, functional, brick-and-mortar structure can be obtained:

$$\begin{aligned} \left(c_{11} \frac{\partial^2}{\partial x^2} + c_{66} \frac{\partial^2}{\partial z^2} - \rho \frac{\partial^2}{\partial t^2} \right) u_{xi} + (c_{12} + c_{66}) \frac{\partial^2 u_{zi}}{\partial x \partial z} &= \lambda_{11} \frac{\partial T_i}{\partial x} \\ (c_{12} + c_{66}) \frac{\partial^2 u_{xi}}{\partial x \partial z} + \left(c_{66} \frac{\partial^2}{\partial x^2} + c_{11} \frac{\partial^2}{\partial z^2} - \rho \frac{\partial^2}{\partial t^2} \right) u_{zi} &= \lambda_{22} \frac{\partial T_i}{\partial z} \end{aligned} \quad (4.6)$$

$$\frac{\partial T_i}{\partial t} + \tau_q \frac{\partial^2 T_i}{\partial t^2} = \kappa \frac{\partial^2 T_i}{\partial x^2} + \frac{\partial^2 T_i}{\partial z^2} \quad (4.7)$$

here and after, the hat “-” of the variables is neglected for simplicity. The boundary conditions, therefore, are subjected to the following boundary and initial conditions in dimensionless forms

$$\sigma_{zz1}(x, h_1, t) = \sigma_{zz2}(x, -h_2, t) = P$$

$$\sigma_{zx1}(x, h_1, t) = \sigma_{zx2}(x, -h_2, t) = 0$$

$$\sigma_{zz1}(x, 0, t) = \sigma_{zx2}(x, 0, t) = 0 \quad |x| < 1 \quad (4.8)$$

$$\sigma_{zz1}(x, 0, t) = \sigma_{zz2}(x, 0, t), \sigma_{zx1}(x, 0, t) = \sigma_{zx2}(x, 0, t) \quad |x| \geq 1$$

$$u_{z1}(x, 0, t) = u_{z2}(x, 0, t), u_{x1}(x, 0, t) = u_{x2}(x, 0, t) \quad |x| \geq 1$$

for mechanical conditions and

$$\begin{aligned}
T_i(x, z, 0) &= 0 \\
\frac{\partial T_1(x, 0, t)}{\partial z} &= \frac{\partial T_2(x, 0, t)}{\partial z} = 0 & |x| < 1 \\
\frac{\partial T_1(x, 0, t)}{\partial z} &= \frac{\partial T_2(x, 0, t)}{\partial z} & |x| \geq 1 \\
T_1(x, 0, t) &= T_2(x, 0, t) & |x| \geq 1 \\
T_1(x, h_1, t) &= A \sin(\psi t) & |x| \geq 0 \\
T_2(x, -h_2, t) &= 0 & |x| \geq 0
\end{aligned} \tag{4.9}$$

for thermal loading conditions.

4.3 General solutions and stress intensity factors

For solving the problems, we introduce a Laplace transform pair as

$$\begin{aligned}
f^*(x, z, p) &= \int_0^{\infty} f(x, z, t) \exp(-pt) dt \\
f(x, z, t) &= \frac{1}{2\pi i} \int_{Br} f^*(x, z, p) \exp(pt) dt
\end{aligned} \tag{4.10}$$

in which Br stands for the Bromwich path of integration to transform the time variable t into the Laplace variable p , and the superscript ‘*’ indicates the variables in the Laplace domain.

4.3.1 Temperature distribution

First, we should find temperature solutions of the composite under a thermal sine wave. According to superposition, the temperature field can be expressed as uncracked $T^{*(1)}(y, p)$ plus cracked $T_i^{*(2)}(x, z, p)$

$$T_i^*(x, z, p) = T^{*(1)}(y, p) + T_i^{*(2)}(x, z, p) \tag{4.11}$$

where $T^{*(1)}(z, p)$ satisfies the following equation and boundary conditions,

$$(p + \tau_q p^2) T_i^{*(1)} = \frac{d^2 T_i^{*(1)}}{dz^2} \quad (4.12)$$

$$\begin{aligned} T_i^{*(1)}(h_1, p) &= \frac{\psi A}{(\psi^2 + p^2)} \\ T_i^{*(1)}(-h_2, p) &= 0 \end{aligned} \quad (4.13)$$

whereas $T_i^{*(2)}(x, z, p)$ is subject to the relations,

$$(p + \tau_q p^2) T_i^{*(2)} = \kappa \frac{\partial^2 T_i^{*(2)}}{\partial x^2} + \frac{\partial^2 T_i^{*(2)}}{\partial z^2} \quad (4.14)$$

$$\begin{aligned} \frac{\partial T_1^{*(2)}(x, 0, t)}{\partial z} &= \frac{\partial T_2^{*(2)}(x, 0, t)}{\partial z} = -\frac{dT_i^{*(1)}}{dz} & |x| < 1 \\ \frac{\partial T_1^{*(2)}(x, 0, t)}{\partial z} &= \frac{\partial T_2^{*(2)}(x, 0, t)}{\partial z} & |x| \geq 1 \\ T_1^{*(2)}(x, 0, t) &= T_2^{*(2)}(x, 0, t) & |x| \geq 1 \\ T_1^{*(2)}(x, h_1, t) &= T_2^{*(2)}(x, -h_2, t) = 0 & |x| \geq 0 \end{aligned} \quad (4.15)$$

It is easy to solve $T_i^{*(1)}(z, p)$ through Eq. (4.12) combined with Eq. (4.13)

$$T_i^{*(1)}(z, p) = \frac{\psi A}{(\psi^2 + p^2)} \frac{e^{-(h_1-z)\sqrt{\omega}} - e^{-\sqrt{\omega}(h_1+2h_2+z)}}{(1 - e^{-2\sqrt{\omega}(h)})} \quad (4.16)$$

where $\omega = (p + \tau_q p^2)$. By applying the Fourier integral transform to Eq. (4.14) and making use of boundary conditions Eq. (15), we have

$$T_i^{*(2)}(x, z, p) = \frac{1}{2\pi} \int_{-\infty}^{\infty} [D_{i1} \exp(|s|\tau z) + D_{i2} \exp(-|s|\tau z)] \exp(-isx) ds \quad (4.17)$$

in which, $\tau = \sqrt{\kappa + \frac{\omega}{s^2}}$; $D_{ij}(s, p)$ are unknown functions that can be determined by introducing the density function $G_0(x, p)$

$$G_0(x, p) = \begin{cases} \frac{\partial}{\partial x} \{T_1^{*(2)}(x, 0, p) - T_2^{*(2)}(x, 0, p)\} & |x| < 1 \\ 0 & |x| \geq 1 \end{cases} \quad (4.18)$$

from the continuity conditions, the density function satisfies

$$\int_{-1}^1 G_0(\xi, p) d\xi = 0 \quad \text{and,} \quad G_0(\xi, p) = 0 \quad |\xi| \geq 1 \quad (4.19)$$

the singular integral equation of $G_0(\xi, p)$ is finally obtained

$$\frac{1}{2\pi} \int_{-1}^1 G_0(\xi, p) \left\{ \frac{\sqrt{\kappa}}{\xi - x} + M_0(x, \xi, p) \right\} d\xi = -\frac{dT^{*(1)}}{dz} \quad (4.20)$$

where the kernel function reads

$$M_0(x, \xi, p) = \int_0^\infty \left(-\frac{2\sqrt{\kappa s^2 + \omega \rho_2 \rho_1}}{\rho_0 s} - \sqrt{\kappa} \right) \sin(s(\xi - x)) ds \quad (4.21)$$

and

$$\left. \begin{aligned} \rho_0(s, p) &= [1 - \exp(-2h_1\tau|s|)]\rho_2 - [1 - \exp(-2h_2\tau|s|)]\rho_1 \\ \rho_1(s, p) &= -[1 + \exp(-2h_1\tau|s|)] \\ \rho_2(s, p) &= 1 + \exp(-2h_2\tau|s|) \end{aligned} \right\} \quad (4.22)$$

Employing the collocation method by Erdogan²⁰³, the singular integral equation, Eq. (4.20), can be reduced to the following algebraic equation

$$\begin{aligned} \frac{1}{2} \sum_{k=1}^n \frac{1}{n} F(\xi_k, p) \left\{ \frac{\sqrt{\kappa}}{\xi_k - x_r} + M_0(x_r, \xi_k, p) \right\} &= -\frac{dT^{*(1)}}{dz} & |x| \leq 1 \\ \sum_{k=1}^n \frac{\pi}{n} F(\xi_k, p) &= 0 \end{aligned} \quad (4.23)$$

where $\xi_k = \cos \frac{(2k-1)\pi}{2n}$, $k = 1, 2, 3, \dots, \frac{n}{2}$; $x_r = \cos \frac{r\pi}{n}$, $r = 1, 2, 3, \dots, \frac{n-1}{2}$ and

$$F(\xi, p) = G_0(\xi, p)\sqrt{1 - \xi^2} \quad |x| \leq 1 \quad (4.24)$$

4.3.2 General solutions and multiphysical model

Then, based on the multiphysical constitutive equations, the temperature solutions can be coupled with the stress field. Similar to the temperature field, using superposition, the displacements can be separated into uncracked $u_z^{*(1)}(z, p)$ and cracked $u_{xi}^{*(2)}(x, z, p)$, $u_{zi}^{*(2)}(x, z, p)$ situations, written in the Laplace domain is

$$\begin{aligned} u_{xi}^*(x, z, p) &= u_{xi}^{*(2)}(x, z, p) \\ u_{zi}^*(x, z, p) &= u_z^{*(1)}(z, p) + u_{zi}^{*(2)}(x, z, p) \end{aligned} \quad (4.25)$$

where $u_z^{*(1)}(z, p)$ satisfies the following differential equation and boundary conditions,

$$\left(c_{11} \frac{d^2}{dz^2} - \rho p^2 \right) u_z^{*(1)} = \lambda_{22} \frac{dT^{*(1)}}{dz} \quad (4.26)$$

$$\sigma_{zz}^{*(1)}(h_1, p) = P/p, \quad \sigma_{zz}^{*(1)}(-h_2, p) = P/p \quad (4.27)$$

$u_z^{*(1)}$ then equals

$$u_z^{*(1)} = C_1 \exp(\zeta z) + C_2 \exp(-\zeta z) + \delta \frac{\sqrt{\omega} e^{-(h_1-z)\sqrt{\omega}} + \sqrt{\omega} e^{-\sqrt{\omega}(h_1+2h_2+z)}}{(1 - e^{-2\sqrt{\omega}(h)})} \quad (4.28)$$

where $\zeta = \sqrt{\frac{\rho p^2}{c_{11}}}$, $\delta = \frac{\lambda_{22}}{(c_{11}\omega - \rho p^2)} \frac{A}{p}$ and

$$\left. \begin{aligned} C_1 &= \frac{-P/p \exp[-\zeta(h_2 + 2h_1)] + \left(\frac{\lambda_{22}A}{p} - c_{11}\delta\omega + P/p\right) \exp(-\zeta h_1)}{c_{11}\zeta\{1 - \exp(-2\zeta h)\}} \\ C_2 &= \frac{-P/p \exp(-\zeta h_2) + \left(\frac{\lambda_{22}A}{p} - c_{11}\delta\omega + P/p\right) \exp[-\zeta(h_1 + 2h_2)]}{c_{11}\zeta\{1 - \exp(-2\zeta h)\}} \end{aligned} \right\} \quad (4.29)$$

The general solutions of the uncracked composite finally are

$$\begin{bmatrix} \sigma_{xx}^{*(1)} \\ \sigma_{zz}^{*(1)} \\ \sigma_{zx}^{*(1)} \end{bmatrix}_{(y)} = \begin{bmatrix} \nu c_{11} & -\nu c_{11} & 0 \\ c_{11} & -c_{11} & 0 \\ 0 & 0 & 0 \end{bmatrix} \begin{bmatrix} \zeta \exp(\zeta z) C_1 \\ \zeta \exp(-\zeta z) C_2 \\ 0 \end{bmatrix}_{(y)} - \begin{bmatrix} \frac{c_{11}A}{p} - \delta\omega\nu c_{11} \\ \frac{\lambda_{22}A}{p} - \delta\omega c_{11} \\ 0 \end{bmatrix} \frac{e^{-(h_1-z)\sqrt{\omega}} - e^{-\sqrt{\omega}(h_1+2h_2+z)}}{(1 - e^{-2\sqrt{\omega}h})} \quad (4.30)$$

Cracked conditions require $u_{xi}^{*(2)}(x, y, p)$ and $u_{yi}^{*(2)}(x, y, p)$ to satisfy the following differential equations

$$\begin{aligned} \left(c_{11} \frac{\partial^2}{\partial x^2} + c_{66} \frac{\partial^2}{\partial z^2} - \rho p^2 \right) u_{xi}^{*(2)} + (c_{12} + c_{66}) \frac{\partial^2 u_{zi}^{*(2)}}{\partial x \partial z} &= \lambda_{11} \frac{\partial T_i^{*(2)}}{\partial x} \\ (c_{12} + c_{66}) \frac{\partial^2 u_{xi}^{*(2)}}{\partial x \partial z} + \left(c_{66} \frac{\partial^2}{\partial x^2} + c_{11} \frac{\partial^2}{\partial z^2} - \rho p^2 \right) u_{zi}^{*(2)} &= \lambda_{22} \frac{\partial T_i^{*(2)}}{\partial z} \end{aligned} \quad (4.31)$$

with the following boundary conditions

$$\begin{aligned} \sigma_{zz}^{*(2)}(x, h_1, p) &= \sigma_{zz}^{*(2)}(x, -h_2, p) = 0 \\ \sigma_{zx}^{*(2)}(x, h_1, p) &= \sigma_{zx}^{*(2)}(x, -h_2, p) = 0 \\ \sigma_{zzi}^{*(2)}(x, 0, p) &= -\sigma_{zz}^{*(1)}(x, 0, p) & |x| < 1 \\ \sigma_{zxi}^{*(2)}(x, 0, p) &= -\sigma_{zx}^{*(1)}(x, 0, p) & |x| < 1 \\ \sigma_{zz}^{*(2)}(x, 0, p) &= \sigma_{zz}^{*(2)}(x, 0, p) & |x| \geq 1 \\ \sigma_{zx1}^{*(2)}(x, 0, p) &= \sigma_{zx}^{*(2)}(x, 0, p) & |x| \geq 1 \\ u_{z1}^{*(2)}(x, 0, p) &= u_{z2}^{*(2)}(x, 0, p) & |x| \geq 1 \\ u_{x1}^{*(2)}(x, 0, p) &= u_{x2}^{*(2)}(x, 0, p) & |x| \geq 1 \end{aligned} \quad (4.32)$$

The solutions are separated into general solutions and particular solutions. The general solutions can be expressed as

$$\begin{aligned} u_{xi,general}^{*(2)} &= \frac{i}{2\pi} \sum_{j=1}^2 \int_{-\infty}^{+\infty} \{Z_{j1} \operatorname{sgn}(s) [A_{ij} \exp(|s|\lambda_j z) - B_{ij} \exp(-|s|\lambda_j z)]\} \exp(-isx) ds \\ u_{zi,general}^{*(2)} &= \frac{1}{2\pi} \sum_{j=1}^2 \int_{-\infty}^{+\infty} \{Z_{j2} [A_{ij} \exp(|s|\lambda_j z) + B_{ij} \exp(-|s|\lambda_j z)]\} \exp(-isx) ds \end{aligned} \quad (4.33)$$

where $Z_{j1} = -(c_{12} + c_{66})\lambda_j s^2$ and $Z_{j2} = (c_{66}\lambda_j^2 - c_{11})s^2 - \rho p^2$. The coefficients λ_j given in the Appendix B as Eq. (B.1). The particular solutions are

$$\begin{aligned} u_{xi,particular}^{*(2)} &= \frac{i}{2\pi} \int_{-\infty}^{+\infty} (R_x^1 s^3 + R_x^2 s) [D_{i1} \exp(|s|\tau z) + D_{i2} \exp(-|s|\tau z)] \exp(-isx) ds \\ u_{zi,particular}^{*(2)} &= \frac{1}{2\pi} \int_{-\infty}^{+\infty} (R_z^1 s^3 + R_z^2 s) \operatorname{sgn}(s) [D_{i1} \exp(|s|\tau z) - D_{i2} \exp(-|s|\tau z)] \exp(-isx) ds \end{aligned} \quad (4.34)$$

where the parameters R_x^1 , R_x^2 , R_z^1 and R_z^2 are shown in the Appendix B as Eq. (B.2). We can find that the particular values represent the thermal-induced deformations.

Finally, the general solutions of the cracked multiphysical model are

$$\begin{aligned} \sigma_{xxi}^{*(2)} &= \frac{1}{2\pi} \sum_{j=1}^2 \int_{-\infty}^{+\infty} \{P_{j1} [A_{ij} \exp(|s|\lambda_j z) - B_{ij} \exp(-|s|\lambda_j z)]\} \exp(-isx) ds \\ &\quad + \frac{1}{2\pi} \int_{-\infty}^{+\infty} \varphi_1 [D_{i1} \exp(|s|\tau z) + D_{i2} \exp(-|s|\tau z)] \exp(-isx) ds \\ \sigma_{zzi}^{*(2)} &= \frac{1}{2\pi} \sum_{j=1}^2 \int_{-\infty}^{+\infty} \{P_{j2} [A_{ij} \exp(|s|\lambda_j z) - B_{ij} \exp(-|s|\lambda_j z)]\} \exp(-isx) ds \end{aligned}$$

$$\begin{aligned}
& + \frac{1}{2\pi} \int_{-\infty}^{+\infty} \varphi_2 [D_{i1} \exp(|s|\tau z) + D_{i2} \exp(-|s|\tau z)] \exp(-isx) ds \\
\sigma_{zxi}^{*(2)} & = \frac{i}{2\pi} \sum_{j=1}^2 \int_{-\infty}^{+\infty} \{P_{j3} \operatorname{sgn}(s) [A_{ij} \exp(|s|\lambda_j z) + B_{ij} \exp(-|s|\lambda_j z)]\} \exp(-isx) ds \\
& + \frac{i}{2\pi} \int_{-\infty}^{+\infty} \varphi_3 \operatorname{sgn}(s) [D_{i1} \exp(|s|\tau z) - D_{i2} \exp(-|s|\tau z)] \exp(-isx) ds \quad (4.35)
\end{aligned}$$

where $P_{jl}(s, p)$ and $\varphi_l(s, p)$ ($l=1,2,3$) are expressed in the Appendix B as Eqs. (B.3) and (B.4).

Introducing density functions $G_l(x, p)$ ($l = 1,2$) and combining with boundary conditions Eq.

(4.32), we can express unknown parameters A_{ij} and B_{ij} ($i, j = 1,2$) as function of G_l

$$\begin{cases} G_1(x, p) \\ G_2(x, p) \end{cases} = \frac{\partial}{\partial x} \begin{cases} u_{x1}^*(x, 0^+, p) - u_{x2}^*(x, 0^-, p) \\ u_{y1}^*(x, 0^+, p) - u_{y2}^*(x, 0^-, p) \end{cases} \quad |x| < 1 \quad (4.36)$$

Finally, solving $G_l(x, p)$ from the system of singular integral equations

$$\begin{aligned}
\frac{1}{\pi} \int_{-1}^1 \left\{ G_1(\xi, p) M_{11} + G_2(\xi, p) \left(M_{12} + \frac{M_{12}^0}{\xi - x} \right) \right\} d\xi & = -\sigma_{yy}^{*(1)}(x, 0, p) - f_1(x, p) \\
\frac{1}{\pi} \int_{-1}^1 \left\{ G_1(\xi, p) \left(M_{21} + \frac{M_{21}^0}{\xi - x} \right) + G_2(\xi, p) M_{22} \right\} d\xi & = -f_2(x, p) \\
\int_{-1}^1 G_l(\xi, p) d\xi & = 0
\end{aligned} \quad (4.37)$$

one can get the thermomechanical fields of the problem. In Eq. (4.37), $M_{11}, M_{12}, M_{21}, M_{22}, M_{12}^0$ and M_{21}^0 are given in the Appendix B as Eqs. (B.5) and (B.6), while the temperature-induced parameters $f_1(x, p)$ and $f_2(x, p)$ are expressed as

$$\begin{aligned}
f_1(x, p) &= \frac{1}{2\pi} \int_{-\infty}^{+\infty} \left\{ \varphi_1 [D_{11} + D_{12}] + S_{10} D_0 - S_{11} \left(\frac{(R_x^1 s^6 + R_x^2 s^4) D_0}{|s|} \right) \right\} \exp(-isx) ds \\
f_2(x, p) &= \frac{1}{2\pi} \int_{-\infty}^{+\infty} \left[\varphi_3 [D_{11} - D_{12}] + S_{20} D_0 - S_{21} \frac{(R_x^1 s^6 + R_x^2 s^4) D_0}{|s|} \right] \exp(-isx) ds
\end{aligned} \tag{4.38}$$

By virtue of the Lobatto-Chebyshev method ¹⁶³, transforming the singular integral Eq. (4.37) into the following algebraic equations, the solutions of density functions G_l can be finally obtained

$$\begin{aligned}
\frac{1}{\pi} \sum_{k=1}^n A_k \left\{ F_1(\xi_k, p) M_{11} + F_2(\xi_k, p) \left(M_{12} + \frac{M_{12}^0}{\xi_k - x_r} \right) \right\} &= -\sigma_{yy}^{*(1)}(x_r, 0, p) - f_1(x_r, p) \\
\frac{1}{\pi} \sum_{k=1}^n A_k \left\{ F_1(\xi_k, p) \left(M_{21} + \frac{M_{21}^0}{\xi_k - x_r} \right) + F_2(\xi_k, p) M_{22} \right\} &= -f_2(x_r, p) \\
\sum_{k=1}^n A_k F_l(\xi_k, p) &= 0
\end{aligned} \tag{4.39}$$

where $\xi_k = \cos \frac{(k-1)\pi}{n-1}$, $k = 1, 2, 3, \dots, n$; $x_r = \cos \frac{(2r-1)\pi}{2(n-1)}$, $r = 1, 2, 3, \dots, n-1$; $A_k = \frac{\pi}{2(n-1)}$,

$k = 1, n$; $A_k = \frac{\pi}{n-1}$, $k = 2, 3, \dots, n-1$; and

$$F_l(\xi_k, p) = G_l(\xi, p) \sqrt{1 - \xi^2} \quad |x| \leq 1 \quad (l = 1, 2) \tag{4.40}$$

4.3.3 Stress intensity factors

The stress intensity factors $K_I^*(p)$, $K_{II}^*(p)$ in the Laplace domain can be obtained

$$\begin{aligned}
K_I^*(p) &= \lim_{x \rightarrow 1^+} \sqrt{2\pi(x-c)} \sigma_{yy1}^*(x, 0, p) \\
K_{II}^*(p) &= \lim_{x \rightarrow 1^+} \sqrt{2\pi(x-c)} \sigma_{yx}^*(x, 0, p)
\end{aligned} \tag{4.41}$$

then, applying the Laplace inverse transform, the stress intensity factors (SIFs) in the time domain can be obtained as

$$\begin{aligned}
K_I(t) &= -\sqrt{\pi} \frac{1}{2\pi i} \int_{Br} [M_{12}^0 F_2(1, p)] \exp(pt) dp \\
K_{II}(t) &= -\sqrt{\pi} \frac{1}{2\pi i} \int_{Br} [M_{21}^0 F_1(1, p)] \exp(pt) dp
\end{aligned} \tag{4.42}$$

4.4 Results and Verifications

Depending on the multi-material AM (3D printing) techniques, a type of 15mm × 75mm (c×h) functional biomimetic brick-and-mortar composite was produced recently¹⁷⁸. The hard and soft phases of the composite were printed by rigid plastics VeroCyan and rubber-like Agilus30 Black materials, respectively. According to the experimental data, the material constants are listed in Table 4.1 and the corresponding volume fraction of the hard phase, γ is expressed as

$$\gamma = \begin{cases} \Phi_1 z/h_1 + \Phi_0 & i = 1 \\ -\Phi_1 z/h_2 + \Phi_0 & i = 2 \end{cases} \tag{4.43}$$

Table 4. 1 The experimental coefficients of Young's modulus¹⁷⁸.

e_1	e_2	e_3
-75.81	551.41	-0.09

To pursue the benefits of a designed nacre-like functional brick-and-mortar (BM-GRAD) microstructure, a brick-free single gradient (GRAD) arrangement is introduced to compare the results. The values Φ_1 and Φ_0 of two different microstructures are shown in Table 4.2.

Table 4. 2 The values of the coefficients of the volume fraction of the hard phase¹⁷⁸.

Microstructure	Φ_1	Φ_0
GRAD	0.62	0.38
BM-GRAD	0.48	0.52

As the thermal performance of the composite has some missing information in the experiment, considering the soft phase of material generally has a better thermal resistance, we assume $\tau_q = 1.5$ and $\kappa = 1$. Moreover, the biomaterial could respond to the thermal stimuli, let $\bar{\lambda}_{ij} = 1$ ($i = j = x, z$).

4.4.1 Model verifications

The likelihood of crack propagation of functional brick-and-mortar (BM-GRAD) and unbrick single gradient (GRAD) microstructures are compared as shown in Figure 4.3. The single-edged notched experimental specimen is a special condition of the central crack case in fracture mechanics with, $K_{\text{edged}} = 1.12 K_{\text{central}}$. As expected, shear stress intensity factors (K_{II}) are equal to zero under a pure tensile loading, and only an opening crack will happen if P increases. Moreover, it is observed that the values of K_I of the GRAD are always higher than BM-GRAD. The results showed the crack propagation trend of the BM-GRAD is much lower under the single mechanical field, which is consistent with the experimental results (Figure 4.3b), where BM-GRAD has larger maximum stress than the GRAD specimen.

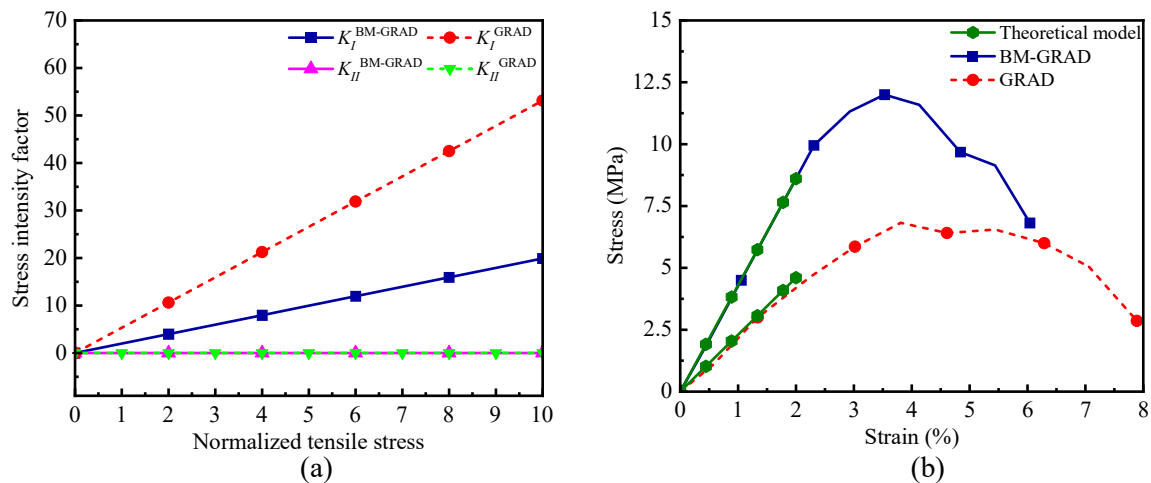


Figure 4. 3 Crack propagation likelihood of functional brick and unbrick microstructures: (a) stress intensity factors under pure tensile stress; (b) experimental and theoretical stress-strain curves ¹⁷⁸.

To further validate the theoretical model, strain patterns around the crack tips are visualized and compared with DIC experiments as well as Abaqus simulations. Figure 4.4 presents the good consistency of the results via the three methods. In all the results with or without brick-and-mortar layouts, a high strain concentration is seen in front of the crack tip. The strain localization for both the BM-GRAD and GRAD exhibits a candle flame-shaped region around the crack tip. A longer and thinner zone of strain localization is shown in the GRAD group than in the BM-GRAD. Moreover, due to the functional gradient introduced in constitutive equations which are ignored in the Abaqus finite element simulation and replaced by averaged values, the strain pattern and exact value obtained via the theoretical model are even closer to the DIC results than the finite element results.

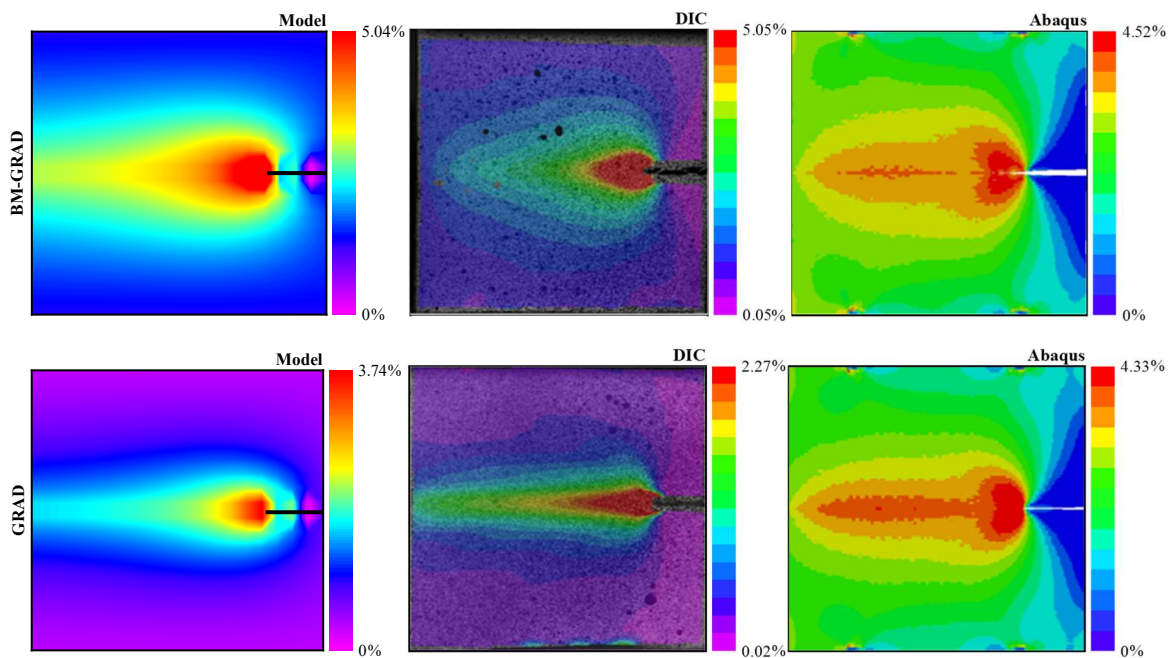


Figure 4. 4 The strain patterns around the crack tip obtained from the present model, DIC experiments ¹⁷⁸, and Abaqus simulations ¹⁷⁸.

So far, after reducing the scale of the field into the single tensile load, all the solutions of the predicted model show good agreement with the experimental and simulation tests. Thus, the

prediction model is reliable and can be extended to predict material performance involving multiphysical structures.

4.4.2 Thermal loading

If the composite undergoes a single thermal pulse $Asin(\omega t) = \sin(0.5t)$, Figure 4.5 compares the temperature changes at the center of the crack ($x=0, z=0$) under classical Fourier and non-Fourier heat conduction models. Both types of the model show an obvious, sinusoidal, thermal response. Meanwhile, a temperature jump happens between the upper and lower faces of the insulated crack as expected. However, owing to the thermal relaxation time, an apparent delay in the thermal response is observed for the non-Fourier model as the peak values occur after that of Fourier heat conduction. At the same time, the temperature predicted by the non-Fourier model exhibits an amplifying phenomenon, with a peak value much larger than the results by the Fourier model. The classical Fourier's law results in a diffusion-type heat transfer, which is different from the wave form heat transfer as expressed in Eq. (4.5). Hence, the introduction of the phase lag of heat flux τ_q in thermal analysis leads to a more conservative design.

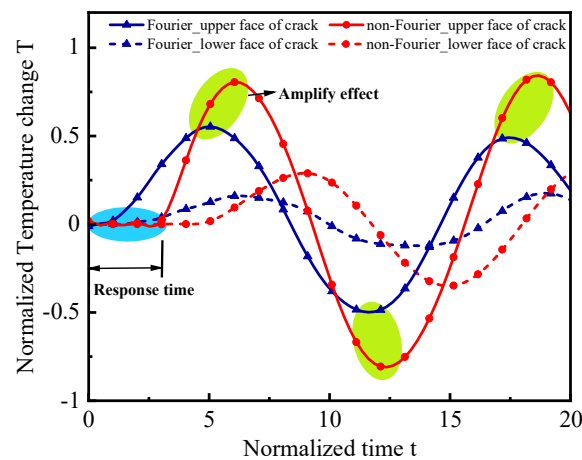


Figure 4. 5 Temperature results with different heat conduction models.

The stress intensity factors (SIFs) measure the intensity of the singular stress field around the crack tip. SIF-based fracture criteria allow us to evaluate the failure mode of the composite. Figure 4.6 plots the mode I and mode II SIFs versus temperature change, showing the SIFs for both BM-GRAD and GRAD exhibit the same trend of variation under single thermal loading, where the magnitudes of K_I decrease with the increase of temperature, while K_{II} remains zero for the pure thermal loading. An opening failure mode (mode I) will likely occur under the cooling condition, while the crack trends to closed under heating conditions due to K_I becoming negative. Therefore, thermal failure needs to be considered in material design.

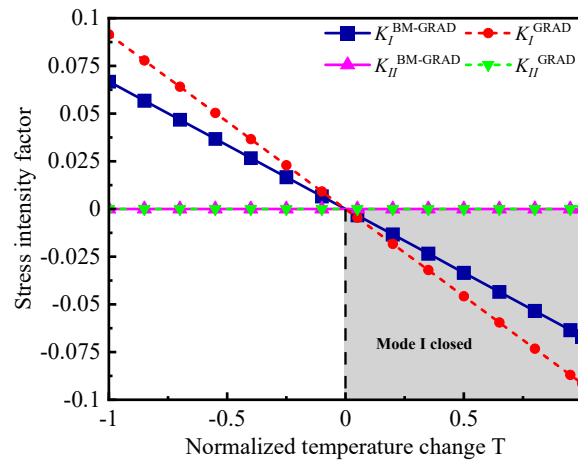


Figure 4. 6 Stress intensity factors under single thermal loading. ($t = 1, \rho = 0.1$)

4.4.3 Thermal-mechanical loading

Now we consider the thermomechanical response of the structure under thermomechanical loading. As shown in Figure 4.1, tensile stress is applied in combination with a sinusoidal temperature variation. Figs. 4.7 and 4.8 present the stress intensity factors and corresponding stress distributions for BM-GRAD and GRAD microstructures, respectively. It is easy to find that BM-GRAD shows better performance than GRAD. According to Figure 4.7, under $P=1$, with the magnitude of T getting bigger, the absolute value of K_I of GRAD is always higher than the BM-

GRAD microstructure before the C point ($T < C$), but it is worth noting that the K_I at point C is negative, which means crack will be closed. Even though, after the temperature rises beyond point C, the K_I of BM-GRAD becomes bigger than GRAD as the temperature rises, they both cause cracks to close and keep the structure safe. It also notices that the K_I value of BM-GRAD gets into the negative regime earlier than GRAD, so as temperature increases, the BM-GRAD enters the safe zone earlier. To further illustrate the thermomechanical behavior of the GM-GRAD and GRAD microstructures, the normal stress distribution in two different conditions: cooling-tensile condition 1 ($T = -40, P = 1$) and heating-tensile condition 2 ($T = 40, P = 1$) are shown in Figure 4.8.

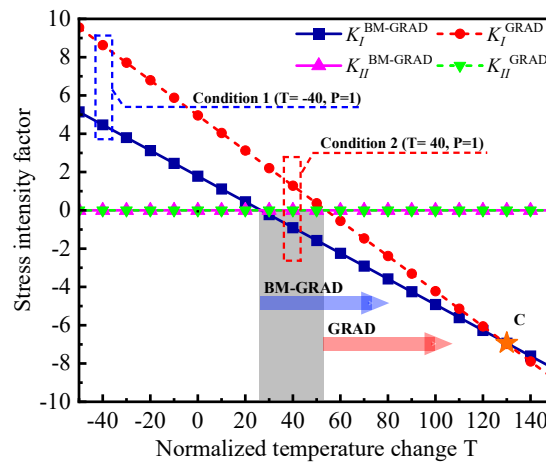


Figure 4. 7 The plots of the SIFs with different microstructures. ($t = 1, \rho = 0.1$)

The line graphs in Figure 4.8 show the stress values on the crack surface equal to zero which satisfies the free surface boundary condition requirement. The stress spikes around crack tips for both conditions: for condition 1, the peak value of GRAD is much larger than BM-GRAD; for condition 2, at crack tips, the normal stress of BM-GRAD already transforms into a negative value, which will cause the crack to close, but the normal stress of GRAD is still positive. By further comparing stress patterns in the whole strip as shown in the contour plot of Figure 4.8, BM-GRAD always shows a smaller substantial zone of stress localization as well as lower values of the normal

stress than GRAD. These stress distributions confirm that introducing brick-and-mortar (BM) microstructure can significantly improve the potential to overcome the crack propagation of the composite under thermal-tensile loading.

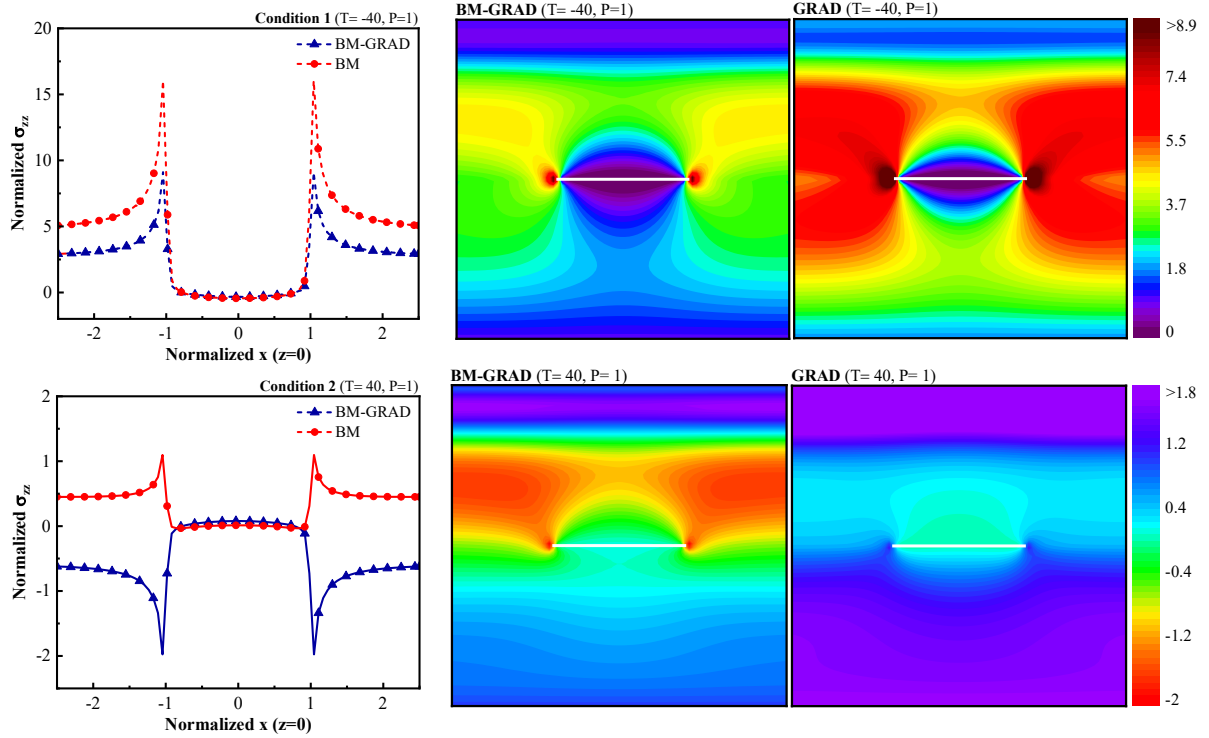


Figure 4. 8 The stress distribution around the crack surface and crack tips. ($t = 1, \rho = 0.1$)

4.4.4 Initial crack propagation predictions

Based on the interface damage models between dissimilar materials⁸³, and, relied on the ratio of the energy release rate for penetrating the interface to deflecting into the interface, G_p/G_d , to the ratio of the mode I toughness of the material of branch to the interface toughness, Γ_c/Γ_{ic} , concretely if

$$\frac{G_p}{G_d} > \frac{\Gamma_c}{\Gamma_{ic}} \quad (4.44)$$

the impinging crack is likely to penetrate the interface, Conversely, the crack will tend to deflect into the interface when the inequality is reversed.

Suppose that the crack forms an infinitesimal kink at an angle ϑ from the plane of the crack. The local stress intensity factors at the tip of this kink differed from the nominal K values of the main crack. If we define a local system r - ϑ , the local Mode I and Mode II stress intensity factors at the tip are obtained by summing the normal and shear stresses, respectively, at ϑ ²⁰⁴

$$\begin{aligned} k_I(\vartheta) &= K_I \left(\frac{3}{4} \cos \frac{\vartheta}{2} + \frac{1}{4} \cos \frac{3\vartheta}{2} \right) + K_{II} \left(-\frac{3}{4} \sin \frac{\vartheta}{2} - \frac{3}{4} \sin \frac{3\vartheta}{2} \right) \\ k_{II}(\vartheta) &= K_I \left(\frac{1}{4} \sin \frac{\vartheta}{2} + \frac{1}{4} \sin \frac{3\vartheta}{2} \right) + K_{II} \left(\frac{1}{4} \cos \frac{\vartheta}{2} + \frac{3}{4} \cos \frac{3\vartheta}{2} \right) \end{aligned} \quad (4.45)$$

The energy release rate for the kinked crack is given by ²⁰⁴

$$G(\vartheta) = \frac{k_I^2(\vartheta) + k_{II}^2(\vartheta)}{E} \quad (4.46)$$

According to experimental results ¹⁷⁸, the crack tips located in the hard layer of the BM-GRAD groups, thus the toughness ratio is equal to monolithically GRAD material, $\Gamma_c/\Gamma_{ic} = 1$. According to Eq. (4.46), the estimated ratios of energy release rate $\Phi = G_p/G_d$ under a single stress field for GRAD and BM-GRAD groups are equal to 3.98 and 3.91 (> 1), respectively, thus, the microcracks in front of the crack tips will penetrate and remain parallel to the original crack faces. The outcomes are consistent with optical microscopy images (Figure 4.9).

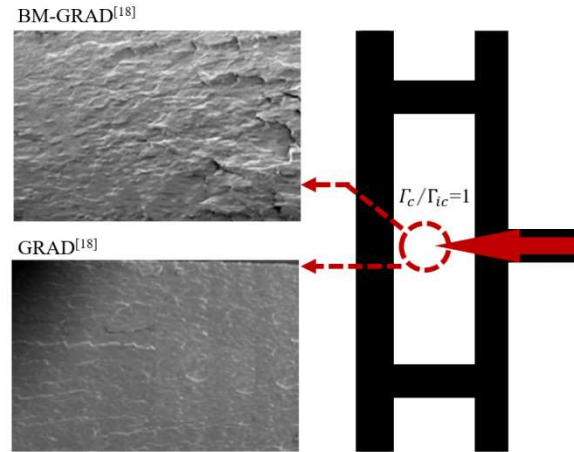


Figure 4. 9 Initial crack propagation directions under a single stress field.

To further understand the influence of external thermomechanical loading on crack deflection between dissimilar soft and hard materials, three loading conditions: single stress ($P=1$), thermal ($T= -40, 40$), and coupled thermal-mechanical ($P=1, T= -40, 40$) fields are considered. Assume the crack tip locates at the interface of soft and hard phases, like Figure 4.2b, then the toughness ratio of BM-GRAD changes to 6.71 based on the experimental results of monolithic materials¹⁷⁸. Table 4.3 shows that the initial crack trends propagate in a straight line for the GRAD group, however, it deflects to the BM-GRAD and the corresponding predictions are drawn in Figure 4.10. In addition, the coupled thermomechanical loading increases the risk of crack penetration except for tensile-heating condition which is consistent with Figure 4.7, owing to the value of K_I becoming negative, and the crack trends to close. Therefore, Φ under $P=1, T=40$ becomes lower than under single heating or tensile condition. These observations suggest that multi-physical fields can lead to different directions of crack propagation which can not be neglected in the application of BM-GRAD materials. Importantly, introducing a brick-and-mortar layout results in a higher prospect of deflecting cracks that can dissipate much more energy and are easier to be terminated than a straight crack path observed in the unbricked pattern.

Table 4. 3 The ratio of the energy release rate for different environments.

Microstructure (Toughness ratio)	The ratio of the energy release ratio	Heating condition (T= 40)			Cooling condition (T= -40)		Predict
		Tensile	Thermal	Tensile-heating	Thermal	Tensile-cooling	
GRAD (1) ^{ic}	$\Phi = G(0)/G(\pi/2)$	3.98	3.94	4.25	3.94	4.01	Penetrate
BM-GRAD (6.27)	$\Phi = G(0)/G(\pi/2)$	3.91	4.00	3.67	4.00	4.00	Deflect

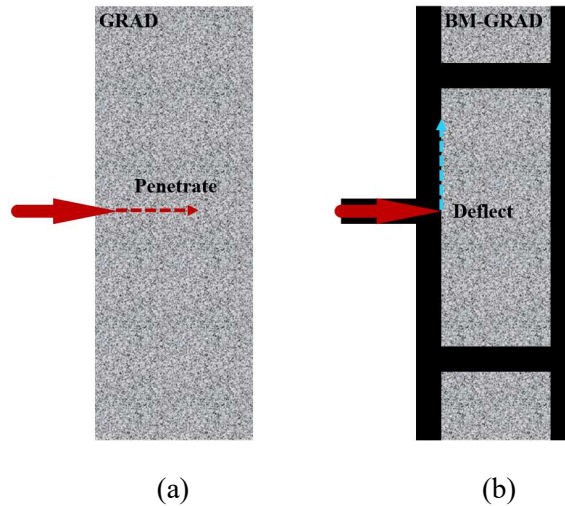


Figure 4. 10 Initial crack propagation direction predictions: (a) Penetrate; (b) Deflect.

4.5 Conclusions

In summary, we have compared the thermomechanical behavior of brick-and-mortar and unbricked gradient patterns under single sinusoidal thermal, single stress, and coupled thermal-stress fields, and used an interface damage model to characterize crack propagation directions. Based on the experimental results and numerical analysis, we differentiate the microstructure layouts by controlling Young's modulus, which varies with the volume fraction of the hard phase γ , and finally propose an elastic model to predict the stress results. The reliability of the present results is verified. Multiphysical conditions have a significant influence on the material performance of different microstructures, while temperature is a vital factor that cannot be ignored. A sudden temperature fall will cause an opening-mode failure risk. Furthermore, under

thermal-tensile loading condition, brick-and-mortar gradient microstructure (BM-GRAD) always shows a smaller zone of extreme stress localization as well as lower values of the normal stress, which significantly improves the crack resistance. It is also highlighted that BM-GRAD microstructure is easier to form deflecting crack once a fracture happens and the crack propagation is more likely to be terminated. The present results show the influence of the multiphysical loading on the fracture of microstructure and provide guidelines for the microstructure design and criteria for obtaining favorable failure patterns.

Chapter 5

Functionally graded Design of Bio-composite Material for Fracture Resistance under Multiphysical

Application

Combining thermal piezoelectric multiphysical behavior and graded hierarchical microstructure property of biomimetic materials, a thermo-electromechanical piezo functionally graded theoretical model is developed in this chapter. To explore the appropriate configuration for different Multiphysics, two configurations, namely symmetric functionally graded piezoelectric material (Sym-FGPM) and exponential functionally graded piezoelectric material (Expo-FGPM), are designed and controlled against fracture using thermal gradation coefficient Ψ and electromechanical gradation coefficient Ω . Comparisons with non-functionally graded piezoelectric material (Non-FGPM) are conducted using a revised critical intensity factor (K_C) in both single and multiphysical environments. The results demonstrate that the Sym-FGPM structure, with high gradation coefficients, achieved lower K_C , indicating superior crack resistance in single stress and electric fields. However, in the thermal field, the functionally graded design amplified the thermal shock effect. For thermo-electromechanical fields, the optimal Sym-FGPM configuration with (Ω, Ψ) values of (1, -0.5) for heating and (1, -1) for cooling reduces K_C by 24% and 48% respectively compared to Non-FGPM. Caution is advised when using Expo-FGPM, as it is suitable for cooling coupling conditions but not for heating coupling environments.

5.1 Introduction

Biomaterials possess ingenious hierarchical construction and smart living organic cells. These two features empower biomaterials performing great strength and toughness mechanical performances²⁰⁵⁻²⁰⁷ as well as intelligent self-optimizing ability²⁰⁸⁻²¹⁰.

The characteristics of biomaterials become the source of inspiration for the designs of engineering structure²¹¹⁻²¹⁵. For example, through mimicking the brick-and-mortar like structure of nacre²¹⁶⁻²²⁰, the multi-layer composite panel exhibits good impact resistance and energy dissipation²²¹⁻²²⁴. In these studies, the brick-and-mortar structure is simulated by finite element method (FEM) and fabricated through additive manufacturing (AM) technique. To achieve the brick-and-mortar grade of nacre-inspired composite, researches separated the composite into different layers²²⁵⁻²²⁷. Then homogeneous elements with constant material properties in each layer were used to approach the non-homogeneous performance of nacre²²⁸. The accuracy of this multi-layered method highly depends on the number of layers utilized. If the number of layers is not large enough, the material gradation becomes discontinuous²²⁹ and leads to the undesirable discontinuities of the stress fields⁴⁹. However, if the number of layers is increased, the associated computational and fabrication costs would be prohibitively high. Hence, as the hierarchical, functional structure becomes more intricate and complex, it becomes very difficult to develop a FEM model or achieve AM fabrication.

Considering the presence of living cells within biomaterials, which consist of a large amount of collagen. The piezoelectricity of collagen is incorporated into the brick-and-mortar functional structural model²³⁰⁻²³⁴. After the structures are equipped with the piezoelectric ability, the bio-composites become self-adaptable which are able to respond to external triggers and widely used

in sensors ²³⁵⁻²³⁸ and actuators ²³⁹⁻²⁴². Researches have conducted various response analyses of functionally graded piezoelectric material (FGPM) model by changing external stimuli, such as mechanical impact ²⁴³⁻²⁴⁷, electrical charge ²⁴⁸⁻²⁵², and electromechanical loading ²⁵³⁻²⁵⁷. The investigations primarily focused on the interaction between mechanical and electrical fields to improve the smart capability of FGPM. However, thermal disturbance is also a common problem that will be faced especially in aerospace applications ²⁵⁸⁻²⁶². When the spaceship returns to earth, the FGPM structure of its surface will undergo an extremely high temperature gradient from outside to inside ²⁶³. This highly thermal change can induce the structure to lose its stability and collapse in a very short time.

Here, aiming at addressing the issues of discontinuity in the model and costly computational and manufacturing expenses in FEM and AM methods, as well as considering the impacts of temperature, a continuous, multiphysical model of functionally graded piezoelectric material was built in this paper. By introducing a pre-existing central crack, the stress and displacement responses at the crack tip, as well as the structure stability, of the FGPM were investigated under thermo-electromechanical loading. This multiphysical boundary makes the model of biomimetic materials more realistic and comprehensive, thus providing a more precise reflection of their performance in complex, real-world environment. It is worth pointing out that, in the theoretical model, the configurations of FGPM can be easily changed by the governing equation. Therefore, we designed symmetric and unsymmetric configurations of FGPM, and introduced thermal gradation coefficient Ψ and electromechanical gradation coefficient Ω to control the gradation profile of configurations. A critical intensity factor (K_C) was defined and calculated, and the results were compared among various gradation parameters, providing guidelines for the design of bio-composite material in both single and multiphysical conditions.

5.2 Statement of the problem

5.2.1 Microstructure of FGPM and its properties

In nature, bamboo is a typical, functionally graded piezoelectric material (FGPM). The microstructure of bamboo is shown in Figure 1 (a) with fibers gradually varying through the wall thickness and, the concentration being most dense near the upper (exterior). According to it, we have designed the gradation profile for the functionally graded piezoelectric material (FGPM) as expressed by Eq. (5.1). The schematic variations of material property parameters are taken to vary continuously along the z-direction as shown in Figure 5.1 (b).

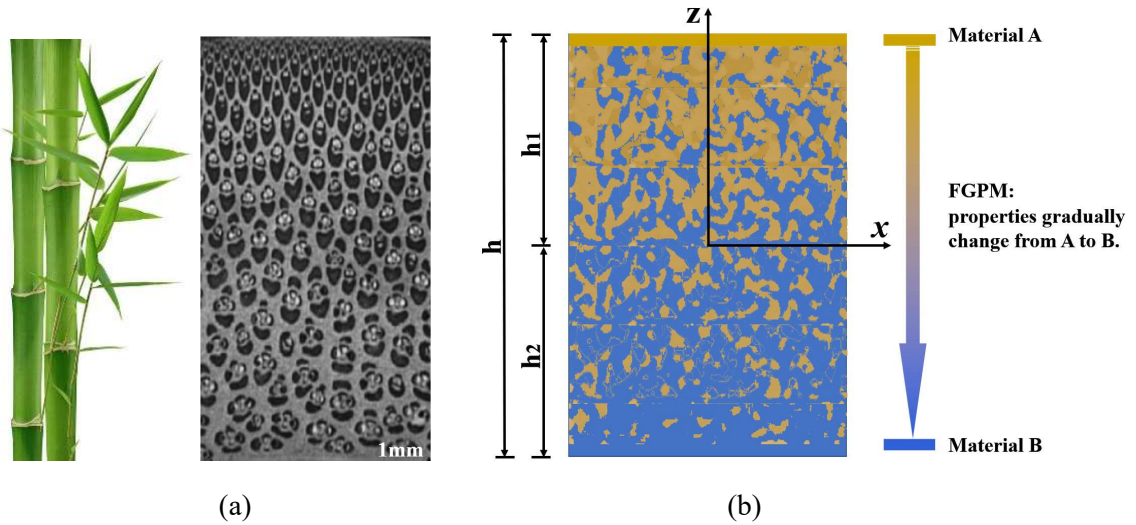
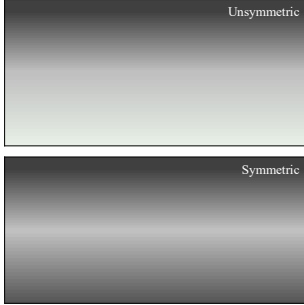


Figure 5. 1 Microstructure of an FGPM that is graded from material A to material B: (a) SEM micrograph of a bamboo ²⁶⁴; (b) the gradation profile of FGPM material.

$$\begin{aligned} (\zeta_{ik}, p_z) &= (\zeta_{ik0}, p_{z0}) e^{\Psi \mu z} && \text{FPGM. } \Psi \\ (c_{ik}, d_{ik}, \varepsilon_{ik}, k_i, \rho) &= (c_{ik}, d_{ik}, \varepsilon_{ik}, k_{i0}, \rho_0) e^{\Omega \mu z} && \text{FPGM. } \Omega \end{aligned} \quad (5.1)$$

where the superscripts Ω and Ψ stand for the gradation coefficients for the FGM, whose values can be used to reschedule the profile of gradation. Additionally, we also introduce μ as a functional

gradient parameter: when $\mu = \text{sgn}(z)$, the material properties of piezoelectric material vary symmetrically along the x-axis, when $\mu = 1$, the variations become unsymmetrical.

$$\mu = \begin{cases} 1 & \text{Unsymmetric} \\ \text{sgn}(z) & \text{Symmetric} \end{cases}$$


For a piezoelectric material, parameters c_{ik} , d_{ik} , ε_{ik} , k_i , ζ_{ik} , p_z and ρ in Eq. (5.1) are, respectively, elastic stiffness, piezoelectric constants, dielectric constants, thermal conductivities, thermal moduli, pyroelectric constants, and mass density.

5.2.2 Thermo-electromechanical orthotropic constitutive model and boundary conditions

Let a central crack of length $2c$ be in the interior of an infinite FGPM as shown in Figure 5.2. Considering that the upper surface of the strip is subjected to an impact tensile stress loading $\sigma(t) = \sigma_0 H(t)$, a thermal shock $T(t) = T_0 H(t)$, and an impact electrical loading $D(t) = D_0 H(t)$, where σ_0 , D_0 and T_0 are the loading amplitudes and $H(t)$ is the Heaviside step function.

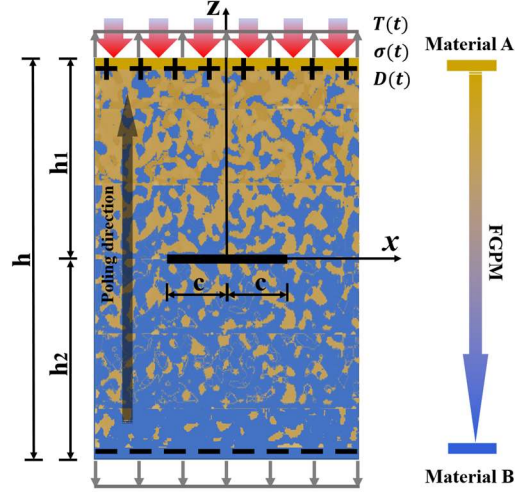


Figure 5. 2 FGPM strip model and boundary conditions.

As a convention, the poling axis of the piezoelectric material is in the z -direction. The constitutive relations for piezoelectric media give the coupled thermo-electromechanical, multiphysical relationship of plane orthotropic piezoelectricity as

$$\begin{bmatrix} \sigma_{xx} \\ \sigma_{zz} \\ \sigma_{zx} \\ D_x \\ D_z \end{bmatrix}_{\text{FGPM}} = \begin{bmatrix} c_{11} & c_{13} & 0 \\ c_{13} & c_{33} & 0 \\ 0 & 0 & c_{44} \\ 0 & 0 & d_{15} \\ d_{31} & d_{33} & 0 \end{bmatrix}_{\text{FGPM},\Omega} \begin{bmatrix} \varepsilon_{xx} \\ \varepsilon_{zz} \\ \gamma_{zx} \end{bmatrix} - \begin{bmatrix} \zeta_{11} \\ \zeta_{33} \\ 0 \\ 0 \\ p_z \end{bmatrix}_{\text{FGPM},\Psi} T - \begin{bmatrix} 0 & d_{31} \\ 0 & d_{33} \\ d_{15} & 0 \\ -\varepsilon_{11} & 0 \\ 0 & -\varepsilon_{33} \end{bmatrix}_{\text{FGPM},\Omega} \begin{bmatrix} E_x \\ E_z \end{bmatrix} \quad (5.2)$$

where σ_{ij} , D_i , ε_{ij} , E_i , and T are components of the stress tensor, electric displacement, strain tensor, electric field vector and change of temperature.

The electric field is derivable from a scalar electric potential:

$$E_i = -\phi_{,i}$$

where ϕ_i is the electric potential, a comma denotes partial differentiation about the coordinates. Finally, combining with the equation of motion without body forces and Maxwell's equation, the thermo-electromechanical, multiphysical governing equations are

$$\begin{aligned}
 & \left(c_{110} \frac{\partial^2}{\partial x^2} + c_{440} \frac{\partial^2}{\partial z^2} - \rho_0 \frac{\partial^2}{\partial t^2} + \mu\Omega c_{440} \frac{\partial}{\partial z} \right) u_x + \left(c_{130} \frac{\partial^2}{\partial x \partial z} + c_{440} \frac{\partial^2}{\partial x \partial z} + \mu\Omega c_{440} \frac{\partial}{\partial x} \right) u_z \\
 & \quad + \left(d_{310} \frac{\partial^2}{\partial x \partial z} + d_{150} \frac{\partial^2}{\partial x \partial z} + \mu\Omega d_{150} \frac{\partial}{\partial x} \right) \phi = \zeta_{110} e^{\mu\phi z} \frac{\partial T}{\partial x} \\
 & \left(c_{130} \frac{\partial^2}{\partial x \partial z} + c_{440} \frac{\partial^2}{\partial x \partial z} + \mu\Omega c_{130} \frac{\partial}{\partial x} \right) u_x + \left(c_{440} \frac{\partial^2}{\partial x^2} + c_{330} \frac{\partial^2}{\partial z^2} - \rho_0 \frac{\partial^2}{\partial t^2} + \mu\Omega c_{330} \frac{\partial}{\partial z} \right) u_z \\
 & \quad + \left(d_{150} \frac{\partial^2}{\partial x^2} + d_{330} \frac{\partial^2}{\partial z^2} + \mu\Omega d_{330} \frac{\partial}{\partial z} \right) \phi = \zeta_{330} e^{\mu\phi z} \left(\frac{\partial T}{\partial z} + \mu\Psi T \right) \quad (5.3) \\
 & \left(d_{150} \frac{\partial^2}{\partial x \partial z} + d_{310} \frac{\partial^2}{\partial x \partial z} + \mu\Omega d_{310} \frac{\partial}{\partial x} \right) u_x + \left(d_{150} \frac{\partial^2}{\partial x^2} + d_{330} \frac{\partial^2}{\partial z^2} + \mu\Omega d_{330} \frac{\partial}{\partial z} \right) u_z \\
 & \quad - \left(\varepsilon_{110} \frac{\partial^2}{\partial x^2} + \varepsilon_{330} \frac{\partial^2}{\partial z^2} + \mu\Omega \varepsilon_{330} \frac{\partial}{\partial z} \right) \phi = p_{z0} e^{\mu\phi z} \left(\frac{\partial T}{\partial z} + \mu\Psi T \right)
 \end{aligned}$$

For simplicity, $\phi = \Psi - \Omega$ in Eq. (5.3).

The component of the temperature T satisfies the non-Fourier, dual-phase lag heat conduction¹⁰⁹ which accommodates a certain time for the process of heat transport and building a local thermal equilibrium in the composites, expressed by

$$\begin{aligned}
 q_x + \tau_q \frac{\partial q_x}{\partial t} &= -k_{x\text{FPGM},\Omega} \left(\frac{\partial T}{\partial x} + \tau_s \frac{\partial}{\partial t} \frac{\partial T}{\partial x} \right) \\
 q_z + \tau_q \frac{\partial q_z}{\partial t} &= -k_{z\text{FPGM},\Omega} \left(\frac{\partial T}{\partial z} + \tau_s \frac{\partial}{\partial t} \frac{\partial T}{\partial z} \right) \quad (5.4)
 \end{aligned}$$

where q_x, q_z are the heat fluxes in the x- and z- directions, τ_q and τ_s are phase lags of the heat flux and temperature gradient, respectively. Considering the graded property of thermal conductivity expressed in Eq. (5.1), further incorporating Eq. (5.4) with the energy equation, the governing equation of temperature change T is finally defined as

$$\rho_0 c_\rho \left(1 + \tau_q \frac{\partial}{\partial t}\right) \frac{\partial T}{\partial t} = \left(1 + \tau_s \frac{\partial}{\partial t}\right) \left[k_{x0} \frac{\partial^2 T}{\partial x^2} + k_{z0} \frac{\partial^2 T}{\partial z^2} + \Omega \mu k_{z0} \frac{\partial T}{\partial z} \right] \quad (5.5)$$

where c_ρ is the specific heat.

Referring to Figure 5.2, the corresponding initial and boundary conditions for the thermal field are

$$\begin{aligned} T(x, z, 0) &= 0 \\ T(x, h_1, t) &= T_0 H(t) \\ T(x, -h_2, t) &= 0 \\ \frac{\partial T(x, 0^+, t)}{\partial z} &= \frac{\partial T(x, 0^-, t)}{\partial z}, \quad T(x, 0^+, t) = T(x, 0^-, t) \quad |x| \geq c \end{aligned} \quad (5.6)$$

and for electromechanical fields are

$$\begin{aligned} \sigma_{zz}(x, h_1, t) &= \sigma_{zz}(x, -h_2, t) = \sigma_0 H(t) \\ \sigma_{zx}(x, h_1, t) &= \sigma_{zx}(x, -h_2, t) = 0 \\ D_z(x, h_1, t) &= D_z(x, -h_2, t) = D_0 H(t) \\ \sigma_{zz}(x, 0, t) &= \sigma_{zx}(x, 0, t) = 0 \quad |x| < c \\ \sigma_{zz}(x, 0^+, t) &= \sigma_{zz}(x, 0^-, t), \quad \sigma_{zx}(x, 0^+, t) = \sigma_{zx}(x, 0^-, t) \quad |x| \geq c \\ D_z(x, 0^+, t) &= D_z(x, 0^-, t), \quad \phi(x, 0^+, t) = \phi(x, 0^-, t) \quad |x| \geq c \\ u_z(x, 0^+, t) &= u_z(x, 0^-, t), \quad u_x(x, 0^+, t) = u_x(x, 0^-, t) \quad |x| \geq c \end{aligned} \quad (5.7)$$

While two different electric and thermal boundary conditions are applied at the crack surface:

- Impermeable crack: the electric crack-face boundary conditions are given by

$$D_z(x, 0^+, t) = D_z(x, 0^-, t) = 0 \quad |x| < c$$

$$\frac{\partial T(x, 0^+, t)}{\partial z} = \frac{\partial T(x, 0^-, t)}{\partial z} = 0 \quad |x| < c$$

- Permeable crack: the electric crack-face boundary conditions are given in such cases by

$$D_z(x, 0^+, t) = D_z(x, 0^-, t) \quad |x| < c$$

$$\phi_z(x, 0^+, t) = \phi_z(x, 0^-, t) \quad |x| < c$$

$$\frac{\partial T}{\partial z} = \Theta [T(x, 0^+, t) - T(x, 0^-, t)] \quad |x| < c$$

where the quantity Θ is the thermal conductivity of the crack surface.

5.3 General solutions and stress intensity factors

Define a Laplace transform pair by

$$\begin{aligned} f^*(x, z, p) &= \int_0^{\infty} f(x, z, t) e^{-pt} dt \\ f(x, z, t) &= \frac{1}{2\pi i} \int_{Br} f^*(x, z, p) e^{pt} dt \end{aligned} \quad (5.8)$$

in which Br stands for the Bromwich path of integration to transform the time variable t into the Laplace variable p , and the superscript ‘*’ indicates the variables in the Laplace domain, which have been omitted in the following analysis for convenience. Then the time dependency in Eq. (5.5) is eliminated and transformed into

$$\kappa \frac{\partial^2 T}{\partial x^2} + \frac{\partial^2 T}{\partial z^2} + \Omega \mu \frac{\partial T}{\partial z} = \delta \frac{(p + \tau_q p^2)}{(1 + \tau_s p)} T \quad (5.9)$$

with $\kappa = \frac{k_{x0}}{k_{z0}}$, and $\delta = \frac{\rho_0 c \rho}{k_{z0}}$. Combing thermal boundary conditions and permeable schemes at crack face ($|x| < c$)

$$T(x, z, 0) = 0$$

$$T(x, h_1, p) = T_0/p$$

$$T(x, -h_2, p) = 0$$

$$\frac{\partial T(x, 0^+, p)}{\partial z} = \frac{\partial T(x, 0^-, p)}{\partial z}, T(x, 0^+, p) = T(x, 0^-, p) \quad |x| \geq c \quad (5.10)$$

- Impermeable crack: $\frac{\partial T(x, 0^+, p)}{\partial z} = \frac{\partial T(x, 0^-, p)}{\partial z} = 0$
- Permeable crack: $\frac{\partial T}{\partial z} = \Theta[T(x, 0^+, p) - T(x, 0^-, p)]$

Solving partial differential equation (PDE) (5.9), after employing Fourier transform, the temperature solutions in the Laplace domain is

$$\begin{aligned} T(x, z, p) &= \frac{1}{2\pi} \int_{-\infty}^{\infty} [D_{11} e^{|s|\lambda_{11}z} + D_{12} e^{|s|\lambda_{21}z}] e^{-isx} ds + F_0 & z > 0 \\ T(x, z, p) &= \frac{1}{2\pi} \int_{-\infty}^{\infty} [D_{21} e^{|s|\lambda_{12}z} + D_{22} e^{|s|\lambda_{22}z}] e^{-isx} ds + F_0 & z < 0 \end{aligned} \quad (5.11)$$

where $\lambda_{1i} = \frac{1}{2} \left(-\frac{\Omega}{|s|} \mu + \tau \right)$, $\lambda_{2i} = \frac{1}{2} \left(-\frac{\Omega}{|s|} \mu - \tau \right)$, $i = 1, 2$ represents upper ($z > 0$) and lower ($z < 0$) domain. $r_1 = \frac{1}{2} (-\Omega + \sqrt{\Omega^2 + 4\omega})$, $r_2 = \frac{1}{2} (-\Omega - \sqrt{\Omega^2 + 4\omega})$ with $\tau =$

$\sqrt{\frac{\Omega^2}{s^2} + 4 \left(\kappa + \frac{\omega}{s^2} \right)}$, $\omega = \delta \frac{(p + \tau q p^2)}{(1 + \tau_s p)}$. Here s is the Fourier transform variable; $D_{ij}(s, p)$ are

unknown functions that can be determined by introducing a density function $G_0(x, p)$

$$G_0(x, p) = \begin{cases} \frac{\partial}{\partial x} \{T^*(x, 0^+, p) - T^*(x, 0^-, p)\} & |x| < c \\ 0 & |x| \geq c \end{cases} \quad (5.12)$$

which satisfies

$$\int_{-c}^c G_0(\xi, p) d\xi = 0 \quad \text{and,} \quad G_0(\xi, p) = 0 \quad |\xi| \geq c \quad (5.13)$$

by using the inverse Fourier transform in Eq. (5.12), and introducing the function $D_0(s, p)$, corresponding to boundary condition Eq. (5.10), the unknown functions $D_{ij}(s, p)$ can be expressed in terms of $D_0(s, p)$:

$$D_{11} = -e^{-|s|h_1\tau} \frac{l_2}{l_0} D_0, \quad D_{12} = \frac{l_2}{l_0} D_0, \quad D_{21} = \frac{l_1}{l_0} D_0, \quad D_{22} = -e^{-|s|h_2\tau} \frac{l_1}{l_0} D_0$$

with $l_1(s, p) = \frac{\lambda_{21}}{\lambda_{12}} - \frac{\lambda_{11}}{\lambda_{12}} e^{-|s|h_1\tau}$, $l_2(s, p) = 1 - \frac{\lambda_{22}}{\lambda_{12}} e^{-|s|h_2\tau}$, $l_0(s, p) = [1 - e^{-|s|h_1\tau}]l_2 - [1 - e^{-|s|h_2\tau}]l_1$. Letting $\bar{\xi} = \xi/c$, $\bar{x} = x/c$, then, the singular equation of $G_0(\xi, p)$ is finally obtained

$$\frac{1}{\pi} \int_{-1}^1 G_0(\bar{\xi}, p) \left[f_0(\bar{x}, \bar{\xi}, p) + \frac{\sqrt{\kappa}}{2c(\bar{\xi} - \bar{x})} \right] d\bar{\xi} = F_0 \quad (5.14)$$

with the kernel function:

$$f_0(\bar{x}, \bar{\xi}, p) = \int_0^\infty \left(- \left[[\lambda_{21} - \lambda_{11} e^{-|s|h_1\tau}] \frac{l_2}{l_0} - \frac{\aleph}{s} \right] - M_0^\infty \right) \sin(cs(\bar{\xi} - \bar{x})) ds$$

According to permeable conditions \aleph defines:

$$\aleph = \begin{cases} 0 & \text{Impermeable crack} \\ \Theta & \text{permeable crack} \end{cases}$$

Furthermore, with the aid of the Lebatto-Chebyshev numerical technique ¹⁶³, the singular Eq. (5.14), is converted into an algebraic equation:

$$\begin{aligned} A_k \sum_{k=1}^n F_p(\bar{\xi}_k, p) \left[f_0(\bar{x}_r, \bar{\xi}_k, p) + \frac{\sqrt{\kappa}}{2c(\bar{\xi}_k - \bar{x}_r)} \right] &= F_0 \quad |\bar{x}| < 1 \\ A_k \sum_{k=1}^n F_p(\bar{\xi}_k, p) &= 0 \end{aligned} \quad (5.15)$$

where $\bar{\xi}_k = \cos \frac{(k-1)\pi}{n-1}$, $k = 1, 2, 3, \dots, n$; $\bar{x}_r = \cos \frac{(2r-1)\pi}{2(n-1)}$, $r = 1, 2, 3, \dots, n-1$; $A_k = \frac{\pi}{2(n-1)}$, $k = 1, n$; $A_k = \frac{\pi}{(n-1)}$, $k = 2, 3, \dots, n-1$ and $F(\bar{\xi}_k, p) = G_0(\bar{\xi}_k, p) \sqrt{1 - \bar{\xi}_k^2}$, $|\bar{x}| < 1$.

In Eq. (5.15), function F_0 corresponds to the temperature components on the x-axis in the absence of the crack, as

$$F_0 = \lambda_{110} D_{110} + \lambda_{210} D_{120} \quad (5.16)$$

with

$$D_{120} = \frac{\left\{ (1 - e^{-\tau_0 h_2}) \frac{\lambda_{110}}{\lambda_{120}} - \left(1 - \frac{\lambda_{220}}{\lambda_{120}} e^{-\tau_0 h_2} \right) \right\} e^{-\lambda_{110} h_1}}{(1 - e^{-\tau_0 h_1}) \left(1 - \frac{\lambda_{220}}{\lambda_{120}} e^{-\tau_0 h_2} \right) - (1 - e^{-\tau_0 h_2}) \left(\frac{\lambda_{210}}{\lambda_{120}} - \frac{\lambda_{110}}{\lambda_{120}} e^{-\tau_0 h_1} \right)} \frac{T_0}{p}$$

$$D_{110} = -e^{-\tau_0 h_1} D_{12} + \frac{T_0}{p} e^{-\lambda_{110} h_1}$$

$$\lambda_{1i0} = \frac{1}{2}(-\Omega\mu + \tau_0), \lambda_{2i0} = \frac{1}{2}(-\Omega\mu - \tau_0); (i = 1, 2)$$

$$\tau_0 = \sqrt{\Omega^2 + 4\omega}$$

After determining the thermal distribution of the strip, Laplace transform is applied to the electro-mechanical field, and the governing Eq. (5.3) and boundary conditions (5.7) change to

$$\begin{aligned} & \left(c_{110} \frac{\partial^2}{\partial x^2} + c_{440} \frac{\partial^2}{\partial z^2} - \rho_0 p^2 + \mu \Omega c_{440} \frac{\partial}{\partial z} \right) u_x + \left(c_{130} \frac{\partial^2}{\partial x \partial z} + c_{440} \frac{\partial^2}{\partial x \partial z} + \mu \Omega c_{440} \frac{\partial}{\partial x} \right) u_z \\ & + \left(d_{310} \frac{\partial^2}{\partial x \partial z} + d_{150} \frac{\partial^2}{\partial x \partial z} + \mu \Omega d_{150} \frac{\partial}{\partial x} \right) \phi = \zeta_{110} e^{\mu \phi z} \frac{\partial T}{\partial x} \\ & \left(c_{130} \frac{\partial^2}{\partial x \partial z} + c_{440} \frac{\partial^2}{\partial x \partial z} + \mu \Omega c_{130} \frac{\partial}{\partial x} \right) u_x + \left(c_{440} \frac{\partial^2}{\partial x^2} + c_{330} \frac{\partial^2}{\partial z^2} - \rho_0 p^2 + \mu \Omega c_{330} \frac{\partial}{\partial z} \right) u_z \\ & + \left(d_{150} \frac{\partial^2}{\partial x^2} + d_{330} \frac{\partial^2}{\partial z^2} + \mu \Omega d_{330} \frac{\partial}{\partial z} \right) \phi = \zeta_{330} e^{\mu \phi z} \left(\frac{\partial T}{\partial z} + \mu \Psi T \right) \end{aligned} \quad (5.17)$$

$$\begin{aligned} & \left(d_{150} \frac{\partial^2}{\partial x \partial z} + d_{310} \frac{\partial^2}{\partial x \partial z} + \mu \Omega d_{310} \frac{\partial}{\partial x} \right) u_x + \left(d_{150} \frac{\partial^2}{\partial x^2} + d_{330} \frac{\partial^2}{\partial z^2} + \mu \Omega d_{330} \frac{\partial}{\partial z} \right) u_z \\ & - \left(\varepsilon_{110} \frac{\partial^2}{\partial x^2} + \varepsilon_{330} \frac{\partial^2}{\partial z^2} + \mu \Omega \varepsilon_{330} \frac{\partial}{\partial z} \right) \phi = p_{z0} e^{\mu \phi z} \left(\frac{\partial T}{\partial z} + \mu \Psi T \right) \end{aligned}$$

$$\begin{aligned} \sigma_{zz}(x, h_1, p) &= \sigma_{zz}(x, -h_2, p) = \frac{\sigma_0}{p} \\ \sigma_{zx}(x, h_1, p) &= \sigma_{zx}(x, -h_2, p) = 0 \\ D_z(x, h_1, p) &= D_z(x, -h_2, p) = \frac{D_0}{p} \\ \sigma_{zz}(x, 0, p) &= \sigma_{zx}(x, 0, p) = 0 & |x| < c \\ \sigma_{zz}(x, 0^+, p) &= \sigma_{zz}(x, 0^-, p), \quad \sigma_{zx}(x, 0^+, p) = \sigma_{zx}(x, 0^-, p) & |x| \geq c \\ D_z(x, 0^+, p) &= D_z(x, 0^-, p), \quad \phi(x, 0^+, p) = \phi(x, 0^-, p) & |x| \geq c \\ u_z(x, 0^+, p) &= u_z(x, 0^-, p), \quad u_x(x, 0^+, p) = u_x(x, 0^-, p) & |x| \geq c \end{aligned} \quad (5.18)$$

- Impermeable crack: $D_z(x, 0^+, p) = D_z(x, 0^-, p) = 0 \quad |x| < c$
- Permeable crack: $D_z(x, 0^+, p) = D_z(x, 0^-, p), \quad \phi_z(x, 0^+, p) = \phi_z(x, 0^-, p) \quad |x| < c$

By further applying Fourier transform, a calculation leads to the expressions for the displacements and electric potential in the Laplace transform domain.

$$\begin{aligned}
 u_{xi}(x, z, p) &= i \operatorname{sgn}(s) \frac{1}{2\pi} \int_{-\infty}^{+\infty} \left\{ \sum_{j=1}^6 Z_{j1i} A_{ij} e^{|s|\gamma_{ji}z} \right. \\
 &\quad \left. + \frac{1}{|s|} \left(P_{x1i} D_{i1} e^{|s|(\lambda_{1i} + \mu \frac{\varphi}{|s|})z} + P_{x2i} D_{i2} e^{|s|(\lambda_{2i} + \mu \frac{\varphi}{|s|})z} \right) \right\} e^{-isx} ds \\
 u_{zi}(x, z, p) &= \frac{1}{2\pi} \int_{-\infty}^{+\infty} \left\{ \sum_{j=1}^6 Z_{j2i} A_{ij} e^{|s|\gamma_{ji}z} \right. \\
 &\quad \left. + \frac{1}{|s|} \left(P_{z1i} D_{i1} e^{|s|(\lambda_{1i} + \mu \frac{\varphi}{|s|})z} + P_{z2i} D_{i2} e^{|s|(\lambda_{2i} + \mu \frac{\varphi}{|s|})z} \right) \right\} e^{-isx} ds \quad (5.19)
 \end{aligned}$$

$$\begin{aligned}
 \phi_{zi}(x, z, p) &= \frac{1}{2\pi} \int_{-\infty}^{+\infty} \left\{ \sum_{j=1}^6 A_{ij} e^{|s|\gamma_{ji}z} \right. \\
 &\quad \left. + \frac{1}{|s|} \left(P_{\phi 1i} D_{i1} e^{|s|(\lambda_{1i} + \mu \frac{\varphi}{|s|})z} + P_{\phi 2i} D_{i2} e^{|s|(\lambda_{2i} + \mu \frac{\varphi}{|s|})z} \right) \right\} e^{-isx} ds
 \end{aligned}$$

Here $i = 1, 2$ indicates the region $z > 0$ and $z < 0$; γ_{ji} ($j = 1, 2, 3, \dots, 6$) are the roots of the following characteristic equation (all the coefficients are shown in Appendix C Eq. (C.1))

$$a\gamma^6 + b\gamma^5 + c\gamma^4 + d\gamma^3 + e\gamma^2 + f\gamma + g = 0$$

and $Z_{jli}(s, p)$ and $P_{xli}, P_{zli}, P_{\phi l}$, ($l = 1, 2$) are given in the Appendix C as Eq. (C.2).

Then the stresses and electric displacements can be obtained by making use of Eqs. (5.2) and (5.11)

$$\begin{aligned}
 \sigma_{zxi} &= i \operatorname{sgn}(s) \frac{1}{2\pi} \int_{-\infty}^{+\infty} \left\{ \sum_{j=1}^6 |s| \chi_{ji}^{zx} A_{ij} e^{|\lambda_{ji} + \mu \frac{\Omega}{|s|}|z} \right. \\
 &\quad \left. - \left\{ P_{1i}^{zx} D_{i1} e^{|\lambda_{1i} + \mu \frac{\varphi}{|s|} + \mu \frac{\Omega}{|s|}|z} + P_{2i}^{zx} D_{i2} e^{|\lambda_{2i} + \mu \frac{\varphi}{|s|} + \mu \frac{\Omega}{|s|}|z} \right\} \right\} e^{-isx} ds \\
 \sigma_{zzi} &= \frac{1}{2\pi} \int_{-\infty}^{+\infty} \left\{ \sum_{j=1}^6 |s| \chi_{ji}^{zz} A_{ij} e^{|\lambda_{ji} + \mu \frac{\Omega}{|s|}|z} \right. \\
 &\quad \left. - \left\{ P_{1i}^{zz} D_{i1} e^{|\lambda_{1i} + \mu \frac{\varphi}{|s|} + \mu \frac{\Omega}{|s|}|z} + P_{2i}^{zz} D_{i2} e^{|\lambda_{2i} + \mu \frac{\varphi}{|s|} + \mu \frac{\Omega}{|s|}|z} \right\} \right\} e^{-i} ds + \sigma_{zzi0} \quad (5.20)
 \end{aligned}$$

$$\begin{aligned}
 D_{zi} &= \frac{1}{2\pi} \int_{-\infty}^{+\infty} \sum_{j=1}^6 |s| \chi_{ji}^{dz} A_{ij} e^{|\lambda_{ji} + \mu \frac{\Omega}{|s|}|z} \\
 &\quad - \left\{ P_{1i}^{dz} D_{i1} e^{|\lambda_{1i} + \mu \frac{\varphi}{|s|} + \mu \frac{\Omega}{|s|}|z} + P_{2i}^{dz} D_{i2} e^{|\lambda_{2i} + \mu \frac{\varphi}{|s|} + \mu \frac{\Omega}{|s|}|z} \right\} e^{-isx} ds + D_{zi}
 \end{aligned}$$

where coefficients $\chi_{ji}^{str}(s, p)$ ($str = zz, zx, dz$) and P_{li}^{str} ($l = 1, 2$) are expressed in Appendix C as Eqs. (C.3) and (C.4).

Submitting the stress and electric displacement expression (5.20) into boundary conditions (5.17), the unknown functions A_{ij} can be expressed by the independent unknowns $A_{2k}(s, p)$ ($k = 4, 5, 6$)

$$A_{ij}(s, p) = \frac{1}{|s|} P_{ij} D_0 + \sum_{k=4}^6 K_k^{ij} A_{2k}$$

where P_{ij} and K_k^{ij} are solved using MATLAB code. Furthermore, the density functions $G_f(x, p)$ ($f = 1, 2, 3$) are introduced to get the solutions of $A_{2k}(s, p)$, as follows

$$\begin{aligned} G_1(x, p) &= \frac{\partial}{\partial x} \left\{ u_{x1}(x, 0^+, p) - u_{x1}(x, 0^-, p) \right\} \\ G_2(x, p) &= \frac{\partial}{\partial x} \left\{ u_{z1}(x, 0^+, p) - u_{z1}(x, 0^-, p) \right\} \\ G_3(x, p) &= \frac{\partial}{\partial x} \left\{ \phi_2(x, 0^-, p) - \phi_1(x, 0^+, p) \right\} \end{aligned} \quad |x| < c$$

After making use of boundary conditions (5.17) and permeable conditions at $|x| < c$, letting $\bar{\xi} = \xi/c$, $\bar{x} = x/c$, normalized crack length $(-c, c)$ to $(-1, 1)$, the density functions $G_f(x, p)$ can be solved through the following simultaneous singular equations

$$\begin{aligned} \frac{1}{\pi} \int_{-1}^1 \left\{ f_1^{zz} G_1(\bar{\xi}, p) - \left(f_2^{zz} + \frac{\lim_{s \rightarrow \infty} \kappa_2^{zz}}{c(\bar{\xi} - \bar{x})} \right) G_2(\bar{\xi}, p) + \left(f_3^{zz} + \frac{\lim_{s \rightarrow \infty} \kappa_3^{zz}}{c(\bar{\xi} - \bar{x})} \right) G_3(\bar{\xi}, p) \right\} d\bar{\xi} \\ = -\sigma_{zzi0} + \frac{1}{2\pi} \int_{-\infty}^{+\infty} \left\{ \kappa_0^{zz} \left(\frac{1}{is} \int_{-1}^1 G_0(\bar{\xi}, p) e^{is\xi} d\bar{\xi} \right) \right\} e^{-i} ds \\ \frac{1}{\pi} \int_{-1}^1 \left\{ - \left(f_1^{zx} + \frac{\lim_{s \rightarrow \infty} \kappa_1^{zx}}{c(\bar{\xi} - \bar{x})} \right) G_1(\bar{\xi}, p) - f_2^{zx} G_2(\bar{\xi}, p) + f_3^{zx} G_3(\bar{\xi}, p) \right\} d\bar{\xi} \\ = \frac{1}{2\pi} \int_{-\infty}^{+\infty} \left\{ \kappa_0^{zx} \left(\frac{1}{|s|} \int_{-1}^1 G_0(\bar{\xi}, p) e^{is\xi} d\bar{\xi} \right) \right\} e^{-isx} ds \end{aligned} \quad (5.21)$$

$$\begin{aligned} \frac{1}{\pi} \int_{-1}^1 \left\{ f_1^{dz} G_1(\bar{\xi}, p) - \left(f_2^{dz} + \frac{\lim_{s \rightarrow \infty} \kappa_2^{dz}}{c(\bar{\xi} - \bar{x})} \right) G_2(\bar{\xi}, p) + \left(f_3^{dz} + \frac{\lim_{s \rightarrow \infty} \kappa_3^{dz}}{c(\bar{\xi} - \bar{x})} \right) G_3(\bar{\xi}, p) \right\} d\bar{\xi} \\ = -D_{zi0} + \frac{1}{2\pi} \int_{-\infty}^{+\infty} \left\{ \kappa_0^{dz} \left(\frac{1}{is} \int_{-1}^1 G_0(\bar{\xi}, p) e^{is\xi} d\bar{\xi} \right) \right\} e^{-isx} ds \end{aligned}$$

where the constants f_t^{str} ($str = zz, zx, dz; t = 1, 2, 3$) are

$$f_t^{str} = \begin{cases} \int_0^{+\infty} \left[\kappa_t^{str} \cos \left(cs(\bar{\xi} - \bar{x}) \right) \right] ds & \text{if } str = zz, dz; t = 1 \\ \int_0^{+\infty} \left[\kappa_t^{str} \sin \left(cs(\bar{\xi} - \bar{x}) \right) \right] ds & \text{if } str = zx, dz; t = 2,3 \\ \int_0^{+\infty} \left[\left(\kappa_t^{str} - \lim_{s \rightarrow \infty} \kappa_t^{str} \right) \sin \left(cs(\bar{\xi} - \bar{x}) \right) \right] ds & \text{if } str = zz, dz; t = 2,3 \\ \int_0^{+\infty} \left[\left(\kappa_t^{str} - \lim_{s \rightarrow \infty} \kappa_t^{str} \right) \cos \left(cs(\bar{\xi} - \bar{x}) \right) \right] ds & \text{if } str = zx, dz; t = 1 \end{cases}$$

where constants κ_t^{str} ($str = zz, zx, dz; t = 1,2,3,0$) are given in Appendix C Eq. (C.5). Similar to the procedure for solving the temperature field, the singular integral equation (5.21) can be transformed into

$$\begin{aligned} A_i \sum_{k=1}^n \left\{ f_1^{zz} F_1(\bar{\xi}_k, p) - \left(f_2^{zz} + \frac{\lim_{s \rightarrow \infty} \kappa_2^{zz}}{c(\bar{\xi} - \bar{x})} \right) F_2(\bar{\xi}_k, p) + \left(f_3^{zz} + \frac{\lim_{s \rightarrow \infty} \kappa_3^{zz}}{c(\bar{\xi} - \bar{x})} \right) F_3(\bar{\xi}_k, p) \right\} \\ = -\sigma_{zz0} + \frac{1}{2\pi} \int_{-\infty}^{+\infty} \left\{ \kappa_0^{zz} \left(\frac{1}{is} \int_{-1}^1 G_0(\bar{\xi}, p) e^{is\xi} d\bar{\xi} \right) \right\} e^{-isx} ds \end{aligned}$$

$$\begin{aligned} A_i \sum_{k=1}^n \left\{ - \left(f_1^{zx} + \frac{\lim_{s \rightarrow \infty} \kappa_1^{zx}}{c(\bar{\xi} - \bar{x})} \right) F_1(\bar{\xi}_k, p) - f_2^{zx} F_2(\bar{\xi}_k, p) + f_3^{zx} F_3(\bar{\xi}_k, p) \right\} \\ = \frac{1}{2\pi} \int_{-\infty}^{+\infty} \left\{ \kappa_0^{zx} \left(\frac{1}{|s|} \int_{-1}^1 G_0(\bar{\xi}, p) e^{is\xi} d\bar{\xi} \right) \right\} e^{-isx} ds \end{aligned}$$

$$\begin{aligned} A_i \sum_{k=1}^n \left\{ f_1^{dz} F_1(\bar{\xi}_k, p) - \left(f_2^{dz} + \frac{\lim_{s \rightarrow \infty} \kappa_2^{dz}}{c(\bar{\xi} - \bar{x})} \right) F_2(\bar{\xi}_k, p) + \left(f_3^{dz} + \frac{\lim_{s \rightarrow \infty} \kappa_3^{dz}}{c(\bar{\xi} - \bar{x})} \right) F_3(\bar{\xi}_k, p) \right\} \\ = -D_{z0} + \frac{1}{2\pi} \int_{-\infty}^{+\infty} \left\{ \kappa_0^{dz} \left(\frac{1}{is} \int_{-1}^1 G_0(\bar{\xi}, p) e^{is\xi} d\bar{\xi} \right) \right\} e^{-isx} ds \end{aligned}$$

where $F_f(\bar{\xi}_k, p) = G_f(\bar{\xi}_k, p) \sqrt{1 - \bar{\xi}_k^2}$ ($f = 1,2,3$).

The functions σ_{zz} and D_{z0} , which correspond to the stress and electric displacement components on the x-axis in the absence of the crack, are obtained as follows

$$\begin{aligned}
 \sigma_{zzi0} &= \int_{-\infty}^{+\infty} \left(\sum_{j=1}^3 \chi_{ji}^{zz} A_{1j} e^{(\gamma_{ji} + \mu\Omega)z} \right. \\
 &\quad \left. - \frac{T_0}{p} \{ P_{1i}^{zz} D_{i10} e^{(\lambda_{1i0} + \mu\varphi + \mu\Omega)z} + P_{2i}^{zz} D_{i20} e^{(\lambda_{2i0} + \mu\varphi + \mu\Omega)z} \} \right) \delta(s) ds \\
 &= \sum_{j=1}^3 \chi_{jis}^{zz} A_{1j} e^{(\gamma_{jis} + \mu\Omega)z} - \frac{T_0}{p} \{ P_{1i0}^{zz} D_{i1} e^{(\lambda_{1i0} + \mu\varphi + \mu\Omega)z} + P_{2i0}^{zz} D_{i20} e^{(\lambda_{2i0} + \mu\varphi + \mu\Omega)z} \}
 \end{aligned}$$

$$\begin{aligned}
 D_{zi} &= \int_{-\infty}^{+\infty} \left(\sum_{j=1}^3 \chi_{ji}^{dz} A_{1j} e^{(\gamma_{jis} + \mu\Omega)z} \right. \\
 &\quad \left. - \frac{T_0}{p} \{ P_{1i}^{dz} D_{i1} e^{(\lambda_{1i0} + \mu\varphi + \mu\Omega)z} + P_{2i}^{dz} D_{i2} e^{(\lambda_{2i0} + \mu\varphi + \mu\Omega)z} \} \right) \delta(s) ds \\
 &= \sum_{j=1}^3 \chi_{jis}^{dz} A_{1j} e^{(\gamma_{jis} + \mu\Omega)z} - \frac{T_0}{p} \{ P_{1i0}^{dz} D_{i10} e^{(\lambda_{1i0} + \mu\varphi + \mu\Omega)z} + P_{2i0}^{dz} D_{i20} e^{(\lambda_{2i0} + \mu\varphi + \mu\Omega)z} \}
 \end{aligned}$$

Based on the inverse Fourier transform and the property of the Dirac delta function

$$\int_{-\infty}^{+\infty} F(s) \delta(s) ds = F(s = 0)$$

where $\chi_{jis}^{str}, P_{li}^{str}$ ($str = zz, dz$) are equal to $\chi_{ji}^{str}, P_{li}^{str}$, when $s = 0$. and γ_{jis} are

$$\gamma_{1is} = \frac{1}{2} \left(-\mu\Omega - \sqrt{\Omega^2 + \omega_0} \right), \gamma_{2i} = \frac{1}{2} \left(-\mu\Omega + \sqrt{\Omega^2 + \omega_0} \right), \gamma_{3is} = -\mu\Omega$$

Therefore, the stress intensity factors $K_I(p)$, $K_{II}(p)$ and the electric displacement intensity factor $K_D(p)$ in the Laplace domain are:

$$K_I(p) = \lim_{x \rightarrow c^+} \sqrt{2\pi(x-c)} \sigma_{zzi}(x, 0, p)$$

$$K_{II}(p) = \lim_{x \rightarrow c^+} \sqrt{2\pi(x-c)} \sigma_{zxi}(x, 0, p)$$

$$K_D(p) = \lim_{x \rightarrow c^+} \sqrt{2\pi(x-c)} D_{zi}(x, 0, p)$$

5.4 Numerical results and Discussions

In order to obtain the solutions in the time domain, the numerical inversion of the Laplace transform proposed by Miller and Guy¹⁶⁵ is employed. All the results were presented in dimensionless form with: $\bar{h} = h/c$ and time $\bar{t} = tc_n/c$ where $c_n = \sqrt{c_{44}/\rho}$. To indicate the ratio between the mechanical, electrical and thermal impacts, the dynamic stress and electric displacement intensity factors (DSIFs) are normalized as follows

- Single temperature and multiphysical condition

$$\bar{K}_I(t) = \frac{K_I(t)}{f\sqrt{\pi c}}, \quad \bar{K}_{II}(t) = \frac{K_{II}(t)}{f\sqrt{\pi c}}, \quad \bar{K}_D(t) = \frac{\zeta_{330} K_I(t)}{p_{z0} f\sqrt{\pi c}} \quad (5.22)$$

where $f = \zeta_{330}|T_0|$.

- Single mechanical and electrical condition

$$\bar{K}_I(t) = \frac{K_I(t)}{f\sqrt{\pi c}}, \quad \bar{K}_{II}(t) = \frac{K_{II}(t)}{f\sqrt{\pi c}}, \quad \bar{K}_D(t) = \frac{d_{330} K_I(t)}{\varepsilon_{330} f\sqrt{\pi c}} \quad (5.23)$$

for pure mechanical condition, $f = \sigma_0$

for pure electrical condition, $f = \frac{d_{330}}{\varepsilon_{330}} D_0$.

The stresses and electric displacement (σ_{ij}, D_i) were normalized following the same procedure as

DSIFs. In the following sections, the normalized hat " $\bar{\quad}$ " is omitted for the sake of brevity.

5.4.1 Model reliability

To verify the accuracy and validity of the numerical results, we considered the case of a strip with a central crack, where $h_1/c = h_2/c = 2.5$ and $\Omega = \varphi = 0$ (Non – FGPM), to check the following boundary conditions of the strip under thermo-electro-mechanical loading. The calculations are carried out for three different piezoelectric materials, whose constants are given in Table 5.1.

Boundary conditions (BCs: $\sigma_0 = D_0 = T_0 = 1$):

at strip surface:	at the crack surface:
BC1: $\sigma_{zz}(x, h_1, t) = \sigma_{zz}(x, -h_2, t) = \sigma_0$	BC4: $\sigma_{zz}(x, 0, t) = 0$
BC2: $\sigma_{zx}(x, h_1, t) = \sigma_{zx}(x, -h_2, t) = 0$	BC5: $\sigma_{zx}(x, 0, t) = 0$
BC3: $D_z(x, h_1, t) = D_z(x, -h_2, t) = D_0$	BC6: $D_z(x, 0^+, t) = D_z(x, 0^-, t)$

- Impermeable crack: $\Theta = 0$, $D_z(x, 0^+, t) = D_z(x, 0^-, t) = 0$
- Permeable crack: $\Theta = 0.5$, $D_z(x, 0^+, t) = D_z(x, 0^-, t)$, $\phi_z(x, 0^+, t) = \phi_z(x, 0^-, t)$

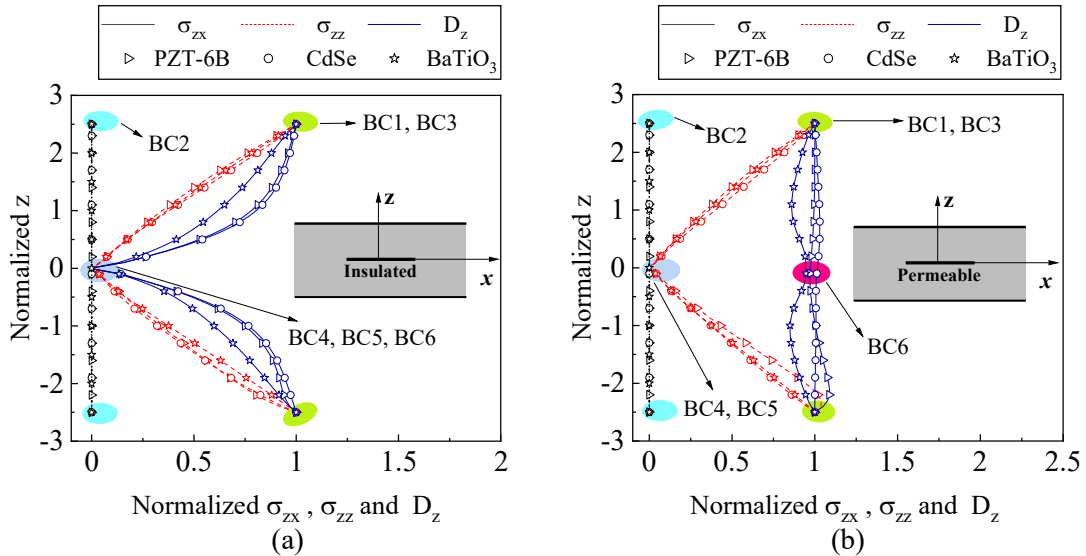


Figure 5. 3 Boundary conditions under thermo-electro-mechanical loading stresses and D_z variations (a)

insulted crack; (b) permeable crack along thickness ($x = 0$). ($\bar{t} = 1$)

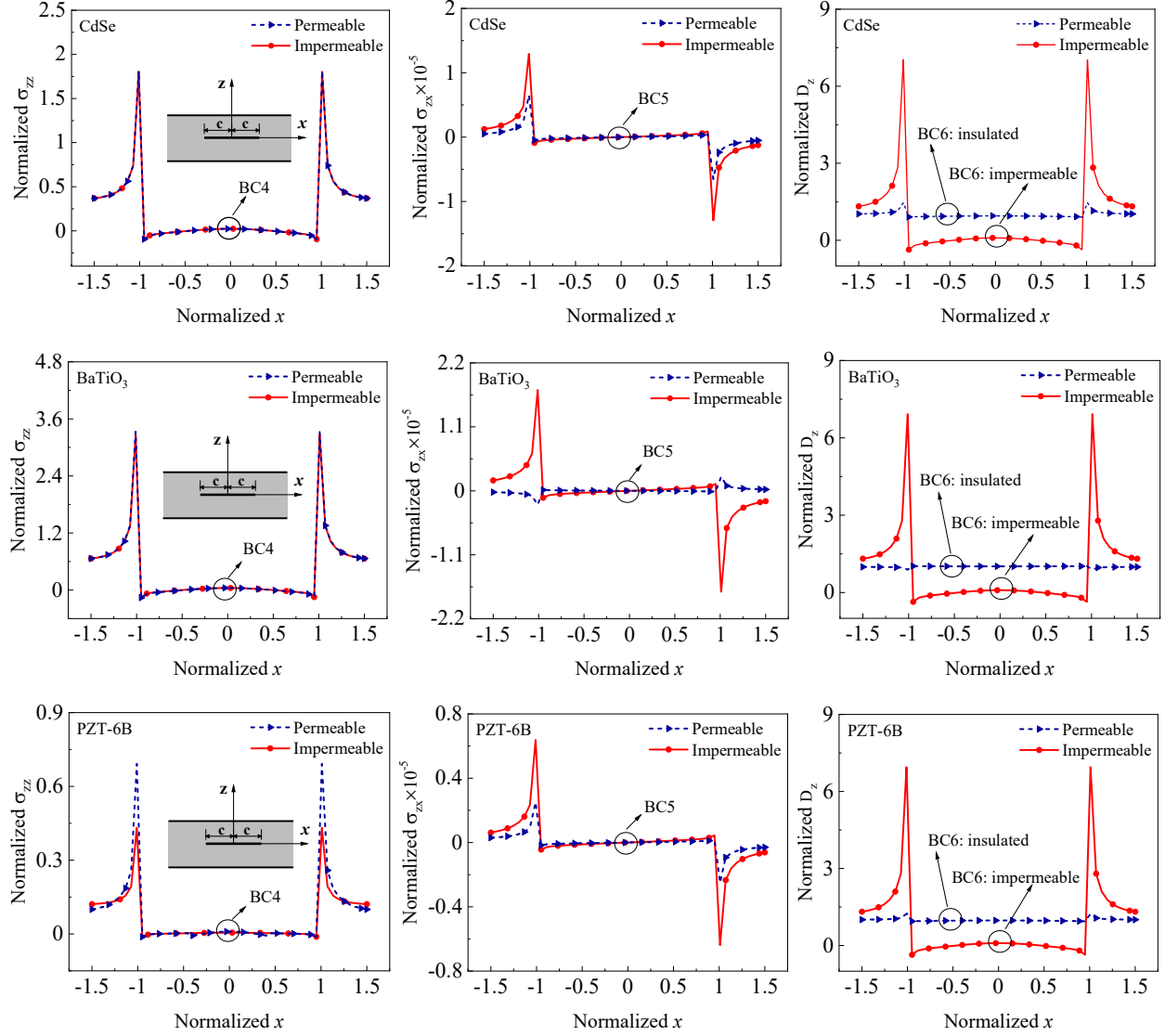


Figure 5. 4 Boundary conditions under thermo-electro-mechanical loading: stresses and D_z variations at the crack surface and extended line ($z = 0$). ($\bar{t} = 1$)

Table 5. 1 Material properties of homogeneous piezoelectric ceramics.

	Elastic stiffnesses ($\times 10^{10} \text{N/m}^2$)				Piezoelectric coefficients (C/m^2)			Dielectric constants ($\times 10^{-10} \text{C/Vm}$)		Thermal Modulus ($\times 10^6 \text{N/Km}^2$)		Pyroelectric coefficients ($\times 10^{-7} \text{C/Km}^2$)	Specific heat ($\text{J/kg}^\circ\text{C}$)	Density ($\times 10^3 \text{kg/m}^3$)
	c_{110}	c_{130}	c_{330}	c_{440}	d_{310}	d_{330}	d_{150}	ϵ_{110}	ϵ_{330}	ζ_{110}	ζ_{330}	p_{z0}	c_p	ρ_0
PZT-6B	16.80	6.00	16.30	2.71	-0.90	7.10	4.60	36	34	2.02	1.98	3700	420	7.60
CdSe	7.41	3.93	8.36	1.32	-0.16	0.35	-0.14	0.83	0.90	0.62	0.55	29.4	490	5.81
BaTiO ₃	22.20	2.40	19.80	3.30	-0.21	0.31	-0.48	0.51	0.45	2.02	3.76	1200	430	5.80

By examining the variations of stresses and electric displacement along the thickness direction (z -axis) as shown in Figure 5.3, and along the x -axis as shown in Figure 5.4, all the boundary conditions have been satisfied. The stresses σ_{zz} , σ_{zx} and electric displacement D_z conform to the applied loadings at the surfaces of the strip (Figure 5.3), and correspondingly meet the requirements for different electric permeable conditions at the crack surface, which should be equal to zero because no electricity is allowed to cross the crack for insulated crack (Figure 5.3a), whereas electric field is continuous at the crack surface for permeable condition (Figure 5.3b). Moreover, considering the free surface of crack, all the stresses should be zero (Figure 5.4). And the stresses are singular near the crack tip which tends to infinite. Therefore, the numerical results are reliable and can be used for further research.

Considering electrically conditions in Figure 5.5, the singular behavior (the value of DSIFs) near the crack tips of impermeable crack is much more pronounced than permeable crack, which is easier to trigger crack and deserve further research. Therefore, in the following discussions, we choose an insulated crack condition and pick PZT-6B as an example.

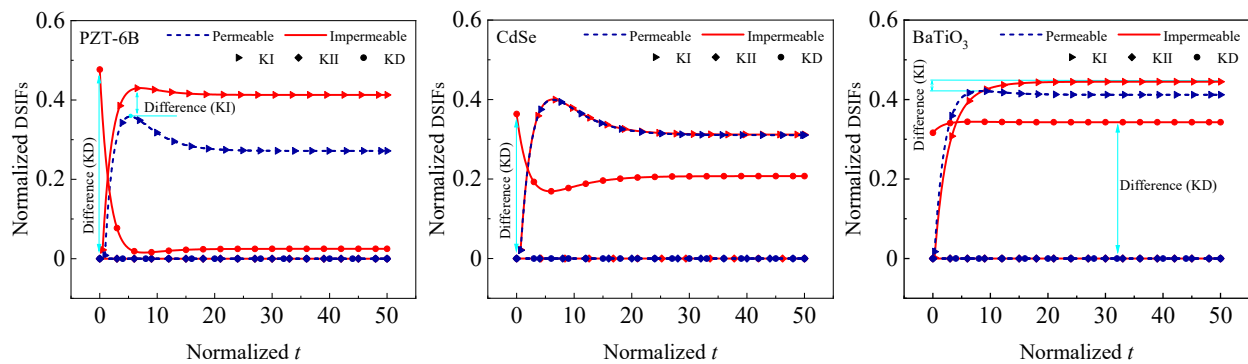


Figure 5. 5 Normalized DSIFs variation of permeable and impermeable crack conditions.

5.4.2 Functional gradient piezoelectric material (FGPM) design

At the macroscale, a functionally graded piezoelectric material was investigated with its properties varying along the thickness based on different gradation functions (Figure 5.6). By controlling the functional gradients parameter μ and gradation coefficients Ω , and Ψ in Eq. (5.1), the profile of the materials along the gradating direction can be changed. Here, we proposed three distinct configurations of FGPM to study the effect of different functional gradient laws on material performance under different physical scenarios. The first configuration is characterized by $\Omega = \Psi = 0$, $\mu = 1$, representing a homogeneous material without gradient. In the second configuration, with $\Omega = \Psi = 1$, $\mu = 1$, the material properties vary exponentially along the thickness direction (z -direction) over the cross-section, gradually decreasing from the upper surface to the lower surface. Finally, the third configuration, with $\Omega = \Psi = 1$, $\mu = \text{sgn}(z)$, demonstrates a symmetric graded property over the thickness.

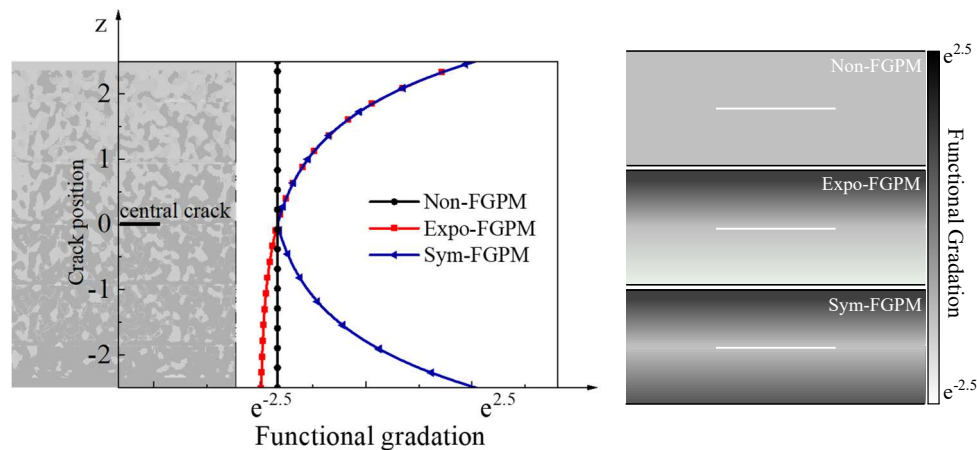


Figure 5. 6 Sketch of functionally graded piezoelectric material (FGPM).

Sketch 1: $\Omega = \Psi = 0$, $\mu = 1$ Nongraded-FGPM (Non-FGPM)

Sketch 2: $\Omega = \Psi = 1$, $\mu = 1$ Exponential-FGPM (Expo-FGPM)

Sketch 3: $\Omega = \Psi = 1$, $\mu = \text{sgn}(z)$ Symmetric-FGPM (Sym-FGPM)

5.4.3 FGPM design under a single physical field

(1) Single dynamic mechanical loading

Figure 5.7 illustrates a comparative analysis of dynamic stress and electric displacement intensity factors under a single mechanical loading condition. In particular, the central-crack strip is subjected to a normalized tensile stress impact, $\sigma_0 H(t)$, and $\sigma_0 = 1$. It is obvious that under a single tensile load, the dynamic stresses and electric displacement intensity factors (DSIFs) rapidly increase over time, reaching a peak ($N_j, E_j, S_j, j=1,2,3$) and then decreasing in magnitude and eventually converging towards the static value for a sufficiently long time. For exponential, functionally graded piezoelectric material (Expo-FGPM), the DSIFs are notably higher compared to those of the non-functionally graded piezoelectric material (Non-FGPM) and symmetric functionally graded piezoelectric material (Sym-FGPM). This discrepancy can be attributed to the presence of dissimilar layers at the interface of the crack surface in the Expo-FGPM, leading to an initiation of an interface crack.

Especially, since the configuration and applied mechanical load of Non-FGPM and Sym-FGPM are symmetric, no shearing stress is induced, resulting in a zero KII value throughout the entire time duration. When comparing the Non-FGPM and Sym-FGPM, it is evident that the symmetric configuration exhibits a lower intensity than the non-graded configuration. Therefore, the symmetric configuration provides greater fracture safety under single mechanical loading, while the exponential design presents the highest level of risk of fracture.

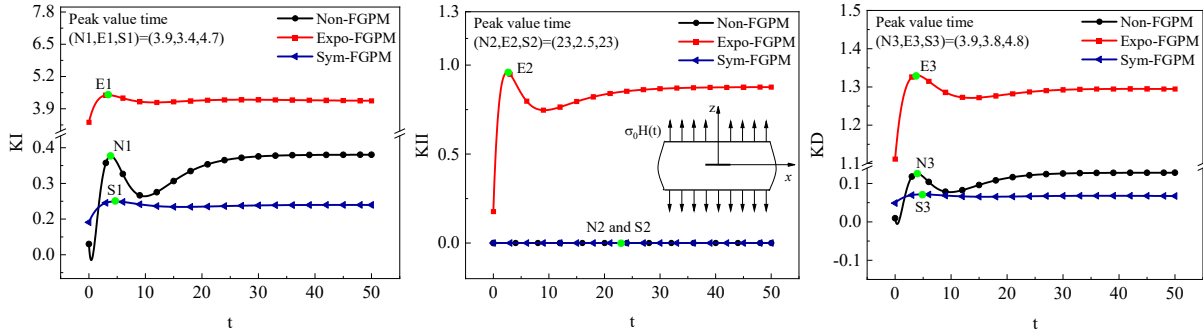


Figure 5. 7 DSIFs versus time under a single mechanical field.

(2) Single dynamic electrical loading

In the case of pure electric loading, a step electrical load, $D_0H(t)$ with $D_0 = 1$, is applied on the strip, where the positive poling direction is along the z-axis. Similar trends are also observed in the resulted electric field. The DSIFs climb to a peak value and then gradually tend to a stable value. The Expo-FGPM demonstrates the highest values of the dynamic stress intensity factors (DSIFs) as depicted in Figure 5.8. Due to the symmetric electric load and configuration, both Non-FGPM and Sym-FGPM exhibit a shearing stress intensity factor KII of zero.

Another intriguing observation is the negative electric displacement intensity factor in the asymmetric exponential configuration when compared to the symmetric configuration for PZT-6B. This indicates a change in the direction of electric displacement around the crack tip after altering the material configuration. In the case of Non-FGPM, the electric response near the crack tip is expected to decrease or become more in magnitude in the negative side due to the piezoelectric coefficients and dielectric properties of PZT-6B. However, the unique characteristics of the exponential, functional grading, with piezoelectric properties decreasing exponentially from the upper to the lower surface, lead to an increasingly larger and positive electric displacement intensity factor. These findings further highlight the enhanced reliability of the symmetric graded

design, emphasizing that Sym-FGPM and Non-FGPM are safer than Expo-FGPM under single electric loading conditions.

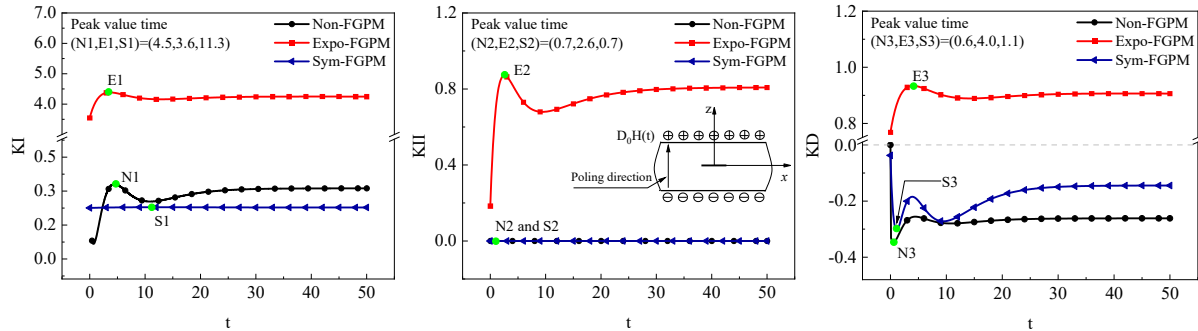


Figure 5. 8 DSIFs versus time under a single electrical field.

(3) Single dynamic Thermal loading

Another important task is the analysis of the temperature distribution of piezoelectric material, which is computed by using Eq. (11) and presented in Fig. 9 (a). In this analysis, a heat shock is applied to the top surface of the strip with $T_0 H(t)$, where $T_0 = 1$, and keep a temperature near zero on the lower surface. It can be observed that for both Non-FGPM and Sym-FGPM, the temperature decreases symmetrically from the upper to the lower surface, with the temperature gradients being higher for Sym-FGPM. Conversely, the temperature distribution gradually decreases from top to bottom as the configuration of Expo-FGPM changes.

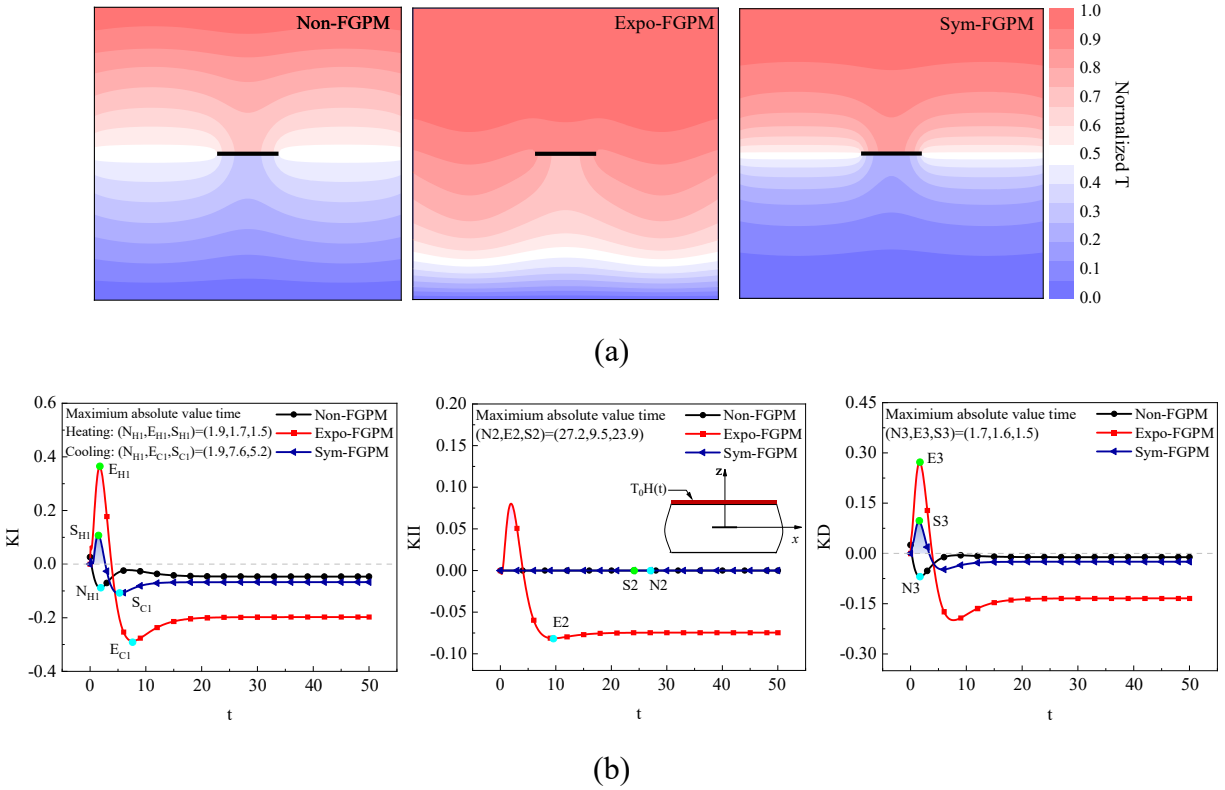


Figure 5. 9 Thermal distribution and DSIFs: (a) stable temperature distribution at $t=50s$; (b) DSIFs versus time under a single thermal field.

Distinguishing from the single stress and single electric field scenarios, the DSIFs of Expo-FGPM and Sym-FGPM exhibit notable fluctuations during the initial stages under single thermal loading. This behavior can be attributed to the non-Fourier heat wave phenomenon, which is further amplified by the nonhomogeneous graded material. Unlike KII and KD, where positive and negative values indicate respective crack propagation in different directions, a positive KI indicates a propensity for crack initiation, while a negative KI suggests the potential for crack closure and enhanced safety. Regarding the KI values depicted in Figure 5.9 (b), it is noteworthy that graded materials such as Expo-FGPM and Sym-FGPM exhibit two distinct peak points with different signs: positive values for E_{H1} and S_{H1} , and negative values for E_{C1} and S_{C1} . Under heating conditions, the material is susceptible to failure at E_{H1} and S_{H1} points, while it is deemed safe at

E_{C1} and S_{C1} points. Conversely, when the boundary loading conditions are altered to cooling, the observed trends are reversed entirely. Moreover, the magnitudes of E_{C1} , S_{C1} and E_{H1} , S_{H1} are different, highlighting the necessity to consider two different thermal conditions: cooling and heating.

Additionally, when comparing the three different configurations under thermal loading, the DSIFs of the homogeneous non-FGPM are consistently lower than those of the inhomogeneous Expo-FGPM and Sym-FGPM. Consequently, for a single thermal load and under the same gradation coefficients, the non-FGPM is the preferred choice, as the inhomogeneous material properties amplify temperature disturbances and lead to higher stress intensity factors.

5.4.4 Fracture evaluation of FGPM under Single field

It is important to note that the field intensity factors discussed above solely provide information regarding the respective field quantities on the crack face plane. As a result, the decoupled field intensity factors alone are insufficient to establish a fracture criterion for the crack problem addressed in this study. To assess the coupled fracture performance of the material, Dascalu²⁶⁵ and Fang⁹³ separately proposed an energy release rate G and critical intensity factor K_C as

$$\begin{cases} G(t) = \frac{1}{4} \{K\}^T \mathbf{H}^{-1} \{K\} \\ K_C(t) = K_I + \frac{(\mathbf{H}^{-1})_{|2,3|}}{(\mathbf{H}^{-1})_{|2,2|}} K_D \end{cases} \quad (5.24)$$

where $\{K\} = \{K_I^*(p) \quad K_{II}^*(p) \quad K_D^*(p)\}^T$.

To determine which fracture criterion is more suitable for our specific problem, we conducted an examination using Non-FGPM under a single thermal load as the test case. We employed the energy release rate G and the critical intensity factor K_C , respectively, to evaluate the single normal stress intensity factor K_I at the peak point NH1. From the results shown in Figure 5.10, it is evident that under the G criterion, the results consistently yield positive values regardless of the heating or cooling conditions. However, as we have already observed in Figure 5.9 (b) when considering only the K_I of Non-FGPM, since its value is negative, indicating crack closure during cooling and positive, indicating crack propagation in heating. In comparison, the K_C intensity factor accurately captures this difference, with the value turning negative upon entering the heating condition. Therefore, we employ the K_C intensity factor to evaluate the coupled field intensity factor in this study.

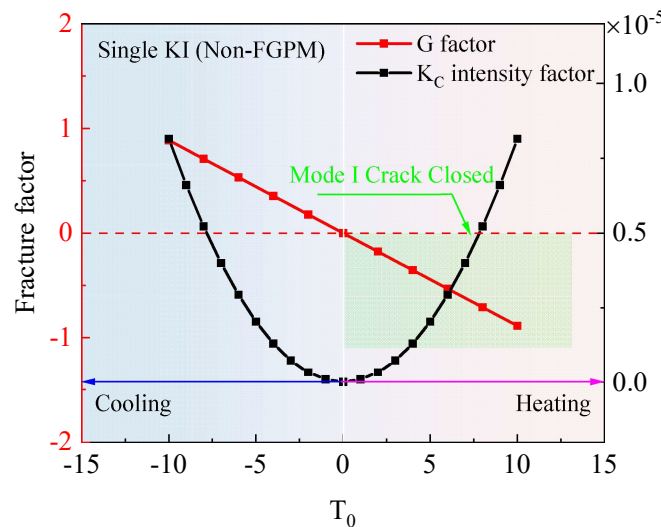


Figure 5. 10 Fracture criteria comparison.

In the context of our study, it is worth noting that the electric displacement near the crack tip can exhibit direction changes, which consequently result in a negative value of electric displacement intensity factor (K_D). According to the definition proposed by Fang⁹³, in Eq. (5.24),

the coefficient of $\frac{(\mathbf{H}^{-1})_{|2,3|}}{(\mathbf{H}^{-1})_{|2,2|}}$ for piezoelectric ceramics is positive, and the negative value of K_D will lead to a smaller value for the critical intensity factor and shift the fracture performance of material towards the safer side. However, it is important to acknowledge that even with a negative K_D , the material can still be susceptible to crack propagation, albeit in a different direction influenced by the electric displacement. Therefore, building upon Fang's definition, we have improved K_C by introducing the absolute value of K_D as

$$K_C(t) = K_I + \frac{(\mathbf{H}^{-1})_{|2,3|}}{(\mathbf{H}^{-1})_{|2,2|}} |K_D| \quad (5.25)$$

here the matrix \mathbf{H} is normalized according to Eqs. (5.22) and (5.23), which is expressed as

$$\mathbf{H} = \begin{bmatrix} -\lim_{s \rightarrow \infty} \kappa_1^{zx} / f & 0 & 0 \\ 0 & -\lim_{s \rightarrow \infty} \kappa_2^{zz} / f & \lim_{s \rightarrow \infty} \kappa_3^{zz} / f \\ 0 & -\lim_{s \rightarrow \infty} \kappa_2^{dz} / f & \lim_{s \rightarrow \infty} \kappa_3^{dz} / f \end{bmatrix}$$

As the gradation coefficients Ω and Ψ in the above sections were defined as $\Omega=\Psi=1$, to further explore the impact of these coefficients on the different material configurations, the gradation coefficients Ω and Ψ vary to -1.0, -0.5, 0.5 and 1.0. And then the results of critical intensity factor K_C for the three configurations under both single mechanical and single electrical fields are compared. The corresponding results are shown in Figure 5.11. Since all the critical stress intensity factors K_C stabilize after $t=10$, the figure only displays the K_C values until that point.

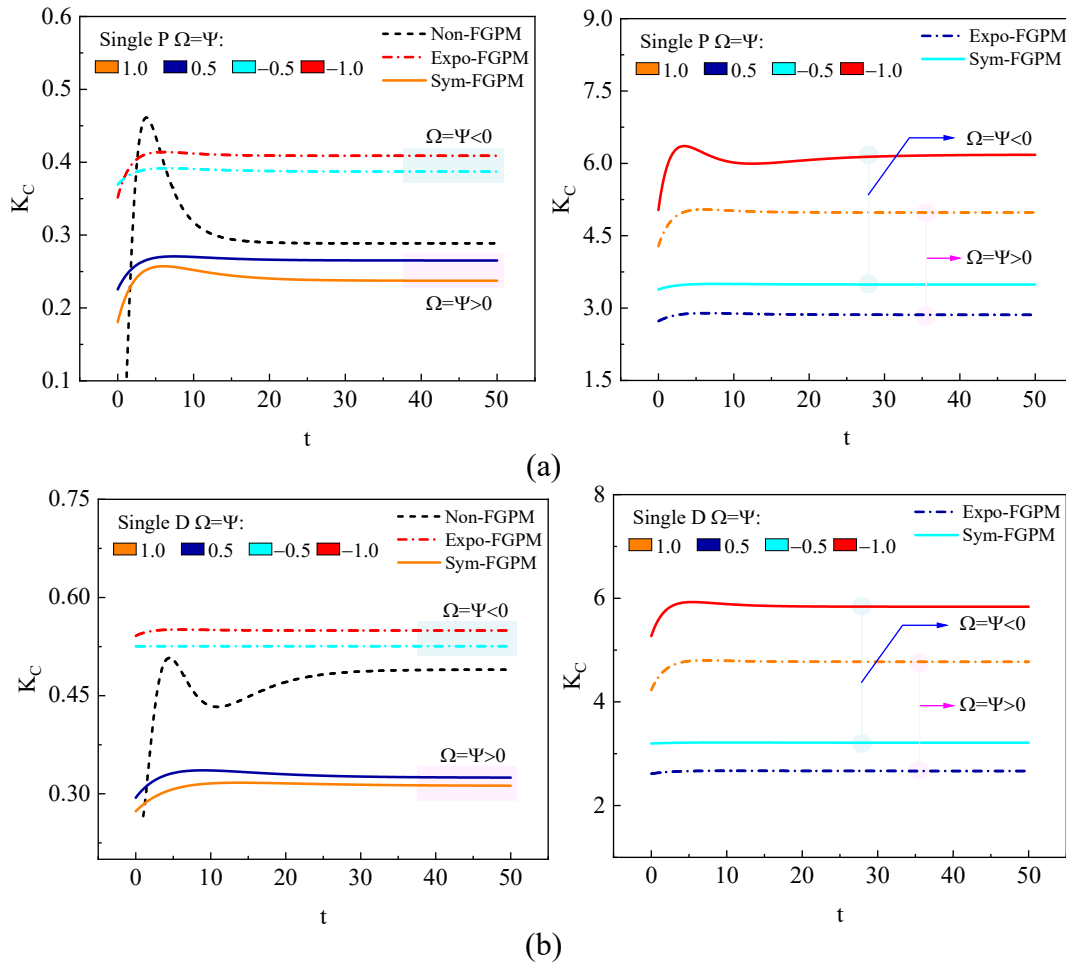


Figure 5. 11 Critical intensity factor K_C comparison (a) under single mechanical load (single P); (b) under single electrical load (single D).

Based on the observations from Figure 5.11, it is evident that the same configuration, with identical gradation coefficients Ω and Ψ , exhibits consistent trends in K_C under either single mechanical or single electrical field when examining the left and right figures in Figure 5.11 (a) and (b) for Expo-FGPM. It is apparent that larger positive values of Ω and Ψ correspond to significantly higher K_C values, indicating increased risk of fracture. Conversely, smaller negative values of Ω and Ψ result in lower K_C values. Moreover, the magnitude of Ω and Ψ plays a crucial role, as higher magnitudes of Ω and Ψ are associated with greater levels of fracture risk. In contrast, for Sym-FGPM, the results are reversed. Specifically, higher values of Ω and Ψ lead to lower K_C ,

suggesting reduced fracture risk. When comparing the three configurations under the same gradation coefficient conditions, the results indicate that the Sym-FGPM configuration performs better against fracture than Expo-FGPM when $\Omega=\Psi>0$, while Expo-FGPM outperforms Sym-FGPM when $\Omega=\Psi<0$. Furthermore, in comparison to the Non-FGPM case, Expo-FGPM with smaller gradation coefficients and Sym-FGPM with larger gradation coefficients exhibit lower K_C values, indicating enhanced material stability and fracture performance. These findings offer valuable insights for selecting the optimal configuration and gradation coefficient to improve material performance against fracture in the single mechanical or electrical loading.

The results within a single thermal field exhibit apparent differences than the other two single field cases, as shown in Figure 5.12. The fluctuating highest and lowest peaks represent the most dangerous conditions under heating and cooling loading. In both heating and cooling conditions, for the inhomogeneous configurations, Expo-FGPM and Sym-FGPM, K_C is increasing with the gradation coefficients Ω and Ψ . Compared to the Expo-FGPM, the Sym-FGPM demonstrates lower K_C when $\Omega=\Psi>0$, and has higher K_C when $\Omega=\Psi<0$. For homogenous Non-FGPM, during the heating condition, K_C is negative which is safer compared to the Expo-FGPM and Sym-FGPM whose values of K_C are positive making the crack easier to propagate. However, during the cooling condition, the K_C value of the Non-FGPM transitions to a positive value. In comparison, the K_C values associated with $\Omega=\Psi<0$ for Expo-FGPM and $\Omega=\Psi>0$ for Sym-FGPM during the same cooling phase are comparatively lower. Accordingly, we have provided specific design suggestions for configurations under single heating and cooling conditions in Table 5.2. This comprehensive analysis and guidance serve to optimize the selection and implementation of appropriate configurations based on the thermal environment, thereby enhancing the overall fracture performance and reliability of the system.

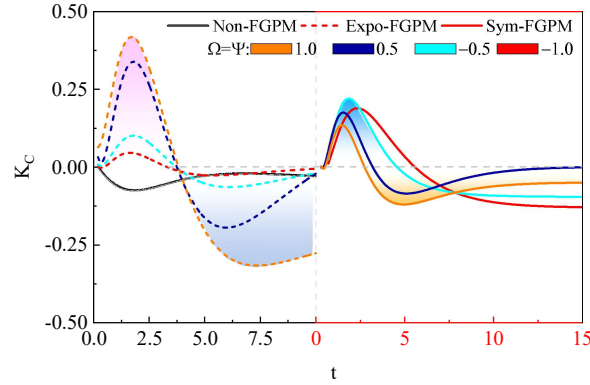
Figure 5. 12 K_C variation and sketch choice of single thermal load.

Table 5. 2 Sketches choice under single thermal load.

	$\Omega=\Psi>0$	$\Omega=\Psi<0$
Heating	Expo-FGPM < Sym-FGPM < Non-FGPM	Sym-FGPM < Expo-FGPM < Non-FGPM
Cooling	Expo-FGPM < Non-FGPM < Sym-FGPM	Sym-FGPM < Non-FGPM < Expo-FGPM

5.4.5 Thermo-electro-mechanical FGPM design

The evidence from single fields demonstrates that the choice of gradient configuration is significantly influenced by the prevailing boundary conditions. Therefore, besides the single field, it is necessary to evaluate the multiphysics problem when determining the optimal configuration.

Since the heating and cooling conditions have a large impact on the choice of configuration, we consider both heating and cooling conditions coupled with tensile mechanical and positive electric loadings. We introduce the ratios RS and RD , which represent the ratios between mechanical and thermal, as well as electrical and thermal loading, respectively.

$$RS = \frac{\sigma_0}{T_0}, \quad RD = \frac{D_0}{T_0}$$

when RS and RD are negative it represents the cooling condition, otherwise, it is the heating condition.

(1) Thermomechanical and Thermoelectrical Fields

In Figure 5.13, the critical stress intensity factors are compared under two gradation coefficient conditions: $\Omega=\Psi=1>0$, and $\Omega=\Psi=-1<0$. The ratios RS and RD vary from -2, -1, 1, to 2. From the figures, it can be observed that the Non-FGPM, Expo-FGPM, and Sym-FGPM configurations exhibit the same trend under thermomechanical and thermoelectrical environments. Taking into account the impact of RS and RD on K_C for each configuration, it is noted that under the same applied stress and electric load, the K_C of the cooling condition (RS and RD < 0) is higher than the heating condition (RS and RD > 0) for Non-FGPM and Expo-FGPM with $\Omega=\Psi=1$, but less for Sym-FGPM and Expo-FGPM with $\Omega=\Psi=-1$. Regardless of the gradation coefficient or heating or cooling condition, the critical stress intensity factor consistently increases with increasing applied stress and electric load.

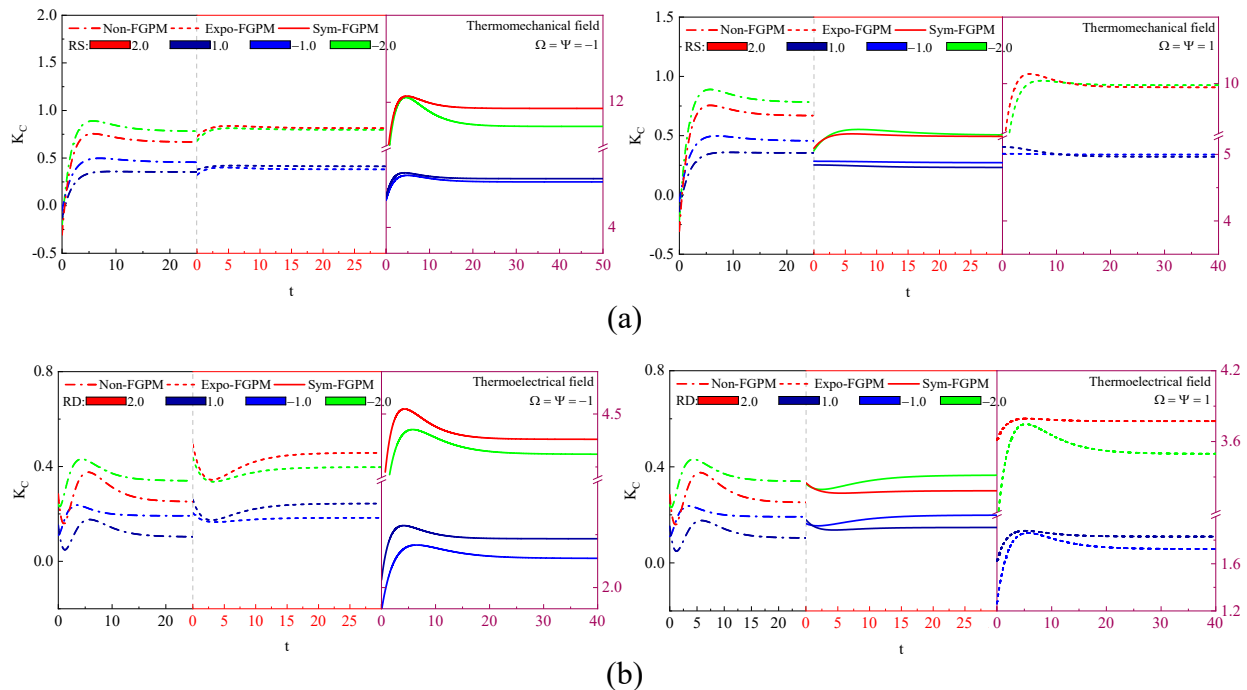


Figure 5. 13 Critical intensity factor comparison under different loading ratios (a) RS of thermomechanical field; (b) RD of thermolectrical field.

Comparing three configurations, when $\Omega=\Psi<0$, the performance of Expo-FGPM is similar to that of the Non-FGPM, while Sym-FGPM performs worse than the Non-FGPM. However, when $\Omega=\Psi>0$, the Expo-FGPM exhibits the worst performance, while the Sym-FGPM shows a slight improvement compared to the Non-FGPM.

(2) Thermo-electromechanical Field

The impact of both RS and RD ratios on the fracture performance of material is illustrated in Figure 5.14, which depicts the thermo-electromechanical results. By comparing the single RS and single RD cases with the coupling results of $RS=RD$, $RS>RD$, and $RS<RD$, it is evident that the coupling of fields leads to a more severe situation in terms of the critical intensity factor. Moreover, when comparing the results of $RS>RD$ and $RS<RD$ with $RS=RD$, it is observed that the K_C value increases more significantly under $RS>RD$, indicating that the stress factor plays a more prominent role under thermo-electromechanical conditions.

Specifically, when $\Omega=\Psi<0$, the Sym-FGPM configuration is identified as the most hazardous design against fracture under both heating and cooling conditions. However, when $\Omega=\Psi>0$, the Sym-FGPM configuration becomes the best performer, while Expo-FGPM exhibits the least favorable performance among the three configurations.

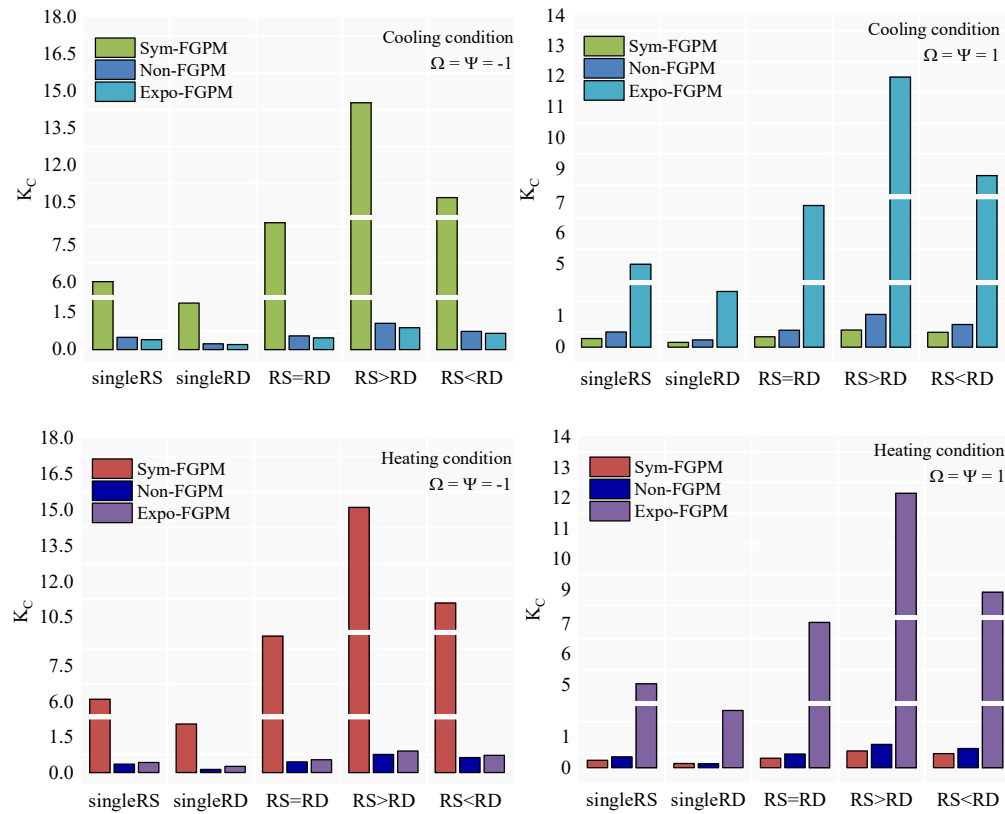


Figure 5. 14 The impact of 122hermos-electromechanical loading.

5.4.6 Gradation profile selection

The electromechanical gradation coefficient Ω and the thermal gradation coefficient Ψ can independently control the profile of functionally graded materials. However, the previous analysis suggests that fixing $\Omega = \Psi$ does not significantly highlight the benefits of functional gradient compared to Non-FGPM. As a result, we now allow for the freedom to set Ω and Ψ separately and analyze their individual effects on the critical intensity factor. The gradation coefficients Ω and Ψ are varied from -1, -0.5, 0, 0.5, to 1. The profiles of Expo-FGPM and Sym-FGPM are presented in Figure 5.15.

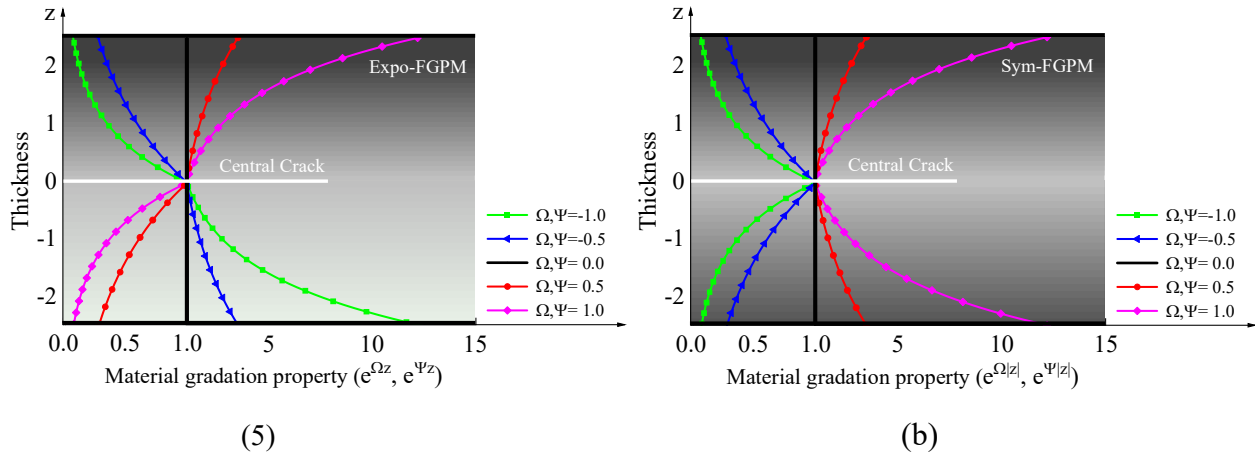


Figure 5. 15 Graded piezoelectric material based on the FGM concept with several laws of gradation.

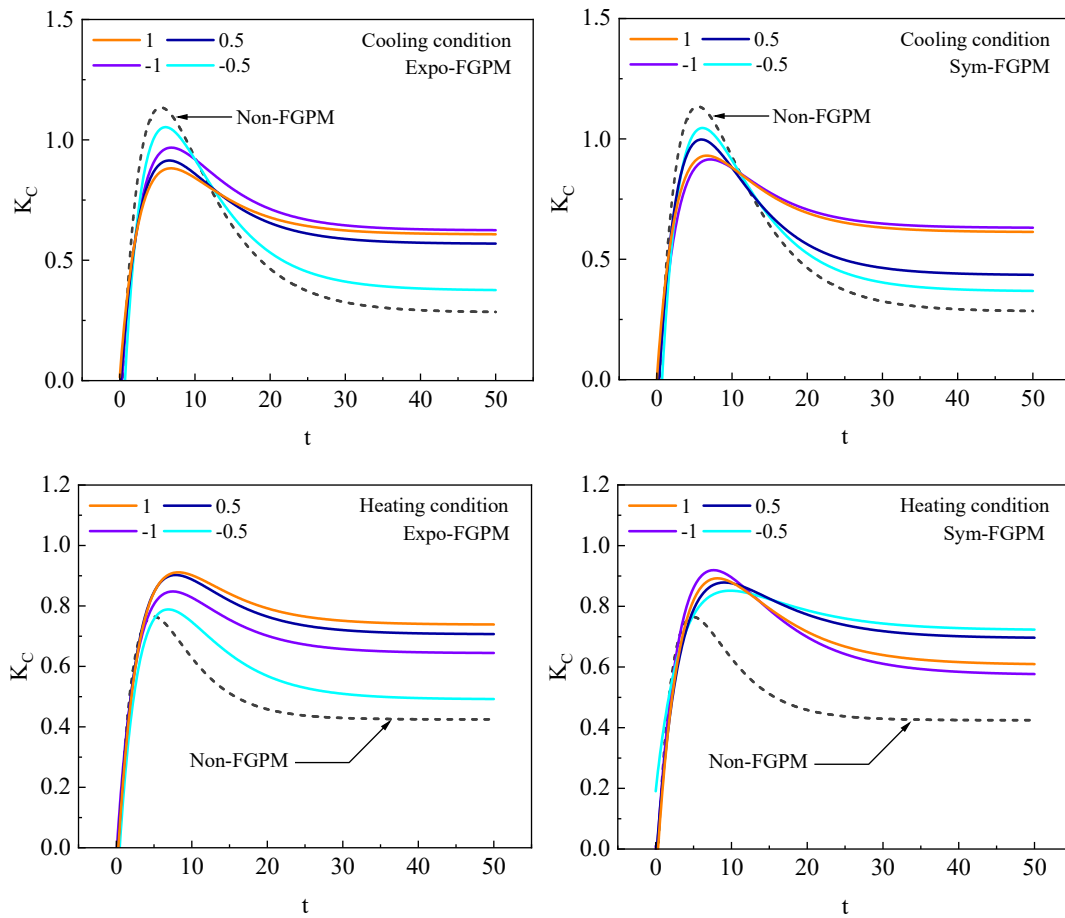


Figure 5. 16 Gradation coefficient Ψ of the thermal property profile.

Under the most dangerous condition $RS > RD$ was extracted from Figure 5.14, with $RS=2$ and $RD=1$ for heating, and: $RS=-2$ and $RD=-1$ for cooling. The effect of the thermal gradation

coefficient Ψ is analyzed in Figure 5.16. In the cooling condition, positive gradation values of Expo-FGPM result in smaller peak values of K_C compare to negative Ψ and decrease as the value of Ψ increases. Sym-FGPM is primarily affected by the thermal coefficient of gradation, with little difference between positive and negative values. Larger absolute values of Ψ indicate greater stability. For heating conditions, the phenomenon is reversed. Cooling conditions improve the fracture performance of all functional configurations compared to Non-FGPM, while higher gradation degrees yield larger critical intensity factors in heating conditions.

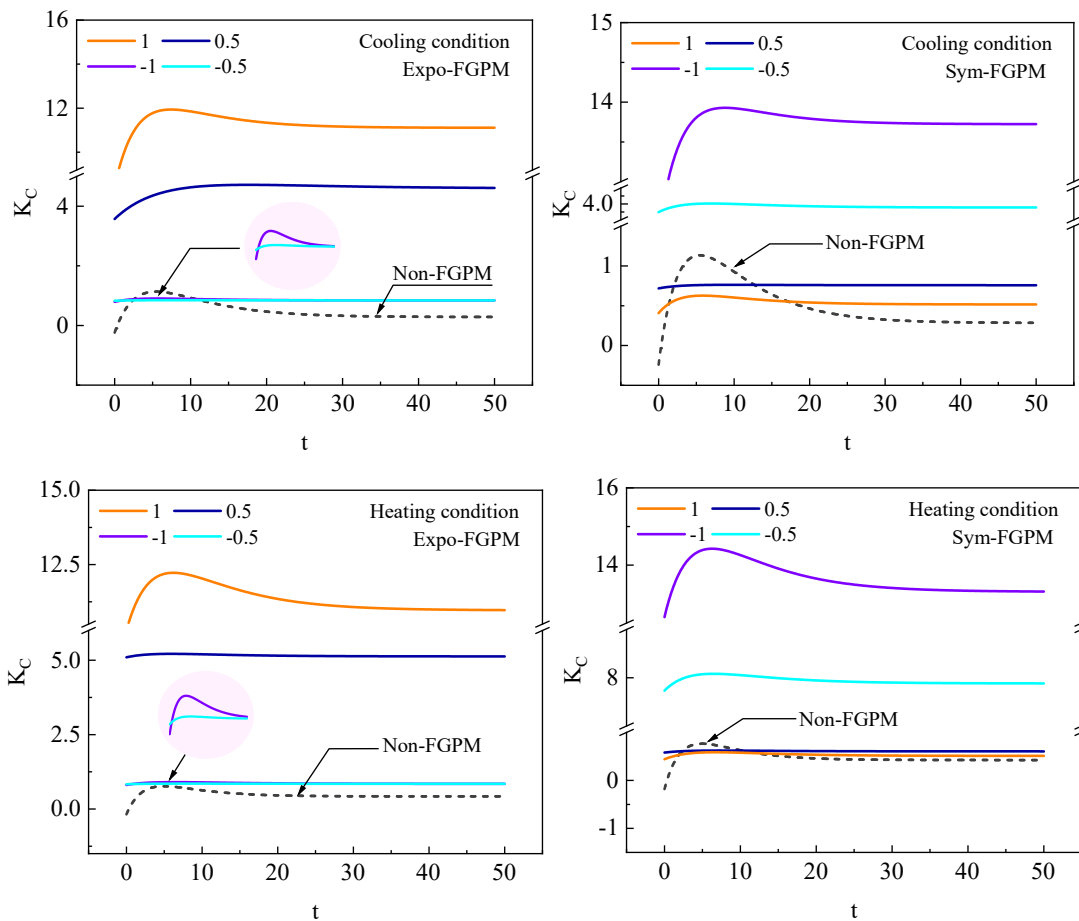


Figure 5. 17 Gradation coefficient Ω of the electromechanical property profile.

Figure 5.17 illustrates the impact of the electromechanical gradation coefficient Ω . In contrast to the thermal gradation coefficient Ψ , where cooling and heating conditions have reversed

impacts, Ω exhibits the same trend under both cooling and heating conditions. As Ω decreases, the critical intensity factor K_C decreases significantly for the Expo-FGPM, while it increases for Sym-FGPM. Although there is a slight difference between -0.5 and -1 for the Expo-FGPM when Ω becomes negative, this difference is negligible.

Figure 5.18 presents the results of peak values of K_C obtained by combining the electromechanical gradation coefficient Ω and the thermal gradation coefficient Ψ . From the figure, it can be observed that Ψ does not have a significant impact on K_C compared to Ω . The main controlling factor is the electromechanical gradation coefficient Ω . As Ω decreases or increases, the performance of the Expo-FGPM and Sym-FGPM improves under both heating and cooling conditions. By separating the field into two phases, namely $\Omega > \Psi$ and $\Omega < \Psi$, a clear trend emerges. Expo-FGPM in phase 1 ($\Omega > \Psi$) is found to be safer, while Sym-FGPM in phase 2 ($\Omega < \Psi$) exhibits better performance.

It is worth pointing out that for the Expo-FGPM under heating condition, even though the K_C values decrease after Ω becomes negative, they are still higher than those of the Non-FGPM design. As we have already seen in Figs. 5.16 and 5.17, lower magnitudes of gradation coefficients lead to lower K_C values. Therefore, even with further reductions in gradation, the Expo-FGPM does not outperform the Non-FGPM design under heating conditions. Hence, the Expo-FGPM may not be the optimal choice for heating environment. In Table 5.3, we compare the profiles of single gradation and combination gradations and provide suggestions for each loading condition.

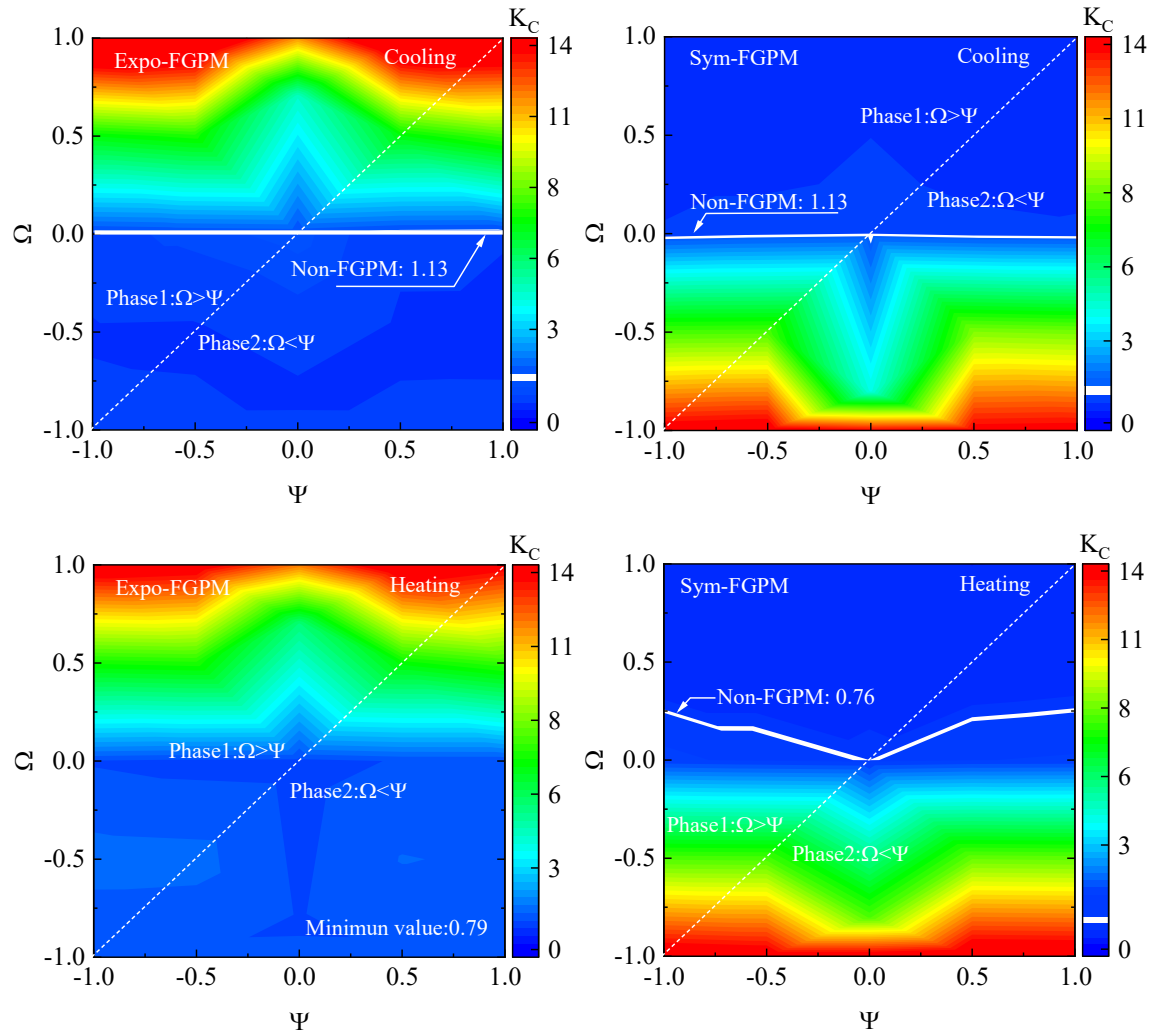

 Figure 5. 18 The value of K_C with different gradation profile for thermo-electromechanical loading.

Table 5. 3 Profile suggestions for thermo-electromechanical loading.

		Single gradient		Combination gradients		Suggestion	
		Ω	Ψ	Ω	Ψ	Ω	Ψ
Expo-FGPM	cooling	-0.5	1	(-1,0)	(-1,1)	-0.5	1
	heating	-0.5	-0.5	(-1,0)	(-1,1)	0	-0.5
Sym-FGPM	cooling	1	-1	(0,1)	(-1,1)	1	-1
	heating	1	-0.5	(0.5,1)	(-1,1)	1	-0.5

To assess the performance of the suggested profiles in Table 5.3, we compare the stresses and electric displacement at the crack surface and its extended line in Figure 5.19. Except the shear

stress and heating condition of the Expo-FGPM, following optimization, it is evident that the stress and electric displacement intensity factors at the crack tips are significantly reduced for the functional designs compared to Non-FGPM, with Sym-FGPM exhibiting the most substantial reduction.

Comparing the functional designs with the homogenous Non-FGPM, the Sym-FGPM with $(\Omega, \Psi) = (1, -0.5)$ for heating and $(1, -1)$ for cooling shows a respective decrease in critical intensity factors of 24% and 48%, as indicated in Table 5.4. Similarly, the Expo-FGPM with $(\Omega, \Psi) = (-0.5, 1)$ under cooling conditions experiences a 25% decrease in the critical intensity factor. However, it is important to note that the Expo-FGPM does not perform well under heating conditions. These results demonstrate that functional designs can enhance material stability under complex multiphysics conditions.

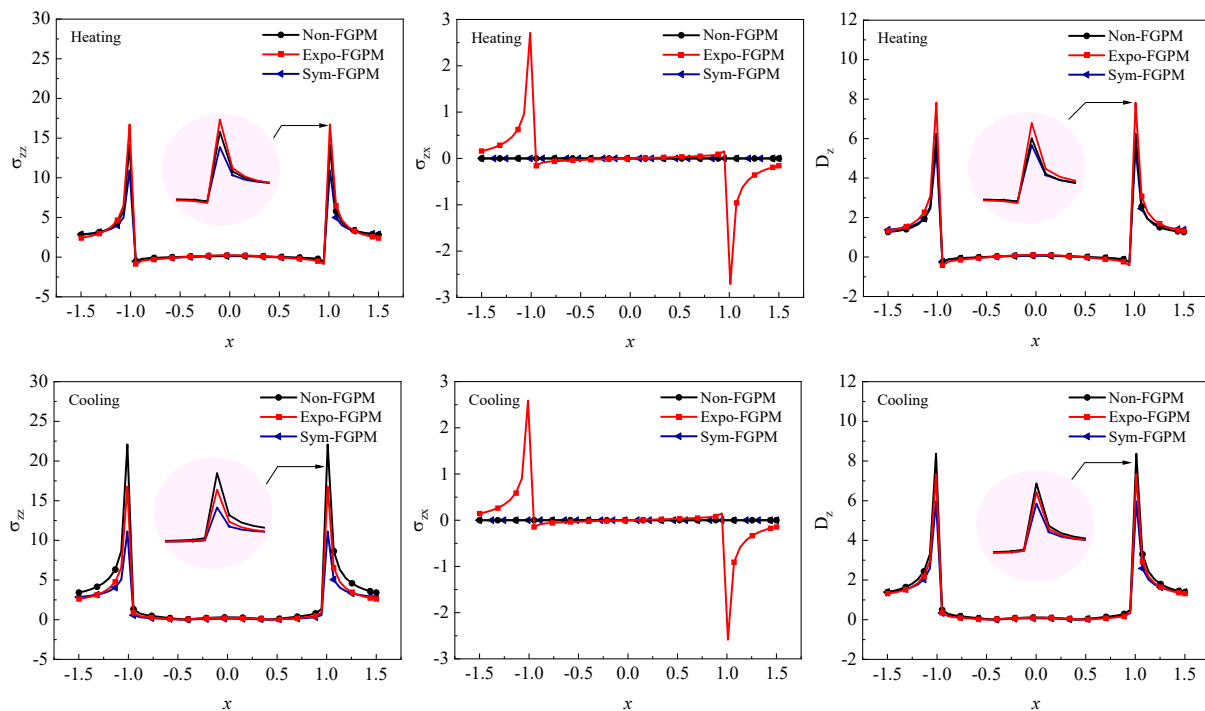


Figure 5. 19 Suggested gradation profile of FGPM and comparison.

Table 5. 4 Different sketches compare at the crack tip.

		Suggest Gradients		Normal Stress and Electric displacement			Critical intensity factor	Comparison
		Ω	Ψ	σ_{zz}	σ_{zx}	D_z	K_c	R_0
Non-FGPM	heating	0	0	14.147	0	6.242	0.764	–
	cooling	0	0	22.084	0	8.368	1.134	–
Expo-FGPM	heating	-0.5	-0.5	16.727	2.711	7.820	0.851	11% ↑
	cooling	-0.5	1	16.792	2.588	7.341	0.847	25% ↓
Sym-FGPM	heating	1	-0.5	10.937	0	5.531	0.577	24% ↓
	cooling	1	-1	11.124	0	5.972	0.593	48% ↓

5.5 Conclusions

Thermo-electromechanical analysis of cracked, graded structure inspired by biomaterials has been performed in the present work. The results give an idea about the potential of applying the piezoelectric functionally graded material concept to design smart, biomimetic composite materials, both in single- and multi-physical loading. It is observed that the piezoelectric material, designed according to the FGM concept, has improved fracture performance in comparison with non-graded ones; for instant, in single stress and electric field, the Sym-FGPM structure with high gradation coefficients allows designing piezoelectric with lower critical intensity factor, which is desirable for obtaining highly crack resistance performance.

Especially, when the FGM concept is implemented solely in the thermal field, a significant increase in the critical intensity factor is observed compared to the non-graded configuration. This observation suggests that the nonhomogeneous functional design amplifies the thermal shock effect. Consequently, it becomes imperative to consider thermal coupling in multiphysics research when designing graded piezoelectric structures against fracture.

From the multiphysics, the analysis reveals that the stress factor plays a prominent role under thermo-electromechanical conditions. Additionally, from the examples, it is clear that both thermal gradation coefficient Ψ and electromechanical gradation coefficient Ω define the fracture behaviour and, hence, a combined optimization must be considered for functional graded design of biomimetic smart materials. Finally, the optimal gradation profile is founded for the thermo-electromechanical fields. The best Sym-FGPM configuration with $(\Omega, \Psi) = (1, -0.5)$ and $(1, -1)$ for heating and cooling, respectively, leads to a decrease in critical intensity factors of 24% and 48% compared to the Non-FGPM. However, caution should be exercised when employing the Expo-FGPM, as it is suitable for cooling coupled multiphysical conditions but not for heating environment.

In conclusion, except for the single thermal environment, to design biomimetic piezoelectric structures considering gradation can improving their crack resistance under single stress, single electric, as well as thermo-electromechanical fields, and broaden the range of applications in the field of smart structures.

Chapter 6

Finite element simulations of a cracked functionally graded piezoelectric strip based on non-Fourier heat conduction

Based on the classical elastic theory, the stress and strain response of a continuum under different boundary conditions can be expressed, which provide direct guidance for materials design. However, when the degree of hierarchy becomes more complex, it will be difficult to build a constitutive equation for biomaterials simply by theoretical method. In addition, multiphysical boundary conditions along with complex structure geometry can lead to the theoretical analysis almost impossible. Benefiting from computer simulation software, it becomes convenient to construct corresponding hierarchical specimens. COMSOL is a powerful multiphysics simulation software that is known for its user-friendly interface and flexibility in solving partial differential equations (PDEs) and strong ability to address multiphysical problems. In this chapter, we establish the corresponding finite element hierarchical structures mentioned in the previous chapters and conduct non-Fourier multiphysical crack simulations in COMSOL Multiphysics platform. The simulation results show good agreement with theoretical models, which can be widely used in various configuration simulations and multiphysical analyses, guiding biomimetic design.

6.1 Introduction

Benefit from the developments of 3D printing technology and computer simulation software, researchers are now exploring new experiments and numerical simulations^{24,266-270}. Through 3D printing technology, it is easy to build corresponding hierarchical specimens, and all the mechanical properties can be obtained by various test methods, like tensile test, bending test, ductility test and so on. For example, Mohammad et al.¹⁷⁸ from tensile experimental data of their 3D printed functionally graded hierarchical soft-hard composite obtained polynomial expressions correlating the obtained mechanical properties. Then, they set the maximum strain separation data as the crack propagation criteria in ABAQUS. Finally, the numerical results of the mechanical behavior of the material were highly consistent with their experiment results.

The materials are inevitably exposed in various environmental conditions, some materials even need to be used in extreme work conditions, which should be considered in their mechanical performance to prevent catastrophic failure. However, letting the specimens work in an extreme condition is very difficult through experiment. Benefited from the strong simulation software, we can build finite element models for almost any environmental conditions, such as strong thermal shock²⁷¹, deadly water pressure impact²⁷², severe electricity shock²⁷³ and much more.

It is worth noting, however, all the numerical thermal analyses preset in simulation software such as ABAQUS, ANSYS or COMSOL Multiphysics are based on the classical, Fourier heat conduction law which allows the thermal disturbance to spread at an infinite speed. However, the establishment of thermal equilibrium actually takes a certain period of time. Although in most thermomechanical problems, Fourier heat conduction works perfectly, it renders unreasonable temperature predictions when the temperature is extremely low, the temperature gradient is

extremely high, or the material has a heterogeneous microstructure. To fix this problem, non-Fourier heat conduction models were proposed by introducing so-called relaxation time which measures the time lag between temperature gradient and heat flux at the same particle of the material. Therefore, in this chapter, we aim to achieve non-Fourier heat conduction in COMSOL Multiphysics which is highly user-friendly and has strong ability to address multiphysical problems. Finally, a 2D cracked piezoelectric strip under thermo-electromechanical fields has been built in the platform, and specifically, the following work has been conducted:

- (1) Modeling non-Fourier heat conduction with partial differential equations in COMSOL Multiphysics.
- (2) Building different functionally graded piezoelectric models according to hierarchical biomimetic materials.
- (3) Coupling thermal, piezoelectric, and structural analyses in COMSOL and comparing with the theoretical results.

6.2 Finite Element Modelling

6.2.1 Design conditions

The cracked strip is designed using functionally graded piezoelectric material, 50 mm in width and 5 mm in height with a 2 mm insulated central crack. Temperature, electric displacements, and stress analyses of the material are carried out with this design. An electric displacement of 0.4 C/m^2 and a tensile stress of 50 MPa applied at the strip surfaces. At same time, a transient thermal load heats the top surface of strip from 293 K to 586 K. The thermally induced tension loads the material and deforms the strip, and then coupled with electric and tensile field causing stresses concentration at crack tips.

The geometric structure of the cracked strip designed as 2-D using COMSOL is shown in Figure 1. Functionally graded piezoelectric material is added to the proposed geometric structure. The most common piezoelectric material PZT-5H is selected and properties are assigned to the selected material. For this study, the functional gradation profile of material is selected from Chapter 5 as Eq. (5.1). We choose the heating multiphysical gradation suggestion (Sym-FGPM with $\bar{\Psi} = 1$ and $\bar{\Omega} = -0.5$) from Chapter 5 as the example conduct simulations, as Eq. (6.1). The gradation laws are edited in COMSOL as analytic functions varying as shown in Figure 6.1(a), here the axis y in COMSOL is the axis z in theoretical model. The homogenous physical properties of the materials used in the analysis phase are given in Table 6.1.

$$\begin{aligned} (\zeta_{ik}, p_z) &= (\zeta_{ik0}, p_{z0})e^{\Psi|z|} & \Psi &= 1 \times 10^3 \\ (\mathbf{c}_{ik}, \mathbf{d}_{ik}, \boldsymbol{\varepsilon}_{ik}, \mathbf{k}_i, \rho) &= (\mathbf{c}_{ik0}, \mathbf{d}_{ik0}, \boldsymbol{\varepsilon}_{ik0}, \mathbf{k}_{i0}, \rho_0)e^{\Omega|z|} & \Omega &= -0.5 \times 10^3 \end{aligned} \quad (6.1)$$

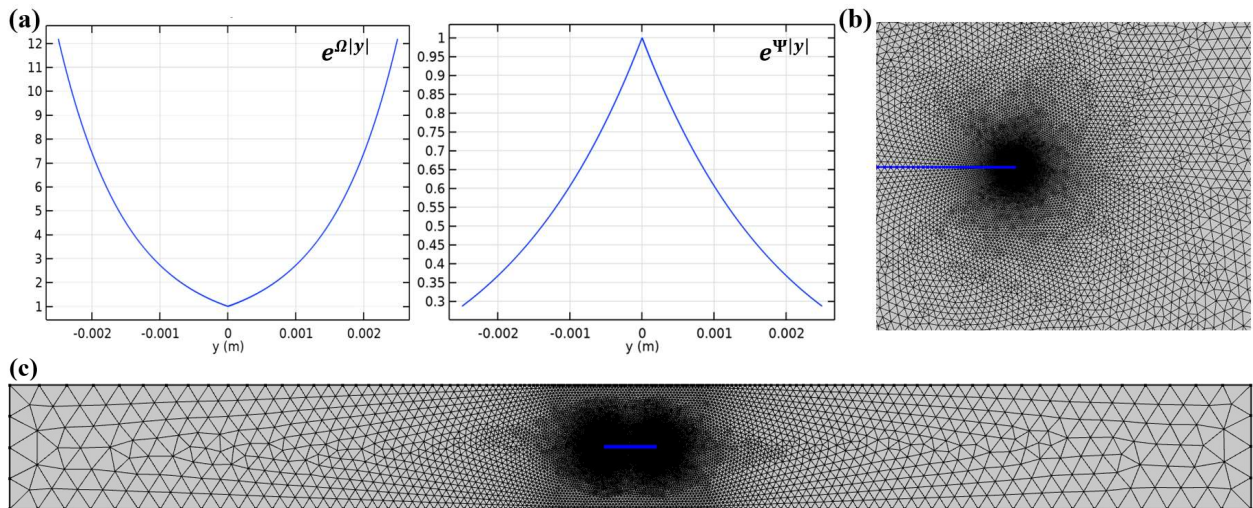


Figure 6. 1 Geometry: (a) gradation law; (b) mesh element around crack tip; (c) whole strip.

Table 6. 1 Material properties of homogeneous PZT-5H ceramics.

Elastic stiffnesses ($\times 10^{10}$ N/m ²)				Piezoelectric coefficients (C/m ²)			Dielectric constants ($\times 10^{-10}$ C/Vm)		Specific heat (J/kg ^o K)	Density ($\times 10^3$ kg/m ³)
c_{110}	c_{130}	c_{330}	c_{440}	d_{310}	d_{330}	d_{150}	ε_{110}	ε_{330}	c_p	ρ_0
12.72	8.47	11.74	2.30	-6.62	23.24	17.03	150.9	126.9	475	7.5

6.2.2 Non-Fourier thermal Modeling

(1) User-defined partial differential equations (PDEs)

The fundamental law governing all heat transfer in COMSOL is the first law of thermodynamics, commonly referred to as the principle of conservation of energy.

$$\rho c_p \frac{\partial T}{\partial t} = -(\nabla \cdot \mathbf{q}) + Q$$

where ρ_0 is the density (kg/m^3), c_p is the specific heat capacity at constant pressure ($\text{J}/(\text{kg} \cdot \text{K})$), T is absolute temperature (K), \mathbf{q} is the heat flux by conduction (W/m^2), and Q contains heat sources other than viscous heating (W/m^3).

However, the heat transfer interfaces use Fourier's law of heat conduction, which states that the conductive heat flux, \mathbf{q} , is proportional to the temperature gradient without considering spread speed:

$$\mathbf{q} = -k\nabla T \quad (6.2)$$

where k is the thermal conductivity ($\text{W}/(\text{m}\cdot\text{K})$). Considering thermal relaxation effect of biomaterials, non-Fourier law of heat conduction was proposed as ¹⁰⁵

$$\left(1 + \tau_q \frac{\partial}{\partial t}\right) \mathbf{q} = -k\nabla T \quad (6.3)$$

Finally, without heating sources, the resulting heat equation is:

$$\left(1 + \tau_q \frac{\partial}{\partial t}\right) \rho c_p \frac{\partial T}{\partial t} = (\nabla \cdot k\nabla T) \quad (6.4)$$

COMSOL provides the Mathematics module for the creation of user-defined partial differential equations (PDEs) through equation-based modeling. This module empowers us to tackle a wide array of PDEs utilizing diverse formulations. In scenarios involving functionally graded issues, where material properties exhibit a functional gradient, the *General form* interface emerges as the optimal selection due to its compatibility with nonlinear PDEs. The general PDE form in *General form* interface is:

$$e_a \frac{\partial^2 T}{\partial t^2} + d_a \frac{\partial T}{\partial t} + \nabla \cdot \Gamma = Q \quad (6.5)$$

According to Eq. (6.3), the terms $e_a = \tau_q \rho c_\rho$, $d_a = \rho c_\rho$, $Q = 0$, and $\Gamma = -k \nabla T$.

(2) Thermal boundary conditions

Here, four thermal boundary conditions (a) to (d) defined as follows are assigned similar to the boundary conditions in chapter 5.

- (a) Initial values $T=293$ K for the whole strip
- (b) Dirichlet Boundary Condition $T=T_{\text{boundary}}$ at Top surface
- (c) Dirichlet Boundary Condition $T=293$ K at Bottom surface
- (d) Zero Flux $-\mathbf{n} \cdot \Gamma = 0$.

The bottom substrate surface is maintained at a constant 293 K. The top surface is heated from 293 K to 586 K in a very short second. The crack surfaces are considered adiabatic.

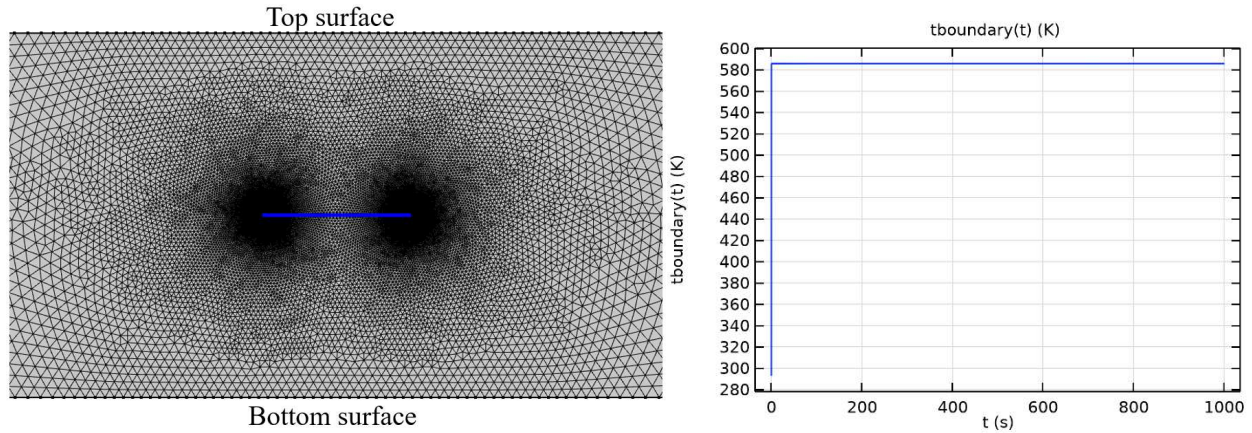


Figure 6. 2 Thermal boundary conditions.

(3) Element quality check

The 2D 1-mm-sized triangular element was chosen and discretized in quadratic order. The mesh becomes finer near the cracked positions as shown in Figure 6.3. After mesh sensitivity study, the final FE model contained a total of 66258 elements, which represents an appropriate meshing considering both computational cost and accuracy. The mesh resolution and mesh element quality are important aspects to consider when validating a finite element model. Low mesh resolution—in relation to the variations in the solution and the geometry—can lead to inaccurate results, and a low mesh element quality—which measures the regularity of the mesh elements' shapes—can lead to inverted mesh elements and convergence issues. COMSOL documentation²⁷⁴ states that element quality in a tetrahedral mesh should not go below 0.1 (where 1 represents 100% quality), or else the user risks compromising the quality of the model's solution. Figure 6.2 shows the mesh quality in the strip at the area of maximum stresses and displacement. All the mesh quality are higher than 0.5 and close to 1.

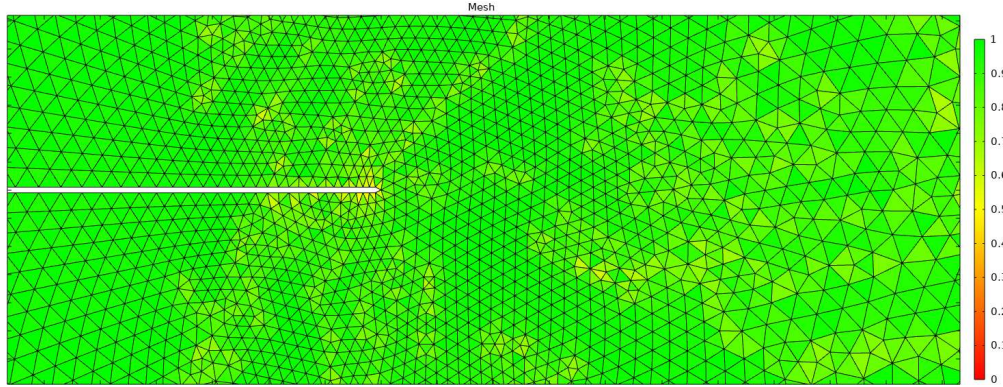


Figure 6. 3 Measure of mesh quality in the thermal model around crack tip.

6.2.3 Functionally graded Piezoelectric Modeling

(1) Piezoelectricity, Solid

The constitutive equations governing piezoelectric behavior within any given material can be written in either “strain-charge” form or “stress-charge” form, both of which are supported by COMSOL, and yield identical results. Here, we chose to enter in material properties in the “stress-charge” form:

$$\boldsymbol{\sigma} = \mathbf{c}_E \boldsymbol{\varepsilon} - \mathbf{e}^T \mathbf{E} \quad (6.6)$$

$$\mathbf{D} = \mathbf{e} \boldsymbol{\varepsilon} + \varepsilon_0 \boldsymbol{\varepsilon}_r \mathbf{E} \quad (6.7)$$

where $\boldsymbol{\varepsilon}$ is strain tensor, \mathbf{E} is electric field strength (V/m), \mathbf{e} is indirect coupling matrix which is elastic stiffness \mathbf{c}_{ij} in Table 6.1, $\boldsymbol{\varepsilon}_r$ and ε_0 are relative electrical permittivity and electrical permittivity of free space = $8.854187817e^{-12}$ (F/m), $\varepsilon_0 \boldsymbol{\varepsilon}_r$ is dielectric constants $\boldsymbol{\varepsilon}_{ij}$. The material properties used in the piezoelectric analysis are found in Table 6.1. For a 2D piezoelectric analysis in COMSOL, the default material coordinate plane is XY. However, because the strip is polarized along z direction. Hence, in the modeling process it was necessary to specify that the material coordinate systems of materials be X-Z.

(2) Boundary conditions

Given the central emphasis on transient thermal dynamics, to ensure convergence and accuracy, we have simplified the transient stress and electric boundaries, discussed in chapter 5, into static loads applied to the upper and lower surfaces. Additionally, the crack surface is free and insulated. The following boundary conditions have been set within the COMSOL platform.

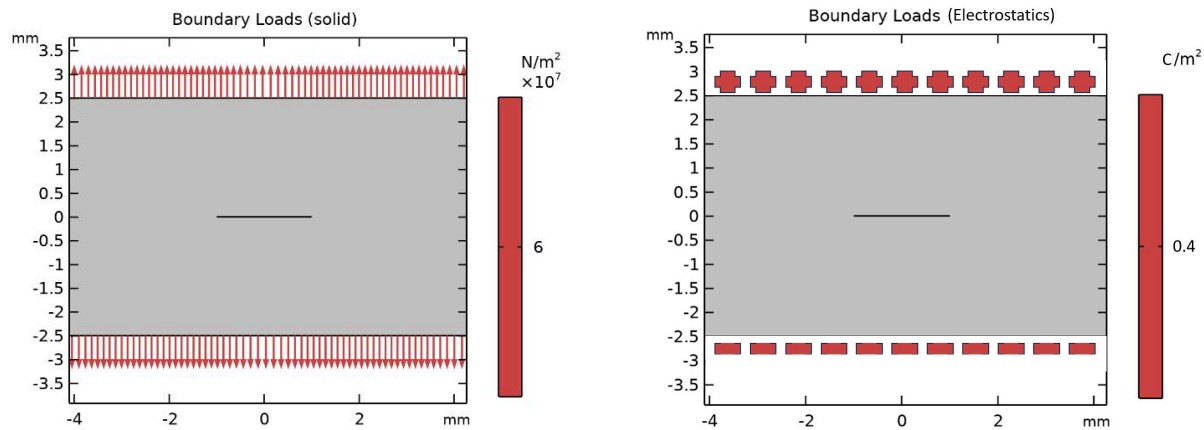


Figure 6. 4 Mechanical-electrical boundary conditions.

Solid Mechanics interface	Electrostatics interface
(a) Free boundary at crack surfaces (b) Initial values displacement field = 0 (c) Boundary load 1: upper stress $F_A = p_0 \text{ N/m}^2$ (d) Boundary load 2: lower stress $F_A = -p_0 \text{ N/m}^2$ (d) Roller Constraint: left and right surfaces * $p_0 = 50 \text{ MPa}$	(a) Charge Conservation, Piezoelectric for whole geometry (d) Electric Displacement Field: upper and lower displacement $D_0 = d_0 \text{ C/m}^2$ (b) Initial values electric potential = 0 (c) Ground: crack surfaces (c) Zero Charge: left and right surfaces * $d_0 = 0.4 \text{ C/m}^2$

6.2.4 Coupled Thermo-Piezo-Electro-Mechanical Model

(1) Thermal expansion

The equation for thermal expansion in thermo-mechanical situations is: $\varepsilon_{th} = \alpha(T - t_0)$, where α is the coefficient of thermal expansion of the given material and ΔT is the change in temperature from the reference temperature (t_0). The coefficient of thermal expansion of PZT-5H is $\alpha(T) = 7 \times 10^{-6}$ (unit:1/K). Then Eq. (6.6) is expanded into:

$$\boldsymbol{\sigma} = \mathbf{c}_E \boldsymbol{\varepsilon} - \mathbf{c}_E \varepsilon_{th} - \mathbf{e}^T \mathbf{E} \quad (6.8)$$

(2) Piezoelectric Material

COMSOL adds the remanent term “ D_r ” to the governing equation of the piezoelectric material, which helps in coupling other fields with the electric field. The Eq. (6.7) expanded into

$$\mathbf{D} = \mathbf{e} \boldsymbol{\varepsilon} + \varepsilon_0 \boldsymbol{\varepsilon}_r \mathbf{E} + D_r \quad (6.9)$$

in which $D_r = -p_z(T - t_0)$ for electrical-thermal field according to Eq. (5.2) in chapter 5.

Table 6. 2 Thermal properties of homogeneous PZT-5H ceramics.

Elastic stiffnesses ($\times 10^{10}$ N/m ²)				Coefficient of thermal expansion (1/K)	Thermal Modulus (N/Km ²)		Pyroelectric coefficients ($\times 10^{-4}$ C/Km ²)
c_{110}	c_{130}	c_{330}	c_{440}	α	ζ_{110}	ζ_{330}	p_{z0}
12.72	8.47	11.74	2.30	7×10^{-6}	$c_{110} \times \alpha$	$c_{330} \times \alpha$	4.16

6.3 Results and Discussions

The simulation processes are carried out in two stages. Initially the time-dependent temperature distributions are studied and the resulted displacement is transferred into second stage

as preset values. In the second stage, stress and electric displacement are performed for stable condition.

Step 1: Time Dependent: Thermal study — General Form PDE

Step 2: Stationary: Solid Mechanics and Electrostatics — Multiphysics

6.3.1 Temperature distributions

In comparison with the theoretical outcomes, the simulation results demonstrate a significant level of consistency, effectively achieving the application of the non-Fourier theory within the COMSOL Multiphysics platform. To offer a more comprehensive understanding of the relaxation phenomenon, Figure 6.5 also presents Fourier-based results. When compared to the non-Fourier results, the Fourier temperature outcomes rapidly attain equilibrium without generating temperature fluctuations.

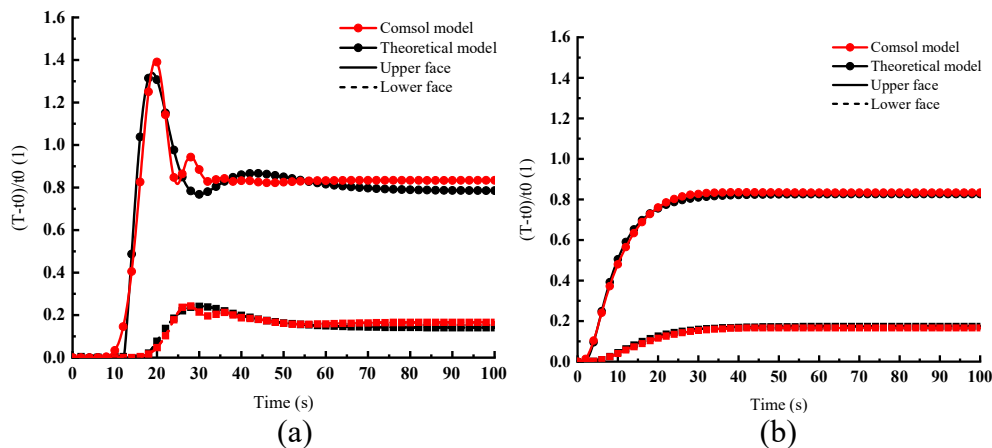


Figure 6. 5 Measure of mesh quality in the thermal model around crack tip: (a) non-Fourier; (b) Fourier.

According to Figure 6.5, the peak temperature occurs at approximately 19.7 seconds after the thermal load is applied, and the corresponding temperature distribution result is illustrated in Figure 6.6. It becomes evident that utilizing the Fourier law alone would result in overlooking the

critical time period of risk, which leads directly to a steady state value (at $t=100$ seconds) without considering relaxation effects. Therefore, in the context of biomaterial analysis, the adoption of a non-Fourier heat conduction law is preferable. Moreover, upon comparing the steady temperature distributions depicted in the Figure for Sym-FGPM and Non-FGPM, it is evident that the heterogeneous symmetric functionally graded sketch exhibits higher temperature gradients in the strip. This aligns well with the theoretical findings outlined in Section 5.4.3 of Chapter 5, which supplies further validation for the reliability of the theoretical models.

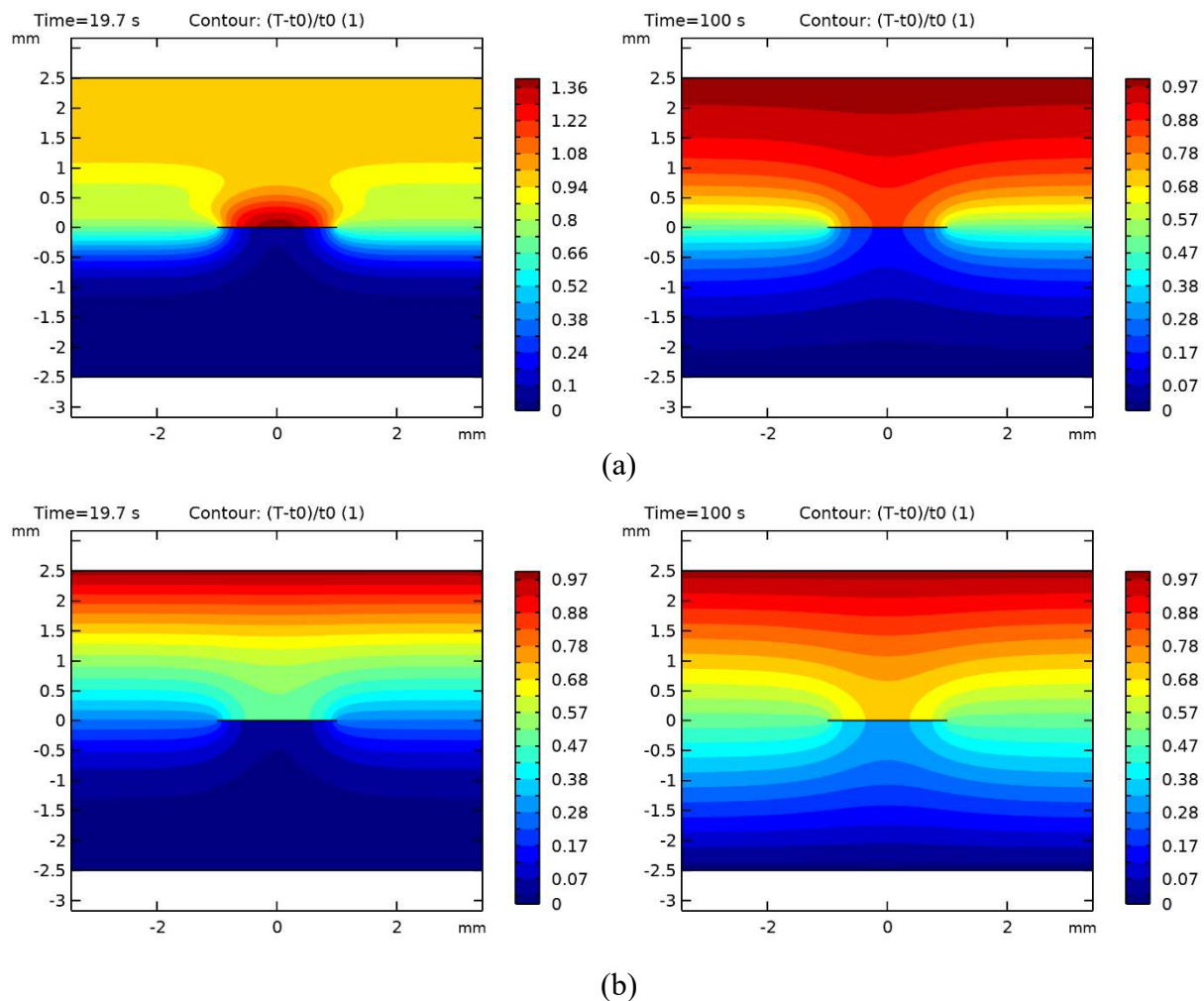


Figure 6. 6 Temperature distributions of: (a) Sym-FGPM; (b) Non-FGPM.

6.3.2 Stress distributions

Figure 6.7 presents von Mises stress distribution around crack tip of symmetric functionally graded PZT-5H under single stress and thermal-mechanical loads. We can see that after adding a heating source, the stress concentration near the tip is higher than single stress field, which can be attributed to the thermal SIFs observed in Figure 5.9 (b) of Chapter 5, Section 5.4.3. The heating source causes a normal stress intensity rise at the S_{H1} point because of the non-Fourier thermal wave effect, and finally the higher stress concentration at crack tip for coupled thermal-stress field.

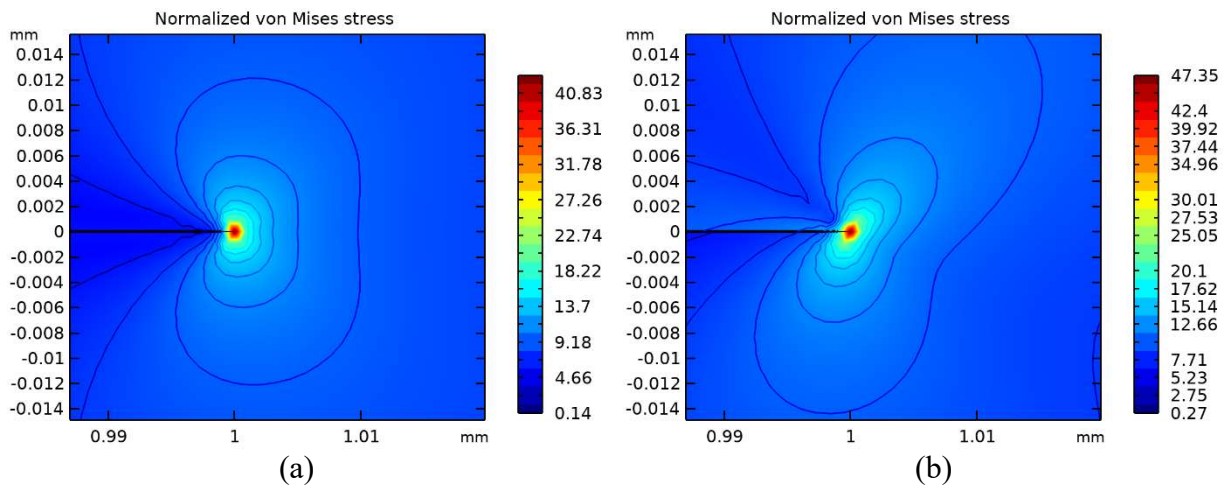


Figure 6. 7 Von Mises stress distribution around crack tip of Sym-FGPM: (a) Mechanical; (b) Thermal-mechanical.

The last step of the simulation is carried out for thermomechanical effect coupled with an electric field. The thermal-mechanical-electrical results of three microstructure configurations: Sym-FGPM, Non-FGPM and Expo-FGPM are presented in Figure 6.8. The gradation configurations of Sym-FGPM and Expo-FGPM both follow with suggested gradients, respectively, $(\bar{\Omega}, \bar{\Psi}) = (1, -0.5)$ and $(-0.5, -0.5)$. Based on the findings presented in Chapter 5, it is evident that the Sym-FGPM is the most suitable sketch for the heating-mechanical-stress conditions. Conversely, the Expo-FGPM exhibits a dangerous trend. These findings are further

demonstrated by the outcomes observed in the simulation results. Comparing Figures 6.8 (a), (b), and (c), the von Mises stress near the crack tip of the Sym-FGPM is 30.5% lower than Non-FGPM sketch; however, the Expo-FGPM is 3.2% higher than the Non-FGPM. The suggested gradation improvement for the Expo-FGPM is further substantiated through a comparison of Figures 6.8 (c) and (d). The observation reveals that the Expo-FGPM, when employed the identical gradation profile of Sym-FGPM: $(\bar{\Omega}, \bar{\Psi}) = (1, -0.5)$, demonstrates significantly elevated results compared to the recommended configuration $(\bar{\Omega}, \bar{\Psi}) = (-0.5, -0.5)$. Finally, the simulation and theoretical models have been mutually validated.

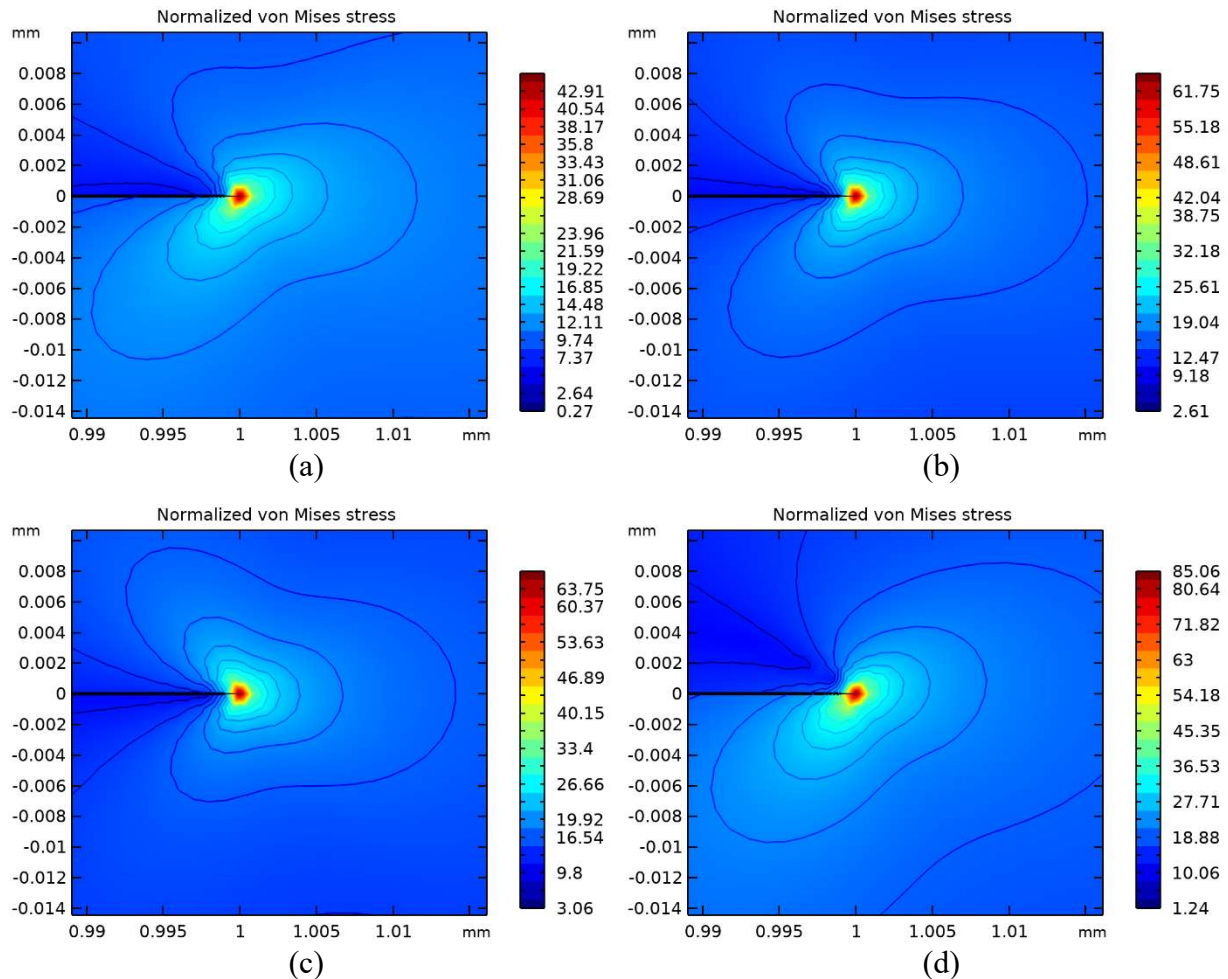


Figure 6. 8 Thermal-mechanical-electrical von Mises stress distribution around crack tip: (a) Sym-FGPM (1, -0.5); (b) Non-FGPM; (c) Expo-FGPM (-0.5, -0.5); (d) Expo-FGPM (1, -0.5).

6.4 Conclusions

In this chapter, we have successfully implemented Multiphysics finite element simulations for functionally graded piezoelectric materials, and first realized the non-Fourier heat conduction model within the COMSOL Multiphysics platform. From the results, we observed that the temperature and stress simulation results are consistent well with theoretical models. For thermal results, the non-Fourier model successfully replicates the thermal relaxation effect of biomaterials and shows an obvious thermal amplification in symmetric functionally graded configuration. Furthermore, the suggested gradations for biomimetic composites under heating-mechanical-electrical field proposed from the theoretical model in Chapter 5, have been further substantiated in finite element models. The multiphysical finite element model and theoretical models provide valuable insights into functionally graded design and performance analysis of biomimetic composites.

Chapter 7

Conclusions and Future Perspectives

7.1 Conclusions

In order to overcome the drawbacks of homogenous structural design and single field functional property examinations, as well as the overlook of thermal relaxation effect of biomimetic materials, multiphysical, functionally graded models have been built based on non-Fourier heat conduction theory to provide guidelines for biomimetic gradation design under different working environments. Through this work, major conclusions are summarized as follows.

- (1) Significant discrepancies of transient stresses intensity factors exist between non-Fourier and Fourier models. Fracture may occur at a much earlier stage in the non-Fourier model under thermal shock than the Fourier one based on the predicted stress intensity factors.
- (2) Multiphysical conditions have a significant influence on the fracture resistance of heterogeneous material, while temperature is a vital factor that cannot be ignored. A sudden temperature fall will cause an opening-mode failure. While a positive electric shock will slightly reduce the likelihood of an opening crack occurrence.
- (3) Functional gradient concept is not always optimal for every scenario which is greatly influenced by the surrounding environment. Particularly, for single thermal loading, the non-graded configuration displays superior fracture resistance over graded ones.

- (4) Except for the single thermal environment, designing biomimetic piezoelectric structures considering gradation can improve their crack resistance under single stress, single electric, as well as thermo-electromechanical fields. The symmetric functional configuration, characterized by a higher value of the electromechanical gradation coefficient Ω and thermal gradation coefficient Ψ , shows remarkable fracture resistance under single stress and single electric environments when $\Omega = \Psi$. The best sketches for heating-mechanical-electrical and cooling-mechanical-electrical fields are Sym-FGPM designs with $(\Omega, \Psi) = (1, -0.5)$ and $(1, -1)$, respectively.
- (5) Non-Fourier theory is first realized within COMSOL Multiphysics platform, successfully replicates the thermal relaxation effect of biomaterials. The temperature and stresses simulation results are consistent well with theoretical models. Furthermore, the suggested gradations for biomimetic composites under heating-mechanical-electrical have been further validated numerically. With the aid of multiphysical numerical model, even with more complex micro- or nanoscale arrangements as well as high degree of coupling environments, the strongly nonlinear problem can be easily solved.

There exist some limitations of this thesis because of the theoretical nature of the work. Classical elasticity cannot describe the creep or stress relaxation phenomena caused by the rheological properties of soft materials, such as polymer matrix composites, nanocomposites hydrogels and soft elastomers. In dealing with the fracture of these materials, it is necessary to develop a more comprehensive viscoelastic model.

7.2 Future perspectives

For the investigation of biomimetic materials, due to the viscoelastic time-dependent nature of biomaterial, the linear elastic models are inadequate in addressing issues characterized by significant creep and stress relaxation phenomena. The viscosity of biomaterials would become particularly pronounced during dynamic or cyclic loading, as well as in their protracted interaction with biological systems. To address these complexities, the incorporation of a linear viscoelastic constitutive law can be introduced to the framework of multi-physical functionally graded models. Besides, in the context of finite element modeling, the geometric configuration can be composed of two distinct material phases: a viscoelastic soft material and a linear elastic hard material. The strategic arrangement of these two phases would offer a more accurate means to study the functionally graded design enhancing overall fracture resistance. Therefore, integrating viscoelastic analysis into future studies promises a more accurate representation of biomimetic material behavior, ensuring their optimal fracture resistance performance in diverse fields.

References

- 1 Wat, A. *et al.* Bioinspired nacre-like alumina with a bulk-metallic glass-forming alloy as a compliant phase. *Nat Commun* **10**, 961 (2019).
- 2 Wilkerson, R. P. *et al.* High-temperature damage-tolerance of coextruded, bioinspired (“nacre-like”), alumina/nickel compliant-phase ceramics. *Scripta Materialia* **158**, 110-115, doi:10.1016/j.scriptamat.2018.08.046 (2019).
- 3 Zadpoor, A. A. Mechanical performance of additively manufactured meta-biomaterials. *Acta Biomater* **85**, 41-59 (2019).
- 4 Chen, P.-Y. *et al.* Structure and mechanical properties of selected biological materials. *Journal of the mechanical behavior of biomedical materials* **1**, 208-226 (2008).
- 5 Li, X.-W., Ji, H.-M., Yang, W., Zhang, G.-P. & Chen, D.-L. Mechanical properties of crossed-lamellar structures in biological shells: A review. *Journal of the Mechanical Behavior of Biomedical Materials* **74**, 54-71 (2017).
- 6 Meyers, M. A., McKittrick, J. & Chen, P.-Y. Structural Biological Materials: Critical Mechanics-Materials Connections. *Science* **339**, 773-779 (2013).
- 7 Lopes-Lima, M., Rocha, A., Gonçalves, F., Andrade, J. & Machado, J. Microstructural characterization of inner shell layers in the freshwater bivalve *Anodonta Cygnea*. *Journal of Shellfish Research* **29**, 969-973 (2010).
- 8 Pina, C. M., Checa, A. G., Sainz-Díaz, C. I. & Cartwright, J. H. Nacre: an ancient nanostructured biomaterial. (2013).
- 9 Zaremba, C. M. *et al.* Critical transitions in the biofabrication of abalone shells and flat pearls. *Chemistry of Materials* **8**, 679-690 (1996).
- 10 Ritchie, R. O. The conflicts between strength and toughness. *Nature materials* **10**, 817-822 (2011).
- 11 Wegst, U. G., Bai, H., Saiz, E., Tomsia, A. P. & Ritchie, R. O. Bioinspired structural materials. *Nat Mater* **14**, 23-36 (2015).

- 12 Sun, J. & Bhushan, B. Hierarchical structure and mechanical properties of nacre: a review. *RSC Advances* **2** (2012).
- 13 Liu, Y., Luo, D. & Wang, T. Hierarchical structures of bone and bioinspired bone tissue engineering. *Small* **12**, 4611-4632 (2016).
- 14 Tertuliano, O. A. & Greer, J. R. The nanocomposite nature of bone drives its strength and damage resistance. *Nature materials* **15**, 1195-1202 (2016).
- 15 Launey, M. E., Buehler, M. J. & Ritchie, R. O. On the mechanistic origins of toughness in bone. *Annual review of materials research* **40**, 25-53 (2010).
- 16 Huang, W. *et al.* Multiscale Toughening Mechanisms in Biological Materials and Bioinspired Designs. *Adv Mater* **31**, e1901561 (2019).
- 17 Currey, J. D. Hierarchies in Biomineral Structures. *Science* **309**, 253-254, doi:10.1126/science.1113954 (2005).
- 18 Wang, R. & Gupta, H. S. Deformation and fracture mechanisms of bone and nacre. *Annual Review of Materials Research* **41**, 41-73 (2011).
- 19 Peng, X. *et al.* Bioinspired strategies for excellent mechanical properties of composites. *Journal of Bionic Engineering* **19**, 1203-1228 (2022).
- 20 Gu, G. X., Dimas, L., Qin, Z. & Buehler, M. J. Optimization of composite fracture properties: method, validation, and applications. *Journal of Applied Mechanics* **83**, 071006 (2016).
- 21 Mertgen, A. S. *et al.* Multifunctional Biomaterials: Combining Material Modification Strategies for Engineering of Cell-Contacting Surfaces. *ACS Appl Mater Interfaces* **12**, 21342-21367 (2020).
- 22 Zhang, Y., Gandhi, A., Zeglinski, J., Gregor, M. & Tofail, S. A complementary contribution to piezoelectricity from bone constituents. *IEEE Transactions on Dielectrics and Electrical Insulation* **19**, 1151-1157 (2012).
- 23 Kapat, K., Shubhra, Q. T., Zhou, M. & Leeuwenburgh, S. Piezoelectric nano - biomaterials for biomedicine and tissue regeneration. *Advanced Functional Materials* **30**, 1909045 (2020).
- 24 Jia, Z. & Wang, L. 3D printing of biomimetic composites with improved fracture toughness. *Acta Materialia* **173**, 61-73 (2019).

- 25 Kobayashi, T., Nakamura, S. & Yamashita, K. Enhanced osteobonding by negative surface charges of electrically polarized hydroxyapatite. *Journal of Biomedical Materials Research: An Official Journal of The Society for Biomaterials, The Japanese Society for Biomaterials, and The Australian Society for Biomaterials and the Korean Society for Biomaterials* **57**, 477-484 (2001).
- 26 Hiratsuka, T. *et al.* Enhanced bone formation onto the bone surface using a hydroxyapatite/collagen bone - like nanocomposite. *Journal of Biomedical Materials Research Part B: Applied Biomaterials* **108**, 391-398 (2020).
- 27 Eagleson, W., Deckert, K., Townsend, E. & Arnott, J. The effect of heat on the healing of fractures: a preliminary experimental report. *Canadian Medical Association Journal* **97**, 274 (1967).
- 28 Mayer, G. Rigid biological systems as models for synthetic composites. *Science* **310**, 1144-1147 (2005).
- 29 Bouville, F. *et al.* Strong, tough and stiff bioinspired ceramics from brittle constituents. *Nature materials* **13**, 508-514 (2014).
- 30 Bai, H., Chen, Y., Delattre, B., Tomsia, A. P. & Ritchie, R. O. Bioinspired large-scale aligned porous materials assembled with dual temperature gradients. *Science advances* **1**, e1500849 (2015).
- 31 Koyama, M. *et al.* Bone-like crack resistance in hierarchical metastable nanolaminate steels. *Science* **355**, 1055-1057 (2017).
- 32 Yang, Y. *et al.* Electrically assisted 3D printing of nacre-inspired structures with self-sensing capability. *Science advances* **5**, eaau9490 (2019).
- 33 Yang, X., Zhu, J., Qiu, L. & Li, D. Bioinspired effective prevention of restacking in multilayered graphene films: towards the next generation of high - performance supercapacitors. *Advanced materials* **23**, 2833-2838 (2011).
- 34 Guo, W. *et al.* Bio - inspired two - dimensional nanofluidic generators based on a layered graphene hydrogel membrane. *Advanced Materials* **25**, 6064-6068 (2013).
- 35 Hong, D. *et al.* Electrochemical release of amine molecules from carbamate-based, electroactive self-assembled monolayers. *Langmuir* **28**, 17-21 (2012).

- 36 Walther, A. *et al.* Large-area, lightweight and thick biomimetic composites with superior material properties via fast, economic, and green pathways. *Nano letters* **10**, 2742-2748 (2010).
- 37 Cruz-Silva, R. *et al.* Super-stretchable graphene oxide macroscopic fibers with outstanding knotability fabricated by dry film scrolling. *ACS nano* **8**, 5959-5967 (2014).
- 38 Wang, Z. *et al.* Bioinspired water - vapor - responsive organic/inorganic hybrid one - dimensional photonic crystals with tunable full - color stop band. *Advanced Functional Materials* **20**, 3784-3790 (2010).
- 39 Martini, R. & Barthelat, F. Stability of hard plates on soft substrates and application to the design of bioinspired segmented armor. *Journal of the Mechanics and Physics of Solids* **92**, 195-209 (2016).
- 40 Guttag, M. & Boyce, M. C. Locally and dynamically controllable surface topography through the use of particle - enhanced soft composites. *Advanced Functional Materials* **25**, 3641-3647 (2015).
- 41 Tandon, B., Magaz, A., Balint, R., Blaker, J. J. & Cartmell, S. H. Electroactive biomaterials: Vehicles for controlled delivery of therapeutic agents for drug delivery and tissue regeneration. *Advanced drug delivery reviews* **129**, 148-168 (2018).
- 42 Liu, Y. *et al.* Built - in electric fields dramatically induce enhancement of osseointegration. *Advanced Functional Materials* **27**, 1703771 (2017).
- 43 Holder, K. M. *et al.* Humidity-responsive gas barrier of hydrogen-bonded polymer-clay multilayer thin films. *The Journal of Physical Chemistry C* **116**, 19851-19856 (2012).
- 44 Zhuk, A., Mirza, R. & Sukhishvili, S. Multiresponsive clay-containing layer-by-layer films. *Acs Nano* **5**, 8790-8799 (2011).
- 45 Dou, Y. *et al.* Temperature-controlled electrochemical switch based on layered double hydroxide/poly (N-isopropylacrylamide) ultrathin films fabricated via layer-by-layer assembly. *Langmuir* **28**, 9535-9542 (2012).

- 46 Gao, H. Application of fracture mechanics concepts to hierarchical biomechanics of bone and bone-like materials. *International Journal of fracture* **138**, 101-137 (2006).
- 47 Ji, B. & Gao, H. Mechanical properties of nanostructure of biological materials. *Journal of the Mechanics and Physics of Solids* **52**, 1963-1990 (2004).
- 48 Liu, G., Ji, B., Hwang, K.-C. & Khoo, B. C. Analytical solutions of the displacement and stress fields of the nanocomposite structure of biological materials. *Composites Science and Technology* **71**, 1190-1195 (2011).
- 49 Almajid, A., Taya, M. & Hudnut, S. Analysis of out-of-plane displacement and stress field in a piezocomposite plate with functionally graded microstructure. *International Journal of Solids and Structures* **38**, 3377-3391 (2001).
- 50 NĂSTĂSESCU, V. & Marzavan, S. An overview of functionally graded material models. *Proceedings of the Romanian Academy, Series A: Mathematics, Physics, Technical Sciences, Information Science* **23** (2022).
- 51 Reuß, A. Berechnung der fließgrenze von mischkristallen auf grund der plastizitätsbedingung für einkristalle. *ZAMM - Journal of Applied Mathematics and Mechanics/Zeitschrift für Angewandte Mathematik und Mechanik* **9**, 49-58 (1929).
- 52 Mishnaevsky Jr, L. L. *Computational mesomechanics of composites: numerical analysis of the effect of microstructures of composites of strength and damage resistance*. (John Wiley & Sons, 2007).
- 53 Ju, J. Effective elastic moduli of two-phase composites containing randomly dispersed spherical inhomogeneities. *Acta Mechanica* **103**, 123-144 (1994).
- 54 Toudehdehghan, A., Lim, J., Foo, K. E., Ma'Arof, M. & Mathews, J. in *MATEC Web Conferences*. (EDP Sciences).
- 55 Akbarzadeh, A., Abedini, A. & Chen, Z. Effect of micromechanical models on structural responses of functionally graded plates. *Composite Structures* **119**, 598-609 (2015).
- 56 Mahamood, R. M., Akinlabi, E. T., Shukla, M. & Pityana, S. L. Functionally graded material: an overview. (2012).

- 57 Gasik, M. M. & Zhang, B. in *Materials Science Forum*. 183-186
(Aedermannsdorf, Switzerland: Trans Tech Publications, 1984-).
- 58 Bhardwaj, G., Singh, I. V., Mishra, B. & Bui, T. Numerical simulation of
functionally graded cracked plates using NURBS based XIGA under different
loads and boundary conditions. *Composite Structures* **126**, 347-359 (2015).
- 59 Cheng, Z., Gao, D. & Zhong, Z. Crack propagating in functionally graded coating
with arbitrarily distributed material properties bonded to homogeneous substrate.
Acta Mechanica Solida Sinica **23**, 437-446 (2010).
- 60 Zenkour, A. & Alghanmi, R. Stress analysis of a functionally graded plate
integrated with piezoelectric faces via a four-unknown shear deformation theory.
Results in Physics **12**, 268-277 (2019).
- 61 Jin, Z.-H. & Dodds Jr, R. Crack growth resistance behavior of a functionally
graded material: computational studies. *Engineering Fracture Mechanics* **71**,
1651-1672 (2004).
- 62 Tilbrook, M. T., Moon, R. J. & Hoffman, M. Crack propagation in graded
composites. *Composites science and technology* **65**, 201-220 (2005).
- 63 Li, Y. & Pan, E. Static bending and free vibration of a functionally graded
piezoelectric microplate based on the modified couple-stress theory. *International
Journal of Engineering Science* **97**, 40-59 (2015).
- 64 Torshizian, M. R. & Kargarnovin, M. H. The mixed-mode fracture mechanics
analysis of an embedded arbitrary oriented crack in a two-dimensional
functionally graded material plate. *Archive of Applied Mechanics* **84**, 625-637
(2014).
- 65 Fartash, A., Ayatollahi, M. & Bagheri, R. Transient response of dissimilar
piezoelectric layers with multiple interacting interface cracks. *Applied
Mathematical Modelling* **66**, 508-526 (2019).
- 66 Zhang, K. *et al.* Advanced smart biomaterials and constructs for hard tissue
engineering and regeneration. *Bone research* **6**, 31 (2018).
- 67 Jacob, J., More, N., Kalia, K. & Kapusetti, G. Piezoelectric smart biomaterials for
bone and cartilage tissue engineering. *Inflammation and regeneration* **38**, 2
(2018).

- 68 Naillon, M. Analysis of piezoelectric structures by a finite element method. *Acta electronica* **25**, 341-362 (1983).
- 69 Hosokawa, A. Numerical simulation of piezoelectric effect of bone under ultrasound irradiation. *Japanese Journal of Applied Physics* **54**, doi:10.7567/jjap.54.07hf06 (2015).
- 70 Abouelregal, A. E., Askar, S., Marin, M. & Mohamed, B. The theory of thermoelasticity with a memory-dependent dynamic response for a thermo-piezoelectric functionally graded rotating rod. *Scientific Reports* **13**, 9052 (2023).
- 71 Zhou, H. *et al.* Numerical simulation of failure of composite coatings due to thermal and hygroscopic stresses. *Coatings* **9**, 243 (2019).
- 72 Sih, G. C., Michopoulos, J. & Chou, S.-C. *Hygrothermoelasticity*. (Springer Science & Business Media, 1986).
- 73 Hou, P.-F. & Leung, A. Y. The transient responses of magneto-electro-elastic hollow cylinders. *Smart Materials and Structures* **13**, 762 (2004).
- 74 Jin, Z.-H. & Feng, Y. Thermal fracture resistance of a functionally graded coating with periodic edge cracks. *Surface and Coatings Technology* **202**, 4189-4197 (2008).
- 75 Ueda, S. & Nishimura, N. An annular crack in a functionally graded piezoelectric strip under thermoelectric loadings. *Journal of Thermal Stresses* **31**, 1079-1098 (2008).
- 76 Ueda, S., Okada, M. & Nakae, Y. Transient thermal response of a functionally graded piezoelectric laminate with a crack normal to the bimaterial interface. *Journal of Thermal Stresses* **41**, 98-118 (2018).
- 77 Mabuchi, Y. & Ueda, S. Transient thermal response of functionally graded piezoelectric laminates with an infinite row of parallel cracks normal to the bimaterial interface. *Theoretical and Applied Mechanics Letters* **9**, 289-292 (2019).
- 78 Nematollahi, M., Dini, A. & Hosseini, M. Thermo-magnetic analysis of thick-walled spherical pressure vessels made of functionally graded materials. *Applied Mathematics and Mechanics* **40**, 751-766 (2019).

- 79 Zenkour, A. Hygrothermoelastic responses of inhomogeneous piezoelectric and exponentially graded cylinders. *International Journal of Pressure Vessels and Piping* **119**, 8-18 (2014).
- 80 Dai, H. & Wang, X. Magneto–thermo–electro–elastic transient response in a piezoelectric hollow cylinder subjected to complex loadings. *International Journal of Solids and Structures* **43**, 5628-5646 (2006).
- 81 Dini, A. & Abolbashari, M. H. Hygro-thermo-electro-elastic response of a functionally graded piezoelectric cylinder resting on an elastic foundation subjected to non-axisymmetric loads. *International Journal of Pressure Vessels and Piping* **147**, 21-40 (2016).
- 82 Saadatfar, M. & Aghaie-Khafri, M. Hygrothermomagnetoelastic analysis of a functionally graded magnetoelastic hollow sphere resting on an elastic foundation. *Smart Materials and Structures* **23**, 035004 (2014).
- 83 Qin, Q.-H. & Zhang, X. Crack deflection at an interface between dissimilar piezoelectric materials. *International journal of fracture* **102**, 355-370 (2000).
- 84 Ming-Yuan, H. & Hutchinson, J. W. Crack deflection at an interface between dissimilar elastic materials. *International journal of solids and structures* **25**, 1053-1067 (1989).
- 85 Simha, N., Fischer, F., Kolednik, O. & Chen, C. Inhomogeneity effects on the crack driving force in elastic and elastic–plastic materials. *Journal of the Mechanics and Physics of Solids* **51**, 209-240 (2003).
- 86 Kolednik, O., Predan, J., Fischer, F. D. & Fratzl, P. Improvements of strength and fracture resistance by spatial material property variations. *Acta materialia* **68**, 279-294 (2014).
- 87 Fratzl, P., Gupta, H. S., Fischer, F. D. & Kolednik, O. Hindered crack propagation in materials with periodically varying Young's modulus—lessons from biological materials. *Advanced Materials* **19**, 2657-2661 (2007).
- 88 Suresh, S. *Fatigue of materials*. (Cambridge university press, 1998).
- 89 Rooke, D. P. & Cartwright, D. J. Compendium of stress intensity factors. (*No Title*) (1976).

- 90 Park, S. & Sun, C.-T. Effect of electric field on fracture of piezoelectric ceramics. *International Journal of Fracture* **70**, 203-216 (1993).
- 91 Banks-Sills, L. in *Proceedings of 13th International Conferences on Fracture*. 1-7.
- 92 Hu, K., Jin, H., Yang, Z. & Chen, X. Interface crack between dissimilar one-dimensional hexagonal quasicrystals with piezoelectric effect. *Acta Mechanica* **230**, 2455-2474 (2019).
- 93 Fang, D., Zhang, Z.-K., Soh, A. K. & Lee, K. L. Fracture criteria of piezoelectric ceramics with defects. *Mechanics of Materials* **36**, 917-928, doi:10.1016/j.mechmat.2003.08.011 (2004).
- 94 Park, S. & Sun, C. T. Fracture criteria for piezoelectric ceramics. *Journal of the american ceramic society* **78**, 1475-1480 (1995).
- 95 Kaminski, W. Hyperbolic heat conduction equation for materials with a nonhomogeneous inner structure. (1990).
- 96 Rastenaar, S. in *Thermal and Optical Interactions with Biological and Related Composite Materials*. 114-117 (SPIE).
- 97 Mitra, K., Kumar, S., Vedevarz, A. & Moallemi, M. Experimental evidence of hyperbolic heat conduction in processed meat. (1995).
- 98 Ozisik, M. & Tzou, D. On the wave theory in heat conduction. (1994).
- 99 Shih, T. C., Kou, H. S., Liauh, C. T. & Lin, W. L. The impact of thermal wave characteristics on thermal dose distribution during thermal therapy: a numerical study. *Medical Physics* **32**, 3029-3036 (2005).
- 100 Liu, J. Preliminary survey on the mechanisms of the wave-like behaviors of heat transfer in living tissues. *Forschung im Ingenieurwesen* **66**, 1-10 (2000).
- 101 Liu, J., Chen, X. & Xu, L. X. New thermal wave aspects on burn evaluation of skin subjected to instantaneous heating. *IEEE transactions on biomedical engineering* **46**, 420-428 (1999).
- 102 Lu, W.-Q., Liu, J. & Zeng, Y. Simulation of the thermal wave propagation in biological tissues by the dual reciprocity boundary element method. *Engineering Analysis with Boundary Elements* **22**, 167-174 (1998).

- 103 Deng, Z.-S. & Liu, J. Non-Fourier heat conduction effect on prediction of temperature transients and thermal stress in skin cryopreservation. *Journal of Thermal Stresses* **26**, 779-798 (2003).
- 104 Banerjee, A., Ogale, A. A., Das, C., Mitra, K. & Subramanian, C. Temperature distribution in different materials due to short pulse laser irradiation. *Heat transfer engineering* **26**, 41-49 (2005).
- 105 Vernotte, P. Some possible complications in the phenomena of thermal conduction. *Compte Rendus* **252**, 2190-2191 (1961).
- 106 Cattaneo, C. A form of heat-conduction equations which eliminates the paradox of instantaneous propagation. *Comptes rendus* **247**, 431 (1958).
- 107 Wang, L. & Wei, X. Equivalence between dual-phase-lagging and two-phase-system heat conduction processes. *International Journal of Heat and Mass Transfer* **51**, 1751-1756 (2008).
- 108 Wang, L. & Wei, X. Heat conduction in nanofluids. *Chaos, Solitons & Fractals* **39**, 2211-2215 (2009).
- 109 Tzou, D. Y. *Macro-to microscale heat transfer: the lagging behavior*. (John Wiley & Sons, 2014).
- 110 Hristov, J. Bio-heat models revisited: Concepts, derivations, nondimensionalization and fractionalization approaches. *Frontiers in Physics* **7**, 189 (2019).
- 111 Du, B., Xu, G., Xue, D. & Wang, J. Fractional thermal wave bio-heat equation based analysis for living biological tissue with non-Fourier Neumann boundary condition in laser pulse heating. *Optik* **247**, 167811 (2021).
- 112 Kaur, I., Lata, P. & Handa, K. Effects of memory dependent derivative of bio-heat model in skin tissue exposed to laser radiation. *EAI Endorsed Transactions on Pervasive Health and Technology* **6** (2020).
- 113 Wang, X., Qi, H., Yang, X. & Xu, H. Analysis of the time-space fractional bioheat transfer equation for biological tissues during laser irradiation. *International Journal of Heat and Mass Transfer* **177**, 121555 (2021).
- 114 Hobiny, A., Alzahrani, F., Abbas, I. & Marin, M. The effect of fractional time derivative of bioheat model in skin tissue induced to laser irradiation. *Symmetry* **12**, 602 (2020).

- 115 Ezzat, M. A., El - bary, A. A. & Al - sowayan, N. S. Tissue responses to fractional transient heating with sinusoidal heat flux condition on skin surface. *Animal Science Journal* **87**, 1304-1311 (2016).
- 116 Ezzat, M. A., AlSowayan, N. S., Al-Muhiameed, Z. I. & Ezzat, S. M. Fractional modelling of Pennes' bioheat transfer equation. *Heat and Mass Transfer* **50**, 907-914 (2014).
- 117 Ghanmi, A. & Abbas, I. A. An analytical study on the fractional transient heating within the skin tissue during the thermal therapy. *Journal of thermal biology* **82**, 229-233 (2019).
- 118 Mondal, S., Sur, A. & Kanoria, M. Transient heating within skin tissue due to time-dependent thermal therapy in the context of memory dependent heat transport law. *Mechanics Based Design of Structures and Machines* **49**, 271-285 (2021).
- 119 Caponetto, R., Sapuppo, F., Tomasello, V., Maione, G. & Lino, P. Fractional-order identification and control of heating processes with non-continuous materials. *Entropy* **18**, 398 (2016).
- 120 Bashir, M. & Rajendran, P. Recent trends in piezoelectric smart materials and its actuators for morphing aircraft development. *IREME* **13**, 117-125 (2019).
- 121 Daniela, R. & Tolley, M. Design fabrication and control of origami robots. *Nature Reviews Materials* **3**, 101-112 (2018).
- 122 Wang, Y. *et al.* Hydro-sensitive sandwich structures for self-tunable smart electromagnetic shielding. *Chemical Engineering Journal* **344**, 342-352 (2018).
- 123 Qian, W., Yang, W., Zhang, Y., Bowen, C. R. & Yang, Y. Piezoelectric materials for controlling electro-chemical processes. *Nano-Micro Letters* **12**, 1-39 (2020).
- 124 Ueda, S. Transient response of a cracked piezoelectric strip under thermoelectric loading. *Journal of Thermal Stresses* **29**, 973-994 (2006).
- 125 Arani, A. G., Kolahchi, R. & Barzoki, A. M. Effect of material in-homogeneity on electro-thermo-mechanical behaviors of functionally graded piezoelectric rotating shaft. *Applied Mathematical Modelling* **35**, 2771-2789 (2011).
- 126 Shi, P. Singular integral equation method for 2D fracture analysis of orthotropic solids containing doubly periodic strip-like cracks on rectangular lattice arrays

- under longitudinal shear loading. *Applied Mathematical Modelling* **77**, 1460-1473 (2020).
- 127 Wang, P., Wang, K., Wang, B., Zhang, C. & Fang, D. Fracture of thermoelectric materials: An electrical and thermal strip saturation model. *Engineering Fracture Mechanics* **235**, 107186 (2020).
- 128 Wang, Z.-h. *et al.* Anti-plane crack problem of a functionally graded piezoelectric materials strip with arbitrarily distributed properties. *Acta Mechanica* **231**, 1029-1043 (2020).
- 129 Zhou, Y.-T. & Kim, T.-W. A moving thermal dielectric crack in piezoelectric ceramics with a shearing force applied on its surface. *Applied Mathematical Modelling* **63**, 1-17 (2018).
- 130 Dhanesh, N. & Kapuria, S. Edge effects in elastic and piezoelectric laminated panels under thermal loading. *Journal of Thermal Stresses* **41**, 1577-1596 (2018).
- 131 Barati, M. R. & Zenkour, A. M. Electro-thermoelastic vibration of plates made of porous functionally graded piezoelectric materials under various boundary conditions. *Journal of Vibration and Control* **24**, 1910-1926 (2018).
- 132 Guo, S., Wang, K. & Wang, B. Dual-phase-lagging heat conduction and associated thermal shock fracture of sandwich composite plates. *International Journal of Heat and Mass Transfer* **139**, 317-329 (2019).
- 133 Ahmed, E. A., Abou-Dina, M. & Ghaleb, A. Plane wave propagation in a piezo-thermoelastic rotating medium within the dual-phase-lag model. *Microsystem Technologies* **26**, 969-979 (2020).
- 134 Li, J. & Wang, B. Numerical analysis of temperature field and thermal stress associated with dual-phase-lag heat conduction. *Mechanics of Advanced Materials and Structures* **27**, 1304-1311 (2020).
- 135 Babaei, M. & Chen, Z. The transient coupled thermo-piezoelectric response of a functionally graded piezoelectric hollow cylinder to dynamic loadings. *Proceedings of the Royal Society A: Mathematical, Physical and Engineering Sciences* **466**, 1077-1091 (2010).

- 136 Pourasghar, A. & Chen, Z. Hyperbolic heat conduction and thermoelastic solution of functionally graded CNT reinforced cylindrical panel subjected to heat pulse. *International Journal of Solids and Structures* **163**, 117-129 (2019).
- 137 Chen, Z. & Hu, K. Thermoelastic analysis of a cracked substrate bonded to a coating using the hyperbolic heat conduction theory. *Journal of Thermal Stresses* **37**, 270-291 (2014).
- 138 Zhou, Y.-T., Zhang, C., Zhong, Z. & Wang, L. Transient thermo-electro-elastic contact analysis of a sliding punch acting on a functionally graded piezoelectric strip under non-Fourier heat conduction. *European Journal of Mechanics-A/Solids* **73**, 90-100 (2019).
- 139 Mondal, S., Sur, A. & Kanoria, M. Transient response in a piezoelectric medium due to the influence of magnetic field with memory-dependent derivative. *Acta Mechanica* **230**, 2325-2338 (2019).
- 140 Wang, B. & Li, J. E. Hyperbolic heat conduction and associated transient thermal fracture for a piezoelectric material layer. *International Journal of Solids and Structures* **50**, 1415-1424 (2013).
- 141 Povstenko, Y. Theories of thermal stresses based on space–time-fractional telegraph equations. *Computers & Mathematics with Applications* **64**, 3321-3328 (2012).
- 142 Povstenko, Y. Fractional Cattaneo-type equations and generalized thermoelasticity. *Journal of thermal Stresses* **34**, 97-114 (2011).
- 143 Povstenko, Y. Z. Fractional heat conduction equation and associated thermal stress. *Journal of Thermal Stresses* **28**, 83-102 (2004).
- 144 Li, X. & Tian, X. Fractional order thermo-viscoelastic theory of biological tissue with dual phase lag heat conduction model. *Applied Mathematical Modelling* **95**, 612-622 (2021).
- 145 Zhang, X.-Y., Xie, Y.-J. & Li, X.-F. Transient thermoelastic response in a cracked strip of functionally graded materials via generalized fractional heat conduction. *Applied Mathematical Modelling* **70**, 328-349 (2019).

- 146 Abo - Dahab, S., Abouelregal, A. E. & Ahmad, H. Fractional heat conduction model with phase lags for a half - space with thermal conductivity and temperature dependent. *Mathematical Methods in the Applied Sciences* (2020).
- 147 Povstenko, Y. & Kyrylych, T. Time-fractional heat conduction in an infinite plane containing an external crack under heat flux loading. *Computers & Mathematics with Applications* **78**, 1386-1395 (2019).
- 148 Povstenko, Y. & Kyrylych, T. Time-fractional heat conduction in a plane with two external half-infinite line slits under heat flux loading. *Symmetry* **11**, 689 (2019).
- 149 Povstenko, Y. & Kyrylych, T. Fractional thermoelasticity problem for a plane with a line crack under heat flux loading. *Journal of Thermal Stresses* **41**, 1313-1328 (2018).
- 150 Abro, K. A. & Atangana, A. A comparative analysis of electromechanical model of piezoelectric actuator through Caputo–Fabrizio and Atangana–Baleanu fractional derivatives. *Mathematical Methods in the Applied Sciences* **43**, 9681-9691 (2020).
- 151 Kumar, R. & Sharma, P. Analysis of plane waves in anisotropic magneto-piezothermoelastic diffusive body with fractional order derivative. (2017).
- 152 Yu, Y. J. & Deng, Z. C. Fractional order theory of Cattaneo-type thermoelasticity using new fractional derivatives. *Applied Mathematical Modelling* **87**, 731-751 (2020).
- 153 Ma, Y. & He, T. The transient response of a functionally graded piezoelectric rod subjected to a moving heat source under fractional order theory of thermoelasticity. *Mechanics of Advanced Materials and Structures* **24**, 789-796 (2017).
- 154 Xue, Z., Liu, J., Tian, X. & Yu, Y. Thermal shock fracture associated with a unified fractional heat conduction. *European Journal of Mechanics-A/Solids* **85**, 104129 (2021).
- 155 Ezzat, M. A. & El Karamany, A. S. Theory of fractional order in electro-thermoelasticity. *European Journal of Mechanics-A/Solids* **30**, 491-500 (2011).

- 156 Ezzat, M. A. Theory of fractional order in generalized thermoelectric MHD. *Applied Mathematical Modelling* **35**, 4965-4978 (2011).
- 157 Ma, Y. & He, T. Investigation on a thermo-piezoelectric problem with temperature-dependent properties under fractional order theory of thermoelasticity. *Mechanics of Advanced Materials and Structures* **26**, 552-558 (2019).
- 158 Guo, H., Li, C. & Tian, X. A modified fractional-order generalized piezoelectric thermoelasticity model with variable thermal conductivity. *Journal of Thermal Stresses* **41**, 1538-1557 (2018).
- 159 Arfken, G. B., Weber, H. J. & Harris, F. E. *Mathematical methods for physicists: a comprehensive guide*. (Academic press, 2011).
- 160 Saha, S. *Differential Equations: First and Second Order Linear Differential Equations*. (Momentum Press, 2015).
- 161 Erdogan, F., Gupta, G. & Cook, T. in *Methods of analysis and solutions of crack problems: Recent developments in fracture mechanics Theory and methods of solving crack problems* 368-425 (Springer, 1973).
- 162 Ding, H.-J., Guo, F.-L. & Hou, P.-F. A general solution for piezothermoelasticity of transversely isotropic piezoelectric materials and its applications. *International journal of engineering science* **38**, 1415-1440 (2000).
- 163 Delale, F. & Erdogan, F. Effect of transverse shear and material orthotropy in a cracked spherical cap. *International Journal of solids and structures* **15**, 907-926 (1979).
- 164 Wang, B. & Mai, Y. A cracked piezoelectric material strip under transient thermal loading. *J. Appl. Mech.* **69**, 539-546 (2002).
- 165 Miller, M. K. & Guy, J., WT. Numerical inversion of the Laplace transform by use of Jacobi polynomials. *SIAM Journal on Numerical Analysis* **3**, 624-635 (1966).
- 166 He, Z., Zhu, Y., Xia, J. & Wu, H. Optimization design on simultaneously strengthening and toughening graphene-based nacre-like materials through noncovalent interaction. *Journal of the Mechanics and Physics of Solids* **133**, 103706 (2019).

- 167 Wang, X. *et al.* Bioinspired highly anisotropic, ultrastrong and stiff, and osteoconductive mineralized wood hydrogel composites for bone repair. *Advanced Functional Materials* **31**, 2010068 (2021).
- 168 Grossman, M. *et al.* Hierarchical toughening of nacre - like composites. *Advanced Functional Materials* **29**, 1806800 (2019).
- 169 Zhou, W., Sun, X., Tsutsumi, Y., Nomura, N. & Hanawa, T. Bioinspired low-magnetic Zr alloy with high strength and ductility. *Scripta Materialia* **199**, 113856 (2021).
- 170 Tan, G. *et al.* Nature - inspired nacre - like composites combining human tooth - matching elasticity and hardness with exceptional damage tolerance. *Advanced Materials* **31**, 1904603 (2019).
- 171 Ji, H.-M., Zhang, W.-Q., Wang, X. & Li, X.-W. Three-point bending fracture behavior of single oriented crossed-lamellar structure in *Scapharca broughtonii* shell. *Materials* **8**, 6154-6162 (2015).
- 172 Li, X. *et al.* Coarsening kinetics of lamellar microstructures: Experiments and simulations on a fully-lamellar Fe-Al in situ composite. *Acta materialia* **127**, 230-243 (2017).
- 173 Grunfelder, L. *et al.* Bio-inspired impact-resistant composites. *Acta biomaterialia* **10**, 3997-4008 (2014).
- 174 Dimas, L. S., Bratzel, G. H., Eylon, I. & Buehler, M. J. Tough composites inspired by mineralized natural materials: computation, 3D printing, and testing. *Advanced Functional Materials* **23**, 4629-4638 (2013).
- 175 Ghimire, A., Tsai, Y.-Y., Chen, P.-Y. & Chang, S.-W. Tunable interface hardening: Designing tough bio-inspired composites through 3D printing, testing, and computational validation. *Composites Part B: Engineering* **215**, 108754 (2021).
- 176 Tan, T. *et al.* Mechanical properties of functionally graded hierarchical bamboo structures. *Acta biomaterialia* **7**, 3796-3803 (2011).
- 177 Mirzaali, M. *et al.* Mechanics of bioinspired functionally graded soft-hard composites made by multi-material 3D printing. *Composite Structures* **237**, 111867 (2020).

- 178 Mirzaali, M. J. *et al.* Multi - material 3D printing of functionally graded hierarchical soft–hard composites. *Advanced Engineering Materials* **22**, 1901142 (2020).
- 179 Ko, K., Jin, S., Lee, S. E., Lee, I. & Hong, J.-W. Bio-inspired bimaterial composites patterned using three-dimensional printing. *Composites Part B: Engineering* **165**, 594-603 (2019).
- 180 Zhang, Y. *et al.* Design ductile and work-hardenable composites with all brittle constituents. *Acta Materialia* **208**, 116770 (2021).
- 181 Wilkerson, R. P. *et al.* A study of size effects in bioinspired, “nacre-like”, metal-compliant-phase (nickel-alumina) coextruded ceramics. *Acta Materialia* **148**, 147-155 (2018).
- 182 Magrini, T. *et al.* Transparent Nacre - like Composites Toughened through Mineral Bridges. *Advanced Functional Materials* **30**, 2002149 (2020).
- 183 Morits, M. *et al.* Toughness and fracture properties in nacre - mimetic clay/polymer nanocomposites. *Advanced Functional Materials* **27**, 1605378 (2017).
- 184 Wat, A. *et al.* Bioinspired nacre-like alumina with a bulk-metallic glass-forming alloy as a compliant phase. *Nature communications* **10**, 961 (2019).
- 185 Meijer, G., Ellyin, F. & Xia, Z. Aspects of residual thermal stress/strain in particle reinforced metal matrix composites. *Composites Part B: Engineering* **31**, 29-37 (2000).
- 186 Zhang, X., Liu, W., Yang, D. & Qiu, X. Biomimetic supertough and strong biodegradable polymeric materials with improved thermal properties and excellent UV - blocking performance. *Advanced Functional Materials* **29**, 1806912 (2019).
- 187 Liu, L. *et al.* A novel strategy for simultaneously improving the fire safety, water resistance and compatibility of thermoplastic polyurethane composites through the construction of biomimetic hydrophobic structure of intumescent flame retardant synergistic system. *Composites Part B: Engineering* **176**, 107218 (2019).

- 188 Giunta, G., Crisafulli, D., Belouettar, S. & Carrera, E. A thermo-mechanical analysis of functionally graded beams via hierarchical modelling. *Composite Structures* **95**, 676-690 (2013).
- 189 Kiani, Y. & Eslami, M. Thermal buckling analysis of functionally graded material beams. *International Journal of Mechanics and Materials in Design* **6**, 229-238 (2010).
- 190 Swaminathan, K. & Sangeetha, D. Thermal analysis of FGM plates—A critical review of various modeling techniques and solution methods. *Composite Structures* **160**, 43-60 (2017).
- 191 Malekzadeh, P. & Monajjemzadeh, S. Dynamic response of functionally graded plates in thermal environment under moving load. *Composites Part B: Engineering* **45**, 1521-1533 (2013).
- 192 Peng, X.-L. & Li, X.-F. Thermal stress in rotating functionally graded hollow circular disks. *Composite Structures* **92**, 1896-1904 (2010).
- 193 Oddone, V., Boerner, B. & Reich, S. Composites of aluminum alloy and magnesium alloy with graphite showing low thermal expansion and high specific thermal conductivity. *Science and Technology of advanced MaTerialS* **18**, 180-186 (2017).
- 194 Fehér, A. & Kovács, R. Novel evaluation method for non-Fourier effects in heat pulse experiments. *arXiv preprint arXiv:2101.01123* (2021).
- 195 Roetzel, W., Putra, N. & Das, S. K. Experiment and analysis for non-Fourier conduction in materials with non-homogeneous inner structure. *International Journal of Thermal Sciences* **42**, 541-552 (2003).
- 196 Gong, X., Bustillo, J., Blanc, L. & Gautier, G. FEM simulation on elastic parameters of porous silicon with different pore shapes. *International Journal of Solids and Structures* **190**, 238-243 (2020).
- 197 Verma, K. P. & Maiti, D. K. Transient analysis of thermo-mechanically shock loaded four-parameter power law functionally graded shells. *Composite Structures* **257**, 113388 (2021).

- 198 He, C. *et al.* A hierarchical multiscale model for the elastic-plastic damage behavior of 3D braided composites at high temperature. *Composites Science and Technology* **196**, 108230 (2020).
- 199 Demirbas, M. D. Thermal stress analysis of functionally graded plates with temperature-dependent material properties using theory of elasticity. *Composites Part B: Engineering* **131**, 100-124 (2017).
- 200 Pandey, S. & Pradyumna, S. A finite element formulation for thermally induced vibrations of functionally graded material sandwich plates and shell panels. *Composite Structures* **160**, 877-886 (2017).
- 201 Gilbert, P. *et al.* Gradual ordering in red abalone nacre. *Journal of the American Chemical Society* **130**, 17519-17527 (2008).
- 202 Abdel-Hamid, B. Modelling non-Fourier heat conduction with periodic thermal oscillation using the finite integral transform. *Applied Mathematical Modelling* **23**, 899-914 (1999).
- 203 Erdogan, F. & Wu, B. Crack problems in FGM layers under thermal stresses. *Journal of thermal stresses* **19**, 237-265 (1996).
- 204 Anderson, T. L. *Fracture mechanics: fundamentals and applications*. (CRC press, 2017).
- 205 Song, P. *et al.* Granular nanostructure: a facile biomimetic strategy for the design of supertough polymeric materials with high ductility and strength. *Advanced Materials* **29**, 1704661 (2017).
- 206 Zhang, Z. *et al.* Lightweight Structural Biomaterials with Excellent Mechanical Performance: A Review. *Biomimetics* **8**, 153 (2023).
- 207 Lv, S. *et al.* Designed biomaterials to mimic the mechanical properties of muscles. *Nature* **465**, 69-73 (2010).
- 208 Zhang, H. *et al.* Rational Design of Soft–Hard Interfaces through Bioinspired Engineering. *Small* **19**, 2204498 (2023).
- 209 Ceylan, H. *et al.* 3D printed personalized magnetic micromachines from patient blood–derived biomaterials. *Science Advances* **7**, eabh0273 (2021).

- 210 Balu, R., Dutta, N. K., Dutta, A. K. & Choudhury, N. R. Resilin-mimetics as a smart biomaterial platform for biomedical applications. *Nature Communications* **12**, 149 (2021).
- 211 Deng, Y., Ren, Y., Fu, X. & Jiang, H. Bionic-bamboo design for enhancing the crashworthiness of composite tube with groove trigger subjected to oblique load. *International Journal of Mechanical Sciences* **206**, 106635 (2021).
- 212 An, L. *et al.* Crack modes and toughening strategies of bioinspired 3D printed double-helicoidal architectures. *International Journal of Mechanical Sciences* **253**, 108388 (2023).
- 213 Wang, Y., Naleway, S. E. & Wang, B. Biological and bioinspired materials: Structure leading to functional and mechanical performance. *Bioactive materials* **5**, 745-757 (2020).
- 214 Song, S. *et al.* Bioinspired engineering of gradient and hierarchical architecture into pressure sensors toward high sensitivity within ultra-broad working range. *Nano Energy* **100**, 107513 (2022).
- 215 Wegst, U. G., Bai, H., Saiz, E., Tomsia, A. P. & Ritchie, R. O. Bioinspired structural materials. *Nature materials* **14**, 23-36 (2015).
- 216 Wei, Z. & Xu, X. Gradient design of bio-inspired nacre-like composites for improved impact resistance. *Composites Part B: Engineering* **215**, 108830 (2021).
- 217 Ko, K., Jin, S., Lee, S. E. & Hong, J.-W. Impact resistance of nacre-like composites diversely patterned by 3D printing. *Composite Structures* **238**, 111951 (2020).
- 218 Zhang, Q., Li, H., Liu, Y., Zhang, Z. & Yuan, Y. Nacre-inspired topological design tuning the impact resistant behaviors of composite plates. *Composite Structures* **299**, 116077 (2022).
- 219 Cong, C., Wei, Y. & Wei, X. Trans-scale dynamic shear-lag model for wave attenuation in staggered composites. *International Journal of Mechanical Sciences* **238**, 107841 (2023).
- 220 Sun, J. & Bhushan, B. Hierarchical structure and mechanical properties of nacre: a review. *Rsc Advances* **2**, 7617-7632 (2012).

- 221 San Ha, N. & Lu, G. A review of recent research on bio-inspired structures and materials for energy absorption applications. *Composites Part B: Engineering* **181**, 107496 (2020).
- 222 Hu, Z.-J., Guo, R.-F., Chen, S.-M., Jin, Q. & Shen, P. Synthesis of damage-tolerant Cu-matrix composites with nacre-inspired laminate-reticular hierarchical architecture via tuning compositional wettability. *Scripta Materialia* **186**, 312-316 (2020).
- 223 Ghazlan, A., Ngo, T., Van Le, T., Nguyen, T. & Remennikov, A. Blast performance of a bio-mimetic panel based on the structure of nacre—a numerical study. *Composite Structures* **234**, 111691 (2020).
- 224 Tran, P., Ngo, T. D., Ghazlan, A. & Hui, D. Bimaterial 3D printing and numerical analysis of bio-inspired composite structures under in-plane and transverse loadings. *Composites Part B: Engineering* **108**, 210-223 (2017).
- 225 Otero, J., Castellero, J. & Ramos, R. Homogenization of heterogeneous piezoelectric medium. *Mechanics Research Communications* **24**, 75-84 (1997).
- 226 Gałka, A., Telega, J. & Wojnar, R. Homogenization and thermopiezoelectricity. *Mechanics Research Communications* **19**, 315-324 (1992).
- 227 Vatanabe, S., Paulino, G. & Silva, E. Design of functionally graded piezocomposites using topology optimization and homogenization—Toward effective energy harvesting materials. *Computer Methods in Applied Mechanics and Engineering* **266**, 205-218 (2013).
- 228 Sanchez-Palencia, E. & Zaoui, A. Homogenization techniques for composite media. *Homogenization techniques for composite media* **272** (1987).
- 229 Rubio, W. M., Buiocchi, F., Adamowski, J. C. & Silva, E. C. N. Modeling of functionally graded piezoelectric ultrasonic transducers. *Ultrasonics* **49**, 484-494 (2009).
- 230 Smith, M. & Kar-Narayan, S. Piezoelectric polymers: Theory, challenges and opportunities. *International Materials Reviews* **67**, 65-88 (2022).
- 231 Bera, S. *et al.* Molecular engineering of piezoelectricity in collagen-mimicking peptide assemblies. *Nature communications* **12**, 2634 (2021).

- 232 Khare, D., Basu, B. & Dubey, A. K. Electrical stimulation and piezoelectric biomaterials for bone tissue engineering applications. *Biomaterials* **258**, 120280 (2020).
- 233 Korostoff, E. Stress generated potentials in bone: relationship to piezoelectricity of collagen. *Journal of biomechanics* **10**, 41-44 (1977).
- 234 Ahn, A. C. & Grodzinsky, A. J. Relevance of collagen piezoelectricity to “Wolff’s Law”: a critical review. *Medical engineering & physics* **31**, 733-741 (2009).
- 235 Zaszczyńska, A., Gradys, A. & Sajkiewicz, P. Progress in the applications of smart piezoelectric materials for medical devices. *Polymers* **12**, 2754 (2020).
- 236 Panda, S. *et al.* Piezoelectric energy harvesting systems for biomedical applications. *Nano Energy* **100**, 107514 (2022).
- 237 Kim, S., Laschi, C. & Trimmer, B. Soft robotics: a bioinspired evolution in robotics. *Trends in biotechnology* **31**, 287-294 (2013).
- 238 Sharma, A. Effect of porosity on active vibration control of smart structure using porous functionally graded piezoelectric material. *Composite Structures* **280**, 114815 (2022).
- 239 Hu, W. & Alici, G. Bioinspired three-dimensional-printed helical soft pneumatic actuators and their characterization. *Soft robotics* **7**, 267-282 (2020).
- 240 Gu, G.-Y., Zhu, J., Zhu, L.-M. & Zhu, X. A survey on dielectric elastomer actuators for soft robots. *Bioinspiration & biomimetics* **12**, 011003 (2017).
- 241 Poppinga, S. *et al.* Toward a new generation of smart biomimetic actuators for architecture. *Advanced Materials* **30**, 1703653 (2018).
- 242 Xavier, M. S., Harrison, S. M., Howard, D., Yong, Y. K. & Fleming, A. J. Modeling of soft fluidic actuators using fluid–structure interaction simulations with underwater applications. *International Journal of Mechanical Sciences* **255**, 108437 (2023).
- 243 Cui, C., Chen, L., Feng, S., Cui, X. & Lu, J. Compressive resistance of the bio-inspired cuttlebone-like sandwich structure under quasi-static load. *International Journal of Mechanical Sciences* **248**, 108222 (2023).

- 244 Li, B., Liu, H., Zhang, Q., Yang, X. & Yang, J. Crushing behavior and energy absorption of a bio-inspired bi-directional corrugated lattice under quasi-static compression load. *Composite Structures* **286**, 115315 (2022).
- 245 Patidar, D. & Pal, V. K. Deformation behaviour of interconnect encapsulated on functionally graded stretchable substrates. *International Journal of Mechanical Sciences*, 108539 (2023).
- 246 Gao, Z., Zhang, H., Zhao, J. & Ruan, D. The axial crushing performance of bio-inspired hierarchical multi-cell hexagonal tubes. *International Journal of Mechanical Sciences* **239**, 107880 (2023).
- 247 Wang, Z., Luo, Q., Li, Q. & Sun, G. Design optimization of bioinspired helicoidal CFRPP/GFRPP hybrid composites for multiple low-velocity impact loads. *International Journal of Mechanical Sciences* **219**, 107064 (2022).
- 248 Abeer, R., Naseer, M. & Abel, E. Capacitively coupled electrical stimulation treatment: results from patients with failed long bone fracture unions. *Journal of orthopaedic trauma* **12**, 510-513 (1998).
- 249 Kamel, N. A. Bio-piezoelectricity: Fundamentals and applications in tissue engineering and regenerative medicine. *Biophysical Reviews* **14**, 717-733 (2022).
- 250 Impagliazzo, A., Mattei, A., Spurio Pompili, G., Setti, S. & Cadossi, R. Treatment of nonunited fractures with capacitively coupled electric field. *Journal of Orthopaedics and Traumatology* **7**, 16-22 (2006).
- 251 Jiao, D. *et al.* Electrical switching of high-performance bioinspired nanocellulose nanocomposites. *Nature communications* **12**, 1312 (2021).
- 252 Shao, H., Wei, S., Jiang, X., Holmes, D. P. & Ghosh, T. K. Bioinspired electrically activated soft bistable actuators. *Advanced Functional Materials* **28**, 1802999 (2018).
- 253 Jayendiran, R. & Arockiarajan, A. Experimental characterization and numerical modeling of time-dependent electro-mechanical response of piezocomposites. *International Journal of Mechanical Sciences* **100**, 250-261 (2015).
- 254 Mha, P. T., Maréchal, P., Ntamack, G. E. & d'Ouazzane, S. C. Homogenized electromechanical coefficients and effective parameters of 1–3 piezocomposites for ultrasound imaging transducers. *Physics Letters A* **408**, 127492 (2021).

- 255 Singh, S., Krishnaswamy, J. A. & Melnik, R. Biological cells and coupled electro-mechanical effects: The role of organelles, microtubules, and nonlocal contributions. *journal of the mechanical behavior of biomedical materials* **110**, 103859 (2020).
- 256 Krishnaswamy, J. A., Rodriguez-Tembleque, L., Melnik, R., Buroni, F. C. & Saez, A. Size dependent electro-elastic enhancement in geometrically anisotropic lead-free piezocomposites. *International Journal of Mechanical Sciences* **182**, 105745 (2020).
- 257 Mamache, F. E., Mesbah, A., Zaïri, F. & Vozniak, I. A Coupled Electro-Mechanical Homogenization-Based Model for PVDF-Based Piezo-Composites Considering $\alpha \rightarrow \beta$ Phase Transition and Interfacial Damage. *Polymers* **15**, 2994 (2023).
- 258 Wang, Y. Q. & Zu, J. W. Vibration behaviors of functionally graded rectangular plates with porosities and moving in thermal environment. *Aerospace Science and Technology* **69**, 550-562 (2017).
- 259 Naik, A. K., Nazeer, M., Prasad, D., Laha, T. & Roy, S. Development of functionally graded ZrB₂-B₄C composites for lightweight ultrahigh-temperature aerospace applications. *Ceramics International* **48**, 33332-33339 (2022).
- 260 Miteva, A. & Bouzekova-Penkova, A. Some aerospace applications of functionally graded materials. *Aerosp. Res. Bulg* **33**, 195-209 (2021).
- 261 Fazzolari, F. & Carrera, E. Thermal stability of FGM sandwich plates under various through-the-thickness temperature distributions. *Journal of Thermal Stresses* **37**, 1449-1481 (2014).
- 262 Zhang, S.-Q., Huang, Z.-T., Zhao, Y.-F., Ying, S.-S. & Ma, S.-Y. Static and dynamic analyses of FGPM cylindrical shells with quadratic thermal gradient distribution. *Composite Structures* **277**, 114658 (2021).
- 263 Koizumi, M. FGM activities in Japan. *Composites part b: engineering* **28**, 1-4 (1997).
- 264 Silva, E. C. N., Walters, M. C. & Paulino, G. H. in *AIP conference proceedings*. 754-759 (American Institute of Physics).

- 265 Dascalu, C. & Maugin, G. On the dynamic fracture of piezoelectric materials. *The Quarterly Journal of Mechanics and Applied Mathematics* **48**, 237-255 (1995).
- 266 Liu, F., Li, T., Jia, Z. & Wang, L. Combination of stiffness, strength, and toughness in 3D printed interlocking nacre-like composites. *Extreme Mechanics Letters* **35**, 100621 (2020).
- 267 Mirzaeifar, R., Dimas, L. S., Qin, Z. & Buehler, M. J. Defect-tolerant bioinspired hierarchical composites: simulation and experiment. *ACS Biomaterials Science & Engineering* **1**, 295-304 (2015).
- 268 Lin, K.-C. *et al.* Erratum: "Ultrafast dynamics of hot electrons and phonons in chemical vapor deposited graphene" [J. Appl. Phys. 113, 133511 (2013)]. *Journal of Applied Physics* **114** (2013).
- 269 Gu, G. X., Chen, C.-T., Richmond, D. J. & Buehler, M. J. Bioinspired hierarchical composite design using machine learning: simulation, additive manufacturing, and experiment. *Materials Horizons* **5**, 939-945 (2018).
- 270 Petrini, M., Ferrante, M. & Su, B. Fabrication and characterization of biomimetic ceramic/polymer composite materials for dental restoration. *Dental Materials* **29**, 375-381 (2013).
- 271 Song, Y., Zhuan, X., Wang, T. & Chen, X. Evolution of thermal stress in a coating/substrate system during the cooling process of fabrication. *Mechanics of Materials* **74**, 26-40 (2014).
- 272 Cheng, X., Liu, S., Zhang, J., Guo, X. & Bao, J. Hygrothermal effects on mechanical behavior of scarf repaired carbon - epoxy laminates subject to axial compression loads: Experiment and numerical simulation. *Polymer Composites* **39**, 904-914 (2018).
- 273 Tselentis, N. & Tserpes, K. A Coupled Electro-Thermal Model for Simulating the Lightning Strike Damage in Cfrps. (2018).
- 274 Multiphysics, C. COMSOL Multiphysics 3.5 a, User's Manual. *User's Manual, COMSOL AB, Stockholm, Sweden* (2008).

Appendix A

Supporting information for Chapter 3

The constants $\lambda_j = \sqrt{r_{sj}}$, ($j = 1,2,3$), r_{sj} are the roots of the following characteristic equation:

$$ar_s^3 + b^*r_s^2 + c^*r_s + d^* = 0$$

$$a = -c_{44}(e_{33}^2 + c_{33}\varepsilon_{33})$$

$$b = e_{33}[-2c_{44}e_{31} - 2c_{13}(e_{15} + e_{31}) + c_{11}e_{33}] - c_{13}(c_{13} + 2c_{44})\varepsilon_{33} \\ + c_{33}((e_{15} + e_{31})^2 + c_{44}\varepsilon_{11} + c_{11}\varepsilon_{33})$$

$$c = [c_{13}^2\varepsilon_{11} - c_{11}(2e_{15}e_{33} + c_{33}\varepsilon_{11}) + 2c_{13}(e_{15}^2 + e_{15}e_{31} + c_{44}\varepsilon_{11}) - c_{44}(e_{31}^2 + c_{11}\varepsilon_{33})]$$

$$d = c_{11}(e_{15}^2 + c_{44}\varepsilon_{11})$$

$$e = (e_{33}^2 + (c_{33} + c_{44})\varepsilon_{33})\rho$$

$$f = -\varepsilon_{33}\rho^2$$

$$g = -((e_{15} + e_{31})^2 + 2e_{15}e_{33} + (c_{33} + c_{44})\varepsilon_{11} + (c_{11} + c_{44})\varepsilon_{33})\rho$$

$$h = \varepsilon_{11}\rho^2$$

$$j = (e_{15}^2 + c_{11}\varepsilon_{11} + c_{44}\varepsilon_{11})\rho$$

$$b^* = b + e\bar{p}^2$$

$$c^* = c + f\bar{p}^4 + g\bar{p}^2$$

$$d^* = d + h\bar{p}^4 + j\bar{p}^2$$

$$p = \bar{p}s$$

The constants R_x^1 , R_x^2 , R_z^1 , R_z^2 , R_ϕ^1 , R_ϕ^2 and R_ϕ^3 are given by:

$$\left. \begin{aligned} R_x^1 &= \omega_{x1}E_{f1} + \omega_{x2}E_{f2} + \omega_{x3}E_{f3} \\ \omega_{x1} &= -(e_{33}^2 + c_{33}\varepsilon_{33})\tau^4 + (2e_{15}e_{33} + c_{33}\varepsilon_{11} + c_{44}\varepsilon_{33})\tau^2 - (e_{15}^2 + c_{44}\varepsilon_{11}) \\ \omega_{x2} &= (e_{15}e_{33} + e_{31}e_{33} + c_{13}\varepsilon_{33} + c_{44}\varepsilon_{33})\tau^4 - (e_{15}^2 + e_{15}e_{31} + c_{13}\varepsilon_{11} + c_{44}\varepsilon_{11})\tau^2 \\ \omega_{x3} &= (c_{13}e_{33} + c_{44}e_{33} - c_{33}e_{15} - c_{33}e_{31})\tau^4 + (c_{44}e_{31} - c_{13}e_{15})\tau^2 \end{aligned} \right\} \quad (\text{A.1})$$

$$\left. \begin{aligned} R_x^2 &= \omega_{x4}E_{f1} + \omega_{x5}E_{f3} \\ \omega_{x4} &= (\varepsilon_{33}\tau^2 - \varepsilon_{11})\rho p^2 \\ \omega_{x5} &= (e_{31} + e_{15})\tau^2 \rho p^2 \end{aligned} \right\} \quad (\text{A.2})$$

$$\left. \begin{aligned} R_z^1 &= \omega_{z1}E_{f1} + \omega_{z2}E_{f2} + \omega_{z3}E_{f3} \\ \omega_{z1} &= -(e_{15}e_{33} + e_{31}e_{33} + c_{13}\varepsilon_{33} + c_{44}\varepsilon_{33})\tau^3 + (e_{15}^2 + e_{15}e_{31} + c_{13}\varepsilon_{11} + c_{44}\varepsilon_{11})\tau \\ \omega_{z2} &= -c_{44}\varepsilon_{33}\tau^5 + [(e_{15} + e_{31})^2 + c_{44}\varepsilon_{11} + c_{11}\varepsilon_{33}]\tau^3 - c_{11}\varepsilon_{11}\tau \\ \omega_{z3} &= -c_{44}e_{33}\tau^5 - (c_{44}e_{31} + c_{13}e_{15} + c_{13}e_{31} - c_{11}e_{33})\tau^3 - c_{11}e_{15}\tau \end{aligned} \right\} \quad (\text{A.3})$$

$$\left. \begin{aligned} R_z^2 &= \omega_{z4}E_{f2} + \omega_{z5}E_{f3} \\ \omega_{z4} &= (\varepsilon_{33}\tau^3 - \varepsilon_{11}\tau)\rho p^2 \\ \omega_{z5} &= (e_{33}\tau^3 - e_{15}\tau)\rho p^2 \end{aligned} \right\} \quad (\text{A.4})$$

$$\left. \begin{aligned}
R_{\phi}^1 &= \omega_{\phi 1} E_{f1} + \omega_{\phi 2} E_{f2} + \omega_{\phi 3} E_{f3} \\
\omega_{\phi 1} &= -(c_{13} e_{33} + c_{44} e_{33} - c_{33} e_{15} - c_{33} e_{31}) \tau^3 - (c_{44} e_{31} - c_{13} e_{15}) \tau \\
\omega_{\phi 2} &= -c_{44} e_{33} \tau^5 - (c_{44} e_{31} + c_{13} e_{15} + c_{13} e_{31} - c_{11} e_{33}) \tau^3 - c_{11} e_{15} \tau \\
\omega_{\phi 3} &= c_{44} c_{33} \tau^5 + (c_{13}^2 + 2c_{13} c_{44} - c_{11} c_{33}) \tau^3 + c_{11} c_{44} \tau
\end{aligned} \right\} \quad (\text{A. 5})$$

$$\left. \begin{aligned}
R_{\phi}^2 &= \omega_{\phi 4} E_{f1} + \omega_{\phi 5} E_{f2} + \omega_{\phi 6} E_{f3} \\
\omega_{\phi 4} &= -(e_{15} + e_{31}) \tau \rho p^2 \\
\omega_{\phi 5} &= (e_{33} \tau^3 - e_{15} \tau) \rho p^2 \\
\omega_{\phi 6} &= [-(c_{44} + c_{33}) \tau^3 + (c_{11} + c_{44}) \tau] \rho p^2
\end{aligned} \right\} \quad (\text{A. 6})$$

$$R_{\phi}^3 = \tau \rho^2 p^4 E_{f3}$$

and:

$$E_{f1}(s, p) = \frac{\lambda_{11}}{E_{f0}(s, p)}, \quad E_{f2}(s, p) = \frac{\lambda_{33}}{E_{f0}(s, p)}, \quad E_{f3}(s, p) = \frac{-p_z}{E_{f0}(s, p)}$$

$$E_{f0}(s, p) = as^6 \tau^6 + (bs^2 + ep^2) s^4 \tau^4 + (cs^4 + fp^4 + gp^2 s^2) s^2 \tau^2 + ds^6 + hp^4 s^2 + jp^2 s^4$$

The functions $C_{j+4}(s, p)$ ($j = 1, 2, 3$) are:

$$\left. \begin{aligned}
C_5(s, p) &= \frac{P_{21} P_{33} - P_{23} P_{31}}{C_{p1}} C_4(s, p) \exp(-|s| \lambda_1 h_1) \\
C_6(s, p) &= \frac{P_{13} P_{31} - P_{11} P_{33}}{C_{p1}} C_4(s, p) \exp(-|s| \lambda_2 h_1) \\
C_7(s, p) &= \frac{P_{11} P_{23} - P_{13} P_{21}}{C_{p1}} C_4(s, p) \exp(-|s| \lambda_3 h_1)
\end{aligned} \right\} \quad (\text{A. 7})$$

where,

$$C_4(s, p) = 2C_2 \exp(-|s|\tau h_1) \frac{\rho_2}{\rho_0}$$

$$C_{p1} = P_{13}P_{22}P_{31} - P_{12}P_{23}P_{31} - P_{13}P_{21}P_{32} + P_{11}P_{23}P_{32} + P_{12}P_{21}P_{33} - P_{11}P_{22}P_{33}$$

The functions $C_{j+15}(s, p)$ ($j = 1, 2, 3$) are:

$$\left. \begin{aligned} C_{16}(s, p) &= \frac{E_{u3}^2 E_{u2}^3 C_{12} - E_{u2}^2 E_{u3}^3 C_{12} - E_{u3}^1 E_{u2}^3 C_{13} + E_{u2}^1 E_{u3}^3 C_{13} + E_{u3}^1 E_{u2}^2 C_{14} - E_{u2}^1 E_{u3}^2 C_{14}}{E_{ap}} \\ C_{17}(s, p) &= \frac{-E_{u3}^2 E_{u1}^3 C_{12} + E_{u1}^2 E_{u3}^3 C_{12} + E_{u3}^1 E_{u1}^3 C_{13} - E_{u1}^1 E_{u3}^3 C_{13} - E_{u3}^1 E_{u1}^2 C_{14} + E_{u1}^1 E_{u3}^2 C_{14}}{E_{ap}} \\ C_{18}(s, p) &= \frac{E_{u2}^2 E_{u1}^3 C_{12} - E_{u1}^2 E_{u2}^3 C_{12} - E_{u2}^1 E_{u1}^3 C_{13} + E_{u1}^1 E_{u2}^3 C_{13} + E_{u2}^1 E_{u1}^2 C_{14} - E_{u1}^1 E_{u2}^2 C_{14}}{E_{ap}} \end{aligned} \right\} \quad (\text{A. 8})$$

where ($n = 1, 2, 3$),

$$E_{uj}^n = P_{jn} + (-1)^n \bar{U}_j^n \exp(-|s|\lambda_j h_2)$$

$$\bar{U}_j^n = P_{1n} U_j^{(1)} + P_{2n} U_j^{(2)} + P_{3n} U_j^{(3)}$$

$$U_j^{(n)}(s, p) = (-1)^n \frac{R_{b2}^{(n)} P_{j1} + R_{b3}^{(n)} P_{j2} + R_{b4}^{(n)} P_{j3}}{C_{p1}} \exp(-|s|\lambda_n h_2)$$

$$R_{b2}^{(1)} = (P_{22}P_{33} - P_{23}P_{32}), \quad R_{b3}^{(1)} = (P_{21}P_{33} - P_{23}P_{31}), \quad R_{b4}^{(1)} = (P_{21}P_{32} - P_{22}P_{31})$$

$$R_{b2}^{(2)} = (P_{12}P_{33} - P_{13}P_{32}), \quad R_{b3}^{(2)} = (P_{11}P_{33} - P_{13}P_{31}), \quad R_{b4}^{(2)} = (P_{11}P_{32} - P_{12}P_{31})$$

$$R_{b2}^{(3)} = (P_{12}P_{23} - P_{13}P_{22}), \quad R_{b3}^{(3)} = (P_{11}P_{23} - P_{13}P_{21}), \quad R_{b4}^{(3)} = (P_{11}P_{22} - P_{12}P_{21})$$

and we have:

$$C_{12}(s, p) = P_{11}C_9 + P_{21}C_{10} + P_{31}C_{111} + P_{11}C_5 + P_{21}C_6 + P_{31}C_7 + C_1$$

$$C_{13}(s, p) = -\{P_{12} + P_{22}C_{10} + P_{32}C_{111}\} + P_{12}C_5 + P_{22}C_6 + P_{32}C_7$$

$$C_{14}(s, p) = P_{13}C_9 + P_{23}C_{10} + P_{33}C_{111} + P_{13}C_5 + P_{23}C_6 + P_{33}C_7 + C_3$$

$$\left. \begin{aligned} C_9(s, p) &= \frac{P_{21}P_{33} - P_{23}P_{31}}{C_{p1}} C_8(s, p) \exp(-|s|\lambda_1 h_2) \\ C_{10}(s, p) &= \frac{P_{13}P_{31} - P_{11}P_{33}}{C_{p1}} C_8(s, p) \exp(-|s|\lambda_2 h_2) \\ C_{111}(s, p) &= \frac{P_{11}P_{23} - P_{13}P_{21}}{C_{p1}} C_8(s, p) \exp(-|s|\lambda_3 h_2) \end{aligned} \right\} \quad (\text{A. 9})$$

$$C_8(s, p) = -2C_2 \exp(-h_2 \tau |s|) \frac{\rho_1}{\rho_0}$$

$$E_{ap} = E_{u3}^1 E_{u2}^2 E_{u1}^3 - E_{u2}^1 E_{u3}^2 E_{u1}^3 - E_{u3}^1 E_{u1}^2 E_{u2}^3 + E_{u1}^1 E_{u3}^2 E_{u2}^3 + E_{u2}^1 E_{u1}^2 E_{u3}^3 - E_{u1}^1 E_{u2}^2 E_{u3}^3$$

The functions $C_{j+18}(s, p)$ ($j = 1, 2, 3$) are:

$$\left. \begin{aligned} C_{19}(s, p) &= U_1^{a(1)} C_{16} + U_2^{a(1)} C_{17} + U_3^{a(1)} C_{18} + C_9 \\ C_{20}(s, p) &= U_1^{a(2)} C_{16} + U_2^{a(2)} C_{17} + U_3^{a(2)} C_{18} + C_{10} \\ C_{21}(s, p) &= U_1^{a(3)} C_{16} + U_2^{a(3)} C_{17} + U_3^{a(3)} C_{18} + C_{111} \end{aligned} \right\} \quad (\text{A. 10})$$

where,

$$U_j^{a(n)} = U_j^{(n)} \exp(-|s|\lambda_j h_2)$$

The functions of $V_j^{*(n)}(s, h_1, p)$, $U_j^{*(n)}(s, h_1, h_2, p)$ and $U_j^{*(n)}(s, h_1, h_2, p)$ are:

$$V_j^{*(n)}(s, h_1, p) = V_j^{(n)} \exp(-|s|\lambda_j h_1) \quad (\text{A. 11})$$

$$V_j^{(n)} = (-1)^n \frac{R_{b2}^{(n)} P_{j1} + R_{b3}^{(n)} P_{j2} + R_{b4}^{(n)} P_{j3}}{C_{p1}} \exp(-|s|\lambda_n h_1)$$

and:

$$\left. \begin{aligned} I_j^{*(1)}(s, h_1, h_2, p) &= \frac{(E_{u_3}^2 E_{u_2}^3 - E_{u_2}^2 E_{u_3}^3) E_{vj}^1 + (E_{u_2}^1 E_{u_3}^3 - E_{u_3}^1 E_{u_2}^3) E_{vj}^2 + (E_{u_3}^1 E_{u_2}^2 - E_{u_2}^1 E_{u_3}^2) E_{vj}^3}{E_{ap}} \\ I_j^{*(2)}(s, h_1, h_2, p) &= \frac{(E_{u_1}^2 E_{u_3}^3 - E_{u_3}^2 E_{u_1}^3) E_{vj}^1 + (E_{u_3}^1 E_{u_1}^3 - E_{u_1}^1 E_{u_3}^3) E_{vj}^2 + (E_{u_1}^1 E_{u_3}^2 - E_{u_3}^1 E_{u_1}^2) E_{vj}^3}{E_{ap}} \\ I_j^{*(3)}(s, h_1, h_2, p) &= \frac{(E_{u_2}^2 E_{u_1}^3 - E_{u_1}^2 E_{u_2}^3) E_{vj}^1 + (E_{u_1}^1 E_{u_2}^3 - E_{u_2}^1 E_{u_1}^3) E_{vj}^2 + (E_{u_2}^1 E_{u_1}^2 - E_{u_1}^1 E_{u_2}^2) E_{vj}^3}{E_{ap}} \end{aligned} \right\} \quad (\text{A. 12})$$

where:

$$E_{vj}^n = \bar{V}_j^n \exp(-|s|\lambda_j h_1) + (-1)^n P_{jn}$$

$$\bar{V}_j^n = P_{1n} V_j^{(1)} + P_{2n} V_j^{(2)} + P_{3n} V_j^{(3)}$$

finally:

$$U_j^{*(n)}(s, h_1, h_2, p) = U_1^{a(n)} I_j^{*(1)} + U_2^{a(n)} I_j^{*(2)} + U_3^{a(n)} I_j^{*(3)} \quad (\text{A. 13})$$

When solving the Eq. (3.46), the functions $C_{pm}^{(j)}(s, p)$ ($m, j = 1, 2, 3$) are:

$$\left. \begin{aligned} C_{p1}^{(1)} &= \frac{\vartheta_3^{(2)} \vartheta_2^{(3)} - \vartheta_2^{(2)} \vartheta_3^{(3)}}{\vartheta_{p0}}, & C_{p1}^{(2)} &= \frac{\vartheta_1^{(2)} \vartheta_3^{(3)} - \vartheta_3^{(2)} \vartheta_1^{(3)}}{\vartheta_{p0}}, & C_{p1}^{(3)} &= \frac{\vartheta_2^{(2)} \vartheta_1^{(3)} - \vartheta_1^{(2)} \vartheta_2^{(3)}}{\vartheta_{p0}} \\ C_{p2}^{(1)} &= \frac{\vartheta_2^{(1)} \vartheta_3^{(3)} - \vartheta_3^{(1)} \vartheta_2^{(3)}}{\vartheta_{p0}}, & C_{p2}^{(2)} &= \frac{\vartheta_3^{(1)} \vartheta_1^{(3)} - \vartheta_1^{(1)} \vartheta_3^{(3)}}{\vartheta_{p0}}, & C_{p2}^{(3)} &= \frac{\vartheta_1^{(1)} \vartheta_2^{(3)} - \vartheta_2^{(1)} \vartheta_1^{(3)}}{\vartheta_{p0}} \\ C_{p3}^{(1)} &= \frac{\vartheta_3^{(1)} \vartheta_2^{(2)} - \vartheta_2^{(1)} \vartheta_3^{(2)}}{\vartheta_{p0}}, & C_{p3}^{(2)} &= \frac{\vartheta_1^{(1)} \vartheta_3^{(2)} - \vartheta_3^{(1)} \vartheta_1^{(2)}}{\vartheta_{p0}}, & C_{p3}^{(3)} &= \frac{\vartheta_2^{(1)} \vartheta_1^{(2)} - \vartheta_1^{(1)} \vartheta_2^{(2)}}{\vartheta_{p0}} \end{aligned} \right\} \quad (\text{A. 14})$$

where,

$$\vartheta_{p0} = \vartheta_3^{(1)} \vartheta_2^{(2)} \vartheta_1^{(3)} - \vartheta_2^{(1)} \vartheta_3^{(2)} \vartheta_1^{(3)} - \vartheta_3^{(1)} \vartheta_1^{(2)} \vartheta_2^{(3)} + \vartheta_1^{(1)} \vartheta_3^{(2)} \vartheta_2^{(3)} + \vartheta_2^{(1)} \vartheta_1^{(2)} \vartheta_3^{(3)} - \vartheta_1^{(1)} \vartheta_2^{(2)} \vartheta_3^{(3)}$$

and $\vartheta_j^{(n)}(s, p)$ ($n = 1, 2, 3$) are:

$$\begin{bmatrix} \vartheta_j^{(1)} \\ \vartheta_j^{(2)} \\ \vartheta_j^{(3)} \end{bmatrix} = \begin{bmatrix} -Z_{j1} \\ Z_{j2} \\ -Z_{j3} \end{bmatrix} + \begin{bmatrix} Z_{11} & Z_{21} & Z_{31} \\ Z_{12} & Z_{22} & Z_{32} \\ -Z_{13} & -Z_{23} & -Z_{33} \end{bmatrix} \begin{bmatrix} V_j^{*(1)} - I_j^{*(1)} \\ V_j^{*(2)} - I_j^{*(2)} \\ V_j^{*(3)} - I_j^{*(2)} \end{bmatrix} + \begin{bmatrix} Z_{11} & Z_{21} & Z_{31} \\ -Z_{12} & -Z_{22} & -Z_{32} \\ Z_{13} & Z_{23} & Z_{33} \end{bmatrix} \begin{bmatrix} U_j^{*(1)} \\ U_j^{*(2)} \\ U_j^{*(3)} \end{bmatrix}$$

And functions $C_{j+24}(s, p)$ ($i, j = 1, 2, 3$) are:

$$\left. \begin{aligned} C_{25}(s, p) &= -\frac{C_{24}\vartheta_3^{(1)}\vartheta_2^{(2)} - C_{24}\vartheta_2^{(1)}\vartheta_3^{(2)} - C_{23}\vartheta_3^{(1)}\vartheta_2^{(3)} + C_{22}\vartheta_3^{(2)}\vartheta_2^{(3)} + C_{23}\vartheta_2^{(1)}\vartheta_3^{(3)} - C_{22}\vartheta_2^{(2)}\vartheta_3^{(3)}}{\vartheta_{p0}} \\ C_{26}(s, p) &= \frac{C_{24}\vartheta_3^{(1)}\vartheta_1^{(2)} - C_{24}\vartheta_1^{(1)}\vartheta_3^{(2)} - C_{23}\vartheta_3^{(1)}\vartheta_1^{(3)} + C_{22}\vartheta_3^{(2)}\vartheta_1^{(3)} + C_{23}\vartheta_1^{(1)}\vartheta_3^{(3)} - C_{22}\vartheta_1^{(2)}\vartheta_3^{(3)}}{\vartheta_{p0}} \\ C_{27}(s, p) &= -\frac{C_{24}\vartheta_2^{(1)}\vartheta_1^{(2)} - C_{24}\vartheta_1^{(1)}\vartheta_2^{(2)} - C_{23}\vartheta_2^{(1)}\vartheta_1^{(3)} + C_{22}\vartheta_2^{(2)}\vartheta_1^{(3)} + C_{23}\vartheta_1^{(1)}\vartheta_2^{(3)} - C_{22}\vartheta_1^{(2)}\vartheta_2^{(3)}}{\vartheta_{p0}} \end{aligned} \right\} \quad (\text{A. 15})$$

where

$$\begin{bmatrix} C_{22}(s, p) \\ C_{23}(s, p) \\ C_{24}(s, p) \end{bmatrix} = \begin{bmatrix} Z_{11} & Z_{21} & Z_{31} \\ Z_{12} & Z_{22} & Z_{32} \\ -Z_{13} & -Z_{23} & -Z_{33} \end{bmatrix} \begin{bmatrix} C_5 - C_{16} \\ C_6 - C_{17} \\ C_7 - C_{18} \end{bmatrix} + \begin{bmatrix} Z_{11} & Z_{21} & Z_{31} \\ -Z_{12} & -Z_{22} & -Z_{32} \\ Z_{13} & Z_{23} & Z_{33} \end{bmatrix} \begin{bmatrix} C_{19} \\ C_{20} \\ C_{21} \end{bmatrix}$$

In singular integral equations Eq. (3.47) and Eq. (3.48), functions $\varphi_{ml}^{(1)}$ ($m = 0, 1, 2, 3; l = 1, 2, 3$) are:

$$\varphi_{ml}^{(1)} = P_{1l} [C_{am}^{(1)} + (-1)^l C_{pm}^{(1)}] + P_{2l} [C_{am}^{(2)} + (-1)^l C_{pm}^{(2)}] + P_{3l} [C_{am}^{(3)} + (-1)^l C_{pm}^{(3)}] \quad (m = 1, 2, 3; l = 1, 2, 3)$$

$$\varphi_{0l}^{(1)} = P_{1l} [C_{a0}^{(1)} + (-1)^l C_{25}] + P_{2l} [C_{a0}^{(2)} + (-1)^l C_{26}] + P_{3l} [C_{a0}^{(3)} + (-1)^l C_{27}] \quad (l = 1, 2, 3)$$

where

$$\begin{aligned} C_{am}^{(j)} &= V_1^{*(j)} C_{pm}^{(1)} + V_2^{*(j)} C_{pm}^{(2)} + V_3^{*(j)} C_{pm}^{(3)} \\ C_{a0}^{(j)} &= V_1^{*(j)} C_{25} + V_2^{*(j)} C_{26} + V_3^{*(j)} C_{27} + C_{j+4} \end{aligned}$$

Appendix B

Supporting information for Chapter 4

The coefficients λ_j is

$$\lambda_1 = \sqrt{\frac{-c + \sqrt{c^2 - 4ad}}{2a}}, \quad \lambda_2 = \sqrt{\frac{-c - \sqrt{c^2 - 4ad}}{2a}} \quad (\text{B. 1})$$

where $a = c_{11}c_{66}$, $b = c_{12}^2 + 2c_{12}c_{66} - c_{11}^2$, $c = b - e\bar{p}^2$, $d = a + e\bar{p}^2 + f\bar{p}^4$, $e = (c_{11} + c_{66})\rho$, and $f = \rho^2$, $p = \bar{p}s$.

The parameters R_x^1 , R_x^2 , R_z^1 and R_z^2 of particular solutions are

$$\begin{aligned} R_x^1 &= \omega_{x1}E_{f1} + \omega_{x2}E_{f2} \\ R_x^2 &= \omega_{x3}E_{f1} \\ R_z^1 &= \omega_{z1}E_{f1} + \omega_{z2}E_{f2} \\ R_z^2 &= \omega_{z3}E_{f2} \end{aligned} \quad (\text{B. 2})$$

in which the coefficients ω_{xi} , ω_{zi} , E_{fi} ($i=1,2,3$) are expressed as

$$\omega_{x1} = c_{11}\tau^2 - c_{66}$$

$$\omega_{x2} = -(c_{12} + c_{66})\tau^2$$

$$\omega_{x3} = -\rho p^2$$

$$\omega_{z1} = (c_{12} + c_{66})\tau$$

$$\omega_{z2} = c_{66}\tau^3 - c_{11}\tau$$

$$\omega_{z3} = -\tau\rho p^2$$

$$E_{f1}(s, p) = \frac{\lambda_{11}}{E_{f3}(s, p)}$$

$$E_{f2}(s, p) = \frac{\lambda_{22}}{E_{f3}(s, p)}$$

$$E_{f3}(s, p) = as^4\tau^4 + (bs^2 - ep^2)s^2\tau^2 + as^4 + ep^2s^2 + fp^4$$

The equations of $P_{jl}(s, p)$ and $\varphi_l(s, p)$ ($l=1,2,3; j=1,2$) for general solutions of the cracked multiphysical model are

$$\begin{aligned} P_{j1}(s, p) &= c_{11}Z_{j1}|s| + vc_{11}Z_{j2}|s|\lambda_j \\ P_{j2}(s, p) &= vc_{11}Z_{j1}|s| + c_{11}Z_{j2}|s|\lambda_j \\ P_{j3}(s, p) &= c_{66}Z_{j1}|s|\lambda_j - c_{66}Z_{j2}|s| \end{aligned} \quad (\text{B. 3})$$

$$\begin{aligned} \varphi_1(s, p) &= c_{11}(R_x^1s^4 + R_x^2s^2) + vc_{11}(R_z^1s^4 + R_z^2s^2)\tau - \lambda_{11} \\ \varphi_2(s, p) &= vc_{11}(R_x^1s^4 + R_x^2s^2) + c_{11}(R_z^1s^4 + R_z^2s^2)\tau - \lambda_{22} \\ \varphi_3(s, p) &= c_{66}(R_x^1s^4 + R_x^2s^2)\tau - c_{66}(R_z^1s^4 + R_z^2s^2) \end{aligned} \quad (\text{B. 4})$$

In the multiphysical singular integral system, the coefficients $M_{11}, M_{12}, M_{21}, M_{22}, M_{12}^0$ and M_{21}^0 are expressed like Eqs. B.5 and B.6

$$\begin{aligned} M_{12}(x, \xi, p) &= \int_0^{+\infty} \left\{ S_{12} \left(\frac{1}{-s} \right) - M_{12}^0 \right\} \sin[s(\bar{\xi} - \bar{x})] ds \\ M_{21}(x, \xi, p) &= \int_0^{+\infty} \left\{ S_{21} \left(\frac{1}{-s} \right) - M_{21}^0 \right\} \sin[s(\bar{\xi} - \bar{x})] ds \\ M_{11}(x, \xi, p) &= \int_0^{+\infty} \left\{ S_{11} \left(\frac{1}{|s|} \right) \right\} \cos[s(\bar{\xi} - \bar{x})] ds \\ M_{22}(x, \xi, p) &= \int_0^{+\infty} \left\{ S_{22} \left(\frac{1}{-s} \right) \right\} \cos[s(\bar{\xi} - \bar{x})] ds \end{aligned} \quad (\text{B. 5})$$

$$\begin{aligned} M_{12}^0 &= \lim_{s \rightarrow \infty} S_{12} \left(\frac{1}{-s} \right) \\ M_{21}^0 &= \lim_{s \rightarrow \infty} S_{21} \left(\frac{1}{-s} \right) \end{aligned} \quad (\text{B. 6})$$

where

$$\begin{bmatrix} S_{11} \\ S_{12} \\ S_{10} \end{bmatrix} = \begin{bmatrix} I_{11} & I_{21} & I_{11} \\ I_{12} & I_{22} & I_{12} \\ I_{10} & I_{20} & I_{10} \end{bmatrix} \left(\begin{bmatrix} V_1^{(11)} \\ V_2^{(11)} \\ -1 \end{bmatrix} P_{11} + \begin{bmatrix} V_1^{(12)} \\ V_2^{(12)} \\ -1 \end{bmatrix} P_{21} \right) + \begin{bmatrix} 0 \\ 0 \\ \Delta_{11} \end{bmatrix} P_{11} + \begin{bmatrix} 0 \\ 0 \\ \Delta_{12} \end{bmatrix} P_{21}$$

$$\begin{bmatrix} S_{21} \\ S_{22} \\ S_{20} \end{bmatrix} = \begin{bmatrix} I_{11} & I_{21} & I_{11} \\ I_{12} & I_{22} & I_{12} \\ I_{10} & I_{20} & I_{10} \end{bmatrix} \left(\begin{bmatrix} V_1^{(11)} \\ V_2^{(11)} \\ 1 \end{bmatrix} P_{13} + \begin{bmatrix} V_1^{(12)} \\ V_2^{(12)} \\ 1 \end{bmatrix} P_{23} \right) + \begin{bmatrix} 0 \\ 0 \\ \Delta_{11} \end{bmatrix} P_{11} + \begin{bmatrix} 0 \\ 0 \\ \Delta_{12} \end{bmatrix} P_{21}$$

$V_j^{(11)}$, $V_j^{(12)}$ and Δ_{1j} ($j = 1, 2$) are separately equal to

$$V_j^{(11)}(s, p) = \frac{(P_{23}P_{j2} + P_{22}P_{j3})}{(P_{12}P_{23} - P_{13}P_{22})} \exp[-|s|(\lambda_1 + \lambda_j)h_1]$$

$$V_j^{(12)}(s, p) = \frac{(P_{13}P_{j2} + P_{12}P_{j3})}{(P_{13}P_{22} - P_{23}P_{12})} \exp[-|s|(\lambda_2 + \lambda_j)h_1]$$

$$\Delta_{11}(s, p) = -\frac{P_{22}\theta_1}{(P_{12}P_{23} - P_{13}P_{22})} \exp(-|s|\lambda_1 h_1)$$

$$\Delta_{12}(s, p) = -\frac{P_{12}\theta_1}{(P_{13}P_{22} - P_{23}P_{12})} \exp(-|s|\lambda_2 h_1)$$

else $\begin{bmatrix} I_{11} & I_{12} \\ I_{21} & I_{22} \end{bmatrix} = \frac{1}{\Theta} \begin{bmatrix} H_2^{(d2)} & -H_2^{(d1)} \\ H_1^{(d2)} & -H_1^{(d1)} \end{bmatrix}$, $I_{10} = -I_{11}\Delta_{d1} - I_{12}\Delta_{d2}$, $I_{20} = -I_{21}\Delta_{d1} - I_{22}\Delta_{d2}$; and

$\Theta = H_1^{(d1)}H_2^{(d2)} - H_1^{(d2)}H_2^{(d1)}$, $\theta_1 = 2\varphi_3 \exp(-|s|\tau h_1) \frac{\rho_2}{\rho_0} H_j^{(d1)}, H_j^{(d2)}$ and Δ_{dj} equal like

$$\begin{bmatrix} H_j^{(d1)} \\ H_j^{(d2)} \end{bmatrix}_{j=1,2} = \begin{bmatrix} Z_{11} & Z_{21} & -Z_{11} & -Z_{21} & Z_{11} & Z_{21} & -Z_{j1} \\ Z_{12} & Z_{22} & -Z_{12} & -Z_{22} & -Z_{12} & -Z_{22} & Z_{j2} \end{bmatrix} \begin{bmatrix} V_j^{(11)} \\ V_j^{(12)} \\ V_j^{(21)} \\ V_j^{(22)} \\ V_j^{(23)} \\ V_j^{(24)} \\ 1 \end{bmatrix} \quad (\text{B.7})$$

$$\begin{bmatrix} \Delta_{d1} \\ \Delta_{d2} \end{bmatrix}_{j=1,2} = \begin{bmatrix} Z_{11} & Z_{21} & -Z_{11} & -Z_{21} & Z_{11} & Z_{21} \\ Z_{12} & Z_{22} & -Z_{12} & -Z_{22} & -Z_{12} & -Z_{22} \end{bmatrix} \begin{bmatrix} \Delta_{11} \\ \Delta_{12} \\ \Delta_{21} \\ \Delta_{22} \\ \Delta_{23} \\ \Delta_{24} \end{bmatrix} \quad (\text{B.8})$$

$$\text{where } V_j^{(21)} = \frac{E_2^{(2)}U_j^{(1)} - E_2^{(1)}U_j^{(2)}}{(E_1^{(1)}E_2^{(2)} - E_1^{(2)}E_2^{(1)})}, \quad V_j^{(22)} = \frac{E_1^{(2)}U_j^{(1)} - E_1^{(1)}U_j^{(2)}}{(E_1^{(2)}E_2^{(1)} - E_1^{(1)}E_2^{(2)})},$$

$$\begin{bmatrix} V_j^{(23)} \\ V_j^{(24)} \end{bmatrix}_{j=1,2} = \begin{bmatrix} V_1^{(210)} & V_2^{(210)} \\ V_1^{(220)} & V_2^{(220)} \end{bmatrix} \begin{bmatrix} V_j^{(21)} \\ V_j^{(22)} \end{bmatrix}$$

$$\text{and } \Delta_{21}(s, p) = \frac{(E_2^{(2)}\Delta_1 - E_2^{(1)}\Delta_2)}{(E_1^{(1)}E_2^{(2)} - E_1^{(2)}E_2^{(1)})}, \quad \Delta_{22}(s, p) = \frac{(E_1^{(2)}\Delta_1 - E_1^{(1)}\Delta_2)}{(E_1^{(2)}E_2^{(1)} - E_1^{(1)}E_2^{(2)})},$$

$$\begin{bmatrix} \Delta_{23} \\ \Delta_{24} \end{bmatrix} = \begin{bmatrix} V_1^{(210)} & V_2^{(210)} \\ V_1^{(220)} & V_2^{(220)} \end{bmatrix} \begin{bmatrix} \Delta_{21} \\ \Delta_{22} \end{bmatrix} + \begin{bmatrix} \Delta_{210} \\ \Delta_{220} \end{bmatrix}.$$

Then $\begin{bmatrix} E_j^{(1)} \\ E_j^{(2)} \end{bmatrix}_{j=1,2}$ and $\begin{bmatrix} U_j^{(1)} \\ U_j^{(2)} \end{bmatrix}_{j=1,2}$ are solve by

$$\begin{bmatrix} E_j^{(1)} \\ E_j^{(2)} \end{bmatrix}_{j=1,2} = \begin{bmatrix} P_{12} & P_{22} & -P_{j2} \\ P_{13} & P_{23} & P_{j3} \end{bmatrix} \begin{bmatrix} V_j^{(210)} \\ V_j^{(220)} \\ 1 \end{bmatrix} \quad (\text{B.9})$$

$$\begin{bmatrix} U_j^{(1)} \\ U_j^{(2)} \end{bmatrix}_{j=1,2} = \begin{bmatrix} -P_{12} & -P_{22} & P_{j2} \\ P_{13} & P_{23} & P_{j3} \end{bmatrix} \begin{bmatrix} V_j^{(11)} \\ V_j^{(12)} \\ 1 \end{bmatrix} \quad (\text{B. 10})$$

in which

$$V_j^{(210)}(s, p) = \frac{(P_{23}P_{j2} + P_{22}P_{j3})}{(P_{12}P_{23} - P_{13}P_{22})} \exp[-|s|(\lambda_1 + \lambda_j)h_2]$$

$$V_j^{(220)}(s, p) = \frac{(P_{13}P_{j2} + P_{12}P_{j3})}{(P_{13}P_{22} - P_{12}P_{23})} \exp[-|s|(\lambda_2 + \lambda_j)h_2]$$

Furthermore Δ_j functions are written as

$$\begin{bmatrix} \Delta_1 \\ \Delta_2 \end{bmatrix} = \begin{bmatrix} -P_{12} & P_{22} \\ P_{13} & P_{23} \end{bmatrix} \begin{bmatrix} \Delta_{11} \\ \Delta_{12} \end{bmatrix} + \begin{bmatrix} P_{12} & P_{22} \\ -P_{13} & -P_{23} \end{bmatrix} \begin{bmatrix} \Delta_{210} \\ \Delta_{220} \end{bmatrix} + \begin{bmatrix} \varphi_2 \\ 0 \end{bmatrix} \quad (\text{B. 11})$$

where $\theta_2 = -2\varphi_3 \exp(-\tau|s|h_2) \frac{\rho_1}{\rho_0}$ and

$$\Delta_{210}(s, p) = -\frac{P_{22}\theta_2}{(P_{12}P_{23} - P_{13}P_{22})} \exp(-|s|\lambda_1 h_2)$$

$$\Delta_{220}(s, p) = -\frac{P_{12}\theta_2}{(P_{13}P_{22} - P_{12}P_{23})} \exp(-|s|\lambda_2 h_2)$$

Appendix C

Supporting information for Chapter 5

The roots of γ_{ji} ($j = 1, 2, 3, \dots, 6$) are given by

$$a\gamma^6 + b\gamma^5 + c\gamma^4 + d\gamma^3 + e\gamma^2 + f\gamma + g = 0 \quad (\text{C.1})$$

where $\Re[\gamma_j] < \Re[\gamma_{j+1}]$, the coefficients are $a = a_1$, $b = \frac{\Omega}{|s|} 3a_1$, $c = a_2 - 3b_1 + c_1$, $d = \frac{\Omega}{|s|} (2a_2 - b_1 + 2c_1)$, $e = a_3 + b_2 - c_2 + d_1 - e_1$, $f = \frac{\Omega}{|s|} (a_3 - b_3 - c_2 - e_1)$, $g = a_4 + b_4 + c_3 - d_2 + e_2$.

in which

$$a_1 = -c_{440}(d_{330}^2 + c_{330}\varepsilon_{330})$$

$$a_2 = c_{110}d_{330}^2 - 2c_{440}d_{310}d_{330} - c_{130}^2\varepsilon_{330} - 2c_{130}((d_{150} + d_{310})d_{330} + c_{440}\varepsilon_{330}) \\ + c_{330}(c_{440}\varepsilon_{110} + c_{110}\varepsilon_{330} + (d_{150} + d_{310})^2)$$

$$a_3 = -c_{440}d_{310}^2 - 2c_{110}d_{150}d_{330} - c_{110}c_{440}\varepsilon_{330} + c_{130}^2\varepsilon_{110} \\ + c_{130}(2d_{150}^2 + 2d_{150}d_{310} + 2c_{440}\varepsilon_{110}) - c_{330}c_{110}\varepsilon_{110}$$

$$a_4 = c_{110}(d_{15}^2 + c_{440}\varepsilon_{110})$$

$$b_1 = a_1 \left(\frac{\Omega}{|s|} \right)^2$$

$$b_2 = (c_{110}d_{330}^2 - 3c_{440}d_{310}d_{330} - c_{130}^2\varepsilon_{330} - 2c_{130}d_{310}d_{330} - 3c_{130}(d_{150}d_{330} + c_{440}\varepsilon_{330}) \\ + c_{330}(d_{150}^2 + d_{310}^2 + c_{440}\varepsilon_{110} + c_{110}\varepsilon_{330} + 3d_{150}d_{310}))\left(\frac{\Omega}{|s|}\right)^2$$

$$b_3 = (c_{440}d_{310}d_{330} + c_{130}c_{440}\varepsilon_{330} + c_{130}d_{150}d_{330} - c_{330}d_{150}d_{310})\left(\frac{\Omega}{|s|}\right)^2$$

$$b_4 = (c_{130}(d_{150}^2 + c_{440}\varepsilon_{110}))\left(\frac{\Omega}{|s|}\right)^2$$

$$c_1 = (d_{330}^2 + c_{440}\varepsilon_{330} + c_{330}\varepsilon_{330})\rho_0\left(\frac{p}{|s|}\right)^2$$

$$c_2 = (c_{440}\varepsilon_{110} + c_{110}\varepsilon_{330} + (d_{150} + d_{310})^2 + 2d_{150}d_{310} + c_{440}\varepsilon_{330} + c_{330}\varepsilon_{110})\rho_0\left(\frac{p}{|s|}\right)^2$$

$$c_3 = (d_{150}^2 + (c_{110} + c_{440})\varepsilon_{110})\rho_0\left(\frac{p}{|s|}\right)^2$$

$$d_1 = (d_{330}^2 + (c_{330} + c_{440})\varepsilon_{330})\rho_0\left(\frac{p}{|s|}\right)^2\left(\frac{\Omega}{|s|}\right)^2$$

$$d_2 = d_{150}d_{310}\rho_0\left(\frac{p}{|s|}\right)^2\left(\frac{\Omega}{|s|}\right)^2$$

$$e_1 = \varepsilon_{330}\rho_0^2\left(\frac{p}{|s|}\right)^4$$

$$e_2 = \varepsilon_{110}\rho_0^2\left(\frac{p}{|s|}\right)^4$$

The coefficients $Z_{jli}(s, p)$ and $P_{xli}, P_{zli}, P_{\phi li}$, ($l = 1, 2$) are expressed as Eq. (C.2).

$$Z_{j2i}(s, p) = \begin{cases} \frac{f_{4i}\gamma_{ji}^4 + f_{3i}\gamma_{ji}^3 + f_{2i}\gamma_{ji}^2 + f_{1i}\gamma_{ji}^1 + f_{0i}}{g_{4i}\gamma_{ji}^4 + g_{3i}\gamma_{ji}^3 + g_{2i}\gamma_{ji}^2 + g_{1i}\gamma_{ji}^1 + g_{0i}} & l = 2 \\ \frac{\left((c_{130} + c_{440})\gamma_{ji} + \mu \frac{\Omega}{|S|} c_{440} \right) Z_{j21} + \left((d_{310} + d_{150})\gamma_{ji} + \mu \frac{\Omega}{|S|} d_{150} \right)}{\left(-c_{110} + c_{440}\gamma_{ji}^2 - \rho_0 \left(\frac{p}{S} \right)^2 + \mu \frac{\Omega}{|S|} c_{440}\gamma_{ji} \right)} & l = 1 \end{cases} \quad (\text{C. 2.1})$$

with

$$f_{4i} = c_{440}\varepsilon_{330}$$

$$f_{3i} = \mu \frac{\Omega}{|S|} 2f_{4i}$$

$$f_{2i} = -(c_{440}\varepsilon_{110} + c_{110}\varepsilon_{330} + (d_{150} + d_{310})^2) + \varepsilon_{330}c_{440} \left(\frac{\Omega}{|S|} \right)^2 - \varepsilon_{330} \frac{p^2}{S^2} \rho_0$$

$$f_{1i} = \mu \frac{\Omega}{|S|} \left(-(c_{440}\varepsilon_{110} + c_{110}\varepsilon_{330} + (d_{150} + d_{310})^2) - \varepsilon_{330} \frac{p^2}{S^2} \rho_0 \right)$$

$$f_{0i} = \varepsilon_{110} \left(c_{110} + \frac{p^2}{S^2} \rho_0 \right) - d_{150}d_{310} \left(\frac{\Omega}{|S|} \right)^2$$

$$g_{4i} = c_{440}d_{330}$$

$$g_{3i} = \mu d_{330}c_{440} 2 \frac{\Omega}{|S|}$$

$$g_{2i} = c_{440}d_{310} - c_{110}d_{330} + c_{130}(d_{150} + d_{310}) + c_{440}d_{330} \left(\frac{\Omega}{|S|} \right)^2 - d_{330} \left(\frac{p}{|S|} \right)^2 \rho_0$$

$$g_{1i} = \mu \left\{ (c_{130} + 2c_{440})d_{310} - c_{110}d_{330} - d_{330} \left(\frac{p}{|S|} \right)^2 \rho_0 \right\} \frac{\Omega}{|S|}$$

$$g_{0i} = c_{110}d_{150} + c_{440}d_{310} \left(\frac{\Omega}{|s|}\right)^2 + d_{150}\rho_0 \left(\frac{p}{|s|}\right)^2$$

$P_{xli}, P_{zli}, P_{\phi l}$, ($l = 1, 2$) are

$$P_{xli} = \frac{L_{xli}}{p_{dli}}, \quad P_{zli} = \frac{L_{zli}}{p_{dli}}, \quad P_{\phi li} = \frac{L_{\phi li}}{p_{dli}} \quad (\text{C. 2.2})$$

where

$$\begin{aligned} L_{xli} &= k_{x4l} \left(\lambda_{li} + \mu \frac{\varphi}{|s|}\right)^4 + k_{x3li} \left(\lambda_{li} + \mu \frac{\varphi}{|s|}\right)^3 + k_{x2li} \left(\lambda_{li} + \mu \frac{\varphi}{|s|}\right)^2 + k_{x1li} \left(\lambda_{li} + \mu \frac{\varphi}{|s|}\right) + k_{x0li} \\ L_{zli} &= k_{z4li} \left(\lambda_{li} + \mu \frac{\varphi}{|s|}\right)^4 + k_{z3li} \left(\lambda_{li} + \mu \frac{\varphi}{|s|}\right)^3 + k_{z2li} \left(\lambda_{li} + \mu \frac{\varphi}{|s|}\right)^2 + k_{z1li} \left(\lambda_{li} + \mu \frac{\varphi}{|s|}\right) + k_{z0li} \\ L_{\phi l} &= k_{\phi 4li} \left(\lambda_{li} + \mu \frac{\varphi}{|s|}\right)^4 + k_{\phi 3li} \left(\lambda_{li} + \mu \frac{\varphi}{|s|}\right)^3 + k_{\phi 2li} \left(\lambda_{li} + \mu \frac{\varphi}{|s|}\right)^2 + k_{\phi 1li} \left(\lambda_{li} + \mu \frac{\varphi}{|s|}\right) + k_{\phi 0li} \end{aligned}$$

$$\begin{aligned} \text{and } p_{dli} &= a \left(\lambda_{li} + \mu \frac{\varphi}{|s|}\right)^6 + |s|b \left(\lambda_{li} + \mu \frac{\varphi}{|s|}\right)^5 + s^2c \left(\lambda_{li} + \mu \frac{\varphi}{|s|}\right)^4 + |s|s^2d \left(\lambda_{li} + \mu \frac{\varphi}{|s|}\right)^3 + \\ & s^4e \left(\lambda_{li} + \mu \frac{\varphi}{|s|}\right)^2 + |s|s^4f \left(\lambda_{li} + \mu \frac{\varphi}{|s|}\right) + s^6g \end{aligned}$$

then the coefficients k_{xnl_i}, k_{znl_i} and $k_{\phi nli}$ ($n = 0, 1, 2, 3, 4$) are

$$k_{x4li} = (d_{330}^2 + c_{330}\varepsilon_{330})\zeta_{110}$$

$$\begin{aligned} k_{x3li} &= \left(\lambda_{li} + \mu \frac{\varphi}{|s|}\right) \{ [(d_{150} + d_{310})c_{330} - (c_{130} + c_{440})d_{330}]p_{z0} \\ & - ((d_{150} + d_{310})d_{330} + (c_{130} + c_{440})\varepsilon_{330})\zeta_{330} \} \\ & + 2\mu \frac{\Omega}{|s|} (d_{330}d_{330} + \varepsilon_{330}c_{330})\zeta_{110} \end{aligned}$$

$$\begin{aligned}
k_{x2li} &= \mu \frac{\Omega}{|S|} \left(\lambda_{li} + \mu \frac{\Psi}{|S|} \right) \left((c_{330}d_{310} - c_{130}d_{330} + 2(c_{330}d_{150} - c_{440}d_{330}))p_{z0} \right. \\
&\quad \left. - (d_{310}d_{330} + c_{130}\varepsilon_{330} + 2(d_{150}d_{330} + c_{440}\varepsilon_{330}))\zeta_{330} \right) \\
&\quad + \left(\frac{\Omega}{S} \right)^2 (d_{330}^2 + c_{330}\varepsilon_{330})\zeta_{110} - (2d_{150}d_{330} + c_{330}\varepsilon_{110} + c_{440}\varepsilon_{330})\zeta_{110} \\
&\quad - \varepsilon_{330}\zeta_{110}\rho_0 \left(\frac{p}{S} \right)^2
\end{aligned}$$

$$\begin{aligned}
k_{x1li} &= \left(\lambda_{li} + \mu \frac{\Psi}{|S|} \right) \left((c_{130}d_{150} - c_{440}d_{310})p_{z0} + (d_{150}^2 + d_{150}d_{310} + (c_{130} + c_{440})\varepsilon_{110})\zeta_{330} \right. \\
&\quad \left. + ((c_{330}d_{150} - c_{440}d_{330})p_{z0} - (d_{150}d_{330} + c_{440}\varepsilon_{330})\zeta_{330}) \left(\frac{\Omega}{|S|} \right)^2 \right. \\
&\quad \left. - (d_{150} + d_{310})p_{z0}\rho_0 \left(\frac{p}{|S|} \right)^2 \right) \\
&\quad - \mu \frac{\Omega}{|S|} \left((c_{330}\varepsilon_{110} + c_{440}\varepsilon_{330} + 2d_{150}d_{330})\zeta_{110} + \varepsilon_{330}\zeta_{110}\rho_0 \left(\frac{p}{|S|} \right)^2 \right)
\end{aligned}$$

$$\begin{aligned}
k_{x0li} &= \mu \left(\lambda_{li} + \mu \frac{\Psi}{|S|} \right) \frac{\Omega}{|S|} \left((d_{150}^2 + \varepsilon_{110}c_{440})\zeta_{330} - d_{150}p_{z0}\rho_0 \frac{p^2}{S^2} \right) + (d_{150}^2 + \varepsilon_{110}c_{440})\zeta_{110} \\
&\quad + \varepsilon_{110}\zeta_{110}\rho_0 \left(\frac{p}{|S|} \right)^2
\end{aligned}$$

$$k_{z4li} = - \left(\lambda_{li} + \mu \frac{\Psi}{|S|} \right) c_{440} (d_{330}p_{z0} + \varepsilon_{330}\zeta_{330})$$

$$\begin{aligned}
k_{z3li} &= -2\mu \frac{\Omega}{|S|} \left(\lambda_{li} + \mu \frac{\Psi}{|S|} \right) (d_{330}p_{z0} + \varepsilon_{330}\zeta_{330})c_{440} \\
&\quad - ((d_{150} + d_{310})d_{330} + (c_{130} + c_{440})\varepsilon_{330})\zeta_{110}
\end{aligned}$$

$$\begin{aligned}
k_{z2li} &= \left(\lambda_{li} + \mu \frac{\Psi}{|S|} \right) \left(-(c_{130}(d_{150} + d_{310}) + c_{440}d_{310} - c_{110}d_{330})p_{z0} \right. \\
&\quad + ((d_{150} + d_{310})^2 + c_{440}\varepsilon_{110} + c_{110}\varepsilon_{330})\zeta_{330} + \frac{p^2}{S^2}\rho_0(d_{330}p_{z0} + \varepsilon_{330}\zeta_{330}) \\
&\quad \left. - (\varepsilon_{330}\zeta_{330} + d_{330}p_{z0})c_{440} \frac{\Omega^2}{S^2} \right) \\
&\quad - \mu \frac{\Omega}{|S|} \left((d_{150}d_{330} + c_{440}\varepsilon_{330} + 2(d_{310}d_{330} + c_{130}\varepsilon_{330}))\zeta_{110} \right)
\end{aligned}$$

$$\begin{aligned}
k_{z1li} &= \mu \frac{\Omega}{|S|} \left(\lambda_{li} + \mu \frac{\Psi}{|S|} \right) \left(c_{110}(d_{330}p_{z0} + \varepsilon_{330}\zeta_{330}) - c_{130}(2d_{150} + d_{310})p_{z0} \right. \\
&\quad \left. + \zeta_{330}(c_{440}\varepsilon_{110} + (d_{150} + d_{310})^2) + \frac{p^2}{S^2}\rho_0(d_{330}p_{z0} + \varepsilon_{330}\zeta_{330}) \right) \\
&\quad - \zeta_{110}(d_{310}d_{330} + c_{130}\varepsilon_{330}) \frac{\Omega^2}{S^2} + (\varepsilon_{110}c_{130} + d_{150}^2 + d_{150}d_{310} + c_{440}\varepsilon_{110})\zeta_{110}
\end{aligned}$$

$$\begin{aligned}
k_{z0li} &= \left(\lambda_{li} + \mu \frac{\Psi}{|S|} \right) \left((\zeta_{330}d_{310} - p_{z0}c_{130})d_{150} \frac{\Omega^2}{S^2} - c_{110}(d_{150}p_{z0} + \varepsilon_{110}\zeta_{330}) \right. \\
&\quad \left. - (d_{150}p_{z0} + \varepsilon_{110}\zeta_{330})\rho_0 \frac{p^2}{S^2} \right) + \mu \frac{\Omega}{|S|} (d_{150}d_{310} + \varepsilon_{110}c_{130})\zeta_{110}
\end{aligned}$$

$$k_{\phi 4li} = \left(\lambda_{li} + \mu \frac{\Psi}{|S|} \right) (c_{330}p_{z0} - d_{330}\zeta_{330})c_{440}$$

$$\begin{aligned}
k_{\phi 3li} &= 2\mu \frac{\Omega}{|S|} \left(\lambda_{li} + \mu \frac{\Psi}{|S|} \right) (c_{330}p_{z0} - d_{330}\zeta_{330})c_{440} \\
&\quad + ((d_{150} + d_{310})c_{330} - (c_{130} + c_{440})d_{330})\zeta_{110}
\end{aligned}$$

$$\begin{aligned}
k_{\phi 2li} &= \left(\lambda_{li} + \mu \frac{\Psi}{|s|} \right) \left((c_{130}^2 - c_{110}c_{330} + 2c_{130}c_{440})p_{z0} + (c_{110}d_{330} - c_{440}d_{310} \right. \\
&\quad \left. - (d_{150} + d_{310})c_{130})\zeta_{330} - ((c_{330} + c_{440})p_{z0} - d_{330}\zeta_{330})\rho_0 \frac{p^2}{s^2} \right. \\
&\quad \left. + \frac{\Omega^2}{s^2} (c_{330}p_{z0} - d_{330}\zeta_{330})c_{440} \right) \\
&\quad + \mu \frac{\Omega}{|s|} (c_{330}d_{150} - c_{440}d_{330} + 2(c_{330}d_{310} - c_{130}d_{330}))\zeta_{110} \\
k_{\phi 1li} &= \mu \frac{\Omega}{|s|} \left(\lambda_{li} + \mu \frac{\Psi}{|s|} \right) \left(c_{130}^2 p_{z0} - d_{310}\zeta_{330}c_{130} - c_{110}(c_{330}p_{z0} - d_{330}\zeta_{330}) + 2(p_{z0}c_{130} \right. \\
&\quad \left. - d_{310}\zeta_{330})c_{440} + (-c_{330}p_{z0} - c_{440}p_{z0} + d_{330}\zeta_{330})\rho_0 \left(\frac{p}{s} \right)^2 \right) \\
&\quad - (d_{150} + d_{310})\zeta_{110}\rho_0 \left(\frac{p}{s} \right)^2 + \left(\frac{\Omega}{s} \right)^2 (c_{330}d_{310} - d_{330}c_{130})\zeta_{110} + (d_{150}c_{130} \\
&\quad - c_{440}d_{310})\zeta_{110} \\
k_{\phi 0li} &= \left(\lambda_{li} + \mu \frac{\Psi}{|s|} \right) \left(p_{z0}\rho_0^2 \left(\frac{p}{s} \right)^4 + (c_{110}p_{z0} + c_{440}p_{z0} - d_{150}\zeta_{330})\rho_0 \left(\frac{p}{s} \right)^2 \right. \\
&\quad \left. + \left(\frac{\Omega}{s} \right)^2 (c_{130}p_{z0} - d_{310}\zeta_{330})c_{440} + c_{110}(c_{440}p_{z0} - d_{150}\zeta_{330}) \right) \\
&\quad + \mu \frac{\Omega}{|s|} \left(c_{130}d_{150} - c_{440}d_{310} - d_{310}\rho_0 \left(\frac{p}{s} \right)^2 \right) \zeta_{110}
\end{aligned}$$

The coefficients $\chi_{ji}^{str}(s, p)$ ($str = zz, zx, dz$) are

$$\begin{aligned}
\chi_{ji}^{zz} &= (c_{440}\gamma_{ji}Z_{j1i} - c_{440}Z_{j2i} - d_{150}) \\
\chi_{ji}^{zx} &= (c_{440}(\gamma_{ji} + Z_{j1i}) + d_{150}Z_{j2i})|s| \\
\chi_{ji}^{dz} &= (d_{310}Z_{j1i} + d_{330}\gamma_{ji}Z_{j2i} - \varepsilon_{330}\gamma_{ji})
\end{aligned} \tag{C.3}$$

The P_{li}^{str} ($l = 1, 2$) defined as

$$\begin{aligned}
P_{li}^{zx} &= c_{440} \left(-\frac{L_{xli}}{p_{dli}} \left(\lambda_{li} + \mu \frac{\varphi}{|s|} \right) + P_{zli} \right) + d_{150} P_{\phi li} \\
P_{li}^{zz} &= c_{130} P_{xli} - c_{330} \frac{L_{zli}}{p_{dli}} \left(\lambda_{li} + \mu \frac{\varphi}{|s|} \right) - d_{330} \frac{L_{\phi li}}{p_{dli}} \left(\lambda_{li} + \mu \frac{\varphi}{|s|} \right) + \zeta_{330} \quad (C.4) \\
P_{li}^{dz} &= d_{310} P_{xli} - d_{330} \frac{L_{zli}}{p_{dli}} \left(\lambda_{li} + \mu \frac{\varphi}{|s|} \right) + \varepsilon_{330} \frac{L_{\phi l}}{p_{dli}} \left(\lambda_{li} + \mu \frac{\varphi}{|s|} \right) + p_{z0}
\end{aligned}$$

The functions κ_t^{str} are solved by

$$\begin{aligned}
\sum_{j=1}^6 |s| \chi_{j1}^{zz} A_{1j} - \{P_{11}^{zz} D_{11} + P_{21}^{zz} D_{12}\} D_0 &= |s| (\kappa_1^{zz} D_1 + \kappa_2^{zz} D_2 + \kappa_3^{zz} D_3) + \kappa_0^{zz} D_0 \\
\sum_{j=1}^6 |s| \chi_{j1}^{zx} A_{1j} - \{P_{11}^{zx} D_{11} + P_{21}^{zx} D_{12}\} D_0 &= |s| (\kappa_1^{zx} D_1 + \kappa_2^{zx} D_2 + \kappa_3^{zx} D_3) + \kappa_0^{zx} D_0 \quad (C.5) \\
\sum_{j=1}^6 |s| \chi_{j1}^{dz} A_{1j} - \{P_{11}^{dz} D_{11} + P_{21}^{dz} D_{12}\} D_0 &= |s| (\kappa_1^{dz} D_1 + \kappa_2^{dz} D_2 + \kappa_3^{dz} D_3) + \kappa_0^{dz} D_0
\end{aligned}$$